SRDS REPORT NUMBER RD 72-71

AD 750071

INSTRUMENT LANDING SYSTEM IMPROVEMENT PROGRAM

THIRD INTERIM REPORT

CONTRACT FA69WA-2066

AVIONICS RESEARCH GROUP

DEPARTMENT OF ELECTRICAL ENGINEERING

OHIO UNIVERSITY

Athens, Ohio 45701

June, 1972

OCT 27 1972

A

Availability is unlimited. Document may be released to the Clearinghouse for Federal Scientific and Technical Information, Springfield, Va. 22151 for sale to the public.

Reproduced by
NATIONAL TECHNICAL
INFORMATION SERVICE
U S Department of Commerce
Springfield Va 22151

Prepared for

FEDERAL AVIATION ADMINISTRATION

SYSTEMS RESEARCH AND DEVELOPMENT SERVICE

Washington, D.C. 20591

The contents of this report reflect the views of the Avionics Research Group, Department of Electrical Engineering, Ohio University, which is responsible for the facts and the accuracy of the data presented herein. The contents do not necessarily reflect the official views or policy of the Department of Transportation. This report does not constitute a standard, specification or regulation.

TECHNICAL REPORT STANDARD TITLE PAGE

1. Report No. SRDS RD FAA-PD-72-71	2. Government Accession No.	3. Recipient's Catalog No.
4. Title and Subtitle INSTRUMENT LANDING SYSTEM IMPROVEMENT PROGRAM		5. Report Date June 1972
		6. Performing Organization Code
7. Author(s) AVIONICS STAFF		8. Performing Organization Report No. EER 5-12
9. Performing Organization Name and Address Avionics Research Group, Department of Electrical Engineering, Ohio University, Athens, Ohio 45701		10. Work Unit No
		11. Contract or Grant No. FA69WA-2066
12. Sponsoring Agency Name and Address Federal Aviation Administration, Systems Research and Development Service, Washington, D. C. 20591		13. Type of Report and Period Covered Interim, February 1971 to January 1972
		14. Sponsoring Agency Code
15. Supplementary Notes		

16. Abstract

Results of the third year of technical investigations at Ohio University to provide improvement in ILS performance are presented. More than 12 separate tasks are reported with major emphases on integral analog monitoring for the glide slope and localizer, new localizer design for minimization of path perturbation due to multipath, and development of a mathematical model for predicting effects on the glide path of signals reflecting from jumbo aircraft. Also, results have been obtained from analyses of snow cover effects on the glide path. Analyses to determine modulator and bridge tolerances are presented together with recommendations for revised tolerances. Specifications and tolerances are presented for preparation of the ground planes in the vicinity of image glide paths. These are based on previously developed mathematical models. Conclusions and recommendations for improvements in glide path performance at specific sites are presented from work done in providing special consultations for the FAA at Travis Air Force Base, Detroit Metropolitan Airport, and Monterey, California.

17. Key Words: Snow Cover Effects, Image Antenna Systems, Theodolite Reference, Multipath, Instrument Landing, Glide Path, Localizer, Modulator Tolerances, Antenna Probes		18. Distribution Statement: Availability is unlimited. Document may be released to the Clearinghouse for Federal and Technical Information, Springfield, Virginia 22151, for sale to the public.
19. Security Classif. (of this report) Unclassified	20. Security Classif. (of this page) Unclassified	21. No. of Pages 310
		22. Price

Form DOT F 1700.7 (8-69)

TABLE OF CONTENTS

		PAGE
	List of Figures	vi
	List of Tables	xv
I	SUMMARY AND INTRODUCTION	1
II	ILS GLIDE SLOPE	3
	A. The Glide Path Theodolite Reference	3
	1. Purpose	3
	2. Discussion of References for Glide Path Measurements	3
	3. Recommendation	5
	4. Comments on Recommendation	8
	a. Philosophy	8
	b. Optimization Considerations	8
	B. Glide Path Siting Problem	12
	C. Special Glide Path Problems	14
	1. Travis Air Force Base Considerations	14
	a. Introduction	14
	b. Statement of the Problem	14
	c. Analysis	14
	d. Measurements	16
	e. Measurement Tolerances	16
	f. Considerations for Location of Reference System	20
	g. Error Analysis of the Theodolite Tracking of Glide Path Due to Theodolite Position	21
	h. Conclusions Relating to the Travis AFB Glide Path Site	27
	i. Recommendations	28
	2. Detroit Glide Path Special Problem	30
	a. Analysis	30
	b. Measurements	32
	c. Conclusions	35

PAGE

3. Monterey, California 38
   a. Introduction 38
   b. Observations 38

4. Pittsburgh Category II Problem 49

D. Glide Path Critical Areas 50
   1. Disturbance of Glide Path by Reflections from Aircraft (Boeing 747) Fuselage and Tail Fin 50
      a. Introduction 50
      b. Incident Fields 50
      c. Tangential H Fields on Cylindrical Fuselage with Axis Parallel to Runway Centerline 57
         1) Approximation by Use of Local Wavenumber 57
         2) Comparison of Results 62
      d. Scattered Electrical Field from Cylindrical Fuselage 62
      e. Scattered Electric Field from Sweptback Vertical Tail Fin in Close Proximity to Antenna 73
      f. Computation of Microampere Course Deviation Indicator Deflection from Scattered Electric Fields 81
      g. Results and Conclusions 83
         1) Results 83
         2) Conclusions 84

   2. Glide Path Derogation Due to Reflections from Aircraft in Selected Location 93

   3. Comparison of Mathematical and Physical Models for Glide Path Performance in the Presence of Reflections from Aircraft 127

E. Snow Cover Effects on Glide Paths 128
   1. A Worst Case Approach to Glide Path Errors Caused by Snow Cover 128
      a. Introduction 128
      b. Geometric Analysis 128
      c. Recommendations 152

		PAGE
	2. Measurements of Far-Field Glide Path Angles at Sites with Heavy Snow Cover	153
	a. Introduction and Background	153
	b. Measurement Technique	156
	c. Discussion of Data	158
	d. Conclusions and Recommendations	159
	3. Snow Site Implementation with Far-Field Monitoring	161
	F. Glide Slope Integral Analog Monitor	166
	G. Effects of Truncated Ground on Image Glide Paths	170
	1. Performance of Glide-Slope Arrays on Sites with Limited Ground Planes	170
	a. Introduction	170
	b. Results of the Analysis	170
	1) Null Reference	170
	2) Capture Effect	170
	2. Additional Study of Capture-Effect Glide Slope	182
	a. Introduction	182
	b. SB to CSB Phase Difference with Limited Ground Plane	182
	c. Radiation from Individual Antennas of Capture-Effect Array	182
	d. Effects of Antenna Offset	189
	3. Extension of Ground Plane of an ILS Glide Slope by Horizontal, Parallel Wires	193
	a. Introduction	193
	b. Theory	193
	c. Computations	196
	H. L-Band Glide Path Investigation	201
III	ILS LOCALIZER	202
	A. Design of a Localizer Array	202
	1. Design and Flight Testing of a Localizer Array That Provides Clearance Signal Only Within $\pm 35°$ of Center Line	202
	a. Introduction	202
	b. Array Design	202

PAGE

1.
c. Distributor and Suppression of Parasitics 207
d. Flight Testing 212
e. Computed Comparison of Scalloping Generated by 35° Localizer and Other Localizer Arrays 218
f. Conclusions 218

B. Localizer Monitors 221
1. Results of Flight Tests of Integral and Seven-Element Near-Field Localizer Monitors 221
a. Summary 221
b. Test Arrangement and Fault Description 221

2. Data for Implementation 225

3. A Method for Minimizing the Effects of Overflight on the Localizer Monitors 226
a. Past Investigations 227

IV ILS MODULATOR TOLERANCE STUDY 230

A. Summary 230

B. Introduction 230

C. Digital Modeling of Localizer Signals in Space 231
1. Program No. 113 231
2. Program No. 114 232
3. Program No. 116 232
4. Program No. 117 232
5. Subroutine No. 113 232
6. "E" Variable Data Deck 234

D. Results of the Digital Modeling of the Signal in Space 234

E. 51R-3 VHF Navigation Receiver Tests 235
1. 51R-3 Bandpass Characteristics 235
2. 51R-3 Response to a Signal Containing Harmonics 235
a. Laboratory Test Arrangement 237
b. Laboratory Test Results 243
c. The Effects of Distortion 245

		PAGE
	F. Fourier Analysis of Waveforms	247
	G. Digital Modeling of Glide Slope Signals in Space	247
	1. Effects of Distortion	251
V	INVESTIGATORS AND ACKNOWLEDGMENTS	253
VI	REFERENCES AND BIBLIOGRAPHY	255
VII	GLOSSARY	257
VIII	APPENDICES	258
	A. Equations Used in the Computation of Radiation Patterns	259
	B. Glide Path Sites Classified as to Likelihood of Presence of Snow on the Ground Planes	262
	C. Glide Path Data Relating to Speed Measurements Made on Snow Effects in February, 1971	269
	D. Calculation of H-Fields on Fuselage	297
	E. Radiation Field of an Antenna Placed Over Irregular Terrain	301
	F. Nature of the Doppler-Shifted Interferences Encountered During Over Flights	303
	G. Mathematical Model of a Monitor Receiver	305

LIST OF FIGURES

		PAGE
Figure 2-1.	Venn Diagram.	4
Figure 2-2.	Glide Path Positions Referenced to the Generating System.	10
Figure 2-3.	Recommended Maximum Allowable Slopes for Grading Terrain in Front of Glide Path Transmitting Array.	13
Figure 2-4.	Selected Terrain Profiles at Travis Air Force Base.	17
Figure 2-5.	Terrain Profile at Travis Air Force Base.	18
Figure 2-6.	Terrain Profile at Travis Air Force Base.	19
Figure 2-7.	Coordinate System.	21
Figure 2-8.	Elevation Angle Re: Coordinate System.	23
Figure 2-9.	Optical Angle Re: Coordinate System.	24
Figure 2-10.	Example of Correction Chart Showing Calculation Introduced by Aircraft Departing from Zero DDM Line of the Glide Path for the Case When the Theodolite Coordinate Center is Not Collocated with the Electronic Glide Path Origin.	26
Figure 2-11.	Ground Plane Terrain Profile at Detroit.	31
Figure 2-12.	Definition of Data Collection Points at Detroit.	34
Figure 2-13.	Experimental Equipment Used in Performing Measurements of Glide Path and Site Conditions on Runway 3L at Detroit Metropolitan Airport. The Capture Effect Array Shown on the Left is the Commissioned Facility. The One on the Right with a Man Making an Antenna Adjustment was Used for Comparative Measurement of Ground Plane Conditions and Parasitic Radiation. The Beechcraft 35 was in the Position Shown to Permit Calibration of Receivers, Theodolite, and Telemetry Equipment.	37

		PAGE
Figure 2-14.	Flight Data, CRW. April 8, 1971.	39
Figure 2-15.	ILS Approach Plate for Monterey, California.	41
Figure 2-16.	Monterey, California. Typical Crossover 1000 Feet. Capture Effect Glide Slope. Centerline. December 1969. Width = 0.69°.	42
Figure 2-17.	Monterey, California, December 29, 1969, Transmitter No. 1, Sideband Reference System.	43
Figure 2-18.	Monterey, California. Normal Approach. Theodolite References Shown as Spots. Transmitter No. 2. Sideband References System. Path Angle -3.0°. June 28, 1971. (No RTT).	44
Figure 2-19.	Monterey Peninsula Airport.	46
Figure 2-20.	Monterey, California.	47
Figure 2-21.	Plan View, Geometry of the Problem.	51
Figure 2-22.	Section A-A of Figure 2-21.	52
Figure 2-23.	Geometry of the Cylindrical Fuselage and Its Image.	53
Figure 2-24.	Geometry of Vertical Tail Fin.	74
Figure 2-25.	Geometry of the Tail Fin and Its Image.	77
Figure 2-26.	Vertical Plane Containing Transmitting Antenna Pole and Aircraft Receiving Point.	82
Figure 2-27.	Geometry of Aircraft Position, Antenna Pole and Runway Centerline for Results Shown in Figures 2-28, 2-29, and 2-30.	85
Figure 2-28.	Amplitude of Glide Path Roughness for D = 200 Feet in Figure 2-27.	86
Figure 2-29.	Amplitude of Glide Path Roughness for D = 500 Feet in Figure 2-27.	87

		PAGE
Figure 2-30.	Amplitude of Glide Path Roughness for D = 800 Feet in Figure 2-27.	88
Figure 2-31.	Amplitude of Glide Path Roughness for D = 1500 Feet, XF = -400 Feet in Figure 2-27. The Axis of the Fuselage Intersects the Centerline at an Angle of 10°.	89
Figure 2-32.	Amplitude of Glide Path Roughness for D = 1200 Feet in Figure 2-27. Fuselage is Parked Perpendicular to Centerline.	90
Figure 2-33.	Amplitude of Glide Path Roughness for D = 1200 Feet in Figure 2-27. Fuselage is Parked Perpendicular to Centerline.	91
Figure 2-34.	Amplitude of Glide Path Roughness for D = 1201.5 Feet in Figure 2-27. Fuselage is Parked Perpendicular to Centerline.	92
Figure 2-35.	Layout of Points of Interest for Calculating Effects of Signals Reflecting From a Boeing 747.	96
Figure 2-36. Through Figure 2-65.	Points of Interest for Boeing 747 Calculation Reference. (Table 2-8) and (Figure 2-35) Preceding.	97
Figure 2-66.	Coordinate System for Geometric Analysis.	129
Figure 2-67.	Phasor Construct Showing the Range of Carrier Phasors due to 80% Surface Reflection.	137
Figure 2-68.	Phasor Construct Showing Range of Sideband Phasors due to 80% Surface Reflection.	138
Figure 2-69.	Construct for Showing Range of DDM for 80% Surface Reflection.	139
Figure 2-70.	Phasor Construct Showing DDM Ranges with 2λ Snow Depth at 2000λ (Far-Field) and 100λ Altitude (on Glide Path).	141

		PAGE
Figure 2-71.	Phasor Construct Showing DDM Ranges with 2λ Snow Depth at 2000λ (Far-Field) and 110λ Altitude (.3° above Glide Path).	142
Figure 2-72.	Phasor Construct for 2000λ (Far-Field) and 100λ Altitude (no Glide Path) with no Snow and with 2λ Snow Depth.	143
Figure 2-73.	Phasor Construct for 2000λ (Far-Field) and 110λ Altitude (.3° above Glide Path) with no Snow and with 2λ Snow Depth.	144
Figure 2-74.	Simplified Sideband Phasor Construct for Worst Case.	145
Figure 2-75.	Path Angle versus Snow Depth -- Worst Cases. $\epsilon_R = 1.1$.	146
Figure 2-76.	Path Angle versus Snow Depth -- Worst Cases. $\epsilon_R = 3.6$.	147
Figure 2-77.	Path Angle versus DDM. Range = 720 Feet, Minimum Snow Depth.	148
Figure 2-78.	Path Angle versus DDM. Range = 720 Feet, Snow Depth = 7.2 Feet.	149
Figure 2-79.	Path Angle versus DDM. Range 7220 Feet, Minimum Snow Depth.	150
Figure 2-80.	Path Angle versus DDM. Range 7220 Feet, Snow Depth= 7.2 Feet.	151
Figure 2-81.	Measured Path Indications for Various Snow Depths.	160
Figure 2-82.	Capture Effect Glide Slope Array Used for Environmental Testing at the Michigan Snow Site. Integral Monitoring is Being Effected with the Coupling Probes not Visible in the Corner Reflector Antenna Units. A Sideband Reference Array for Snow Experiments is Visible in the Background.	162

PAGE

Figure 2-83.	Snow Monitor Site North of Grand Rapids, Michigan. View is looking out From the Transmitting Arrays, the Sideband Reference Antennas are Shown on the Left. Near-Field Monitors are also Shown. There is Approximately 2,000 Feet of Flat, Unobstructed Terrain in the Direction of the Far-Field Monitor Tower Which has Been Retouched in the Photograph for Clarity. This Tower is 3 Miles Distant and Supports the Far-Field Clearance and Course Monitor Probes.	163
Figure 2-84.	Yagi Probe Antenna Which was Mounted on the 900-Foot WZZM-TV Tower for Monitoring Far-Field Path Angle. A Duplicate Antenna was Used for Obtaining Path Width Data.	165
Figure 2-85.	Combining Circuits for Integral Monitor.	167
Figure 2-86.	Grant, Michigan, Snow Site. Error in Readings of Integral or Near-Field Monitors. December 1971.	169
Figure 2-87.	Computed Sideband Patterns of Null Reference Array Over Ground Planes of Several Lengths.	171
Figure 2-88.	Computed DDM Generated by Null Reference Array Over Ground Planes of Several Lengths.	172
Figure 2-89.	Computed Sideband Patterns of Capture Effect Array Over Ground Planes of Several Lengths.	173
Figure 2-90.	Computed Carrier Patterns of Capture Effect Array Over Ground Planes of Several Lengths.	174
Figure 2-91.	Computed Clearance Signal Pattern of Capture Effect Array Over Finite Ground Planes of Several Lengths.	175
Figure 2-92.	Computed DDM Generated by Capture Effect Array, Without Clearance Signal, Over Ground Planes of Various Lengths.	176

PAGE

Figure 2-93.	Sideband Pattern of Sideband Reference Antenna for Several Lengths of Ground Plane.	178
Figure 2-94.	Carrier Pattern of Sideband Reference Antenna for Several Lengths of Ground Plane.	179
Figure 2-95.	DDM Generated by Sideband Reference Antenna for Several Lengths of Ground Plane.	180
Figure 2-96.	Figure of Merit of Several Glide Path Arrays versus Length of Ground Plane.	181
Figure 2-97.	Computed Phase Difference Between SB and SCB Signals--Capture Effect Glide Slope.	183
Figure 2-98.	Capture Effect DDM Over 450' Ground Plane --With and Without SB Lead.	184
Figure 2-99.	Amplitude of Radiation from Top Antenna of Capture Effect System for Several Ground Plane Lengths.	185
Figure 2-100.	Phase of Radiation from Bottom Element of Capture Effect Glide Slope, for Several Lengths of Ground Plane.	186
Figure 2-101.	Phase of Radiation from Center Element of Capture Effect Glide Slope, for Several Lengths of Ground Plane.	187
Figure 2-102.	Phase of Radiation from Top Element of Capture Effect Glide Slope, for Several Lengths of Ground Plane.	188
Figure 2-103.	Effect of 30° Lead in Top Element on DDM Generated by a Capture Effect System Over a 450' Ground Plane.	190
Figure 2-104.	DDM Generated by a Capture Effect System Over a 450' Ground Plane at 8° Off Localizer (G. P. Tower Side) -- With and Without Offset.	191
Figure 2-105.	DDM Generated by a Capture Effect System Over a 600' Ground Plane at 8° Off Localizer (G. P. Tower Side), With and Without Antenna Offset.	192

		PAGE
Figure 2-106.	Assumed Configuration.	193
Figure 2-107.	Program for Calculating Reflection Coefficients.	198
Figure 2-108.	Continuations of Programs for Calculating Reflection Coefficients.	199
Figure 2-109.	Reflection Coefficients for Various Wire Sizes and Spacings.	200
Figure 2-110.	Suggested Laboratory Implementation of L-Band Glide Path.	201
Figure 3-1.	V-Ring Array at Ohio University Test Site Used for Testing the Special Configuration to Provide Localizer Coverage only Within ± 35°. Careful Inspection of the Picture Will Reveal a White Radome on Top of Each Pedestal. These Radomes House the Integral Monitor Coupling Probes.	203
Figure 3-2.	Design Sideband Pattern -- 35°.	206
Figure 3-3.	Design CSB Pattern -- 35°.	208
Figure 3-4.	Computed DDM Width = 7.0°.	209
Figure 3-5.	Divider Section.	210
Figure 3-6.	Measured SB Pattern --35° Localizer.	214
Figure 3-7.	Measured CSB Pattern -- 35° Localizer.	215
Figure 3-8.	Measured DDM - 35° Localizer Width = 4.68°.	216
Figure 3-9.	Measured DDM - 35° Localizer Width = 7.0°.	217
Figure 3-10.	Measured DDM -- 35° Localizer Width = 7.0°.	220
Figure 3-11.	Close-up View of Coupling Probe Used to Sample the Current in a V-Ring Localizer Element. Fifteen such Loops are Used in the Integral Monitoring Scheme.	222

		PAGE
Figure 3-12.	Block Diagram of Overflight System.	226
Figure 3-13.	Over Flight Monitoring and Recording Setup for the Localizer.	228
Figure 4-1.	Radiation Pattern -- Single V-Ring Antenna, Type FA-S549X.	233
Figure 4-2.	Bandpass Characteristic Test Arrangement.	236
Figure 4-3.	Bandpass Response. 51R-3 Receiver -- High Level.	240
Figure 4-4.	Bandpass Response. 51R-3 Receiver -- Low Level.	241
Figure 4-5.	90 Hz Harmonic Generation.	242
Figure 4-6.	90 Hz Output From Mechanical Modulator.	248
Figure 4-7.	150 Hz Output From Mechanical Modulator.	248
Figure 4-8.	Comparison of Actual and Calculated Orbit. Actual ——. Calculated ---.	250
Figure 4-9.	Filter Sensitivity, Collins 51V.	251

Appendices

Figure C-1.	Grand Rapids, Michigan	270
Figure C-2.	Green Bay, Wisconsin	273
Figure C-3.	Appleton, Wisconsin	275
Figure C-4.	Duluth, Minnesota	277
Figure C-5.	Minneapolis, Minnesota	279
Figure C-6.	Minneapolis, Minnesota	280

		PAGE
Figure C-7..	Rochester, Minnesota	282
Figure C-8.	Madison, Wisconsin	284
Figure C-9.	Milwaukee, Wisconsin	286
Figure C-10.	Milwaukee, Wisconsin	286
Figure C-11.	Mansfield, Ohio	289
Figure C-12.	Akron- Canton Ohio	291
Figure C-13.	Youngstown, Ohio	293
Figure D-1.	Assume Antenna and Fuselage in Plane of Paper.	297
Figure F-1.	Overflight Geometry.	303
Figure F-2.	Doppler Shift.	304
Figure G-1.	Monitor Receiver Configuration I.	306
Figure G-2.	Monitor Receiver Configuration II.	308

LIST OF TABLES

		PAGE
Table 2-1.	Calculated Angular Differences (in microamperes) Between a Glide Path Formed by a Flat Ground 5 Feet Lower than a Runway Existing on a Pedestal. These are the Relevant Numbers Showing Why a Glide Path Could Not Meet Specifications for Category II Even if the Path Had a Perfect Shape Leading Correctly to the Threshold Window.	6
Table 2-2.	Calculated Difference between Ideal Path and a Practically Generated Curve with Proper Sensitivities for Differential Amplifier. The Case is for a Pedestal of 5 Feet and an Additional Displacement Down the Runway of 108 Feet to Give a Total of 1233 Feet to the Point Where the Glide Path Transmitting Antennas are Located.	7
Table 2-3.	Results of Field Measurements Made at the Detroit Site.	8
Table 2-4.	Comparison of Incident E_Φ (Φ, 1500) and Scattered E_Φ (Φ, 1500). Columns 3 and 4 are the Scattered E_Φ by the Wave Expansion Method.	61
Table 2-5.	Comparison of Incident E_Φ (Φ, 1500) and Scattered E_Φ (Φ, 1500). Columns 3 and 4 are the Scattered E_Φ by the Wave Expansion Method.	63
Table 2-6.	Comparison of Incident H_Φ (Φ, 1500) and Scattered H_Φ (Φ, 1500). Columns 3 and 4 are the Scattered H_Φ by the Wave Expansion Method.	64
Table 2-7.	Comparison of Incident H_z (Φ, 1500) and Scattered H_z (Φ, 1500). Columns 3 and 4 are the Scattered H_z by the Wave Expansion Method.	65

		PAGE
Table 2-8.	Definition of Points of Interest for Boeing 747 Calculation Reference (Figure 2-35).	95
Table 2-9.	Ray Incidence Angles for Various Snow Depths (Linear Dimensions in Wavelengths).	133
Table 2-10.	Reflection Coefficients for Snow at Incidence Angles of 75° to 89.9° for Relative Dielectric Constant 1.1 to 10.1.	134
Table 2-11.	Summary of Glide Path Measurements.	154
Table 3-1.	35° Localizer SB and CSB Currents at 110.5 MHz.	213
Table 3-2.	Summary of Monitor Test Results.	224
Table 4-1.	Present Allowable Modulator Tolerances.	234
Table 4-2.	Low-Level Bandpass Response 51R-3 (125 μ a).	238
Table 4-3.	High-Level Bandpass Response 51R-3 (250 μ a).	239
Table 4-4.	150 Hz in 90 Hz - 10%.	243
Table 4-5.	180 Hz in 90 - 25%.	243
Table 4-6.	270 Hz in 90 - 33%.	244
Table 4-7.	90 Hz in 150 Hz- 10%.	244
Table 4-8.	300 Hz in 150 Hz -33%.	244
Table 4-9.	450 Hz in 150 Hz - 45%.	245
Table 4-10.	Harmonic Content of 90 and 150 Hz Outputs of Mechanical Modulator.	249
Table 4-11.	Recommended Mechanical Modulator Tolerances.	252

I SUMMARY AND INTRODUCTION

This report summarizes the progress in the work performed by Ohio University during 1971 under Contract FA69WA2066. The purpose of the work is to provide for improvements in contemporary instrument landing systems through the development of new techniques, designs, and analyses. Some of the topics reported here are continuations of previous efforts or are initial investigations which are continuing. This is the third in the series of progress reports, the previous ones carrying the same title with SRDS report numbers RD 70-9 and RD 71-30 respectively.

More than 12 separate topics or tasks have been undertaken and each is discussed in this report. Numerous special consultatations have been provided to the FAA. Of particular note are the Travis AFB, Detroit, and Monterey, California, sites. In each case following the investigation recommendations were made for obtaining improved glide path performance, in the first two cases with respect to Category II operations. Consultations have also been provided on reference theodolite placement, integral monitoring of arrays, and snow effects on glide path performance.

Extensive analyses have been performed to provide predictions of effects of jumbo aircraft on the glide path in space. From this work will come specific identification of zones or critical areas where aircraft must not be allowed to exist during times when instrument approaches are in progress.

Analyses have continued on predicting the effects of snow cover on the ground plane of an image glide path. A worst case approach has been developed and indications are that with less than two feet of snow the glide path should remain in tolerance of the far-field. Aircraft measurements have been completed at over 15 sites to determine the effects of deep layers of snow. These results are also encouraging by indicating that even though the monitor may be at alarm the far-field is well within tolerances. Further, indications are that in all cases the deviations of the path are increases in path angle. A special snow monitoring facility has been established in central Michigan to continuously monitor far-field snow effects on the capture effect, null-reference, and sideband reference system. Near-field effects are also being recorded.

Considerable effort has been expended on the development of integral monitors for the localizer and glide path. Also, investigations of the behavior of image glide paths in the presence of limited ground planes have been conducted.

An investigation aimed at reducing the coverage of the V-Ring localizer array to ± 35 degrees and improving its performance in such areas as mutual coupling and monitoring was initiated.

A special investigation to determine the tolerances which should be applied to the ILS modulators and bridges has been completed. Refinements have been provided for modifying existing specifications. From glide path site analysis, recommendations have been prepared which indicate the specifications and tolerances which should be applied to grading of terrain in the vicinity of an image glide path system.

Performance and stability of the newly-designed directional, collinear antenna for the glide path has been investigated and found to perform well during a variety of environmental conditions. Use in a capture effect system with integral monitoring has been accomplished with encouraging results.

All conclusions and recommendations are presented immediately following the technical discussion for the convenience of the reader. Plans for new investigations are also presented and these are related directly to the overall objective of improved ILS performance.

The reader is encouraged to become familiar with the previous reports in this series in order that he have a good background for that which is written in this report. An effort has been made not to duplicate material contained in the previous reports.

This is an annual documentation which has been preceded in most cases by the issuance of special technical memoranda treating specific problems and revealing relevant results. Memoranda numbered 17 through 33 are summarized in this report.

In each of the investigations the objective has been to obtain results in a form which can be translated efficiently by the FAA into a practical reality. A special effort has been made to avoid recommendations which place undue complications in the process of bringing the results of this work to the ILS user.

II ILS GLIDE SLOPE

A. The Glide Path Theodolite Reference

1. Purpose

First in this section some observations are made concerning the criteria of acceptability used to commission Category II glide path facilities; and then, some recommendations are given which would permit the criteria involving theodolite references in particular to be more generally applicable. One objective is to minimize the number of special cases which must be handled.

2. Discussion of References for Glide Path Measurements

In order for criteria to have meaning, a reference or standard must be established and a kind of yardstick provided with which the observed deviations of the variable of interest may be quantified. With the advent of the radio telemetering theodolite (RTT) a few years ago a reference and yardstick became available for assessing the performance of glide path systems.

Initially, it will be recalled that the theodolite was intuitively placed near the runway to provide for the reference a straight line and angle from the point of intended touchdown on the instrument runway. The geometric problem of having involved in the measurements two different conical geometries, i. e., one of the theodolite reference system and one of the electronic glide path become bothersome. Angular quantities measured in one system with its coordinate center at the base of the antenna could not easily or directly be related to the other system which had its reference displaced many feet to a point near the runway. Direct subtraction of the measured angular quantities by an electronic differential amplifier onboard the aircraft would give meaningless quantitative results.

Considering this it was logical to move the coordinate center of one of the systems to be coincident with the other. Practicality dictated that the theodolite reference coordinates be moved to coincide with the electronic system. Because this coordinate center is near the earth's surface, a compromise point in front of the antenna system on the glide path cone was chosen for convenience of the theodolite operator. Former FAA Order 8200.11A specified this standard and required the electronic path perform within 20 microamperes of the reference.

It was not long before a practical problem at Atlanta, Georgia, revealed that this reference system provided perhaps a good means of checking the electronic qualities of the path but it did not give a true picture of how acceptable the path was for the pilot who had to be using it to approach for landing on the runway. SRDS Report RD 69-4 discusses the Atlanta case where nature fortunately was providing a glide path above the runway centerline extended nearly that obtained

with an ideal, infinite, flat ground plane, but the FAA order was disqualifying the Atlanta site because the reference system was to the base of the antenna located several feet lower in elevation than the runway. In spite of the fact that a nearly ideal hyperbolic path was formed referencing the runway, the theodolite being lower than the runway made the path appear high and out-of-tolerance.

To eliminate this inconsistent behavior between the path and the reference, FAA Order 8200.11B was written which specified that the theodolite system be referenced to the runway elevation while keeping it at the axis of the electronic glide path cone to insure maximum consistency in the angular measurements from the two systems.

With 8200.11B a sound theoretical basis for determining the location of the reference system was established. The practical operating point in front of the transmitting antenna for theodolite operator comfort introduced negligible error. However, a practical problem soon became evident when San Francisco, which had been considered acceptable for Category II, no longer met the Category II requirements given by 8200.11B. All those concerned nevertheless agreed that the San Francisco path was safe and was Category II quality as evidenced by the safe operation over past years.

A note concerning some logic concepts is appropriate here. Order 8200.11B provided some sound, sufficient conditions for Category II flyability. It said in effect that if one meets the requirements of this order, then one has Category II flyability. It did not say, that if one has Category II flyability, then one meets the conditions of 8200.11B. In other words, the order specifies sufficient but not necessary conditions for Category II.

It may be instructive to refer to the two circles A and B of Figure 2-1.

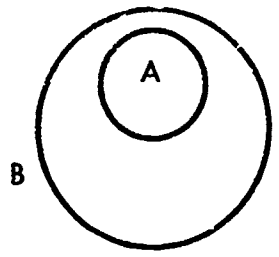

Figure 2-1. Venn Diagram.

The proposition can be stated: If A, then B, A being a sufficient condition for B. The converse of the proposition is not true. The inverse of the statement, viz., if not A, then not B may or may not be true. A is not a necessary condition for B.

For most purposes it would be desirable to have both the statement and its converse, if B, then A be true which would mean that the two circles could be superimposed and A would be both a necessary and sufficient condition for B. With practical regulations and rules, this desirable situation usually cannot be realized without extreme complication and the best that can be hoped for is that the circle A be made as large as possible. If one considers A to be "meets criteria of 8200.11B" and B to be "Category II flyability" the argument can readily be applied to the glide path acceptability problem as was done in the preceding paragraph.

The circle A was not large enough to include the San Francisco case. No fundamental error existed. An enlargement of circle A was accomplished by paying a penalty of complication in providing a sliding scale to insure proper threshold crossing values. This was published as FAA Order 8240.20.

An investigation of existing terrain configurations at Travis Air Force Base, and reported to exist at other U. S. Air Force bases, indicates that the circle should be broadened further to include more cases which produce Category II flyable paths. The reluctance to do this naturally comes from the desire to minimize the complexity of orders (specifications) which frequently present significant difficulties for those applying them in the field.

Accordingly a recommendation follows which increases the area of the specification circle somewhat to include more cases where Category II flyability can exist, some of which may be expected to be found at Air Force base sites. The following recommendation is consistent with the theory and philosophy used for previous orders.

3. Recommendation

The recommendation is that the specification of the FAA Order 8240.20 be changed to the following: Placement of the theodolite eyepiece should be at runway elevation above a point defined by the intersection of the straight line joining the antenna and the threshold and the line perpendicular to the runway centerline at the point of intersection with the straight line glide path (asymptote of the hyperbola). The straight line glide path is defined by a given elevation angle and crossing the threshold at a specified height.

In the event calculations such as given in Table 2-1 involving the geometries and relative positions of the transmitting antennas, theodolite position, and threshold, indicate errors greater than 15 microamperes, then an alternate position of the theodolite at the base of the antennas may be appropriate, provided calculations show errors are no greater than 6 microamperes (0.03 degree) at the threshold. An example of the results of such a calculation are shown in Table 2-2.

Distance in feet from point on runway opposite antenna mast. For the Travis case, distance = 1217' from threshold.	Difference in microamperes between Path (3) and Path (4). Reference Figure 2-2.
0.0	126.1
200.0	116.6
400.0	97.35
600.0	79.36
800.0	65.46
1000.	55.11
1200.	47.32
1400.	41.34
1600.	36.64
1800.	32.66
2000.	29.77
2200.	27.19
2400.	25.02
2600.	23.16
2800.	21.56
3000.	20.16
3200.	18.93
3400.	17.84
3600.	16.86
3800.	15.99
4000.	15.20
4200.	14.49
4400.	13.84
4600.	13.24
4800.	12.70
5000.	12.19
5200.	11.73
5400.	11.30
5600.	10.90
5800.	10.53
6000.	10.18
6200.	9.851
6400.	9.545
6600.	9.257
6800.	8.986
7000.	8.730
7200.	8.489
7400.	8.261
7600.	8.044
7800.	7.839
8000.	7.643
8200.	7.458
8400.	7.281
8600.	7.112
8800.	6.951
9000.	6.797
9200.	6.649
9400.	6.508
9600.	6.373
9800.	6.243
10000.	6.119

Table 2-1. Calculated Angular Differences (in microamperes) Between a Glide Path Formed by a Flat Ground 5 Feet Lower than a Runway Existing on a Pedestal. These are the Relevant Numbers Showing Why a Glide Path Could Not Meet Specifications for Category II Even if the Path Had a Perfect Shape Leading Correctly to the Threshold Window.

Distance in feet from Ideal Reference Touchdown 1125' from Threshold Path (1)	Difference in microamperes between Path (1) and Path (3) Reference Figure 2-2.
0.0	112.2
200.0	62.79
400.0	31.01
600.0	15.71
800.0	8.587
1000.	5.072
1200.	3.202
1400.	2.135
1600.	1.488
1800.	1.075
2000.	0.8005
2200.	0.6112
2400.	0.4770
2600.	0.3791
2800.	0.3061
3000.	0.2507
3200.	0.2078
3400.	0.1741
3600.	0.1473
3800.	0.1259
4000.	0.1089
4200.	0.09400
4400.	0.08236
4600.	0.07214
4800.	0.06356
5000.	0.05620
5200.	0.05027
5400.	0.04516
5600.	0.04067
5800.	0.03678
6000.	0.03311
6200.	0.03004
6400.	0.02779
6600.	0.02534
6800.	0.02309
7000.	0.02084
7200.	0.01941
7400.	0.01819
7600.	0.01655
7800.	0.01553
8000.	0.01451
8200.	0.01328
8400.	0.01247
8600.	0.01185
8800.	0.01083
9000.	0.01022
9200.	0.009605
9400.	0.008992
9600.	0.008379
9800.	0.008174
10000.	0.007357

Table 2-2. Calculated Difference Between Ideal Path and a Practically Generated Curve with Proper Sensitivities for Direct Readout of Differential Amplifier. The Case is for a Pedestal of 5 Feet and an Additional Displacement Down the Runway of 108 Feet to Give a Total of 1233 Feet to the Point Where the Glide Path Transmitting Antennas are Located.

For cases where these conditions cannot be met then a special data reduction is necessary and theodolite should be positioned in the location prescribed first in this recommendation.

4. Comments on Recommendation

a. Philosophy. The philosophy used in formulating this recommendation remains the same as that used previously in theodolite placement. The reference is established with respect to the ideal path the pilot uses as he approaches the runway. This ideal glide path is defined as that formed with an infinite, flat plane which contains the runway.

It is important to be able to specify the reference without knowing the location of the glide path transmitting site. The recommendation is written, however, using a line containing the glide slope antenna mast. This wording indicates an apparent contradiction but is really just a matter of convenience, because most sites where this specification would be applied will have the mast in place. However, if the site is being established for the first time, an understanding of the geometries involved will suggest that the theodolite reference be established 350 to 400 feet from centerline for sites where non-uniform grading favors a pedestal case with the runway elevated above the glide path reflecting plane. This will place the transmitting antenna in the vicinity of 400 feet from the centerline.

b. Optimization Considerations. Because of the more complicated geometries involved with the glide path, the measurement and standardization of such systems are more difficult. There are two fundamental considerations which must be recognized. The first is that a good reference path shape must be established. This should serve the user approaching for landing on the runway and be invariant from site to site. General agreement exists that this shape should be a hyperbola whose asymptote has a given elevation angle for obstruction clearance purposes and which crosses the threshold of the runway at approximately 55 feet.

The second consideration is that deviations from this reference be measured in consistent units which implies that the coordinate system centers should be coincident. This consideration is one of incremental, angular measurement or path sensitivity.

Siting criteria now being promulgated by the FAA will provide for obtaining optimization of both of these conditions. However, certain sites, which have not been prepared according to the FAA specifications may not permit meeting both conditions simultaneously. An optimization must then be made with respect to one and the error produced because of non-compliance with the other must be calculated. An error bound must then be determined.

For example, if the reflecting plane is perfectly flat but the runway is elevated on a pedestal, the glide path transmitting antennas should be located farther from the threshold than the antennas would be if the site were ideal* or graded to current FAA specifications. Referring to Figure 2-2 one observes the ideal path (1) leading to runway as if the site were ideal. Path (2) indicates the path shape and location if the reflecting plane is lowered but the runway remains the same. Obviously, the path does not serve the runway adequately. To correct for this without regarding the site the transmitting antennas can be moved back away from the threshold to produce curve (3).

Judicious placement of the antennas can produce a path shape outside the threshold which coincides very closely with the ideal curve (1). Specifications of FAA Order 8240.20 will provide curve (4) for the reference curve which for this particular case is not the ideal. Path (3) when compared to (4) very likely will produce unsatisfactory indications for Category II. Curve (1) should be specified for the reference but there is a compromise on the sensitivities and this must be ascertained through calculation of error bounds. An alternative method is to obtain the optimum in incremental angular values (sensitivity) by placing the optical tracking system to generate curve (3) and then calculate the error bound between it and the ideal (1) for which it is substituting. It will be found in many cases that curves (1) and (3) are close enough when considering only the region beyond the threshold that they may be regarded as identical. One sample case for a specific site indicates that there is a maximum of 5 microamperes (0.023 degree) maximum difference. If this is mathematically demonstrated to be the case for the site of interest, then the theodolite can be referenced to the base of the transmitting antennas.

A major consideration when implementing this recommendation is the maintenance of the angular sensitivites between the electronic path and the reference geometry. Lateral displacement of the axes of the two cones will introduce a disparity between angular deviations referenced to two different systems. This is a disadvantage incurred in this approach and is precisely the same problem which encouraged abandonment of the first FAA order specifying the theodolite placement near the runway to form an approximate straight line path.

Without range information it is not possible to remove precisely the error that is introduced; however, as second best, an error bound can be determined which will specify the maximum error in microamperes that will be introduced as the point of interest on the glide path moves closer to threshold. Realistically maximum permissible aircraft deviations from the zero DDM line and the theodolite index

---

*Ideal is defined to mean that the ground plane is perfectly flat and contains the runway.

Path (1) formed by ideal, infinite ground plane containing the runway surface.

Path (2) formed by infinite, flat ground plane at elevation h units lower than the runway surface.

Path (3) formed by infinite, flat, lowered ground plane but antenna system displayed S units farther from the threshold than the antenna systems which produced curves (1) and (2).

Path (4) is reference specified in 8240.20 which preserves sensitivities but compromises the ideal reference.

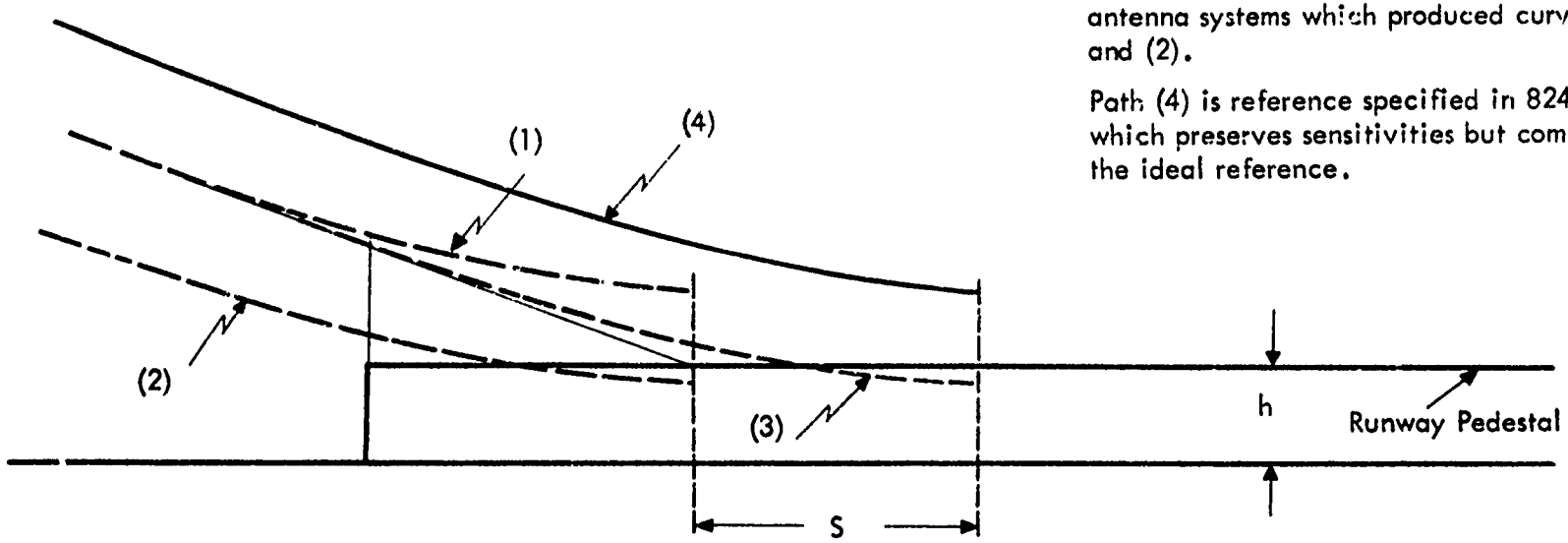

Figure 2-2. Glide Path Positions Referenced to the Generating System.

angle must be specified. This is expected to be broad enough (estimated 45 microamperes) to permit all reasonable flight tracks to be acceptable.

The location of the reference above the line joining the base of the antenna mast and the runway threshold rather than a line parallel to the runway centerline is recommended to minimize the sensitivity error at the threshold.

Finally, theodolite placement for convenience of the operator will introduce error. In the past this has involved moving forward on the surface of the cone of the ideal theodolite location. If this is planned, a quantitative assessment of the errors should be made.

A very minor error will be introduced if the ideal cone and reference cone have axes tilted α units apart (α being the angle describing the longitudinal slope of the runway). It would be impractical to adjust the theodolite base parallel to the runway rather than with the gravitational level. The angles of the conics are adjusted to provide equal approach angles.

B. Glide Path Siting Problem

Because it is highly desirable to have initial airport design include grading appropriate for forming a high quality glide path, specifications have been prepared for inclusion in FAA manuals discussing site preparations. The specifications are based on calculations for predicting glide path performance given specific terrain contours.

Figure 2-3 summarizes the results of this study. It is possible to form a good glide path while still providing for adequate drainage away from the runway. Of great importance is that the terrain alongside the runway have uniform negative slope with no discontinuities. The magnitude of the slope should be no greater than $1\frac{1}{2}$%.

If rapid runoff shoulders of 12 to 18 inches in height at the edge of the runway are provided more than $\frac{1}{2}$ of the allowable Category II tolerance can be expected to be consumed.

Reversal in the slope of the terrain is permitted once past a line making a 10 degree cut with the runway and passing through the antenna mast. Maximum slope which should be permitted is 15%.

All calculations were based on maximum allowable path disturbance of $\pm 2\frac{1}{2}$ microamperes.

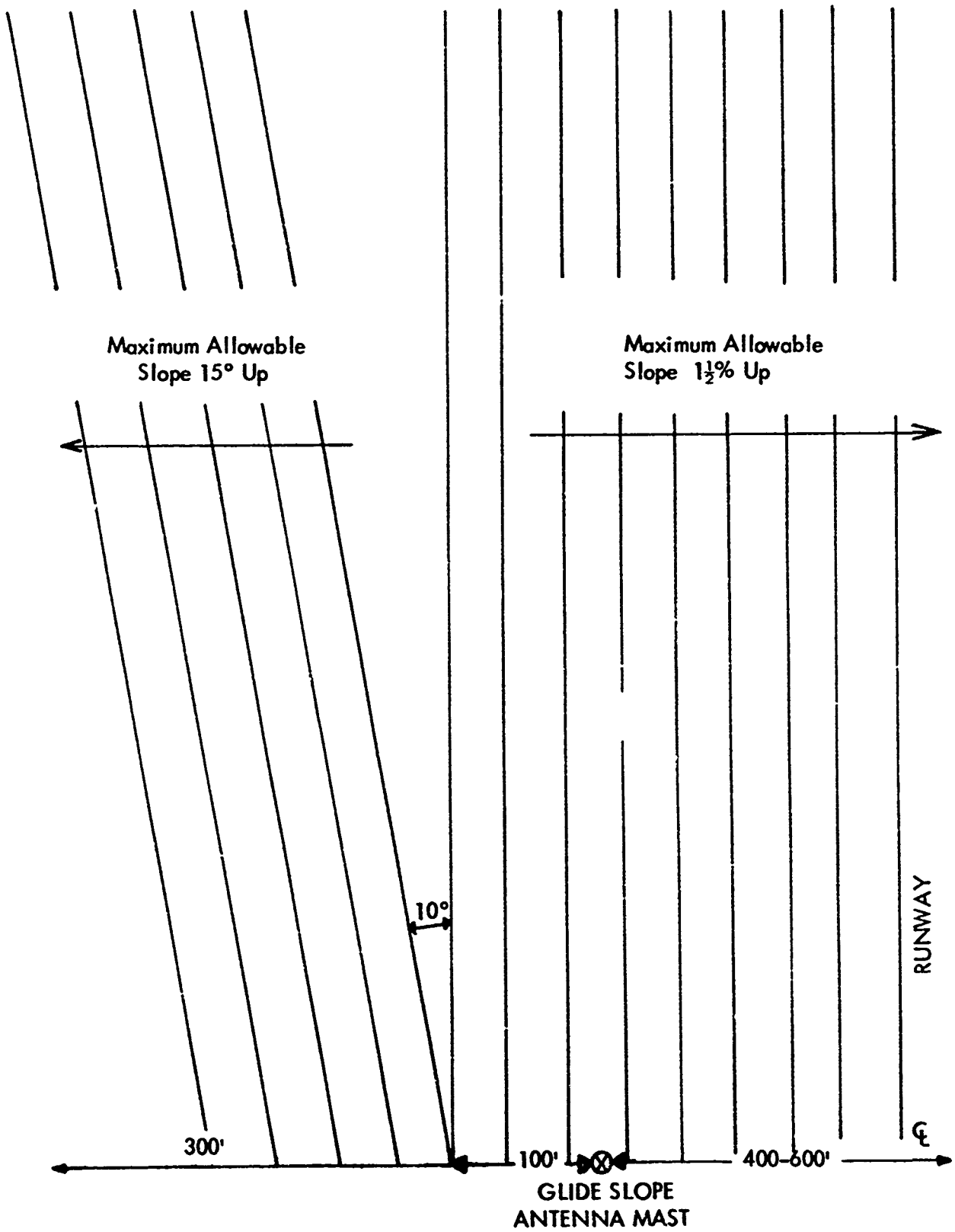

Figure 2-3. Recommended Maximum Allowable Slopes for Grading Terrain in Front of Glide Path Transmitting Array.

C. Special Glide Path Problems

1. Travis Air Force Base Considerations

a. Introduction. During initial flight measurements involving the Texas Instrument Company glide path equipment procured in the summer of 1971, it became apparent the Category II requirements as set forth in Change 17 (8/26/70) of the FAA Flight Inspection Manual could not be met. The question legitimately was asked, did Category II flyability exist even though the specifications of Change 17 were not met. Since the specifications are only sufficient conditions for Category II flyability and do not represent necessary conditions, the possibility did exist that the flyability was adequate. A discussion of this logic is contained in section II A.

A visit was made to the Travis AFB site and data were collected through the cooperation of the Oakland FIDO team and several other FAA and Air Force personnel. Four sets of flight data were taken with the purpose of ascertaining the precise location of the path in space for it is this location on which true acceptability must be judged. An analysis of terrain profiles was undertaken to correlate observations with that predicted by knowing the earth's features. Contour data provided prior to the site visit were grossly in error and this was obvious when the site was first viewed. A request was made for an accurate plot and this subsequently was received thus permitting completion of the analysis.

b. Statement of the Problem. Flight recordings indicate that the Travis AFB glide path is well outside the tolerance limits for Category II operation when the theodolite is positioned in accordance with the FAA Flight Inspection Manual. Intuitive considerations indicate to observers that the path may very well lead safely to the runway even though the Category II tolerances are not being met. A solution to the problem will be to indicate a means of determining if Category II flyability does in fact exist and if it does not, to recommend the most inexpensive means of obtaining it.

c. Analysis. Three principal criteria used in determining the acceptability of a glide path are: (1) the average angle must be maintained with approximately ±0.1 degree; (2) no rates of change ($d\theta/dy$) in the on-course signal may exist greater than 0.12 degree per 1000 feet; and (3) the average path leading to the threshold must exist so as to penetrate a 47 to 60 foot lineal window at the threshold. There is no requirement on the path inside the threshold. (Table 2-1).

It is important to note that these criteria should relate to a path in space referenced to an optimum landing point on an airport runway. They are independent of a reference system which serves only as a device to facilitate a quantitative determination of path parameters.

The present specifications for theodolite placement for reference purposes are designed to provide the maximum ease in making determination of path characteristic by direct readout of analog recordings taken onboard the flight check aircraft. Optimum path shape and one-one correspondence between sensitivities or reference and electronic glide path have been provided for. This means that because of the correspondence between the units of the reference and glide path systems, one may use the direct readout of a differential amplifier which subtracts the reference from the glide path signal to give indication of the zero DDM line in space independent of the aircraft performing the measurement.

Full benefit from this reference system is available when grading for the glide path site has been accomplished in accordance with current FAA specifications. If such grading has not been provided, it is possible to have a path which will not be within specification given in the FAA Flight Inspection Handbook, yet it may be a perfectly safe path for Category II operations. The necessary and sufficient conditions discussed in section IIA 2 are applicable here.

An analysis of the Travis AFB 21 L glide path site reveals that this is an example of a case where non-standard grading combines with reference system coordinates optimized for direct readout to give an apparently unacceptable path. The explanation of this is relatively simple. To obtain a 52-foot threshold crossing height with a 2.65° path angle at an ideal site one would locate the transmitting antennas 1125 feet down the runway. Should the runway be located on an elevated, pedestal-type surface the transmitting antennas would have to move farther down the runway 21.6 feet for every foot the pedestal is elevated. The use of the term pedestal implies that standard, uniform, transverse grading does not exist, rather a discontinuity exists between the path forming terrain and the terrain on which the aircraft lands. The problem which is created can best be seen through the use of a drawing and an example.

Path (1) of Figure 2-2 is produced when the world is flat and the runway and path forming surface are in the same plane. Path (2) indicates the path shape and location if the reflecting plane and antenna are lowered but the runway remains fixed. Obviously this path (2) does not serve the runway adequately because it crosses the threshold at too low an elevation. If one is concerned about the path only in the region outside the threshold then the transmitting site may be moved down the runway 21.6 feet for every foot of pedestal height. In the case of Travis where the runway is elevated approximately 5 feet at the threshold, the antennas would be located 108 feet further down the runway or approximately 1233 feet from the threshold. Reportedly engineers used such a calculation in locating the transmitting site location because the antennas are 1217 feet down the runway from the threshold. Should the terrain be perfect except for the pedestal, path (3) would be produced. Note that this coincides very closely with the ideal path (1) if the region inside the threshold is excluded.

Unfortunately for this terrain case the prescribed reference, optimized for convenient readout, does not describe the ideal path for the Travis runway configuration. Path (4) is the reference path and is readily seen to have a high threshold crossing height and a projected touchdown farther down the runway than desired. Figure 2-19 shows a computer printout of the angular difference between Path (3) and the reference Path(4) presently specified by the FAA Handbook. The values exceed Category II tolerances.

Practically Path (3) can be generated for a reference with proper sensitivities and this path is shown to be very close in value to that of ideal Path (1). The difference between (3) and the ideal (1) has been calculated, and Table 2-1 shows a copy of a computer tabulation for this. The maximum error of interest, of course, exists at the threshold and is found to be approximately 4 microamperes. This is a minimal amount and indicates that a theodolite reference to the base of the antenna mast can be used in this case to provide an acceptable reference provided no use is made of information inside the threshold.

d. Measurements. Measurements made with reference coordinate centers at different locations including the one suggested in section II G 2c by the FAA Oakland FIDO. In general, all indicated the path departed the reference value of 2.65° between one and two miles from the runway and crossed the threshold at approximately 52 feet elevation. The path angle depresses to approximately 2.52° if referenced at the coordinate center for ideal Path (1). This is 34 microamperes low and at the tolerance limit for Category II acceptability. Figures 2-4, 2-5, and 2-6 show four selected profiles taken from the topographic information provided by the U. S. Air Force. The path is remarkably good considering the grading provided at this site.

e. Measurement Tolerances. In this as in many studies some variations in data become apparent. For example, reduction of flight data showed three sets giving threshold crossings of 52.9, 52.7, and 52.0 feet. The fourth set gave 55.6 feet. Another example is that three sets of data show a far-field path angle of 2.65° whereas one indicates 2.59°. Calculations predict a 2.59° path angle.

An example is given below of height of zero DDM line obtained by two different measurements.

	900 FT. Overrun	Threshold
Flight Record	101 ft.	53 ft.
Cherry Picker	93 ft.	54 ft.

Rough air, theodolite operator, theodolite makeshift platform, and other factors are known to contribute to these inconsistencies. Other factors not identified are also undoubtedly involved.

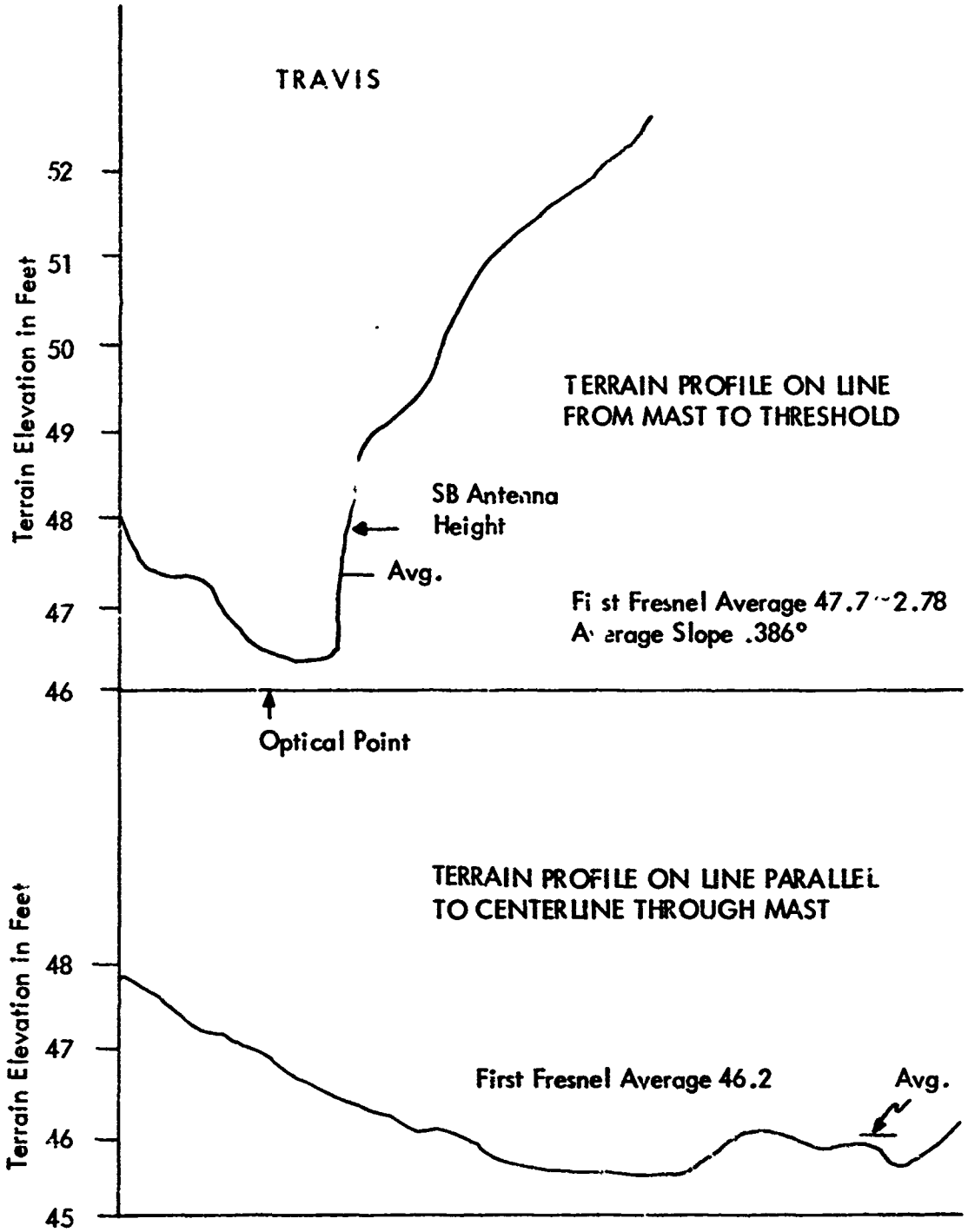

Figure 2-4. Selected Terrain Profiles at Travis Air Force Base.

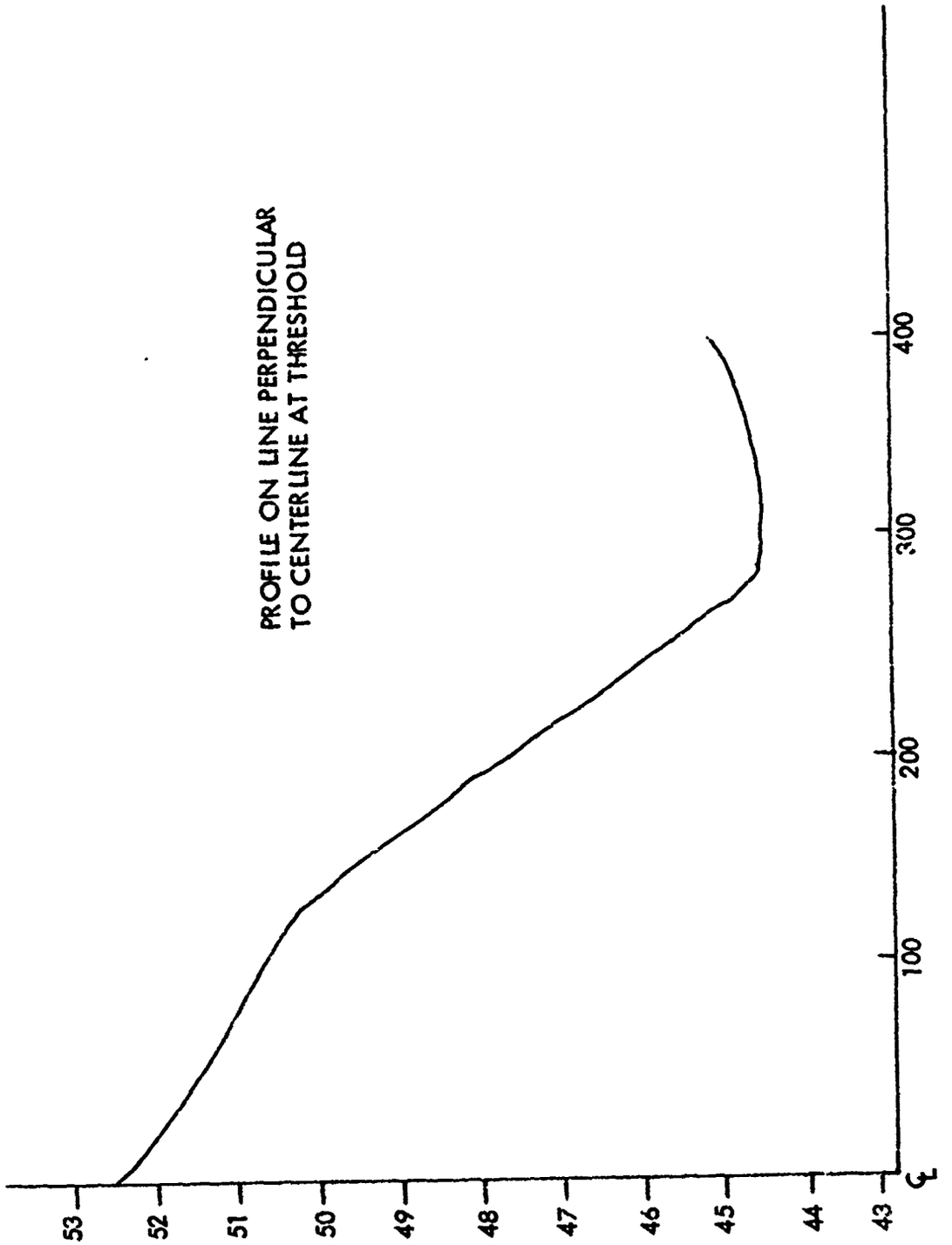

Figure 2-5. Terrain Profile at Travis Air Force Base.

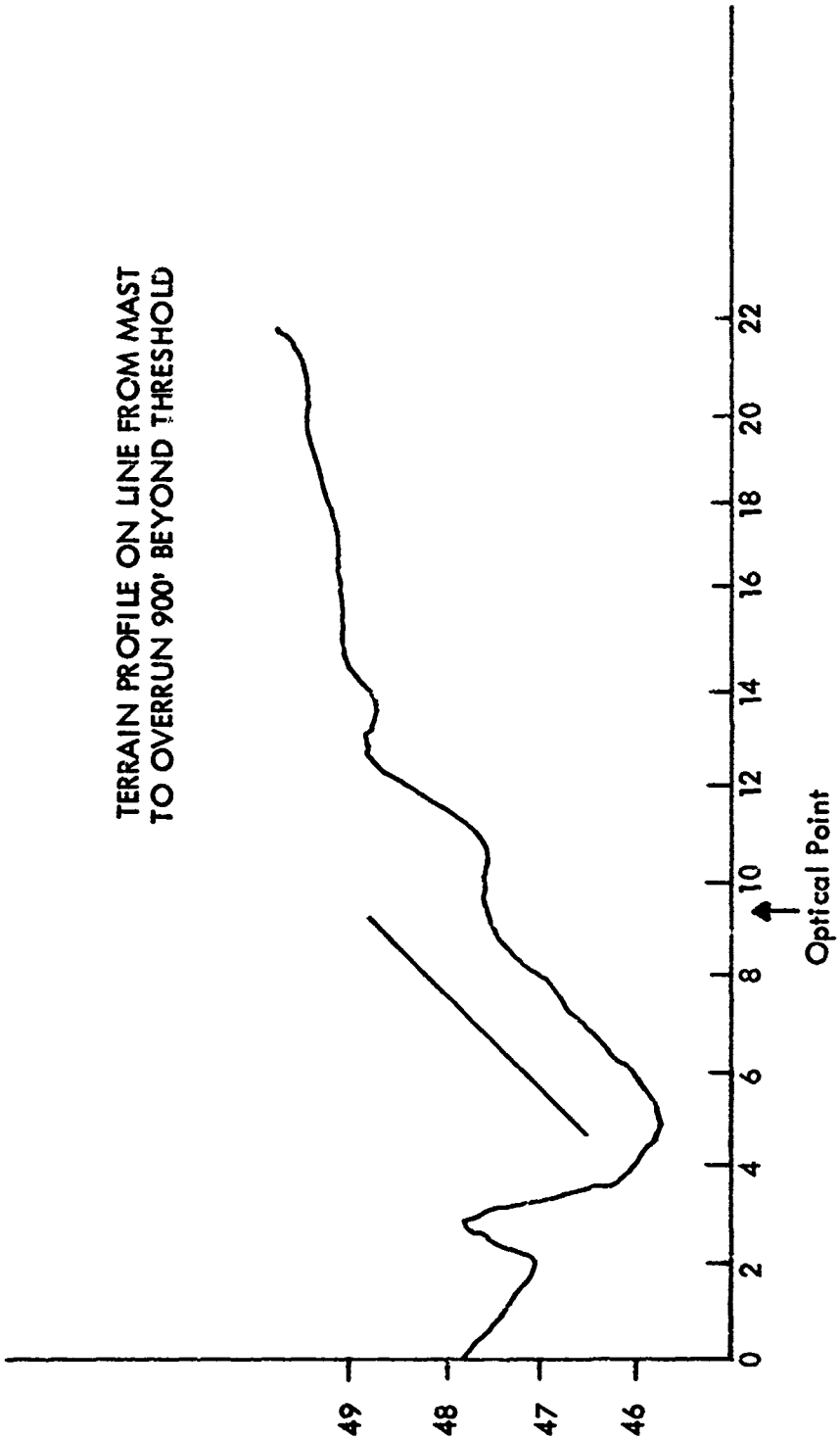

Figure 2-6. Terrain Profile at Travis Air Force Base.

f. Considerations for Location of Reference System. If range information is provided or assumed, as is currently done from the time base of the recordings, the reference coordinate system center usually in practice is taken to be the location of the radio telemetering theodolite which if desired could be located at any reasonable point on the airdrome. Once the center and orientation of the coordinate system is known, the data collected with range information can be used to determine the path in space. Then criteria of acceptability can be applied.

Unfortunately the geometries of both the electronic path to be measured and the theodolite reference involve conics and when these are combined complications are introduced. Concern for optimization is thus justified, and over the past years the emphasis has been to provide for a direct readout of data on a recording which will have specific relation to tolerances that can be placed directly on the records. An ideal reference path shape turns out to be a straight line on the record and angular units from the electronic glide path and the reference system are essentially identical. Therefore, these can be subtracted using a differential amplifier. Assuming path linearity, the result is a direct recording of path position.

Among the penalties paid in doing this are that the human tracker must manipulate the azimuth controls as he tracks vertically and thus requiring more experience and skill. Any implementation of an automatic tracker would require both elevation and azimuth capabilities unless a development of an anisogonic lens is accomplished thus eliminating the need for azimuth tracking. Also, although not usually a serious problem, the theodolite operator, and transmitting equipment are all located in the area from which signal is reflected to form the path.

A location of the theodolite at the base of the antenna optimizes the consistency of units between the electronic path and the RTT system; however, it may provide a poor representation of what should be the reference path in space. Such was the case at Atlanta (SRDS Technical Report RD 69-4) [2].

Consideration has been given to the possibility of locating the reference at a point which would minimize azimuth tracking requirements and establish a straight line leading to the threshold window. The key to the success of this reference location would be the capability to process a conversion of units in order that the location of the path in space may be ascertained. Consistency of angular units would be lacking and would be inversely releated to the lineal spacing between the theodolite and the transmitting antenna. One would expect that with ease of the tracking operation greater consistency could be obtained with minimum tracking error. Alternatively an error bound could be established and direct readout accomplished knowing what this error is. The following section treats a derivation of this error bound.

g. Error Analysis of the Theodolite Tracking of Glide Path Due to Theodolite Position. Since the elevation angle of the optical system changes at a different rate than that of the electronically-detected path angle when the theodolite is at any location other than the apex of the cone of which the sideband null is a section, it is desirable to know the correction to be applied to the indicated difference. The following analysis presents a general formulation and an error correction curve for a special case of interest.

In the following it is assumed that all readings are at a sufficient distance from the antenna to allow the 1/r term to be considered essentially identical for antenna and image.

The theodolite is assumed to be set to zero DDM at the asymptote of the null hyperbola. DDM indications are assumed proportional to angular deviation from the asymptotic angle. Figure 2-7 shows the coordinate system.

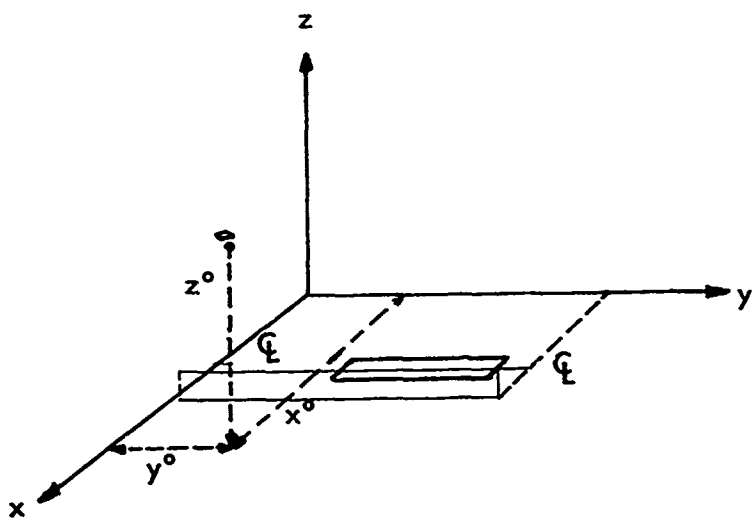

Figure 2-7. Coordinate System.

in which:

y is parallel to runway
x is horizontal
z is vertical
Antenna is at (0,0,h)
Theodolite at $(x^\circ, y^\circ, z^\circ)$

The equation of the sideband antenna null, with all distances measured in wavelengths, is

$$\sqrt{(x^2 + y^2 + (z+h)^2)} - \sqrt{(x^2 + y^2 + (z-h)^2)} = 1 \qquad (2.1)$$

Adding the second radical to both sides and squaring

$$x^2 + y^2 + z^2 + h^2 + 2hz = x^2 + y^2 + z^2 + h^2 - 2hz + 2\sqrt{(\cdot)} + 1$$

Rearranging gives

$$z^2 (4h^2 - 1) = x^2 + y^2 + h^2 - 0.25$$

Or,

$$z = \frac{\sqrt{x^2 + y^2 + h^2 - 0.25)}}{\sqrt{(4h^2 - 1)}} \qquad (2.2)$$

(2.2) may be put in the standard hyperbolic form:

$$\frac{(4h^2 - 1)\ z^2}{(x^2 + h^2 - 0.25)} - \frac{y^2}{(x^2 + h^2 - 0.25)} = 1 \qquad (2.3)$$

The asymptote is

$$z = \frac{y}{\sqrt{(4h^2 - 1)}}$$

The half apex angle of the cone is atan $\sqrt{(4h^2 - 1)}$ and

$$z = \frac{\sqrt{(x^2 + h^2 - 0.25)}}{\sqrt{(4h^2 - 1)}} \qquad \text{when } y = 0 \tag{2.4}$$

Thus the apex of the cone is located at

$$\begin{aligned} y &= 0 \\ z &= 0 \\ x &= \sqrt{(x^2 + h^2 - 0.25)} - x_1 \end{aligned} \tag{2.5}$$

where x_1 is the x coordinate of the runway centerline.

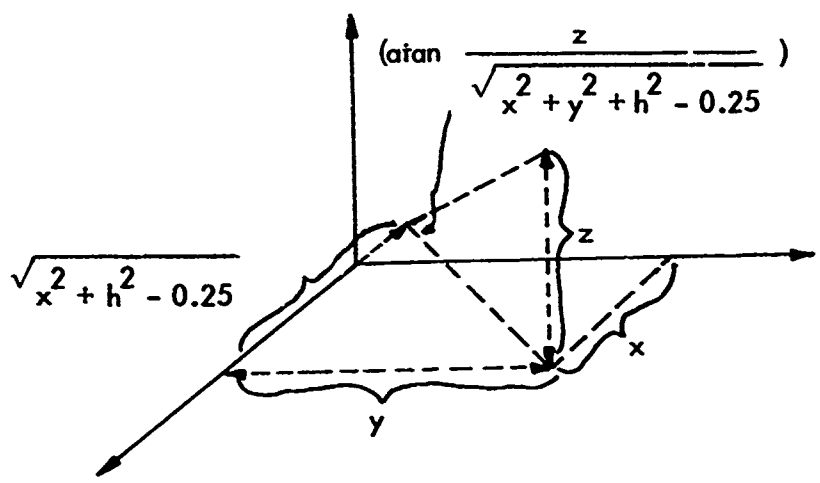

Figure 2-8. Elevation Angle Re: Coordinate System.

From Figure 2-8 it can be seen that the elevation angle of an observer above the horizontal at the cone apex is given by

$$\text{atan} \frac{z}{\sqrt{(x^2 + y^2 + h^2 - 0.25)}} \tag{2.6}$$

Substituting the value of z on the null from (2.107) gives

$$\text{atan} \frac{1}{\sqrt{4h^2 - 1}} \tag{2.7}$$

The difference in these is very nearly proportional to the DDM.

$$DDM_E = K \left(\text{atan} \frac{z}{\sqrt{x^2 + y^2 + h^2 - 0.25)}} - \text{atan} \frac{1}{\sqrt{(4h^2 - 1)}}\right) \tag{2.8}$$

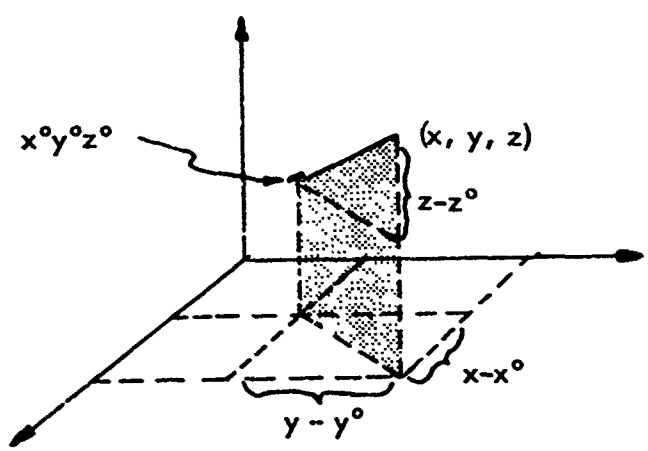

Figure 2-9. Optical Angle Re: Coordinate System.

Reference to Figure 2-9 shows the optical angle given by

$$\text{atan} \quad \frac{z - z^{\circ}}{\sqrt{((x-x^{\circ})^2 + (y-y^{\circ})^2)}} \tag{2.9}$$

Thus

$$DDM_o = K\left(\text{atan} \frac{z-z^{\circ}}{\sqrt{(x-x^{\circ})^2 + (y-y^{\circ})^2}} - \text{atan} \frac{1}{\sqrt{(4h^2 - 1)}}\right) \tag{2.10}$$

A correction factor can be derived. Using the formula for the tangent of the difference of two angles and setting $DDM_E = KE$ and $DDM_0 = KT$ gives:

$$F = \frac{d(T - E)}{dT}$$

where F is the correction factor by which T is multiplied to find the system error.

Then

$$E = \text{atan} \frac{(z/A) - (1/B)}{1 + (z/AB)} \tag{2.11}$$

$$T = \text{atan} \frac{((z-z^{\circ})/C) - (1/B)}{1 + ((z-z^{\circ})/CB)} \tag{2.12}$$

where

$$A = \sqrt{(x^2 + y^2 + h^2 - 0.25)}$$

$$B = \sqrt{(4h^2 - 1)}$$

$$C = \sqrt{((x-x^{\circ})^2 + (y-y^{\circ})^2)}$$

And

$$F = 1 - \frac{dE}{dT} = 1 - \frac{dE}{dz}\frac{dz}{dT} \tag{2.13}$$

$$F = 1 - \frac{AB^2 + A}{(AB + z)^2} \quad \frac{(CB + z - z^\circ)^2}{CB^2 + C} \tag{2.14}$$

where $\quad$ atan $\delta = \delta$ for small δ. (δ being $< .5°$)

but, on the null, $z = A/B$

$$F = 1 - \frac{C}{A} \quad \frac{((B^2)^2)}{(1 + B^2)^2} \left(1 + \frac{A}{CB^2} - z^\circ \frac{1}{CB}\right) \tag{2.15}$$

Consider a special case where

$B^2 = 485$ (2.6° reference angle)
$y^\circ = 8.5844$
$x = 133$ (400 ft.)
$z^\circ = 1.33$ (4 ft.) (Theodolite on Runway ℄)

Results are plotted on Figure 2-10.

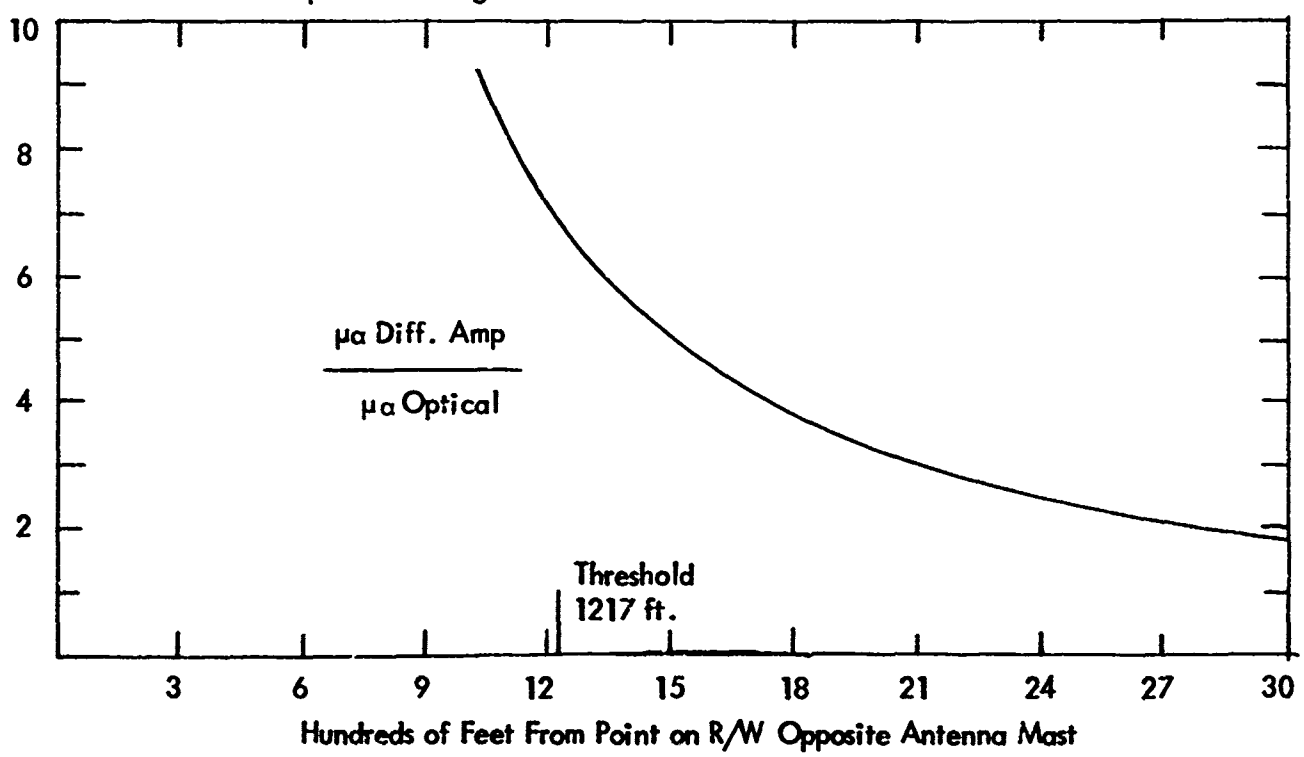

Figure 2-10. Example of Correction Chart Showing Calculation Introduced by Aircraft Departing from Zero DDM Line of the Glide Path for the Case When the Theodolite Coordinate Center is Not Collocated with the Electronic Glide Path Origin.

h. Conclusions Relating to the Travis AFB Glide Path Site. The following conclusions are reached following the investigation of the RTT problem at Travis AFB.

(1) The sufficiency condition given in FAA Flight Inspection Manual Change 17 for Category II path conditions is not broad enough to take into account the non-standard terrain grading which exists at Travis.

(2) Indications are that with the present nominal path angle of 2.65°, the recorded path angle decrease of approximately 0.10° during the last mile of flight is undesirable from threshold crossing height considerations. Improved performance would be obtained by raising the nominal path to 2.75°.

(3) Inconsistencies in available data make precise determination of lineal quantities such as threshold crossing height difficult, but improvements would be undoubtedly available if less work load was placed on the theodolite operator during tracking. This could be accomplished by relieving him of azimuth tracking.

(4) The path in space with reference to path angle as seen from the runway, rate of change of this path with respect to distance, and final penetration of the threshold window should be the overriding considerations as to the acceptability of any single glide path. Central processing with use of a computer to account for coordinate electronic system disparities would be useful in providing the most scientific method of resolving special cases such as Travis.

(5) Present FAA standards given in the FAA Flight Inspection Handbook are correct but must be recognized as sufficient, not necessary, conditions for Category II flyability. The capability to provide direct readout must be traded against the necessity to examine special cases such as Travis.

i. Recommendations. The following suggestions are made for the purpose of providing a valid and correct RTT reference for Travis AFB glide path measurements.

(1) For the Travis site the theodolite should be located referenced to the base of the transmitting antennas. This will provide the maximum in compatibility of units between the electronic glide path and the theodolite reference system. It will optimize on providing a satisfactory reference path assuming no measurements are taken inside the threshold. Practically this recommendation can be interpreted to place the eyepiece on the cone of path angle at a convenient height for the operator. This will mean moving in front of the antenna slightly over 100 feet in a direction towards the threshold. This is the placement formerly specified in FAA Order 8200.11A and can be used here because the calculated error when using a correct ideal path is shown not to exceed 4 microamperes and this will occur at the threshold.

(2) Subtract 4 microamperes from the error bound specified in the Flight Inspection Handbook and apply directly to the differential amplifier recording to determine acceptability in the usual manner.

(3) Raise the nominal path angle to 2.75° by reducing the antenna heights above ground. This will provide for a threshold crossing height well within Category II tolerance.

(4) Investigate the possibility and feasibility of establishing a central processing capability within the FAA so that glide paths may be evaluated consistently from site to site and permit processing of data without constraint on theodolite placement. From such a facility a true path in space could be calculated and its acceptability determined independent of local reference problems. Because of the complicated geometries involved the availability of a computer is needed together with the development of some special software.

(5) Emphasis on proper site preparation should be continued by the FAA. As can be seen from the Travis case poor site preparation cannot only affect the electronic path but the reference system applicability as well.

2. Detroit Glide Path Special Problem

A request was received to investigate the anomalous condition which appears in the glide path structure for Runway 3L Detroit Metropolitan Airport. The recorded path showed a flare-down below allowable tolerances and thus the facility was not acceptable for Category II.

The glide path site at Detroit had been recently graded and appeared nearly perfect. Tolerances on the grading were extremely good and all indications were that the path shape could not be attributed to deformations of the ground plane. Static measurements with a cherry picker were made which indicated that the path and the null position formed by the middle antenna were from 0.1 to 0.15 degree lower than those that would be calculated for the ideal ground plane case. From flight measurements the path is low and out-of-tolerance at the runway threshold and is below the ideal hyperbola and even the straight line extension (asymptote). The cause of this anomalous condition is not fully understood at this time, however, it appears that more than one factor is contributing to the low path.

The simplest, least expensive and most expeditious means for producing a satisfactory Category II glide path was to raise the path from 2.5 to 2.6 degrees. This recommendation was followed and a path meeting Category II criteria was obtained and commissioned. However the basic problem was not solved, that of determining and correcting the anomalous depressed path angle near the threshold.

a. Analysis. As background, flight recordings had been obtained that showed the path to be approximately 40 microamperes low at the threshold. These records showed the path to begin at an angle of 2.50° near the middle marker and descend to 2.31° at the threshold. These were referenced to a theodolite positioned as specified in Order 8240.20.

An analysis of the contour map of the site indicated that recent grading was provided a superb ground plane with a minimum of longitudinal slope (less than $\frac{1}{4}$%) and approximately $\frac{1}{2}$% transverse slope. The deviations from uniform slope were minimal. A recheck of the contours was accomplished by the Wayne County Engineers. A measured profile is shown in Figure 2-11.

Antenna heights were reported to be 50'6", 33'9", and 16'10". Using these heights with the ground plane data indicated that the path should be at 2.50° which would place the zero DDM line 55.2 feet above the threshold. This must be compared with the 49.3 feet indicated from the flight measurements.

An unfortunate circumstance is that the tolerances being used for Category II acceptability are being determined incorrectly because the threshold crossing height

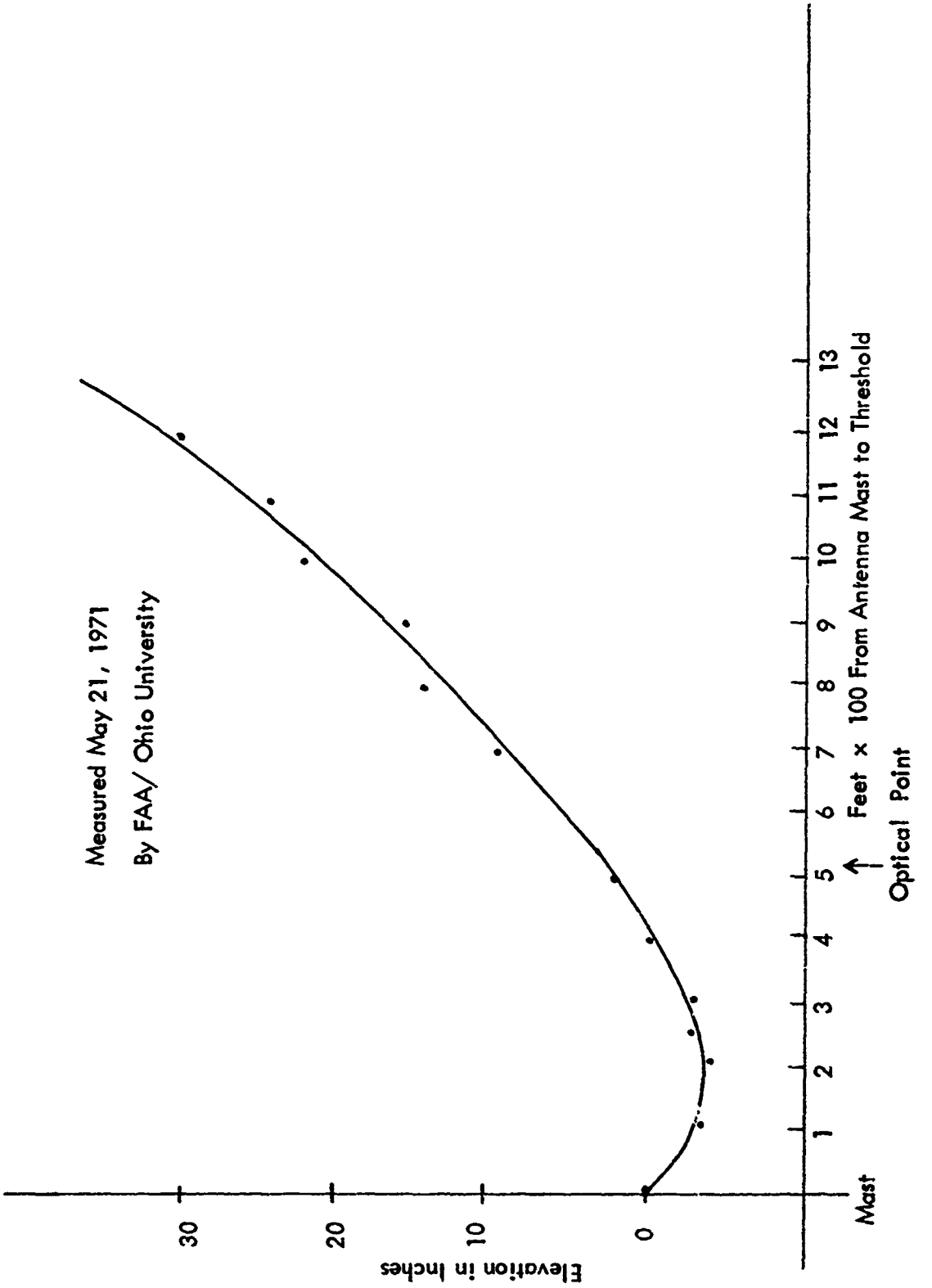

Figure 2-11. Ground Plane Terrain Profile at Detroit.

used to enter the sliding scale in Order 8240.20 is being calculated incorrectly. The formula formerly in the TERPS manual which has been deleted by FAA letter FS-4060:8260.3A, dated December 18, 1970, is being used. This calculation involves the base of the antenna which is not correct for determining the threshold crossing height for tolerance purposes. Numerous discussions have been held with OP-4 and FS personnel in FAA have encouraged the dissemination of information to provide a uniform, consistent, and correct calculation for all flight inspection offices in the United States. The present calculations at Detroit are penalizing the facility there by requiring an unusually tight tolerance below path. Using the correct calculation will provide a greater margin but this alone would not be sufficient to insure Category II operational requirements being met with a 2.5° path angle.

b. Measurements. In cooperation with the FAA the following measured data was obtained prior to raising the angle. Obviously a considerable discrepancy existed between the measured path and that indicated from calculations. A visit was made to the DTW site where the following measurements were accomplished through the cooperation of the local facility sector office, the Wayne County airport crew, and two Battle Creek FIDO personnel.

Tape line height of zero DDM line above threshold with cherry picker --50'3" ± 1 inch.

Elevation angle of zero DDM line above threshold with theodolite at theoretically correct location at antenna mast at the elevation of the runway opposite the mast -- 2.36° ± 0.005°.

Elevation angle of zero DDM line above threshold with theodolite at location specified in Order 8240.20--2.27°.

Tape line height of null above threshold produced by middle antenna only--52.0'.

Elevation angle of null with theodolite at point specified in order 8240.20--2.35°.

Elevation angle of zero DDM in far-field measured by Ohio University flight --2.50° ± .01° on localizer.

Elevation angle of zero DDM in near threshold measured by Ohio University flight --2.44° ± 0.05° Turbulence reduced the accuracy of this measurement.

Average elevation angle of zero DDM at an angle arctan 400/1200 south of the localizer --2.32°

Measured height of point on runway opposite mast and threshold referenced to base of antenna-- +32" and + 35" respectively, ±3 inches.

Measured distance between point opposite mast and threshold-- 1194 feet ± 1 foot.

Measured distance between mast and threshold--1255 feet, ± 1 foot.

With reference to Figure 2-12 profiles of field strength from the upper and middle antenna individually were obtained at point C. A profile of the field strength generated by the upper antenna was obtained at point D and the first null generated by the middle antenna was obtained. Also, the elevation of the zero LDM line was measured at point D both with the clearance transmitter on and off. The field strength readings were obtained from a PFCD augmented by a preamplifier for determining the nulls. Elevation was determined by a tape line and positions of the nulls and maxima were confirmed by using a theodolite located at the antenna mast at the elevation of the runway.

In Summary:

CONDITION	CALCULATED	POINT A Measured 5/21/71	POINT C Measured 6/2/71	POINT D Measured 6/2/71
Upper Antenna Only				
Minimum	1.64°		1.56°	1.62°
Maximum	2.50°			2.41°
Minimum	3.33°		3.22°	3.22°
Middle Antenna Only				
Minimum	2.50°	2.40°	2.35°	2.35°
Zero DDM, No Clearance Signal	2.50°			2.31°
Zero DDM, With Clearance Signal	2.50°	2.36°		2.38°

Table 2-3. Results of Field Measurements Made at the Detroit Site.

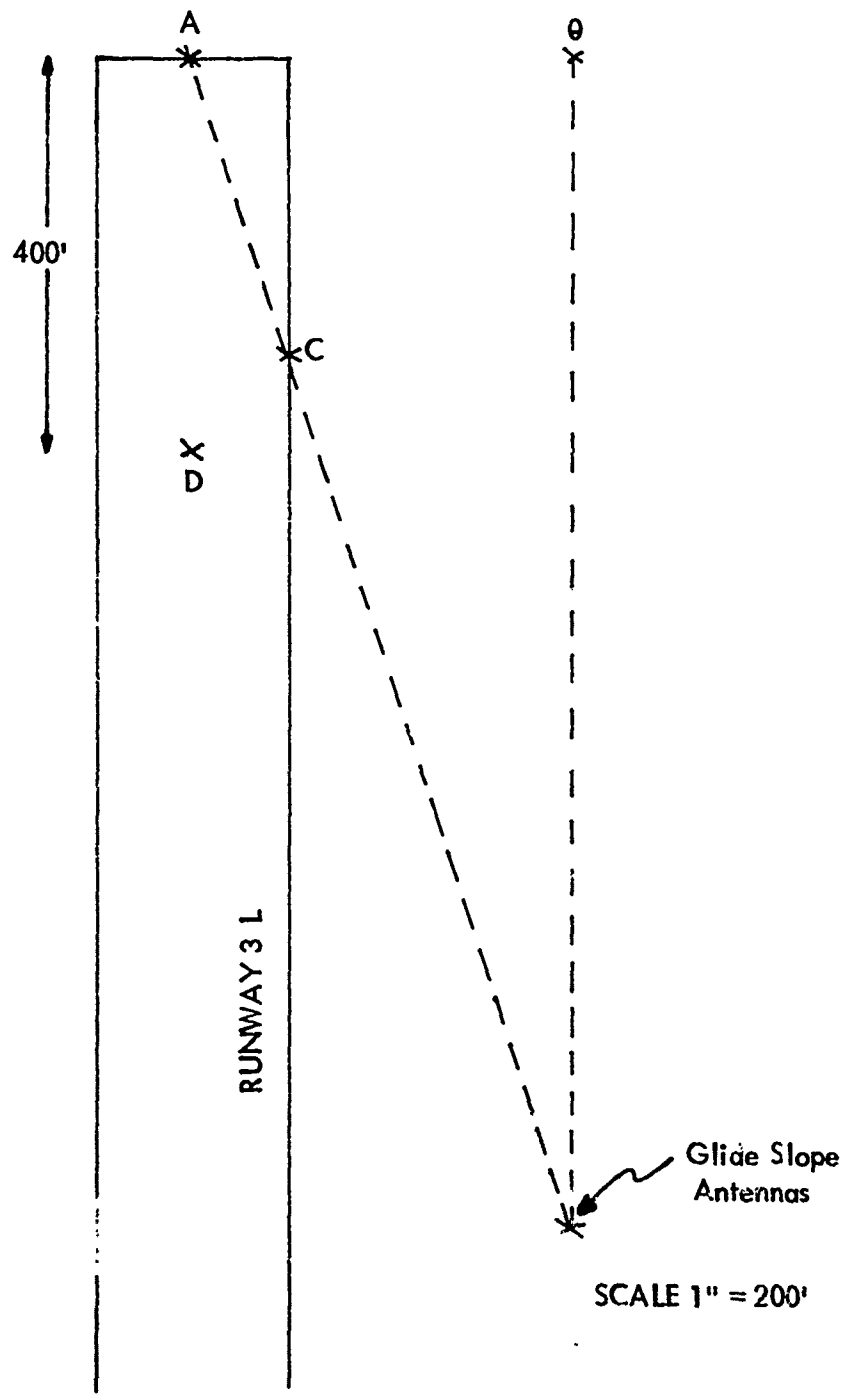

Figure 2-12. Definition of Data Collection Points at Detroit.

Measurements indicated that the field patterns are representative of a ground plane lower in elevation than that given on the topo charts.

The ground plane was very wet which helped make a more level surface.

Some checks were made for parasitic radiation and spurious radiation from the transmitter building. There was no evidence that any significant amount exists.

Impedance measuring equipment and a vector voltmeter were used to make measurements on antennas, lines, and signal conditions. SWR's were 1.2:1 or better and phases within 3° of the desired phase at the terminals of the antennas with the exception of the lower antenna feed which had a 30° delay. Apparently the antenna was defective producing a 30° shift in the radiated signal which was compensated by the 30° measured as existing in the line.

c. Conclusions. From this reported information some conclusions can be given:

(1) The path at the threshold is approximately 0.15 degree lower than the angle measured for the path in the region beyond the middle marker.

(2) The difference in elevation of the zero DDM line and the null of the second antenna would indicate that a power or phase anomaly exists in the system.

(3) The elevation angle of the null (and the path) cannot be predicted simply from the known antenna height and the measured terrain profile. Measured path is approximately 0.12 degree lower than that predicted.

(4) The far-field path angle calculation agrees with those measured to within 0.01 degree.

Although the recommendation was followed and an acceptable path was obtained the investigation continued because the need existed for learning what was causing the path to perform in the unpredictable manner. Application of this information could be useful at other sites. The changes in the system made by the Great Lakes region produced a commissioned path and thus eliminated it from being used as a test facility.

In order to circumvent this limitation Ohio University moved another glide path system to the Detroit site and established it alongside the commissioned system. This permitted both systems to use essentially the same ground plane. Flight measurements were made by Ohio University and FAA Battle Creek FIDO. See Figure 2-13. Preliminary results of the analysis showed approximately 50% less downward flare to exist with the experimental system. Ground-based and airborne-collected data did not point to any obvious cause of the Detroit path problem. A very careful and detailed analysis of all data is underway to attempt to uncover subtleties which could be the key factors. This analysis is not yet complete.

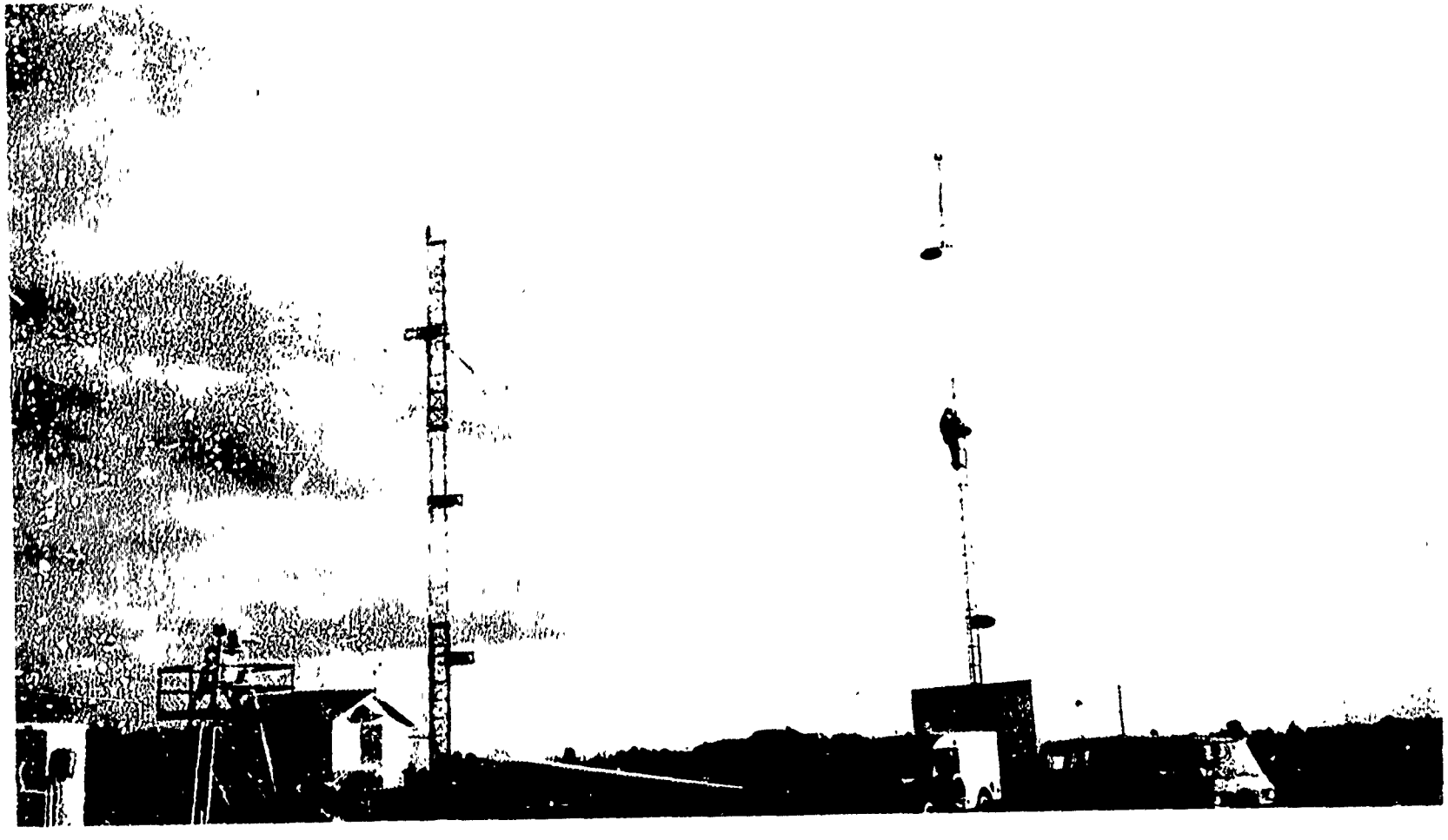

Figure 2-13. Experimental Equipment Used in Performing Measurements of Glide Path and Site Conditions on Runway 3L at Detroit Metropolitan Airport. The Capture Effect Array Shown on the Left is the Commissioned Facility. The One on the Right with a Man Making an Antenna Adjustment was Used for Comparative Measurement of Ground Plane Conditions and Parasitic Radiation. The Beechcraft 35 was Used to Obtain Preliminary Flight Check Data on the Experimental Glide Path and was in the Position Shown to Permit Calibration of Receivers, Theodolite, and Telemetry Equipment.

3. Monterey, California

a. Introduction. Several recommendations are presented in this section concerning reported problems associated with the operation of the glide slope at Monterey, California. These recommendations are based on (1) several analyses performed at Ohio University dealing with effects of imperfect ground planes, (2) measurements made at a Charleston, West Virginia, glide-slope site which has a limited ground plane, (3) an analysis of flight recordings of two glide slope systems which have been installed at Monterey, and (4) a visit to the Monterey site involving discussions with technical people who have worked with the Monterey systems.

The problem at Monterey was articulated in a request made by the FAA Western Region. Evidence exists that the problem at Monterey is not peculiar to that airport but represents a category of problems which have been described generally as those produced by inadequate or truncated ground planes.

b. Observations. The ground plane at Monterey is adequately smooth, slightly sloped (one percent) in both longitudinal and transverse directions, but it is quite limited in extent, viz., 900 feet at 0°, 530 feet at 10°, and 300 feet at 20° from runway centerline. The theory presented in section II G 1 and measurement data to be presented show the effect of a limited ground to soften and lower an image path.

Evidence of the significant effect of the truncated ground plane at Monterey is that to provide a 3.0 degree glide path in space with a null-reference system the antenna heights had to be those for a 3.6 degree path. The theory which predicts a 0.2 degree lowering of the null with a 900 foot ground plane, reference Figure 2-87.

In an attempt to obtain some data concerning the effects of limited ground planes on capture effect systems some flight measurements were made using the commissioned capture effect system at Charleston, West Virginia. By making approaches at different angles with respect to the runway centerline different amounts of ground plane were exposed to the array. A plot of the results is shown in Figure 2-14. No changes in phasing or antenna offsets were made for these tests. Future plans call for more extensive measurements involving use of an experimental system installed especially for this purpose. Control of this system will permit changes that cannot be accomplished with the commissioned facility. Investigation of means of correcting the problem of depressed, soft path structures will also be made with this facility.

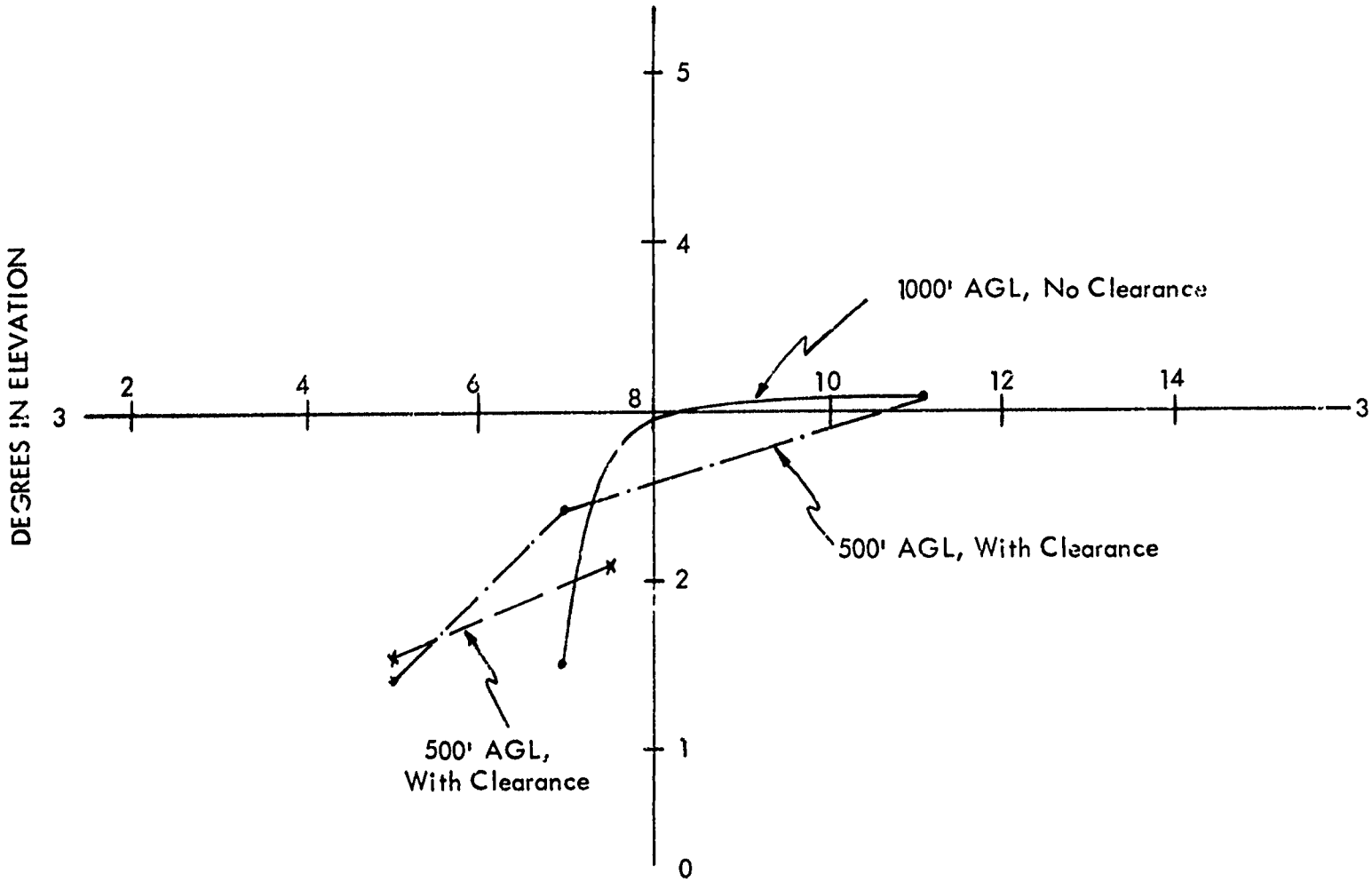

HUNDREDS OF FEET OF FLAT TERRAIN IN DIRECTION RECEIVER

Figure 2-14. Flight Data, CRW. April 8, 1971

A consultation visit was made to the Monterey, California, glide path facility (Reference Figure 2-15). A major purpose of this visit was to determine the feasibility and practicality of improving the glide-path structure which exists there.

The Monterey history has involved a null-reference, capture effect and now sideband reference facilities have been installed there. Data shown in Figures 2-16, 2-17, and 2-18 exemplify the better glide path structures produced at Monterey. Unsatisfactory reports have related principally to vertical path structures when flying an azumith angle 5 to 10° north of centerline, e. g, one inspector said that there was a fly down signal below the path.

From theoretical and practical evidence there appears to be no justification for expecting an inverted path with a limited ground, however, when flying at an elevation below a normal path angle, with truncated ground effects one may still be on top of a depressed path angle. This would give the appearance during a spot check that there was fly down signal below path. A check made by Ohio University flight did confirm that the sideband reference system is providing good clearance below path well north of the centerline.

The presently commissioned sideband reference system is better than envisioned from the verbal descriptions available. Flight recordings obtained from the Oakland FIDO, examples of which are shown in Figures 2-17 and 2-18, would indicate that the path is within Category I tolerances and in general is quite smooth. The exception is the region between 4 and 5 miles where the reflections from the hills at 2.7 miles are producing some irregularities. Quite probably this is a site where the path conditions are very much a function of the lateral track on the localizer. (see pages 186-190 of report RD 68-60). The three-dimensional picture of the glide path structure should be carefully measured at Monterey. [3]

Comments from the FIDO-2 inspectors who have worked extensively with the Monterey glide path are that the sideband reference system is a difficult glide path to fly in part because of prevailing tailwinds and turbulence and that course aberrations appear to be getting worse with time. They encourage action that will provide for a smoother path, e. g. , establishment of a capture effect system.

c. Recommendations. Assuming that an improved path is needed at Monterey, several steps can be taken. A capture effect system is needed to provide the improved flyability and to insure proper path structures the following suggestions are made.

A possible site on the opposite side of the runway appears to be available and if available this would eliminate the problem of a dropoff occuring in reflecting terrain as one moved off the centerline. A ground plane of at least 1000 feet extending uniformly perpendicular to runway centerline would be available. The recording of Figure 2-16 gives evidence that with a 900-foot ground plane a good structure can be generated. Details of the topography of the reflecting area are

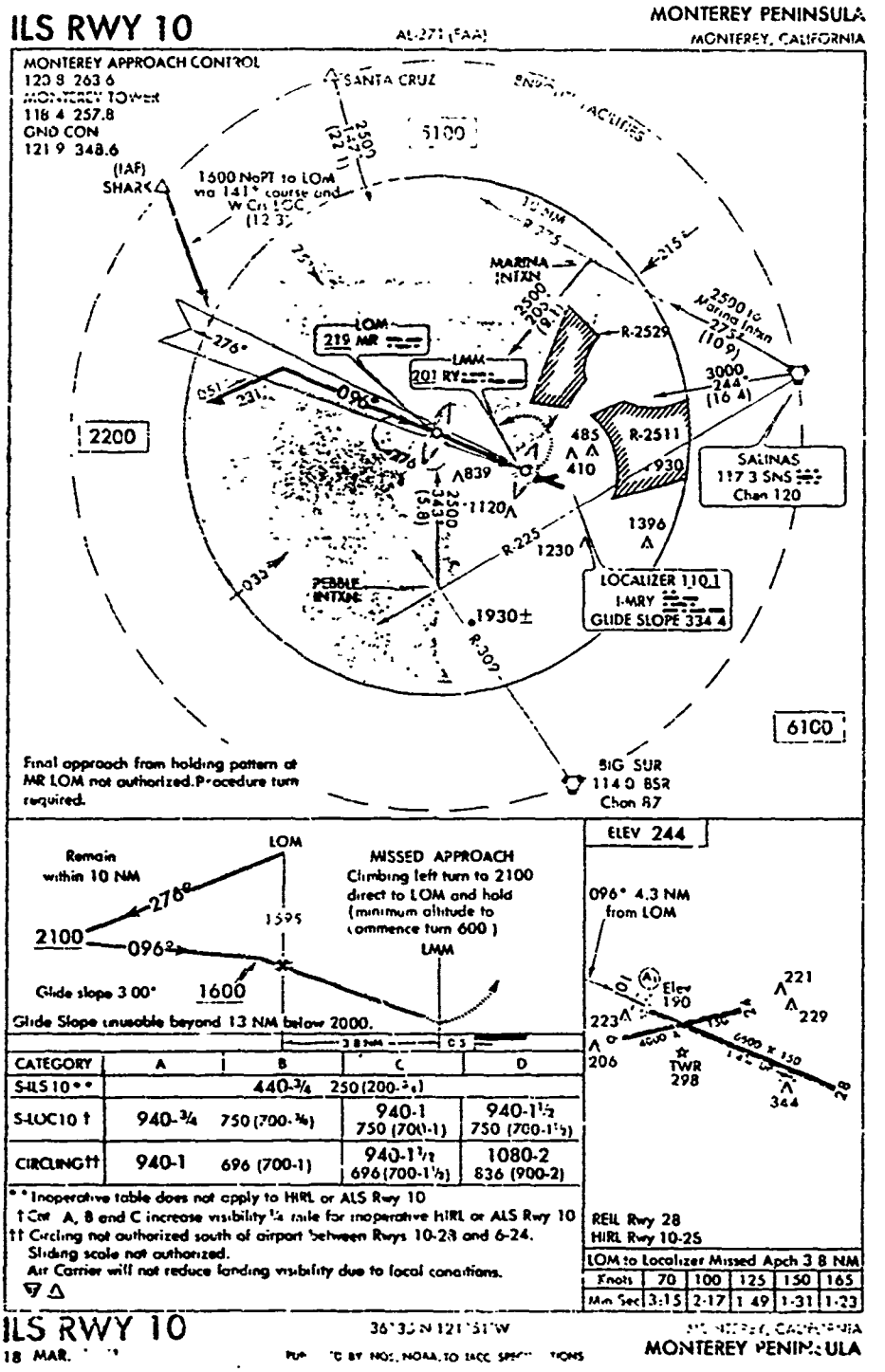

Figure 2-15. ILS Approach Plate for Monterey, California.

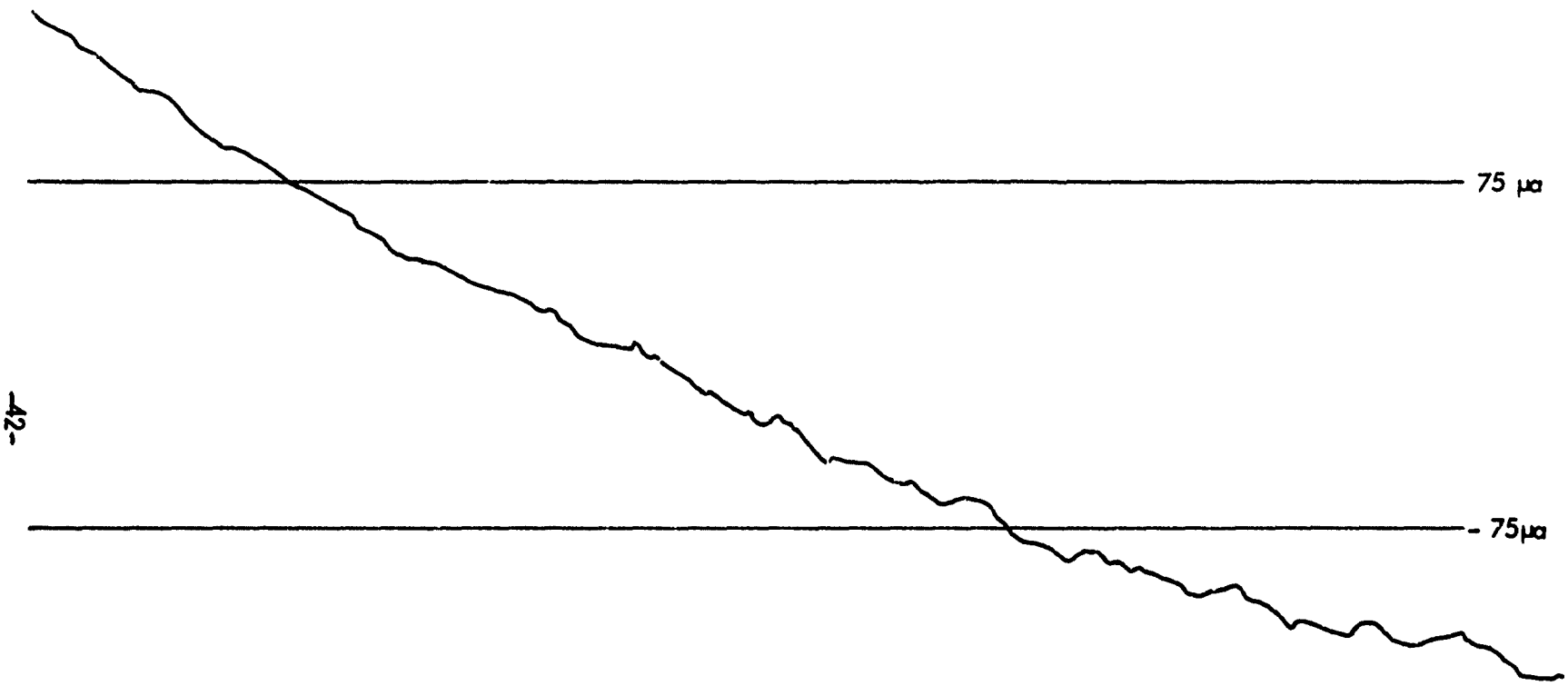

Figure 2-16. Monterey, California. Typical Crossover 1000 feet. Capture Effect Glide Slope. Centerline. December 1969. Width = 0.69°.

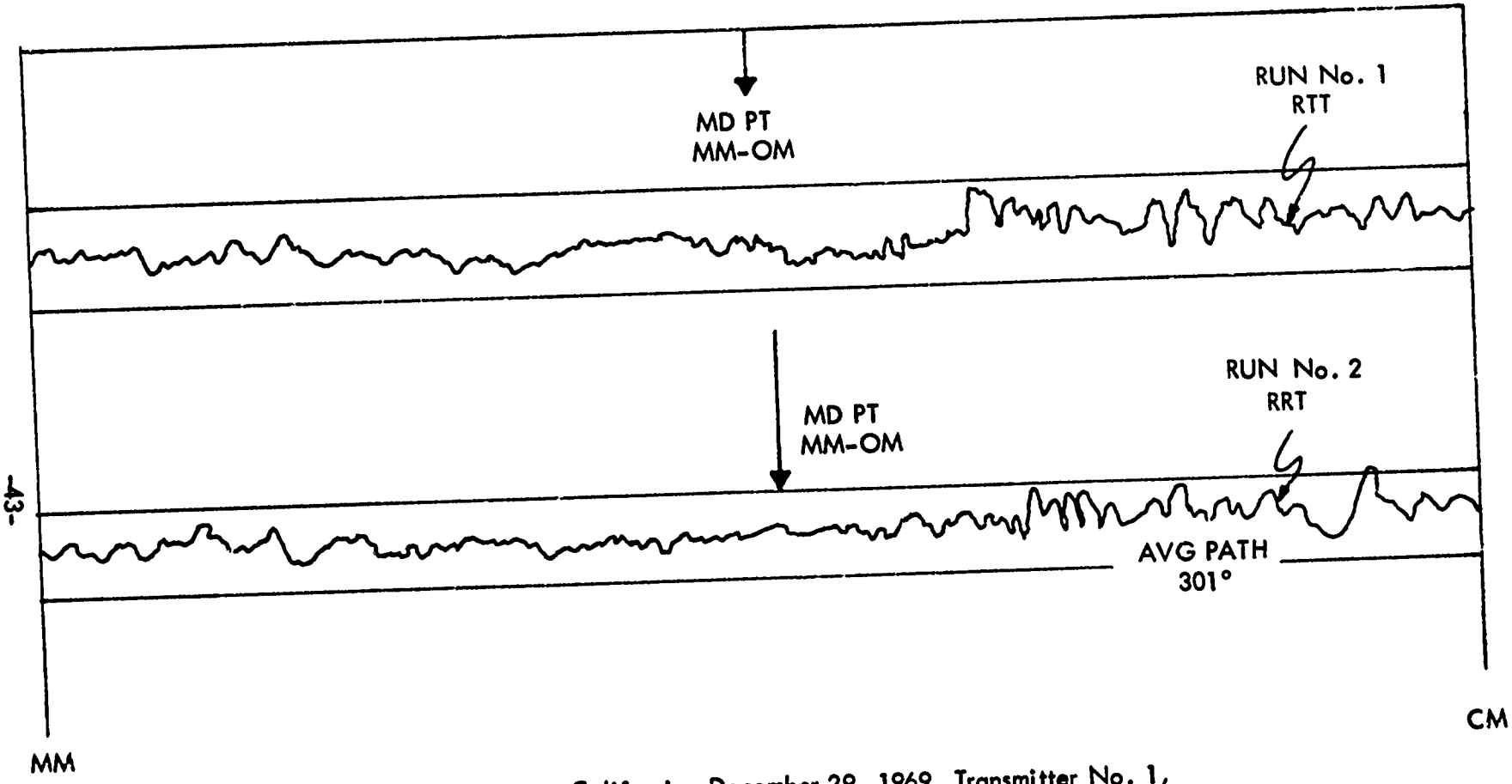

Figure 2-17. Monterey, California, December 29, 1969, Transmitter No. 1, Sideband Reference System.

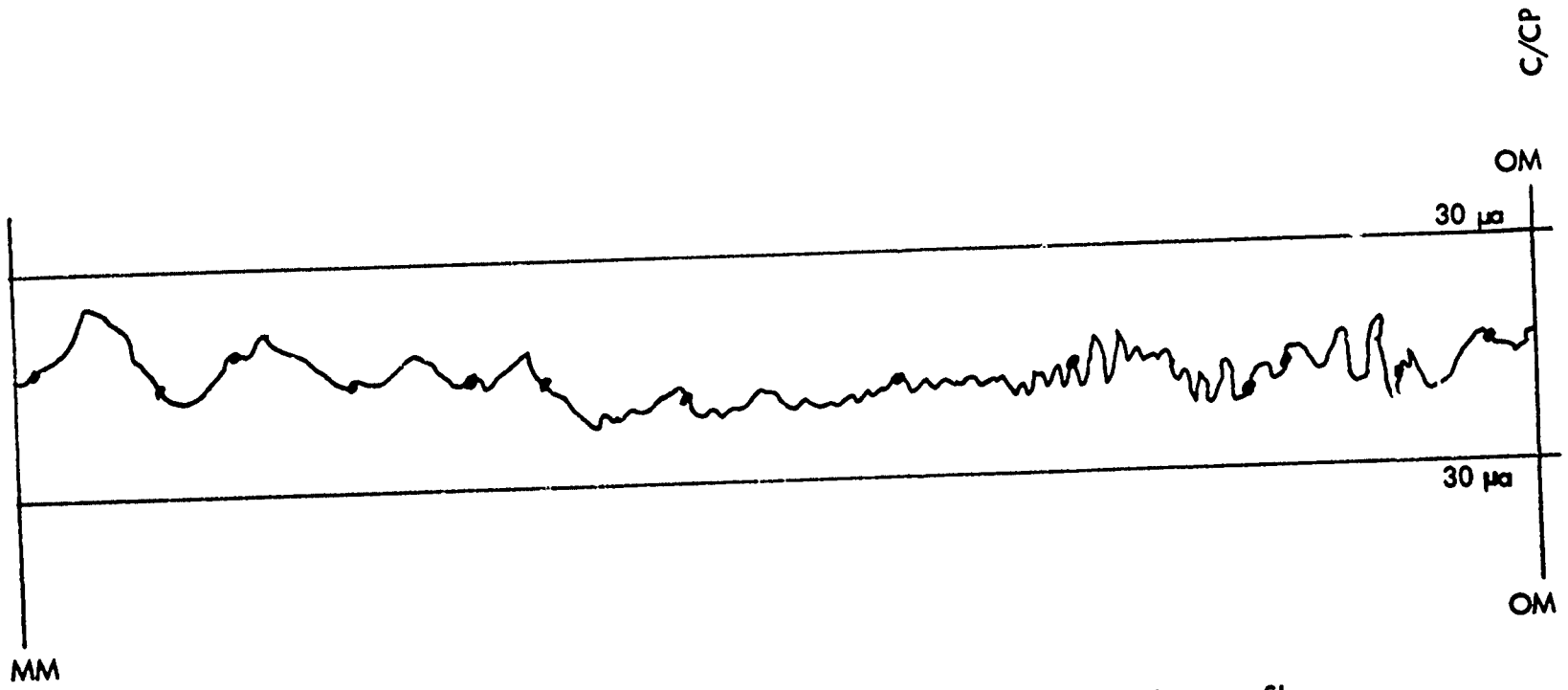

Figure 2-18. Monterey, California. Normal Approach. Theodolite References Shown as Spots. Transmitter No. 2. Sideband References System. Path Angle -3.0°. June 28, 1971. (No RTT).

needed before a final conclusion can be reached. Figure 2-19 illustrates the areas of interest.

Results of calculations based on theory developed for an image glide path operating with a limited extent of ground plane suggest a simple and rather elegant means of correcting for the adverse effects of the ground plane. Calculations show that with limited ground there is increased signal at low elevations from the higher antennas in particular but at the same time DDM is reduced. Indications are that phase lag is introduced and this causes low DDM. An approach to obtaining improvement would be to insert a phase lead into the main sideband feeder with approximately 30 electrical degrees being required. Because at Monterey the problem of low clearance occurs on the side opposite the direction of antenna offset the problem is compounded. To alleviate this, calculations indicate that a phase advance should be provided for the upper antenna of the array. Experiments needed to validate this approach are planned in the Charleston tests.

The drop-off area bending from 900 feet in front of the array to 200 feet aside the array has typically a 20% slope with small bushes growing in the sandy soil. Inasmuch as this does not represent a severe physical problem for extending a ground plane, consideration has been given to an approach providing an extended ground plane. Although earth fill would be possible, less expensive means would be to build a grid of wires parallel to the electric field incident on the area and suspend this grid from a utility pole-type structure. Cost of conductors to cover the approximate 121,000 square foot area (Figure 2-20 would be close to $2500 plus the supporting structures. To this must be added the installation costs.

Another alternative would be to consider a broadside type of array located on an elevated platform on the south side of the parking area shown in Figure 2-101.

The following data is needed for the sideband reference system as it presently exists at Monterey Peninsula Airport to ascertain the three-dimensional structure of the glide path. Use of the RRT is essential.

(1) Level passes on centerline at 500, 1000, and 1500 feet. (3 runs)

(2) Level passes at 1000 feet at the following angles referenced to centerline--10°S, 5°S, $2\frac{1}{2}$°N, 5°N, 8°N, 10°N, 15°N, 20°N. (8 runs)

(3) Normal approoches centerline, 1°N and S, $2\frac{1}{2}$°N and S. (5 runs)

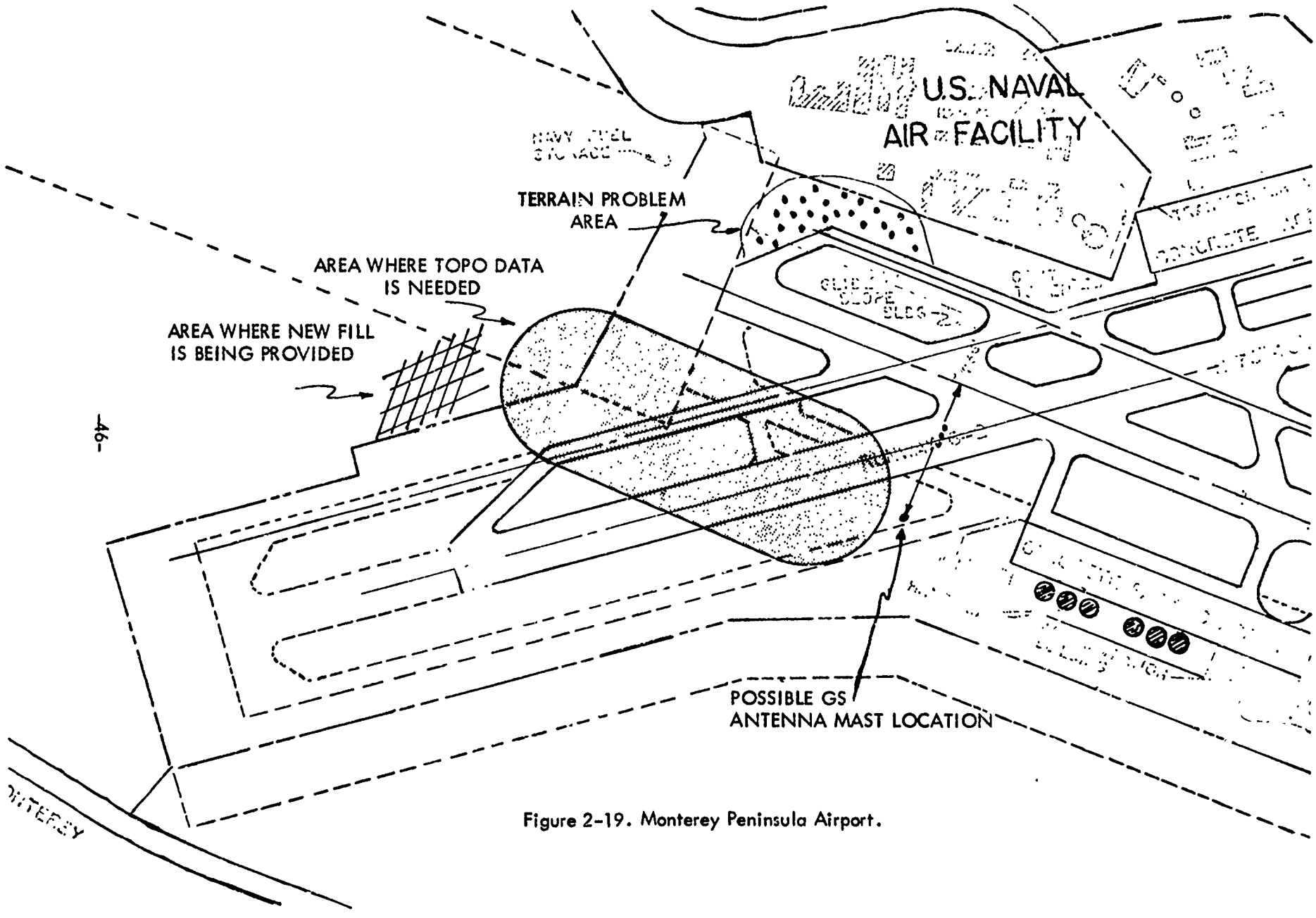

Figure 2-19. Monterey Peninsula Airport.

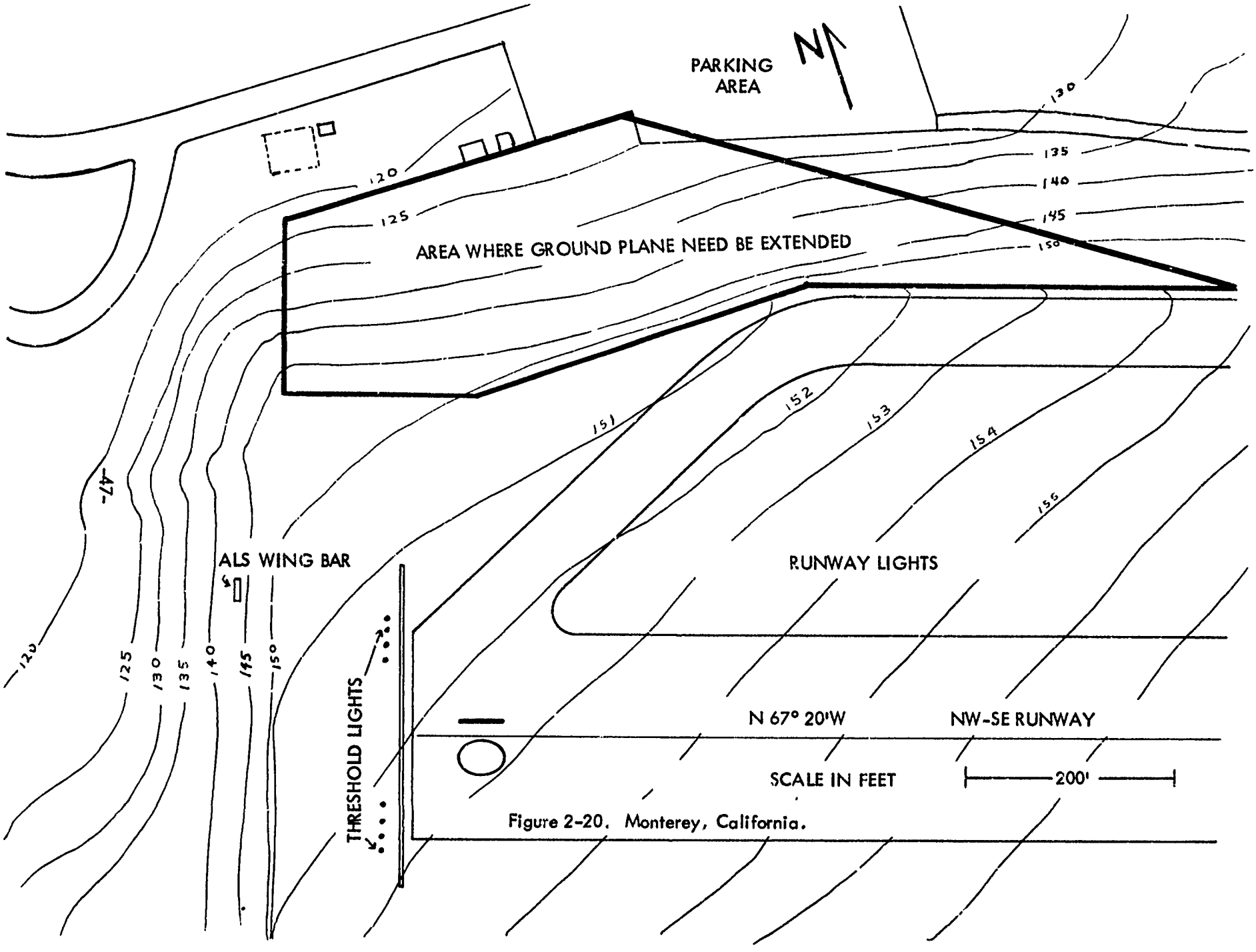

Figure 2-20. Monterey, California.

(4) Centerline tracks at 2.30, 2.65, 3.35, and 3.70 degrees elevation. (4 runs)

This is a total of 20 runs which should clearly indicate the anomalies which exist at Monterey.

One should note that flaws become apparent from data collected. As suggested above continued operation with the present sideband reference system presents no major problems. This system is appropriate for the present Monterey site for several reasons.

(1) It appears to be producing an acceptable Category I path.

(2) The low antennas require less ground plane to form a satisfactory path.

(3) There is no snow problem at Monterey.

(4) Finally there can be an obstruction at the present site if the higher capture effect towers or poles are used.

Minimum obstruction heights are desirable because the tower is located only 200 feet from the edge of the runway and only 50 feet from the edge of the taxiway. Earlier the glide path was removed from service when an aircraft moved the monitor pole. The sideband reference system, as is well known, requires a tower only approximately one-third of the height for the capture effect system.

4. Pittsburgh Category II Problem

The preceding report in this series, RD 71-30 discussed the problem of obtaining a Category II glide path on runway 10L at Greater Pittsburgh Airport and made certain recommendations.

As of this writing Category II certification has not been provided Pittsburgh and a review of the circumstances has been made.

The recommendations made one year ago were that the threshold crossing height calculation be made using only heights referred to the runway and that the path angle be raised approximately one-tenth of one degree (0.1°). Even though these corrections were made, a recent investigation to determine Category II acceptability revealed there is still another factor to be considered. On the last set of recordings only, there is indicated a path reversal which does not permit the flight inspection first derivative criteria to be met. During this investigation it was found that there were no recent recordings of this glide path and a request was made to obtain some recent theodolite recordings so that a current evaluation of this could be accomplished. Reported settling in the ground plane encouraged taking another look. New flight recordings were obtained by FAA Columbus FIDO and these showed the path to be within Category II tolerances and action is now being taken by the FAA to certify the facility for Category II operations.

There still remains the problems of calculating threshold crossing height and discrepancies in reported elevation differences between threshold and the point on the runway opposite the glide path antennas. Fortunately the path is of sufficiently high quality to be independent of these discrepancies.

D. Glide Path Critical Areas

1. Disturbance of Glide Path by Reflections from Aircraft (Boeing 747) Fuselage and Tail Fin

a. Introduction. With the advent of larger transport aircraft operating on the surface of airfields and the simultaneous lowering of landing minima it becomes increasingly important that some accurate estimate be made of the effect of reflections from these large aircraft on the navigational signals supplying the guidance to touchdown.

The problem of the operation of large aircraft in the vicinity of the localizer has been reported in RD 70-9 and further results have been reported in RD 71-30. This previously reported work is here extended to cover the effect of reflections from large aircraft on the glide path portion of the instrument landing system.

The fuselage of the aircraft is approximated by a cylinder and the tangential component of the electric field incident on the fuselage is matched by a series of TE and TM cylindrical waves. The incident tangential magnetic field is then added to the tangential magnetic field of the cylindrical waves in order to determine the surface currents on the fuselage.

In all that follows the time factor $e^{j\omega t}$ which occurs in each term has been suppressed. A single antenna, the sideband antenna for a null-reference glide path, at a height of 30 feet is considered as the source of radiation. The carrier antenna is ignored since it produces second order effects.

b. Incident Fields. Taking into account the image antenna, the electric field incident at any point on the conducting cylinder or vertical wall may be expressed as Figure 2-21, and Figure 2-22:

$$E_{inc} = \bar{u} E_o f(\theta) \left(\frac{e^{-j\beta R_o}}{R_o} - \frac{e^{-j\beta R_i}}{R_i} \right) \qquad (2.16)$$

where

$\bar{u}$ = a unit vector normal to the plane of Figure 2-23.

E_o = the value of the electric field strength at a unit distance from the transmitting antenna which will be set equal to unity for computational ease.

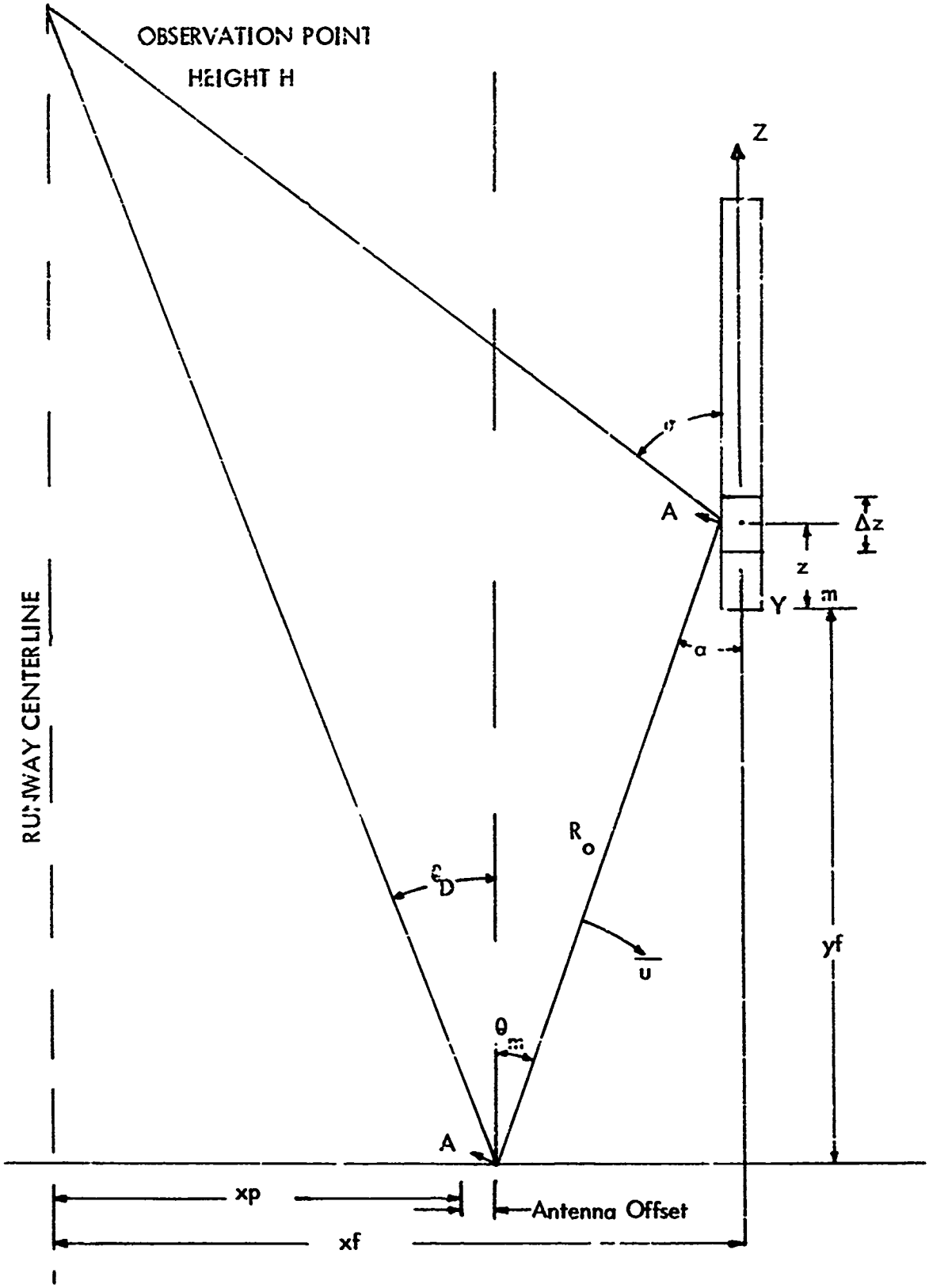

Figure 2-21. Plan View, Geometry of the Problem.

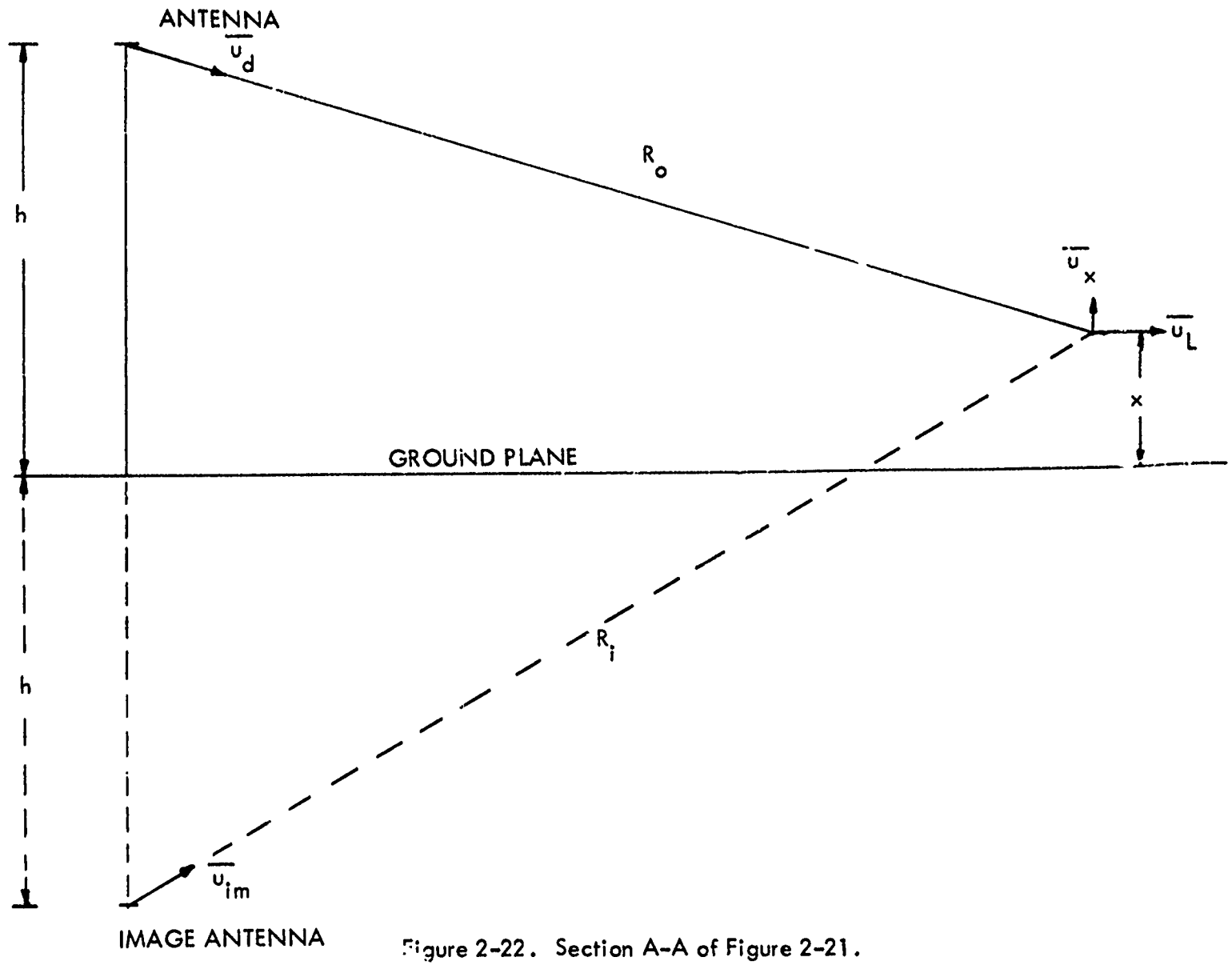

Figure 2-22. Section A-A of Figure 2-21.

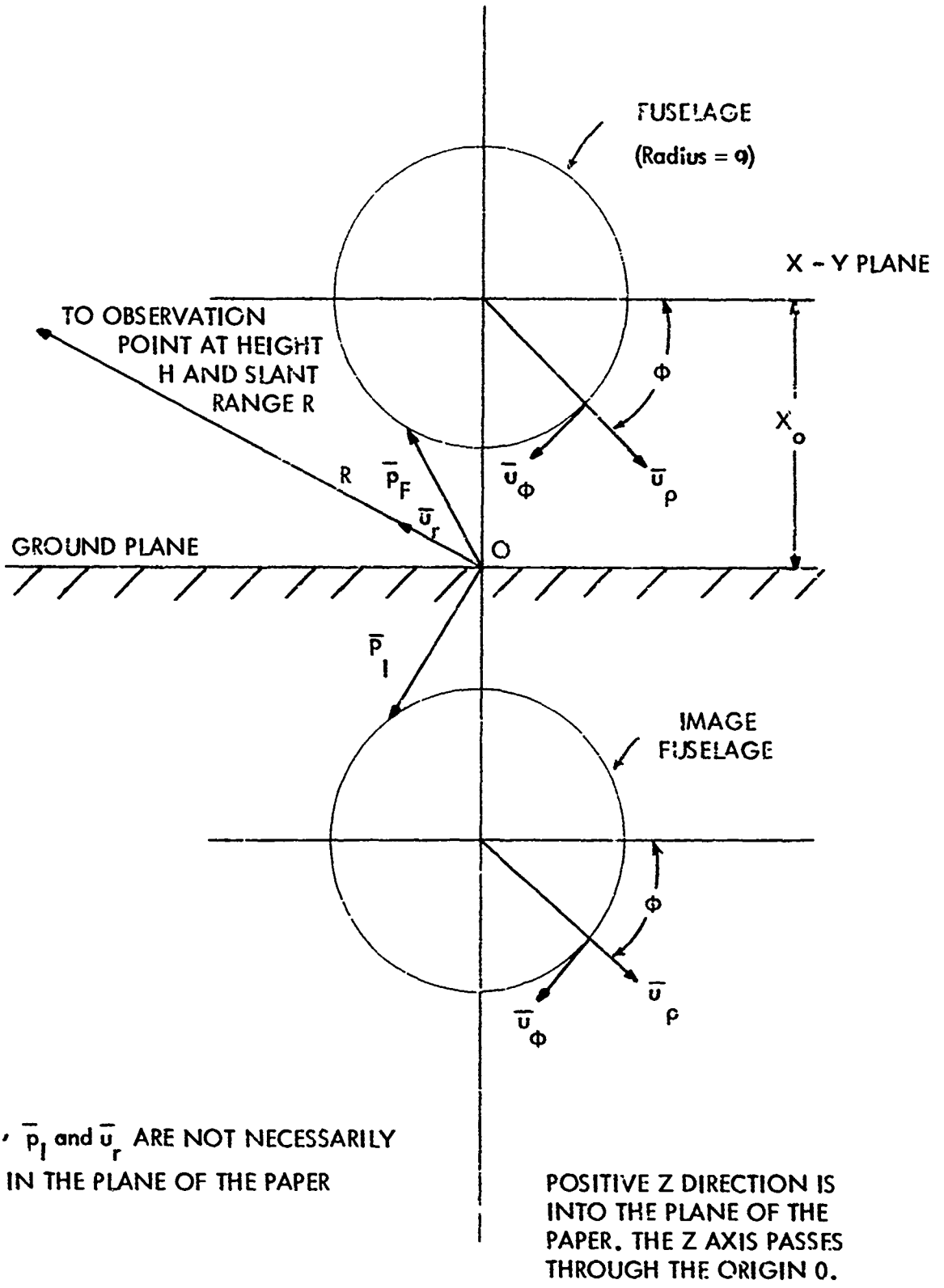

Figure 2-23. Geometry of the Cylindrical Fuselage and Its Image.

$f(\theta)$ = an expression defining the horizontal pattern of the particular antenna being used.

R_o = length of a line drawn from the transmitting antenna to a point on the fuselage.

R_i length of a line drawn from the image antenna to a point on the fuselage.

β = 2π/wavelength.

The incident H-field in the radiation zone is given by:

$$\bar{H}_{inc} = \frac{E_o\ f(\theta)}{\eta} \left(\frac{e^{-j\beta R_o}}{R_o} (\bar{u}_d \times \bar{u}) - \frac{e^{-j\beta R_i}}{R_i} (\bar{u}_{im} \times \bar{u}) \right) \qquad (2.17)$$

where

η = 20π ohms

u_d = a unit vector in the direction of R_o

u_{im} = a unit vector in the direction of R_i

Expressing the cross products in terms of $\bar{u}_L$ and $\bar{u}_x$ gives

$$\bar{H}_{inc} = \frac{E_o f(\theta)}{\eta} \left(\frac{e^{-j\beta R_o}}{R_o} \left(\bar{u}_L \frac{(x-h)}{R_o} - \bar{u}_x \left(\frac{\sqrt{R_o^2 - (h-x)^2}}{R_o} \right) \right) - \frac{e^{-j\beta R_i}}{R_i} \left(\bar{u}_L \frac{(h+x)}{R_i} - \bar{u}_x \frac{\sqrt{R_o^2 - (h-x)^2}}{R_i} \right) \right) \qquad (2.18)$$

where $\bar{u}_L$ = a unit vector in the vertical plane AA parallel to the ground plane.

$\bar{u}_x$ = a unit vector normal to the ground plane.

Expressing the incident fields in fuselage coordinates (Figure 2-23) with the aid of the identity $u_L = u_z \cos\alpha + u_y \sin\alpha$

$$\bar{E}_{inc} = E_o f(\theta)\,(\bar{u}_y \cos\alpha - \bar{u}_z \sin\alpha)\left(\frac{e^{-j\beta R_o}}{R_o}\right) - \left(\frac{e^{-j\beta R_i}}{R_i}\right) \tag{2.19}$$

$$\bar{H}_{inc} = \frac{E_o f(\theta)}{\eta}\left[\frac{e^{-j\beta R_o}}{R_o}\left(\frac{(x-h)}{R_o}\left[\bar{u}_z \cos\alpha + \bar{u}_y \sin\alpha\right] - \bar{u}_x \frac{\sqrt{R_o^2 - (h-x)^2}}{R_o}\right)\right.$$

$$\left. - \frac{e^{-j\beta R_i}}{R_i}\left(\left[\bar{u}_z \cos\alpha + \bar{u}_y \sin\alpha\right]\frac{(h+x)}{R_i} - \bar{u}_x \frac{\sqrt{R_o^2 - (h-x)^2}}{R_i}\right)\right] \tag{2.20}$$

To convert the fuselage coordinates to circular cylindrical coordinates, the following identities are employed:

$$x = x_o - \rho \sin\Phi$$

$$y = \rho \cos\Phi$$

$$\bar{u}_x = -(\bar{u}_\rho \sin\Phi + \bar{u}_\Phi \cos\Phi)$$

$$\bar{u}_y = \bar{u}_\rho \cos\Phi - \bar{u}_\Phi \sin\Phi \tag{2.21}$$

Substituting these identities in Equations (2.19) and (2.20) for the incident fields yields the following expressions for the components of the incident fields.

<u>Incident E Field</u>

$$E_\rho = E_o f(\theta) \cos\Phi \cos\alpha \left(\frac{e^{-j\beta R_o}}{R_o} - \frac{e^{-j\beta R_i}}{R_i}\right)$$

$$E_\Phi = -E_o f(\theta) \sin\Phi \cos\alpha \left(\frac{e^{-j\beta R_o}}{R_o} - \frac{e^{-j\beta R_i}}{R_i}\right)$$

$$E_z = -E_o f(\theta) \sin\alpha \left(\frac{e^{-j\beta R_o}}{R_o} - \frac{e^{-j\beta R_i}}{R_i} \right) \tag{2.22}$$

Incident H Field

$$H_\rho = \frac{E_o f(\theta)}{\eta} \left[\left(\frac{(x-h)}{R_o} \cos\Phi \sin\alpha \frac{\sqrt{R_o^2 - (h-x)^2}}{R_o} \right) \frac{e^{-j\beta R_o}}{R_o} - \left(\cos\Phi \sin\alpha \frac{(h+x)}{R_i} + \sin\Phi \frac{\sqrt{R_o - (h-x)^2}}{R_i} \right) \frac{e^{-j\beta R_i}}{R_i} \right]$$

$$H_\Phi = \frac{-E_o f(\theta)}{\eta} \left[\left(\sin\Phi \sin\alpha \frac{(x-h)}{R_o} - \cos\Phi \frac{\sqrt{R_o^2 - (h-x)^2}}{R_o} \right) \frac{e^{-j\beta R_o}}{R_o} - \left(\sin\Phi \sin\alpha \frac{(h+x)}{R_i} - \cos\Phi \frac{\sqrt{R_o^2 - (h-x)^2}}{R_i} \right) \frac{e^{-j\beta R_i}}{R_i} \right]$$

$$H_z = \frac{E_o f(\theta)}{\eta} \left[\cos\alpha \frac{(x-h)}{R_o} \frac{e^{-j\beta R_o}}{R_o} - \cos\alpha \frac{(h+x)}{R_i} \frac{e^{-j\beta R_i}}{R_i} \right] \tag{2.23}$$

where

$$R_o = \sqrt{(h-x)^2 + A^2 + B^2}$$

$$R_i = \sqrt{(h+x)^2 + A^2 + B^2}$$

$$A = xf + \rho\cos\Phi - xp - \text{offset}$$

$$B = yf + z_m \qquad (z_m \text{ is as shown in Figure 2-21})$$

The standard glide-path antenna currently in use is a horizontal dipole over a ground plane. The following assumptions will be made in the work that follows.

(1) The horizontal pattern of this antenna will be approximated by a cosine variation with θ, where

$$\theta = f(z) = \tan^{-1} \frac{A}{B}$$

(2) Any radiation by this antenna to the rear will be considered negligible.

(3) The ground will be considered perfectly flat and acting as a perfect mirror to the incident energy, so that image theory is applicable.

c. Tangential H Fields on Cylindrical Fuselage with Axis Parallel to Runway Centerline. If the fuselage is taken to be perfectly conducting the incident plus scattered tangential electric fields must sum to zero at its surface ($\rho = a$) (Figure 2-23). A good approximation to the scattered field at the fuselage can be found by regarding the fuselage as part of an infinite cylinder on whose surface the boundary conditions of zero tangential electrical field is satisfied everywhere. The surface currents found from this viewpoint will then be regarded as "frozen in" the finite length fuselage and used to calculate directly a scattered field.

1) Approximation by Use of Local Wavenumber. A reasonable approximation to make for computing the tangential components of the H fields on the fuselage is to subdivide the fuselage into relatively short lengths and compute the local wavenumber for the center of the short length. Appendix D contains further justification for this technique. The length must be short enough so that the plane wave approximation for the incident field accurately describes the phase variation of the incident field over the interval. The scattered field (TM) cylindrical wave expansion can be determined from the condition $E_z = 0$ at $\rho = a$.

Using this approximation the TM cylindrical wave expansion representing outgoing waves at ∞ and with propagation factor $e^{-i\beta_z z}$ for the subdivided lengths are [5]:

$$H_z = 0$$

$$E_z(\Phi,z)_n = H_n^{(2)}(\beta_y a)(a_n \cos n\Phi + b \sin n\Phi)\, e^{-i\beta_z z},$$

$$E_\Phi(\Phi, z)_n = \frac{i\beta_z n}{\beta_y^2 a} H_n^{(2)}(\beta_y a)(a_n \sin n\Phi - b_n \cos n\Phi)\, e^{i\beta_z z},$$

$$H_\Phi(\Phi,z)_n = -\frac{i\beta}{\eta\beta_y} H_n^{(2)'}(\beta_y a)(a_n \cos n\Phi + b_n \sin n\Phi)\, e^{-i\beta_z z}. \tag{2.24}$$

The wave expansion coefficients are found by equating E_z in Equation (2.24) with the incident E_z in Equation (2.22) modified by the proper phase factor for plane wave incidence which results in the following expression:

$$E_o f(\theta) \sin\alpha \left(\frac{e^{-i\beta R_o}}{R_o} - \frac{e^{-i\beta R_i}}{R_i} \right) e^{-i\beta z \cos\alpha} =$$

$$-\sum_{n=0}^{\infty} H_n^{(2)}(\beta_y a)(a_n \cos n\Phi + b_n \sin n\Phi)\, e \tag{2.25}$$

The expressions for the TM wave expansion coefficients reduce to

$$(a_o)_{z_m} = -\sum_{\Phi=1}^{360} E_{z_{inc}}(\Phi, z_m)/(360\, H^{(2)}(\beta_y a))$$

$$(a_n)_{z_m} = -\sum_{\Phi=1}^{360} E_{z_{inc}}(\Phi,z_m) \cos n\Phi/180\, H_n^{(2)}(\beta_y a))$$

$$(b_n)_{z_m} = -\sum_{\Phi=1}^{360} E_{z_{inc}}(\Phi, z_m) \sin n\Phi / (180\, H_n^{(2)}(\beta_y a)) \tag{2.26}$$

where $E_{z_{inc}}(\Phi, z_m) = E_o f(\theta) \sin\alpha \left(\frac{e^{-i\beta R_o}}{R_o} - \frac{e^{-i\beta R_i}}{R_i} \right)$

A series of TM waves with these coefficients (2.26) will cancel E_z of the incident field, but will generate an E_Φ which adds to the E_Φ of the incident field. The resulting E_Φ must be concelled by a series of TE modes.

Using the aforementioned approximations the TE cylindrical waves representing outgoing waves at ∞ and with propagation factor $e^{-i\beta_z z}$ are

$$E_z = 0$$

$$H_z(\Phi, z)_n = H_n^{(2)}(\beta_y a)(A_n \cos n\Phi + B_n \sin n\Phi)\, e^{-i\beta_z z}$$

$$H_\Phi(\Phi, z)_n = \frac{i\beta_z n}{a\beta_y^2} H_n^{(2)}(\beta_y a)(A_n \sin n\Phi - B_n \cos n\Phi)\, e^{-i\beta_z z}$$

$$E_\Phi(\Phi, z)_n = \frac{i\eta\beta}{\beta_y} H_n^{(2)'}(\beta_y a)(A_n \cos n\Phi + B_n \sin n\Phi)\, e^{-i\beta_z z} \tag{2.27}$$

We solve for this set of coefficients by setting E_Φ in (2.27) equal to the sum of E_Φ in (2.24) and (2.22) which results in the following expression

$$\frac{i\eta\beta}{\beta_y} H_n^{(2)'}(\beta_y a)(A_n \cos n\Phi + B_n \sin n\Phi) = -\frac{i\beta R_i}{\beta_y^2 a} H_n^{(2)}(\beta_y a)(a_n \sin n\Phi - b_n \cos n\Phi)$$

$$+ E_o f(\theta) \sin\Phi \cos\alpha \left(\frac{e^{-i\beta R_o}}{R_o} - \frac{e^{i\beta R_i}}{R_i} \right) \tag{2.28}$$

where $e^{-j\beta \cos \alpha z}$ common to all terms has been cancelled.

The expressions for the TE wave expansion coefficients reduce to

$$\frac{j\eta\beta}{\beta_y} H_o^{(2)'} (\beta_y a)(A_o)_{z_m} = + \sum_{\Phi=1}^{360} E_{\Phi_{inc}} (\Phi, z_m)/360$$

$$\frac{j\eta\beta}{\beta_y} H_n^{(2)'} (\beta_y a)(A_n)_{z_m} = \sum_{\Phi=1}^{360} (E_{\Phi_{inc}} (\Phi, z_m) - E_{\Phi_{TM}} (\Phi, z_m)) \cos n\Phi/180$$

$$\frac{j\eta\beta}{\beta_y} H_n^{(2)'} (\beta_y a)(B_n)_{z_m} = + \sum_{\Phi=1}^{360} (E_{\Phi_{inc}} (\Phi, z_m) - E_{\Phi_{TM}} (\Phi, z_m)) \sin n\Phi/180 \tag{2.29}$$

where $E_{\Phi_{inc}} (\Phi, z_m) = E_o f(\theta) \sin \Phi \cos \alpha \left(\frac{e^{-j\beta R_o}}{R_o} - \frac{e^{-j\beta R_i}}{R_i} \right)$

After completing the computation of the TM wave coefficients (2.26) and TE wave coefficients (2.29) they are substituted in (2.24) and (2.27) to check the cancellation of the incident fields. Provided the cancellation is satisfactory, the tangential components of the H-field are computed in (2.24) and (2.27).

REAL PART INCIDENT EZ	IMAG PART INCIDENT EZ	REAL PART SCATTERED EZ	IMAG PART SCATTERED EZ	PHI
0.110566E-03	-0.601000E-04	-0.110542E-03	0.600425E-04	10
0.109954E-03	-0.369952E-04	-0.109991E-03	0.369540E-04	20
0.106003E-03	-0.782851E-05	-0.105942E-03	0.780149E-05	30
0.939854E-04	0.237058E-04	-0.939267E-04	-0.236811E-04	40
0.716332E-04	0.518951E-04	-0.716527E-04	-0.518915E-04	50
0.400880E-04	0.707106E-04	-0.400954E-04	-0.707497E-04	60
0.394374E-05	0.757628E-04	-0.394298E-05	-0.757575E-04	70
-0.303590E-04	0.657005E-04	0.303262E-04	-0.656180E-04	80
-0.563662E-04	0.426247E-04	0.564294E-04	-0.426247E-04	90
-0.701832E-04	0.116102E-04	0.701463E-04	-0.116067E-04	100
-0.702744E-04	-0.214136E-04	0.702922E-04	0.214174E-04	110
-0.584311E-04	-0.510563E-04	0.584405E-04	0.510812E-04	120
-0.384802E-04	-0.738970E-04	0.384660E-04	0.739077E-04	130
-0.151147E-04	-0.889493E-04	0.151316E-04	0.889107E-04	140
0.705056E-05	-0.976908E-04	-0.705552E-05	0.977258E-04	150
0.247060E-04	-0.103347E-03	-0.246890E-04	0.103366E-03	160
0.354535E-04	-0.109124E-03	-0.354558E-04	0.109121E-03	170
0.372045E-04	-0.117180E-03	-0.372348E-04	0.117202E-03	180
0.281264E-04	-0.127726E-03	-0.280868E-04	0.127714E-03	190
0.588293E-05	-0.137711E-03	-0.587099E-05	0.137740E-03	200
-0.297835E-04	-0.141018E-03	0.298080E-04	0.141030E-03	210
-0.754798E-04	-0.129140E-03	0.754845E-04	0.129133E-03	220
-0.121627E-03	-0.946426E-04	0.121620E-03	0.946561E-04	230
-0.153617E-03	-0.364443E-04	0.153599E-03	0.363954E-04	240
-0.156578E-03	0.368545E-04	0.156570E-03	-0.368606E-04	250
-0.123098E-03	0.107128E-03	0.123092E-03	-0.107135E-03	260
-0.586339E-04	0.154106E-03	0.585905E-04	-0.154115E-03	270
0.197080E-04	0.164685E-03	-0.197358E-04	-0.164700E-03	280
0.907697E-04	0.139121E-03	-0.908542E-04	-0.139072E-03	290
0.139272E-03	0.893576E-04	-0.139293E-03	-0.892737E-04	300
0.160509E-03	0.321621E-04	-0.160520E-03	-0.321426E-04	310
0.159716E-03	-0.181331E-04	-0.159701E-03	0.181228E-04	320
0.146689E-03	-0.542170E-04	-0.146691E-03	0.541436E-04	330
0.130944E-03	-0.742644E-04	-0.130972E-03	0.742508E-04	340
0.118735E-03	-0.804101E-04	-0.118755E-03	0.803686E-04	350
0.112298E-03	-0.750575E-04	-0.112287E-03	0.750151E-04	360

Table 2-4. Comparison of Incident E_Φ (Φ, 1500) and Scattered E_Φ (Φ, 1500). Columns 3 and 4 are the Scattered E_Φ by the Wave Expansion Method.

2) Comparison of Results. Table 2-4 shows the incident fields as the scattered fields at the fuselage surface for the z component of the electric field at $z_m = 1500$ feet. The excellent cancellation of the incident fields confirms that enough cylindrical wave coefficients for the TM expansion were included and that they are correct. Table 2-5 shows the incident fields as well as the scattered fields at the fuselage surface for the Φ component of the electrical field at $z_m = 1500$ feet. Again the excellent cancellation of the incident field confirms that enough cylindrical wave coefficients for the TE expansion were included and they are correct.

These coefficients are now used to determine the tangential components of the scattered H-field at the fuselage surface. Table 2-6 and Table 2-7 show the tangential components of the Scattered H_Φ (Φ, 1500) fields, respectively. Examination of the tables shows that the total H-fields (incident + scattered) are approximately doubled on the side of the fuselage exposed to the antenna ($\Phi = 90$ to $\Phi = 270$) and the total H-field has very small values on the shadow side of the fuselage. This introduces the interesting possibility of merely doubling the incident H-field on the side of the fuselage exposed to the antenna when making a computation of fuselage surface currents and ignoring the small surface currents on the shadow side. This would rapidly yield approximate solution to the problem of scattering off the aircraft fuselage.

In the limit $\lambda/a \longrightarrow 0$, doubling the tangential H-field on the exposed side becomes exactly true. If λ becomes extremely small the diffraction around the fuselage becomes extremely small. If the radius a of the fuselage becomes extremely large the fuselage approaches a large flat wall.

d. Scattered Electric Field from Cylindrical Fuselage. Knowing the incident plus scattered tangential magnetic field at the fuselage surface, the surface currents on the fuselage are given by

$$\bar{J} = \bar{n} \times \bar{H}_{Total} \tag{2.30}$$

where n = a unit vector normal to the fuselage.

The electric field at a point on the aircraft flight path due to the surface currents on the fuselage and its image is given by (Ramo and Whinnery, pp. 506, 507)

$$\vec{E} = \frac{-j\beta\eta e^{-j\beta R}}{4\pi R} \left(\bar{N} - \bar{u}_r (\bar{N} \cdot \bar{u}_r) \right) \tag{2.31}$$

REAL PART EPHI INC	IMAG PART EPHI INC	REAL PART EPHI(TE+TM)	IMAG PART EPHI(TE+TM)	PHI
0.137239E-03	-0.745987E-04	-0.137231E-03	0.745103E-04	10
0.269391E-03	-0.906398E-04	-0.269531E-03	0.905281E-04	20
0.381015E-03	-0.281385E-04	-0.380846E-03	0.280433E-04	30
0.436381E-03	0.110068E-03	-0.436143E-03	-0.109953E-03	40
0.398741E-03	0.288871E-03	-0.398861E-03	-0.288873E-03	50
0.254028E-03	0.448077E-03	-0.254075E-03	-0.448369E-03	60
0.273270E-04	0.524975E-03	-0.273213E-04	-0.524984E-03	70
-0.222303E-03	0.481091E-03	0.222066E-03	-0.480508E-03	80
-0.422747E-03	0.319686E-03	0.423237E-03	-0.319679E-03	90
-0.522918E-03	0.865051E-04	0.522683E-03	-0.864627E-04	100
-0.503890E-03	-0.153542E-03	0.504069E-03	0.153580E-03	110
-0.389253E-03	-0.340124E-03	0.389352E-03	0.340295E-03	120
-0.228423E-03	-0.438662E-03	0.228347E-03	0.438739E-03	130
-0.757690E-04	-0.445856E-03	0.758430E-04	0.445727E-03	140
0.276364E-04	-0.382923E-03	-0.276620E-04	0.383033E-03	150
0.664993E-04	-0.278172E-03	-0.664420E-04	0.278230E-03	160
0.485650E-04	-0.149481E-03	-0.485459E-04	0.149471E-03	170
0.467500E-09	-0.147244E-08	0.156579E-07	-0.515138E-08	180
-0.385275E-04	0.174958E-03	0.384719E-04	-0.174946E-03	190
-0.158345E-04	0.370663E-03	0.157880E-04	-0.370747E-03	200
0.116743E-03	0.552752E-03	-0.116854E-03	-0.552814E-03	210
0.378373E-03	0.647368E-03	-0.378404E-03	-0.647354E-03	220
0.721993E-03	0.561809E-03	-0.721954E-03	-0.561912E-03	230
0.102335E-02	0.242782E-03	-0.102325E-02	-0.242465E-03	240
0.112272E-02	-0.264258E-03	-0.112269E-02	0.264305E-03	250
0.917171E-03	-0.798188E-03	-0.917159E-03	0.798241E-03	260
0.439754E-03	-0.115580E-02	-0.439447E-03	0.115588E-02	270
-0.144312E-03	-0.120591E-02	0.144524E-03	0.120603E-02	280
-0.628962E-03	-0.964002E-03	0.629576E-03	0.963677E-03	290
-0.882538E-03	-0.566240E-03	0.882691E-03	0.565715E-03	300
-0.893464E-03	-0.179029E-03	0.893529E-03	0.178910E-03	310
-0.741576E-03	0.841933E-04	0.741488E-03	-0.841574E-04	320
-0.527257E-03	0.194876E-03	0.527251E-03	-0.194611E-03	330
-0.320819E-03	0.181952E-03	0.320895E-03	-0.181907E-03	340
-0.147381E-03	0.998098E-04	0.147423E-03	-0.997481E-04	350
-0.180242E-08	0.120470E-08	0.263390E-08	-0.104774E-07	360

Table 2-5. Comparison of Incident E_Φ (Φ, 1500) and Scattered E_Φ (Φ, 1500). Columns 3 and 4 are the Scattered E_Φ by the Wave Expansion Method.

REAL PART HPHI INC	IMAG PART HPHI INC	REAL PART HPHI SCATTERED	IMAG PART HPHI SCATTERED	PHI
-0.208265E-05	0.113408E-05	0.207754E-05	-0.946773E-06	10
-0.197978E-05	0.669316E-06	0.177510E-05	-0.590978E-06	20
-0.176525E-05	0.134675E-06	0.149593E-05	-0.268597E-06	30
-0.139224E-05	-0.345497E-06	0.128104E-05	-0.996636E-09	40
-0.898328E-06	-0.642715E-06	0.112315E-05	0.244278E-06	50
-0.368310E-06	-0.687580E-06	0.960657E-06	0.502331E-06	60
-0.345259E-07	-0.509637E-06	0.709295E-06	0.763792E-06	70
0.968300E-07	-0.229326E-06	0.320153E-06	0.960395E-06	80
-0.599443E-06	-0.588239E-06	-0.180072E-06	0.994293E-06	90
-0.249187E-06	0.330955E-07	-0.694633E-06	0.796333E-06	100
-0.489590E-06	-0.150966E-06	-0.109551E-05	0.364762E-06	110
-0.597663E-06	-0.531006E-06	-0.127565E-05	-0.229926E-06	120
-0.508225E-06	-0.988021E-06	-0.119983E-05	-0.871659E-06	130
-0.237373E-06	-0.142286E-05	-0.913[illegible]2E-06	-0.145304E-05	140
0.131101E-06	-0.177418E-05	-0.523026E-06	-0.191664E-05	150
0.490344E-06	-0.204368E-05	-0.153422E-06	-0.226608E-05	160
0.736898E-06	-0.226654E-05	0.794548E-07	-0.254055E-05	170
0.784540E-06	-0.247300E-05	0.846512E-07	-0.277091E-05	180
0.582394E-06	-0.265177E-05	-0.196235E-06	-0.293480E-05	190
0.114015E-06	-0.272039E-05	-0.769772E-06	-0.293570E-05	200
-0.542477E-06	-0.255567E-05	-0.154797E-05	-0.262336E-05	210
-0.120576E-05	-0.205721E-05	-0.231885E-05	-0.187153E-05	220
-0.161707E-05	-0.125450E-05	-0.277884E-05	-0.693774E-06	230
-0.157305E-05	-0.370326E-06	-0.265893E-05	0.681630E-06	240
-0.108455E-05	0.258261E-06	-0.189492E-05	0.186362E-05	250
-0.424355E-06	0.373053E-06	-0.706266E-06	0.248885E-05	260
0.566077E-08	-0.710514E-08	0.516280E-06	0.243413E-05	270
-0.663798E-07	-0.577676E-06	0.143800E-05	0.185889E-05	280
-0.614683E-06	-0.947060E-06	0.195943E-05	0.106685E-05	290
-0.136624E-05	-0.381015E-06	0.219189E-05	0.304398E-06	300
-0.201212E-05	-0.405756E-06	0.231255E-05	-0.328467E-06	310
-0.237042E-05	0.266874E-06	0.242500E-05	-0.830914E-06	320
-0.244879E-05	0.903097E-06	0.252979E-05	-0.120555E-05	330
-0.236243E-05	0.133843E-05	0.257534E-05	-0.142153E-05	340
-0.223904E-05	0.151583E-05	0.251620E-05	-0.143917E-05	350
-0.214782E-05	0.143608E-05	0.234175E-05	-0.126073E-05	360

Table 2-6. Comparison of Incident H_Φ (Φ, 1500) and Scattered H_Φ (Φ, 1500). Columns 3 and 4 are the Scattered H_Φ by the Wave Expansion Method.

REAL PART HZ INC	IMAG PART HZ INC	REAL PART HZ SCATTERED	IMAG PART HZ SCATTERED	PHI
-0.485995E-07	-0.292504E-07	0.522374E-07	0.661529E-07	10
-0.394650E-07	-0.417546E-07	0.283551E-07	0.657795E-07	20
-0.240314E-07	-0.533100E-07	0.153767E-08	0.548258E-07	30
-0.210212E-08	-0.595918E-07	-0.191286E-07	0.355720E-07	40
0.234670E-07	-0.560186E-07	-0.271325E-07	0.135990E-07	50
0.468[illegible]E-07	-0.401116E-07	-0.216039E-07	-0.298176E-08	60
0.608[illegible]1E-07	-0.135491E-07	-0.771089E-08	-0.828605E-08	70
0.603497E-07	0.173694E-07	0.586879E-08	-0.173953E-08	80
0.449693E-07	0.441095E-07	0.116261E-07	0.120696E-07	90
0.195672E-07	0.597631E-07	0.709433E-08	0.257820E-07	100
-0.802715E-08	0.620001E-07	-0.508199E-08	0.335726E-07	110
-0.310477E-07	0.535266E-07	-0.202209E-07	0.336160E-07	120
-0.462245E-07	0.397885E-07	-0.337596E-07	0.274133E-07	130
-0.539387E-07	0.261227E-07	-0.434125E-07	0.183713E-07	140
-0.565669E-07	0.161379E-07	-0.490734E-07	0.971045E-08	150
-0.566647E-07	0.114215E-07	-0.517716E-07	0.357689E-08	160
-0.557401E-07	0.123378E-07	-0.524424E-07	0.884531E-09	170
-0.537675E-07	0.186109E-07	-0.516844E-07	0.193403E-08	180
-0.492044E-07	0.293961E-07	-0.490521E-07	0.634753E-08	190
-0.396724E-07	0.428561E-07	-0.437683E-07	0.133086E-07	200
-0.229610E-07	0.554302E-07	-0.351181E-07	0.214179E-07	210
0.113715E-08	0.618924E-07	-0.231520E-07	0.287620E-07	220
0.290620E-07	0.568738E-07	-0.931007E-08	0.331041E-07	230
0.536988E-07	0.377572E-07	0.382501E-08	0.329614E-07	240
0.666374E-07	0.731235E-08	0.131569E-07	0.280232E-07	250
0.625683E-07	-0.263955E-07	0.163165E-07	0.191735E-07	260
0.424728E-07	-0.533331E-07	0.133384E-07	0.899972E-08	270
0.133713E-07	-0.664949E-07	0.624252E-08	-0.693620E-10	280
-0.156949E-07	-0.650105E-07	-0.567841E-09	-0.581462E-08	290
-0.379740E-07	-0.532680E-07	-0.277914E-08	-0.708163E-08	300
-0.511439E-07	-0.377857E-07	0.294336E-08	-0.354483E-08	310
-0.567456E-07	-0.239216E-07	0.169633E-07	0.423006E-08	320
-0.578234E-07	-0.146264E-07	0.361806E-07	0.156568E-07	330
-0.569968E-07	-0.109498E-07	0.549121E-07	0.295248E-07	340
-0.555540E-07	-0.125410E-07	0.665544E-07	0.445190E-07	350
-0.532517E-07	-0.189432E-07	0.661075E-07	0.579381E-07	360

Table 2-7. Comparison of Incident H_z (Φ, 1500) and Scattered H_z (Φ, 1500). Columns 3 and 4 are the Scattered H_z by the Wave Expansion Method.

$$\bar{N} = \iint_{\text{fuselage}} \bar{J}^F e^{j\beta(\bar{p}_F \cdot \bar{u}_r)} dS_F + \iint_{\text{image}} \bar{J}^I e^{j\beta(\bar{p}_I \cdot \bar{u}_r)} dS_I \qquad (2.32)$$

where $\bar{u}_r$ = a unit vector directed along the line from point "0" to the aircraft point,

$\bar{p}$ = a position vector from "0" to any point on the fuselage with subscript identifying fuselage and image,

$\bar{N}$ = Schelkunoff's radiation vector, and

$\bar{J}$ = vector surface current on the fuselage with superscript identifying the fuselage and image.

$\bar{p}_F$, $\bar{p}_I$, and $\bar{u}_r$ are given by: (Figure 2-23).

$$\bar{p}_F = \bar{u}_x (x_o - a \sin \Phi) + \bar{u}_y (a \cos \Phi) + \bar{u}_z (z - z_m)$$

$$\bar{p}_I = \bar{u}_x (-x_o - a \sin \Phi) + \bar{u}_y (a \cos \Phi) + \bar{u}_z (z - z_m)$$

$$\bar{u}_r = \bar{u}_x \left(\frac{H}{R}\right) = \bar{u}_y (-\sin \sigma) + \bar{u}_z (\cos \sigma) \qquad (2.33)$$

$\bar{J}^F$ and $\bar{J}^I$ are related as follows by the conditions for imaging in a perfectly conducting plane

$$J_x^I (\Phi) = J_x^F (-\Phi)$$

$$J_y^I (\Phi) = J_y^F (-\Phi)$$

$$J_z^I (\Phi) = J_z^F (-\Phi) \qquad (2.34)$$

Using (2.30) and relating the rectangular components of H to its cylindrical components gives:

$$J_x^F = H_z \cos\Phi$$

$$J_y^F = H_z \sin\Phi$$

$$J_z^F = H_\Phi \tag{2.35}$$

where the components of H represents the sum of the incident plus the wave expansion fields.

Substituting (2.33) through (2.35) into (2.32) gives the following expressions for the components of the radiation vector:

$$N_x = a \int_{z=z_m-\frac{\Delta z}{2}}^{z=z_m+\frac{\Delta z}{2}} \int_{\Phi=0}^{2\pi} \cos\Phi \Big[(H_{z_{inc}}(\Phi,z) + H_{z_{scat}}(\Phi,z))\, e^{j\beta x_o H/R}$$

$$+ (H_{z_{inc}}(-\Phi,z) + H_{z_{scat}}(-\Phi,z))\, e^{-j\beta x_o H/R} \Big] e^{-j\beta\left(\frac{aH}{R}\right)\sin\Phi + a\sin\sigma\cos\Phi}$$

$$- (z-z_m)\cos\sigma\,) \; d\Phi\, dz \tag{2.36}$$

$$N_y = a \int_{z=z_m-\frac{\Delta z}{2}}^{z=z_m+\frac{\Delta z}{2}} \int_{\Phi=0}^{2\pi} \sin\Phi \Big[(H_{z_{inc}}(\Phi,z) + H_{z_{scat}}(\Phi,z))\, e^{j\beta x_o H/R}$$

$$+ (H_{z_{inc}}(-\Phi,z) + H_{z_{scat}}(-\Phi,z))\, e^{-j\beta x_o H/R} \Big] e^{-j\beta\left(\frac{aH}{R}\sin\Phi + a\sin\sigma\cos\Phi\right.}$$

$$- (z-z_m)\cos\sigma\,) \; d\Phi\, dz \tag{2.37}$$

$$N_z = a \int_{z=z_m - \frac{\Delta z}{2}}^{z=z_m + \frac{\Delta z}{2}} \int_{\Phi=0}^{2\pi} \sin\Phi \; [(H_{\Phi_{inc}}(\Phi,z) + H_{\Phi_{scat}}(\Phi,z)) \, e^{i\beta x_o H/R}$$

$$- (H_{\Phi_{inc}}(-\Phi,z) + H_{\Phi_{scat}}(-\Phi,z)) \, e^{-i\beta x_o H/R}] \, e^{-i\beta (\frac{a H}{R} \sin\Phi + a \sin\sigma \cos\Phi}$$

$$- (z-z_m) \cos\sigma) \; d\Phi \, dz \qquad (2.38)$$

where the limits on z represent the edges of the short length of fuselage being considered.

All the incident and scattered magnetic field components appearing in (2.36), (2.37) and (2.38) include the propagation factor $e^{-i\beta (z-z_m) \cos a}$.

The integral over z is identical in (2.36), (2.37), and (2.38). It can be designated as I and is given by

$$I = \int_{z = z_m - \frac{\Delta z}{2}}^{z = z_m + \frac{\Delta z}{2}} e^{i\beta (z-z_m) (\cos\sigma - \cos a)} \, dz \qquad (2.39)$$

Carrying out the integration gives

$$I = \Delta z \; \frac{\sin \frac{\beta \Delta z}{2} (\cos\sigma - \cos a)}{\frac{\beta \Delta z}{2} (\cos\sigma - \cos a)} \qquad (2.40)$$

We shall see later that the N_x component will not contribute to the scattered field and the computation of this component will not be continued. Recalling that the incident H field was computed for one degree increments on Φ and combining the incident and scattered terms in the integrand the integrals become

$$N_y = a\,I\Big(\frac{\pi}{180}\sum_{\Phi=1}^{360} \sin\Phi\,\big[\,(H_{z_{inc}}(\Phi,z)\,e^{j\delta H} + H_{z_{inc}}(-\Phi,z)\,e^{-j\delta H})\,e^{-j\beta\left(\frac{aH}{R}\sin\Phi + a\sin\sigma\cos\Phi\right)}\big]$$

$$+\int_{\Phi=0}^{2\pi} \sin\Phi\,\Big[\sum_{n=0}^{\infty} H_n^{(2)}(\beta_y a)\,(A_n\cos n\Phi + B_n\sin n\Phi)\,e^{j\delta H} + (A_n\cos(-n\Phi) + B_n\sin(-n\Phi))\,e^{-j\delta H}\Big]$$

$$e^{-j\beta\left(\frac{aH}{R}\sin\Phi + a\sin\sigma\cos\Phi\right)}\,d\Phi\Big) \qquad (2.41)$$

$$N_z = a\,I\Big[\frac{\pi}{180}\sum_{\Phi=1}^{360}(H_{\Phi_{inc}}(\Phi,z)e^{j\delta H} - H_{\Phi_{inc}}(-\Phi,z)e^{-j\delta H})e^{-j\beta\left(\frac{aH}{R}\sin\Phi + a\sin\sigma\cos\Phi\right)}$$

$$+\int_0^{2\pi}\frac{j\beta_z}{a\beta_y^2}\Big(\sum_{n=0}^{\infty} n\,H_n^{(2)}(\beta_y a)\,((A_n\sin n\Phi - B_n\cos n\Phi)e^{j\delta H}$$

$$-(A_n\sin(-n\Phi) - B_n\cos(-n\Phi)\,e^{-j\delta H}))\,e^{-j\beta\left(\frac{aH}{R}\sin\Phi + a\sin\sigma\cos\Phi\right)}\,d\Phi\Big]$$

$$-\int_0^{2\pi}\frac{j\beta}{\eta\beta_y}\sum_{n=0}^{\infty} H_n^{(2)'}(\beta_y a)\,((a_n\cos n\Phi + b_n\sin n\Phi)\,e^{j\delta H}$$

$$-(a_n\cos(-n\Phi) + b_n\sin(-n\Phi))\,e^{-j\delta H})e^{-j\beta\left(\frac{aH}{R}\sin\Phi + a\sin\sigma\cos\Phi\right)}\,d\Phi$$

where $\qquad \delta = \beta x_o / R \qquad (2.42)$

Applying the following relationships simplifies the summation on the incident fields

$$H_{\Phi_{inc}}(\Phi,z) = H_{\Phi_{inc}}(-(360-\Phi),\ z)$$

$$H_{z_{inc}}(\Phi,z) = H_{z_{inc}}(-(360-\Phi),\ z) \qquad (2.43)$$

Combining some terms in the integrals results in the following relationships for the components of the radiation vector

$$N_y = a\,I\,[\ \frac{\pi}{90}\, i \sum_{\Phi=1}^{360} H_{z_{inc}}(\Phi,z)\sin\Phi\sin(\delta H - \frac{\beta a H}{R}\sin\Phi)\,e^{-j\beta a \sin\sigma\cos\Phi}$$

$$+2\int_0^{2\pi} \sin\Phi\,[\sum_{n=0}^{\infty} H_n^{(2)}(\beta_y a)(A_n\cos(\delta H)\cos n\Phi + jB_n\sin(\delta H)\sin n\Phi)$$

$$e^{-j\beta(\frac{aH}{R}\sin\Phi + a\sin\sigma\cos\Phi)}\,d\Phi\,] \qquad (2.44)$$

$$N_z = \frac{a\pi}{90}\,I\,j \sum_{\Phi=1}^{360} H_{\Phi_{inc}}(\Phi,z)\sin(\delta H - \frac{\beta a H}{R}\sin\Phi)\,e^{-j\beta a\sin\sigma\cos\Phi}$$

$$+2\,I\,a\int_0^{2\pi} (j\sin\delta H_{n=0}\,C\cos n\Phi + \cos\delta H_{n=0}\,D\sin n\Phi)$$

$$e^{-j\beta(\frac{aH}{R}\sin\Phi + a\sin\sigma\cos\Phi)}\,d\Phi \qquad (2.45)$$

where

$$C_n = -\frac{i}{\beta a \sin\alpha \tan\alpha} H_n^{(2)}(\beta_y a)\, n B_n - \frac{i}{\eta \sin\alpha} H_n^{(2)'}(\beta_y a)\, a_n$$

$$D_n = \frac{i}{\beta a \sin\alpha \tan\alpha} H_n^{(2)}(\beta_y a)\, n A_n - \frac{i}{\eta \sin\alpha} H_n^{(2)}(\beta_y a)\, b_n$$

The integrations (2.44) and (2.45) can be carried out with the aid of identities and definitions as follows

$$\int_0^{2\pi} e^{i c \cos(\Phi - \psi)} \cos n\Phi \, d\Phi = 2\pi i^n \cos n\psi \, J_n(c)$$

$$\int_0^{2\pi} e^{i c \cos(\Phi - \psi)} \sin n\Phi \, d = 2\pi i^n \sin n\psi \, J_n(c)$$

$$C_1 = \beta a \sqrt{\left(\frac{H}{R}\right)^{(2)} + \sin^2\sigma}$$

$$\tan\psi_1 = \frac{H}{R \sin\sigma} \qquad (2.46)$$

The resulting expression for the two components of N are

$$N_y = 2a\pi I \Big[\frac{j}{180} \sum_{\Phi=1}^{360} H_{z_{inc}}(\Phi,z)\sin\Phi \sin(\delta H - \frac{\beta a H}{R}\sin\Phi) e^{-j\beta a \sin\sigma\cos\Phi}$$

$$+ 2j\cos(\delta H) H_o^{(2)}(\beta_y a) A_o \sin\psi_1 J_1(C_1) +$$

$$\sum_{n=1}^{\infty} j^n H_n^{(2)}(\beta_y a)\big(jA_n \cos\delta H(\sin((n+1)\psi_1)J_{n+1}(C_1) + \sin((n-1)\psi_1)J_{n-1}(C_1))$$

$$+ B_n \sin\delta H(\cos((n-1)\psi_1)J_{n-1}(C_1) + \cos((n+1)\psi_1)J_{n+1}(C_1))\big) \Big] \qquad (2.47)$$

$$N_z = 2a\pi I \Big[\frac{j}{180} \sum_{\Phi=1}^{360} H_{\Phi_{inc}}(\Phi,z)\sin(\delta H - \frac{\beta a H}{R}\sin\Phi) e^{-j\beta a \sin\sigma\cos\Phi} +$$

$$2(j\sin(\delta H) C_o J_o(C_1) + \sum_{n=1}^{\infty} j^n (j\sin(\delta H)\cos(n\psi_1)C_n + \cos(\delta H)\sin(n\psi_1)D_n) J_n(C_1))\Big] \qquad (2.48)$$

The scattered $\bar{E}$ - field can be computed from (2.44, [illegible]), and (2.31). Only the horizontal components of E are of interest. These are

$$E_y = \frac{-j\beta\eta}{4\pi R} e^{-j\beta R} [N_y \cos^2\sigma + N_x \frac{H}{R} \sin [illegible] + N_z \sin\sigma\cos\sigma] \qquad (2.49)$$

$$E_z = \frac{-j\beta\eta}{4\pi R} e^{-j\beta R} [N_z \sin^2\sigma - N_x \cos\sigma + N_y \sin\sigma\cos\sigma] \qquad (2.50)$$

The receiving antenna is assumed omni-directional and the voltage induced at its terminals by the scattered field may be expressed as

$$V_s \sim [E_y \cos\sigma + E_z \sin\sigma] \tag{2.51}$$

Inserting (2.46) and (2.47) in (2.48) justifies our previous neglect of $\overline{N}_x$ and yields

$$V_s \sim \frac{-j\beta\eta}{4\pi R} e^{-j\beta R} [N_y \cos\sigma + N_z \sin\sigma] \tag{2.52}$$

The term in parenthesis represents a complex quantity and we may write (2.52) in the following form

$$V_s \sim \frac{-j\beta\eta}{4\pi R} e^{-j\beta R} N \; e^{jp'} \tag{2.53}$$

where $|N|$ = the magnitude of the radiation vector

p' = the phase angle of the radiation vector

e. Scattered Electric Field from Sweptback Vertical Tail Fin in Close Proximity to Antenna. Reference is made to Figures 2-21 and 2-22 and the vertical tail fin lies in the x-z plane. The incident H-field is given by Equation (2.54) and is repeated here for ready reference. Ignoring the component of H_{inc} in the y direction gives the tangential components of the incident H field at any point on the tail fin.

$$H_T = \frac{E_o f(\theta)}{\eta} \left[\frac{e^{-j\beta R_o}}{R_o} \left(\bar{u}_z \cos\alpha \frac{(x-h)}{R_o} - \bar{u}_x \frac{\sqrt{R_o^2 - (h-x)^2}}{R_o}\right) - \frac{e^{-j\beta R_i}}{R_i} \left(\bar{u}_z \cos\alpha \frac{(h+z)}{R_i} - \bar{u}_x \frac{\sqrt{R_o^2 - (h-z)^2}}{R_i}\right)\right] \tag{2.54}$$

Assuming the currents induced in the wall are the same as would exist if the wall occupied the whole of the x-z plane, the tangential components of the H-field would be doubled. Introducing this factor of two in the tangential component of the H-field the induced wall currents at any point are given by ($\bar{J} = \bar{n} \times \bar{H}$)

$$\bar{J} = K_1 \left[\frac{e^{-j\beta R_o}}{R_o} \bar{u}_x \cos\alpha \frac{(h-x)}{R_o} - \bar{u}_z \frac{\sqrt{R_o^2 - (h-x)^2}}{R_o} \right)$$

$$+ \frac{e^{-j\beta R_i}}{R_i} \left(\bar{u}_x \cos\alpha \frac{(h+x)}{R_i} + \bar{u}_z \frac{\sqrt{R_o^2 - (h-x)^2}}{R_i} \right) \Bigg] \qquad (2.55)$$

where $K_1 = \dfrac{2E_o f(\theta)}{\eta}$

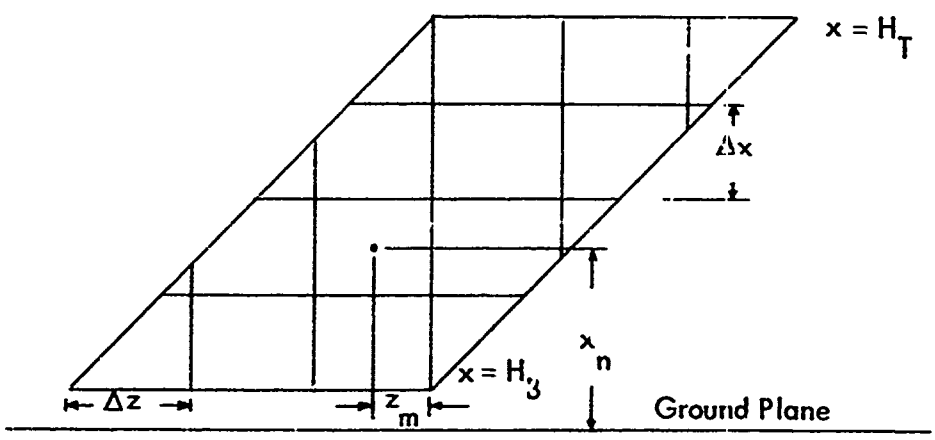

Figure 2-24. Geometry of Vertical Tail Fin.

The tail fin is divided up into strips of height Δx parallel to the ground plane and further subdivided into rectangular areas of length Δz where the z-coordinate of the center of any rectangle is z_m and the x-coordinate of any rectangle is x_n. The height of the increment Δx may be made small enough so that the vertical variation in phase across the increment may be described by (Figure 2-24)

$$e^{+\beta (x-x_n)(h-x_n)/R_o(x_n, z_m)} \text{ for the real antenna and}$$

$$e^{-j\beta (x-x_n)(h+x_n)/R_i(x_n, z_m)} \text{ for the image antenna.}$$

Similarly the lateral increments Δz may be made small enough so that the lateral variation in phase within m^{th} increment may be described by (Figure 2-24)

$$e^{-j\beta (z-z_m)\cos\alpha}$$

Including these phase terms the sheet currents in the neighborhood of any point (x_n, z_m) on the tail fin can be closely approximated by the following expression where R_o and R_i correspond to the point (x_n, z_m).

$$\bar{J}(x,z) = K_1 \left[\frac{e^{-j\beta(R_o - (x-x_n)(h-x_n)/R_o)}}{R_o} \left(\bar{u}_x \cos\alpha \frac{(h-x_n)}{R_o} - \bar{u}_z \frac{\sqrt{R_o^2 - (h-x_n)^2}}{R_o}\right) + \frac{e^{-j\beta(R_i + (x-x_n)(h+x_n)/R_i)}}{R_i} \left(\bar{u}_x \cos\alpha \frac{(h+x_n)}{R_i} + \bar{u}_z \frac{\sqrt{R_o^2 - (h-x_n)^2}}{R_i}\right)\right] e^{-j\beta(z-z_m)\cos\alpha} \tag{2.56}$$

Examining this expression reveals that the amplitude of the sheet current is independent of x and y over the small rectangular area. The reradiated E-field is given by

$$\bar{E}^R = \frac{\eta\beta}{4\pi} \left((\bar{u} \times \bar{N}) \times \bar{u}\right) \tag{2.57}$$

where $\bar{N}$ is the Schelkunoff radiation vector given by (Figure 2-21)

$$\bar{N} = \iint_{\text{wall}} \bar{J}^{w}(x,z)\, e^{j\beta(z-z_m)\cos\sigma}\, e^{j\beta(x-x_n)(H-h_n)/R_R^R}\, \frac{e^{-j\beta R_R^R}}{R_R^R}\, dx\, dz$$

$$+ \iint_{\text{Image}} \bar{J}^{i}(x,z)\, e^{j\beta(z-z_m)\cos\sigma}\, e^{-j\beta(x-x_n)(H+h_n)/R_i^R}\, \frac{e^{-j\beta R_i^R}}{R_R^R}\, dx\, dz \tag{2.58}$$

where H = the height of the aircraft and R_i^R, R_R^R are defined in Figure 2-25)

Examination of the equation for $\bar{N}$ shows that $\bar{N}$ has the same vector direction as the sheet current. Examining the cross product terms in the equation for the reradiated electric field shows that it is no longer necessary to carry through the x-component of the sheet current since it will generate a vertically polarized E-field at the horizontally polarized omni-directional aircraft receiving antenna.

$\bar{J}^{w}$ and $\bar{J}^{i}$ for imaging in a perfectly conducting ground plane are related by.

$$\bar{J}_z^{-i}(-x,z) = -\bar{J}_z^{w}(x,z)$$

Substituting in the equation for $\bar{N}$ results in the following integral

$$\bar{N}_z = \int_{z=z_m-\frac{\Delta z}{2}}^{z=z_m+\frac{\Delta z}{2}} \left[\int_{x=x_n-\frac{\Delta x}{2}}^{x=x_n+\frac{\Delta x}{2}} \bar{J}_z^{w}(x,z)\left(e^{j\beta(x-x_n)(H-x_n)/R_R^R}\, \frac{e^{-j\beta R_R^R}}{R_R^R} - e^{-j\beta(x-x_n)(H+x_n)/R_i^R}\, \frac{e^{-j\beta R_i^R}}{R_i^R}\right) dx \right] e^{j\beta(z-z_m)\cos\sigma}\, dz \tag{2.59}$$

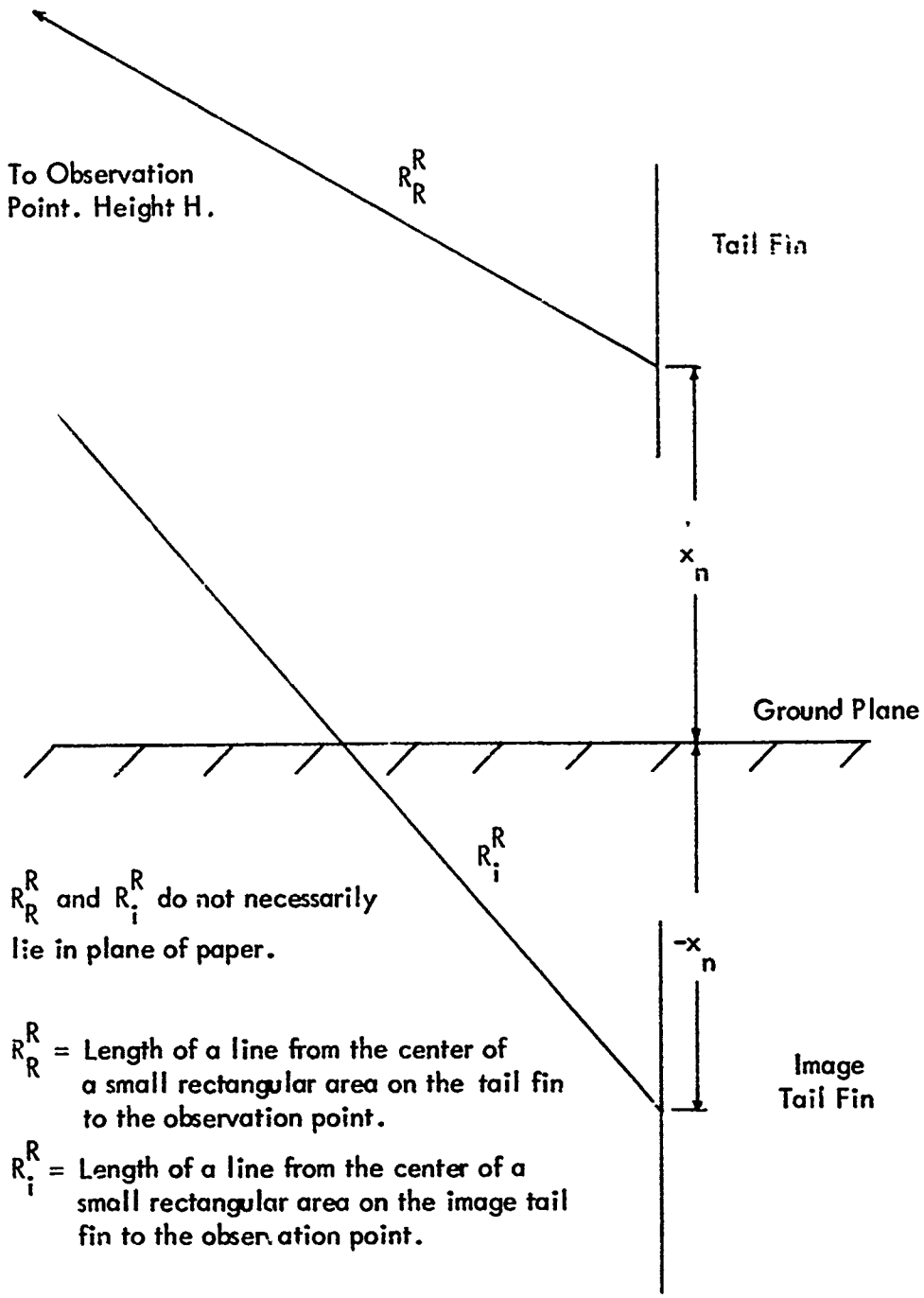

R_R^R and R_i^R do not necessarily lie in plane of paper.

R_R^R = Length of a line from the center of a small rectangular area on the tail fin to the observation point.

R_i^R = Length of a line from the center of a small rectangular area on the image tail fin to the observation point.

Figure 2-25. Geometry of the Tail Fin and Its Image.

The integration on the variable z is straightforward, since the z dependence of $\bar{J}^{w}(x, z)$ is quite simple. Designating this integral S_1 we have

$$S_1 = \int_{z=z_m - \frac{\Delta z}{2}}^{z=z_m + \frac{\Delta z}{2}} e^{i\beta(z-z_m)(\cos\sigma - \cos\alpha)} dz \tag{2.60}$$

$$S_1 = \left. \frac{e^{i\beta(z-z_m)(\cos\sigma - \cos\alpha)}}{i\beta(\cos\sigma - \cos\alpha)} \right|_{z=z_m - \frac{\Delta z}{2}}^{z=z_m + \frac{\Delta z}{2}} \tag{2.61}$$

$$S_1 = \frac{\Delta z \sin\beta \frac{\Delta z}{2}(\cos\sigma - \cos\alpha)}{\beta \frac{\Delta z}{2}(\cos\sigma - \cos\alpha)} \tag{2.62}$$

Substituting this result and the expression for the tail fin sheet currents in Equation (2.59) gives

$$\bar{N}_z = K_2 \int_{x=x-\frac{\Delta x}{2}}^{x=x_n+\frac{\Delta x}{2}} \left(\frac{e^{-i\beta(R_i+(x-x_n)(h+x_n)/R_i}}{R_i^2} - \frac{e^{-i\beta(R_o-(x-x_n)(h-x_n)/R_o)}}{R_o^2}\right)$$

$$\left(e^{i\beta(x-x_n)(H-x_n)/R_R^R} \frac{e^{-i\beta R_R^R}}{R_R^R} - e^{-i\beta(x-x_n)(H+x_n)/R_i^R} \frac{e^{-i\beta R_i^R}}{R_i^R}\right) dx \tag{2.63}$$

where $K_2 = S_1 K_1 \sqrt{R_o^2 - (h-x_n)^2}$

To evaluate the integral on x, four separate but similar integrations must be carried out. Integrating the product of the first and third term in the integrand and calling the result S_2 we have

$$S_2 = \frac{e^{-j\beta(R_i+R_R^R)}}{R_i^2 \; R_R^R} \int_{x=x_n-\frac{\Delta x}{2}}^{x=x+\frac{\Delta x}{2}} e^{-j\beta(x-x_n)((h+x_n)/R_i-(H-x_n)/R_R^R)} dx \tag{2.64}$$

$$S_2 = \frac{e^{-j\beta(R_i+R_R^R)}}{R_i^2 \; R_R^R} \; \frac{e^{-j\beta(x-x_n)((h+x_n)/R_i-(H-x_n)/R_R^R}}{-j\beta((h+x_n)/R_i-(H-x_n)/R_R^R} \Bigg|_{x=x_n-\frac{\Delta x}{2}}^{x=x_n+\frac{\Delta x}{2}} \tag{2.65}$$

$$S_2 = \frac{e^{-j\beta(R_i+R_R^R)}}{R_i^2 \; R_R^R} \; \frac{\Delta x \sin(A_2)}{A_2} \tag{2.66}$$

where $A_2 = \beta \frac{\Delta x}{2} ((h+x_n)/R_i - (H-x_n)/R_R^R)$

Similarly

$$S_3 = \frac{e^{-j\beta(R_o+R_i^R)}}{R_o^2 \; R_i^R} \; \frac{\Delta x \sin(A_3)}{A_3} \tag{2.67}$$

where $A_3 = \beta \frac{\Delta x}{2} ((h-x_n)/R_o - (H+x_n)/R_i^R)$

$$S_4 = -\frac{e^{-j\beta(R_i + R_i^R)}}{R_i^2 \; R_i^R} \quad \frac{\Delta x \sin(A_4)}{(A_4)} \tag{2.68}$$

where $A_4 = \beta \frac{\Delta x}{2} \left((h + x_n)/R_i + (H + x_n)/R_i^R \right)$

and

$$S_5 = -\frac{e^{-j\beta(R_o + R_R^R)}}{R_o^2 \; R_R^R} \quad \frac{\Delta x \sin(A_5)}{(A_5)} \tag{2.69}$$

where $A_5 = \beta \frac{\Delta x}{2} \left((h - x_n)/R_o + (H - x_n)/R_R^R \right)$

The radiation vector has been evaluated for a small rectangular area on the wall and is given below:

$$\overline{N}_z = K_2 S_T \overline{u}_z \tag{2.70}$$

where $S_T = S_2 + S_3 - S_4 - S_5$

The result must be substituted in the expression for the reradiated field Equation (2.57). Substituting for the cross products

$$\overline{E}^R = \frac{\eta \beta}{4\pi} \left((-\overline{u}_x K_2 S_T \sin \sigma) \times \overline{u} \right) = \left| \overline{E}^R \right| e^{jp} \tag{2.71}$$

where p = phase angle of S_T

and

$$\left|\bar{E}^{R}\right| = \frac{\eta \beta}{4\pi} \sin \sigma K_2 \left|ST\right| \tag{2.72}$$

The total reradiated E field from the tail fin is found by summing the complex contribution from each small rectangular area at each of the points on the aircraft flight path.

The receiving antenna is assumed omni-directional and the voltage induced at its terminal by the total scattered field may be expressed as

$$V_s \sim \sum_{z_m} \sum_{x_n} -j \left|\bar{E}\right|^{R} e^{jp} \tag{2.73}$$

f. Computation of Microampere Course Deviation Indicator Deflection from Scattered Electric Fields. The direct sideband voltage V_D induced at the aircraft receiving antenna terminals when the antenna is at an elevation angle Φ and slant range R_4 (Figure 2-26)

$$V_D(\Phi) \sim 2 j E_o f(\theta)_D \frac{e^{-j\beta R_4}}{R_4} \sin(\beta h \sin \Phi) \tag{2.74}$$

where $f(\theta)_D$ = the amplitude of the horizontal radiation pattern of the transmitting antenna at the aircraft receiving point.

$V_D(\Phi)$ will normally be adjusted to be in phase with the carrier sideband signal.

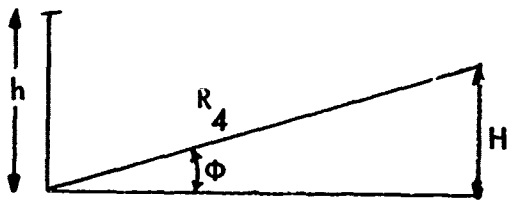

Figure 2-26. Vertical Plane Containing Transmitting Antenna Pole and Aircraft Receiving Point.

The sideband voltage induced at the receiving antenna by the total scattered field (fuselage + tail fin) is given by

$$V_s \sim -j \left[\sum_{x_n} \sum_{z_m} |E|^R e^{jP} + \frac{\eta \beta}{4\pi} \frac{e^{-j\beta R}}{R} N e^{jP'} \right] \quad (2.75)$$

where Equations (2.53) and (2.73) have been added together.

V_s will cause the path to be displaced far enough from the desired glide path position so that the component of V_s in the phase with $V_D(\Phi)$ sums to zero.

Assuming a linear variation in deflection of the cockpit indicator with elevation angle in the neighborhood of the desired path angle the following ratio will hold

$$\frac{D\ (\text{microamps})}{150} = \frac{V_D(\Phi)}{V_D(\Phi_p)} = \frac{\sin(\beta h \sin \Phi)}{\sin(\beta h \sin \Phi_p)} \quad (2.76)$$

where D = deflection of cockpit indicator at angle Φ

$V_D(\Phi_p)$ = sideband voltage amplitude at Φ_p

Φ_p = an angle for which the sideband power has been adjusted to correspond to 150 microamperes

$V_D(\Phi)$ = the amplitude of sideband voltage necessary to cancel in phase component of the field scattered by the fuselage and tail fin

Equating the sum of V_D (Φ) and the in phase component of V_s to zero and substituting for K_2 gives

$$\frac{2 E_o f(\theta)_D}{R_4} \sin(\beta h \sin \Phi) - \frac{\eta \beta}{4 \pi} \left[\sum_{x_n} \sum_{x_m} \sin \sigma \frac{2 E_o f(\theta)_m}{\eta} \right.$$

$$\left. S_1 |S_T| \cos(\beta R_4 + p) \quad R_o^2 - (h - x_n)^2 + \frac{\cos(\beta (R_4 - R) + p')}{R} N \right] = 0$$

(2.77)

Recalling that E_o has been set equal to unity we determine $\sin(\beta h \sin \Phi)$ and substituting in Equation (2.76) which gives the deflection of the cockpit indicator in microamperes

$$D_{(\text{microamps})} = \frac{75}{\lambda} \frac{R_4}{f(\theta)_D \sin(\beta h \sin \Phi_p)} \left[\sum_{x_n} \sum_{x_m} \sin \sigma f(\theta)_m \right.$$

$$\left. S_1 |S_T| \cos(p + \beta R_4) \quad \sqrt{R_o^2 - (h - x_n)^2} + \eta \frac{\cos(\beta (R_4 - R) + p'}{2 R} |N_y \cos \sigma + N_z \sin \sigma| \right]$$

(2.78)

g. Results and Conclusions.

1) Results. In section II D 1 it was noted that the total fuselage tangential H-fields were approximately double the incident field on the side exposed to the transmitting antennas and the total tangential H-field was very small on the shadow side. When the tangential H-fields are converted to surface sheet currents the principal contributor to the Schelkunoff radiation vector is the side exposed to the transmitting antennas.

For the results displayed in this section only the first term in Equations (2.47) and (2.48) were computed and the summation was then doubled to get a rapid approximate solution. The fuselage was subdivided into four foot lengths and the vertical tail fin was subdivided into two foot squares. All these results represent

the filtered output of the aircraft receiver.

Figure 2-26 shows the geometry of the problem and Figures 2-27 through 2-33 show the results corresponding to various values of the parameter D shown in Figure 2-26. In Figures 2-27 through 2-33 the 747 is assumed to be taxiing to the approach end of the runway so that the vertical tail fin is positioned on the end of the cylinder closest to the transmitting antennas. In Figures 2-31 through 2-33 the aircraft is positioned so that the tail is at the coordinates specified and the the nose is approximately 220 feet closer to centerline.

2) Conclusions.

a) For the geometry shown in Figure 2-26 the results show in Figures 2-27 through 2-29 that with the radiation pattern of the transmitting antennas currently in use (approximately a cos θ pattern) the 747 should be positioned so that D does not exceed 200 feet while other aircraft are on final approach.

b) Under no circumstances should the 747 be parked perpendicular to centerline directly in front of the glide slope array. The results in Figures 2-32 and 2-33 show that the shape of the measured path can change drastically with small changes in distance D forward of the array.

c) A transmitting antenna with a more directive horizontal pattern should be employed where large aircraft will be moving about in the vicinity of the glide path. Figure 2-30 shows that a 747 parked on the opposite side of the runway can cause an appreciable level of glide path roughness, which may be reduced and possibly eliminated by the use of a directional glide path antenna.

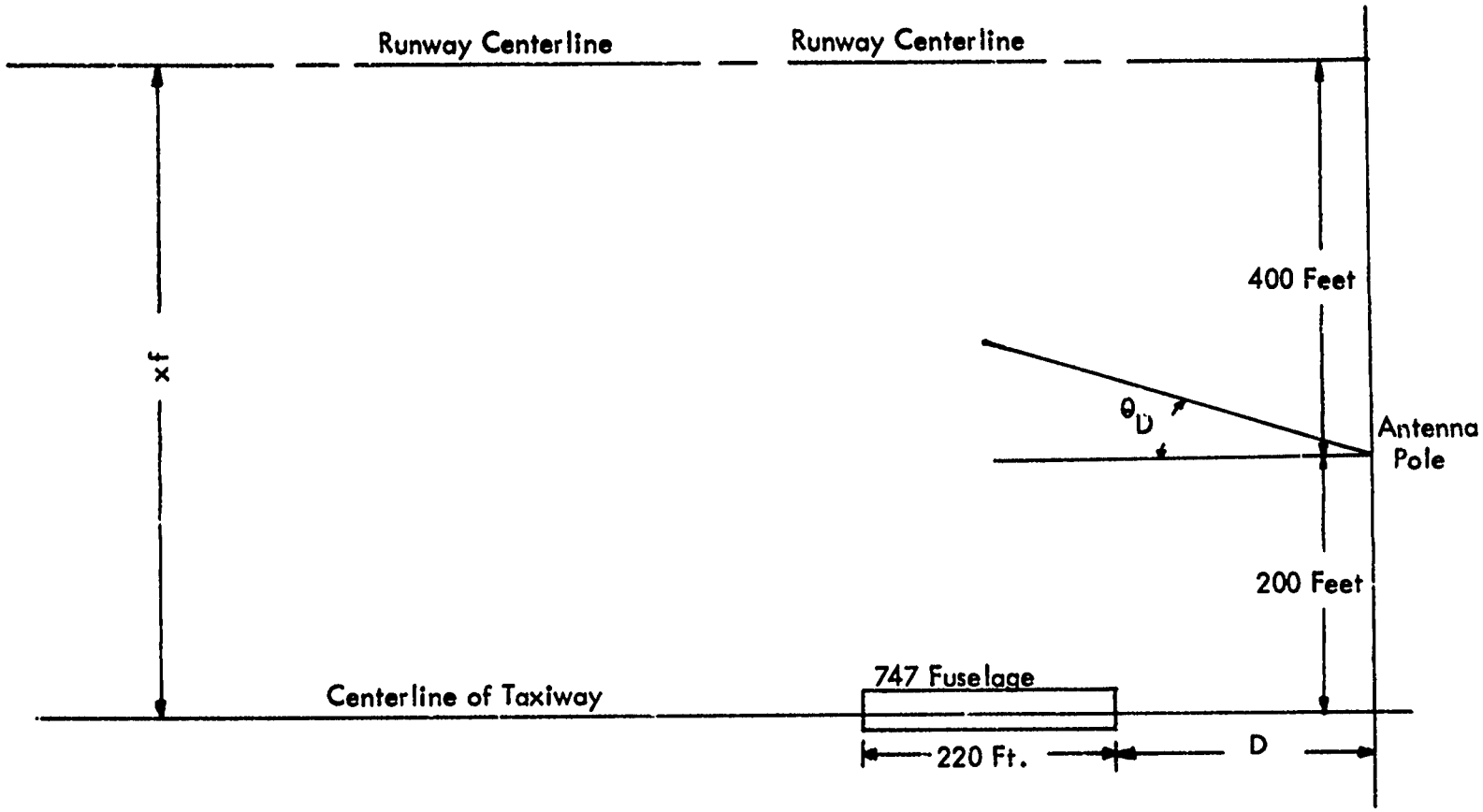

Figure 2-27. Geometry of Aircraft Position, Antenna Pole and Runway Centerline for Results Shown in Figures 2-28, 2-29, and 2-30.

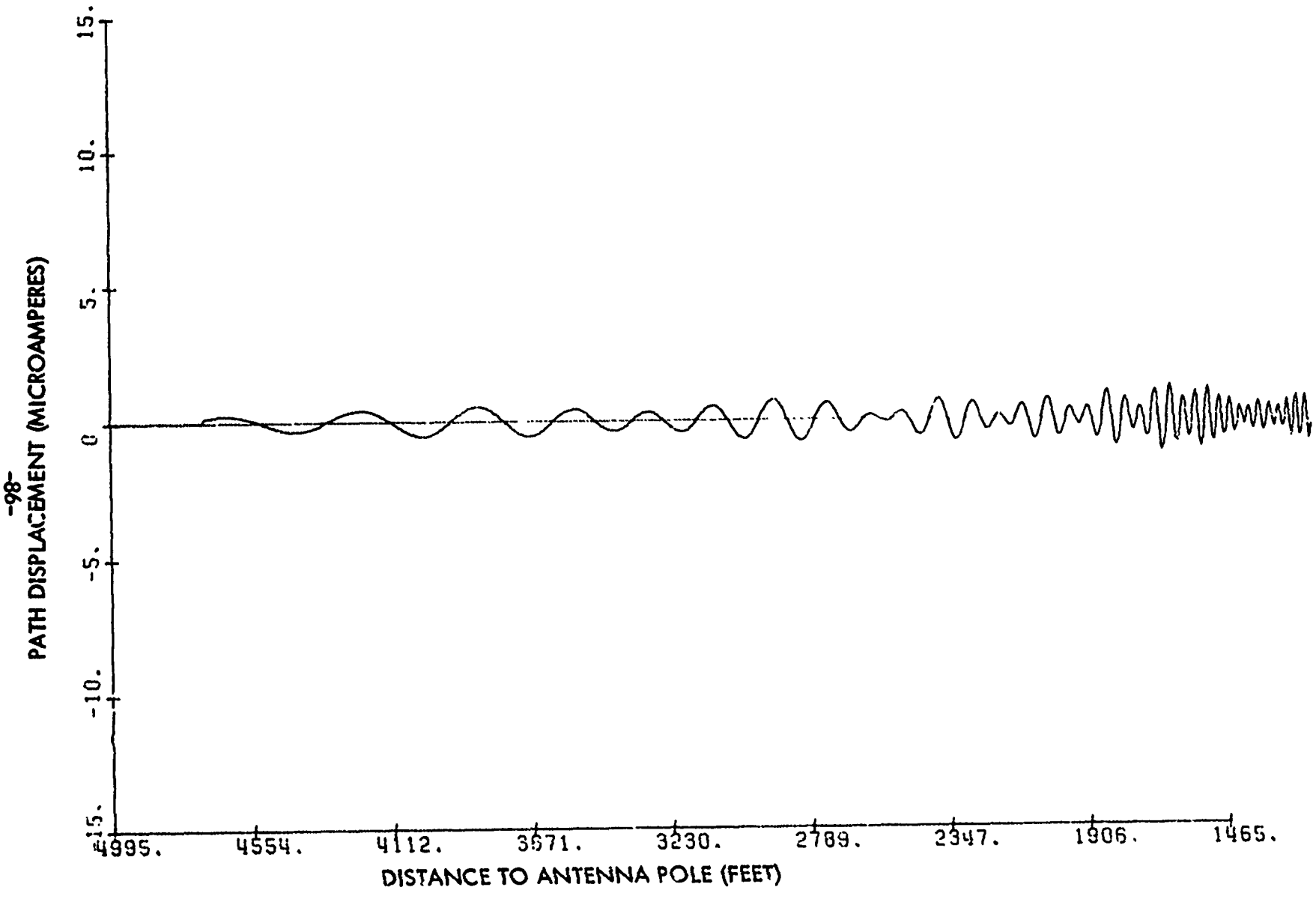

Figure 2-28. Amplitude of Glide Path Roughness for D = 200 Feet in Figure 2-27.

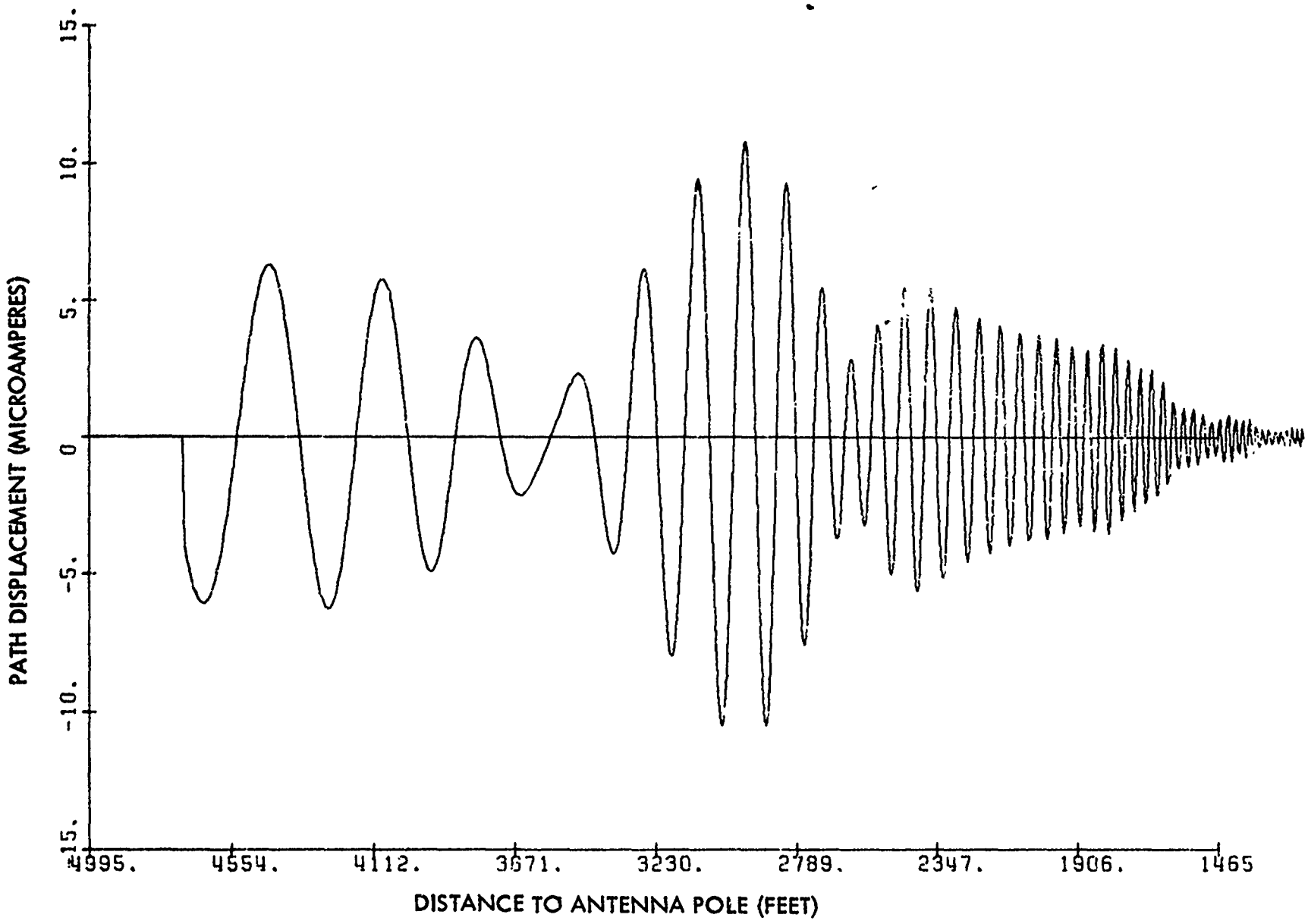

Figure 2-29. Amplitude of Glide Path Roughness for D = 500 Feet in Figure 2-27.

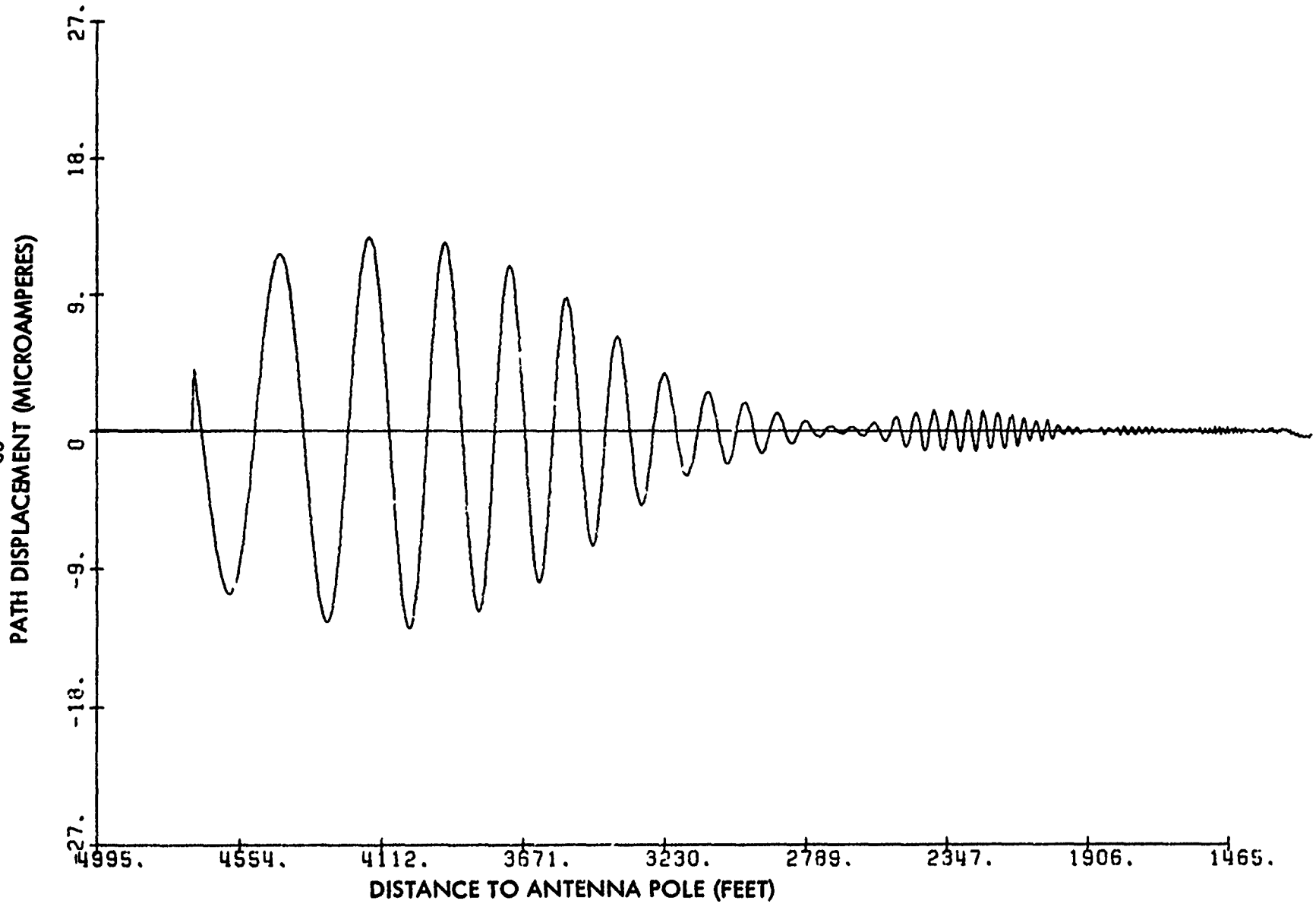

Figure 2-30. Amplitude of Glide Path Roughness for D = 800 Feet in Figure 2-27.

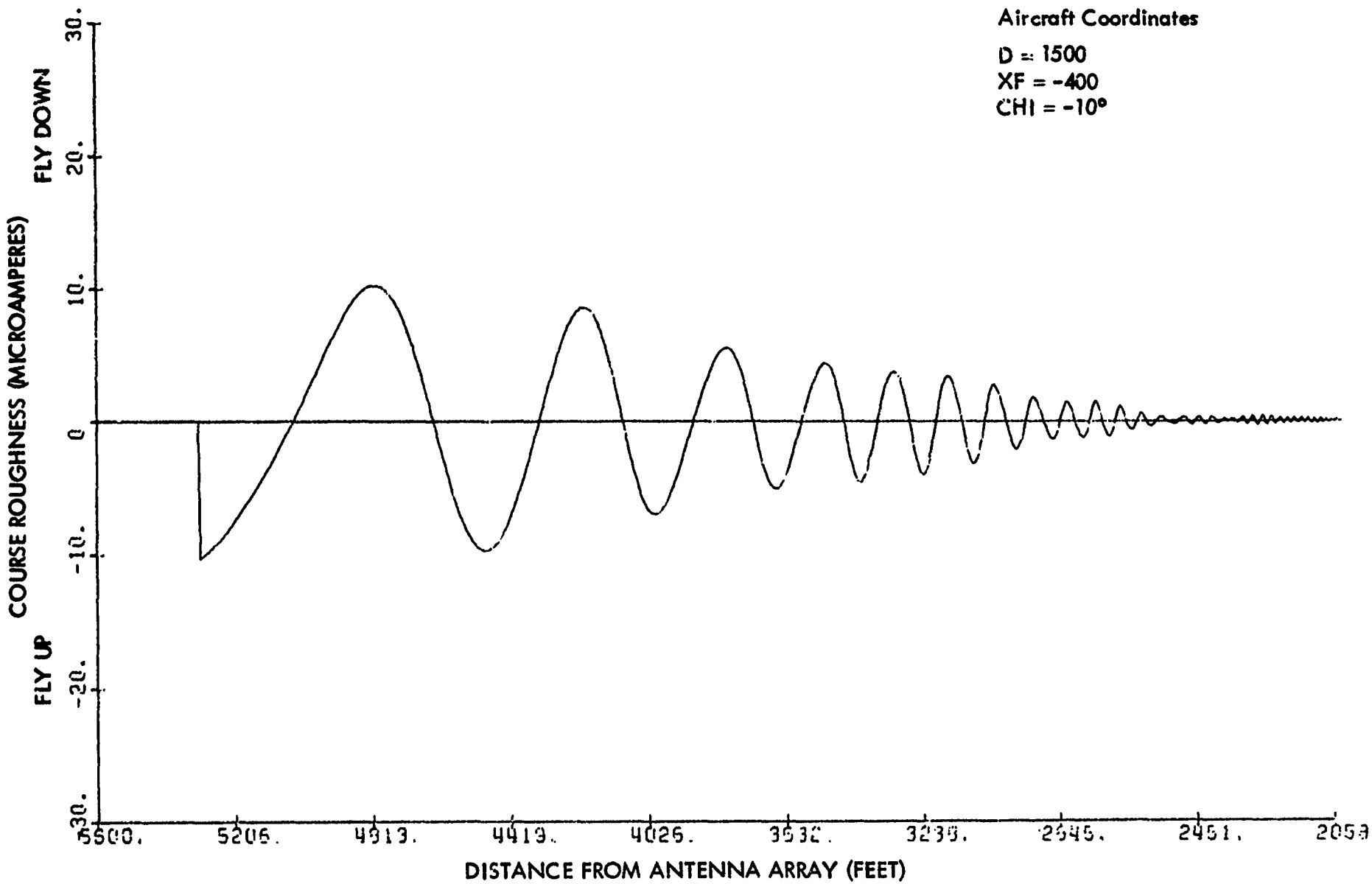

Figure 2-31. Amplitude of Glide Path Roughness for D = 1500 Feet, XF = - 400 Feet in Figure 2-27. The Axis of the Fuselage Intersects the Centerline at an Angle of 10°.

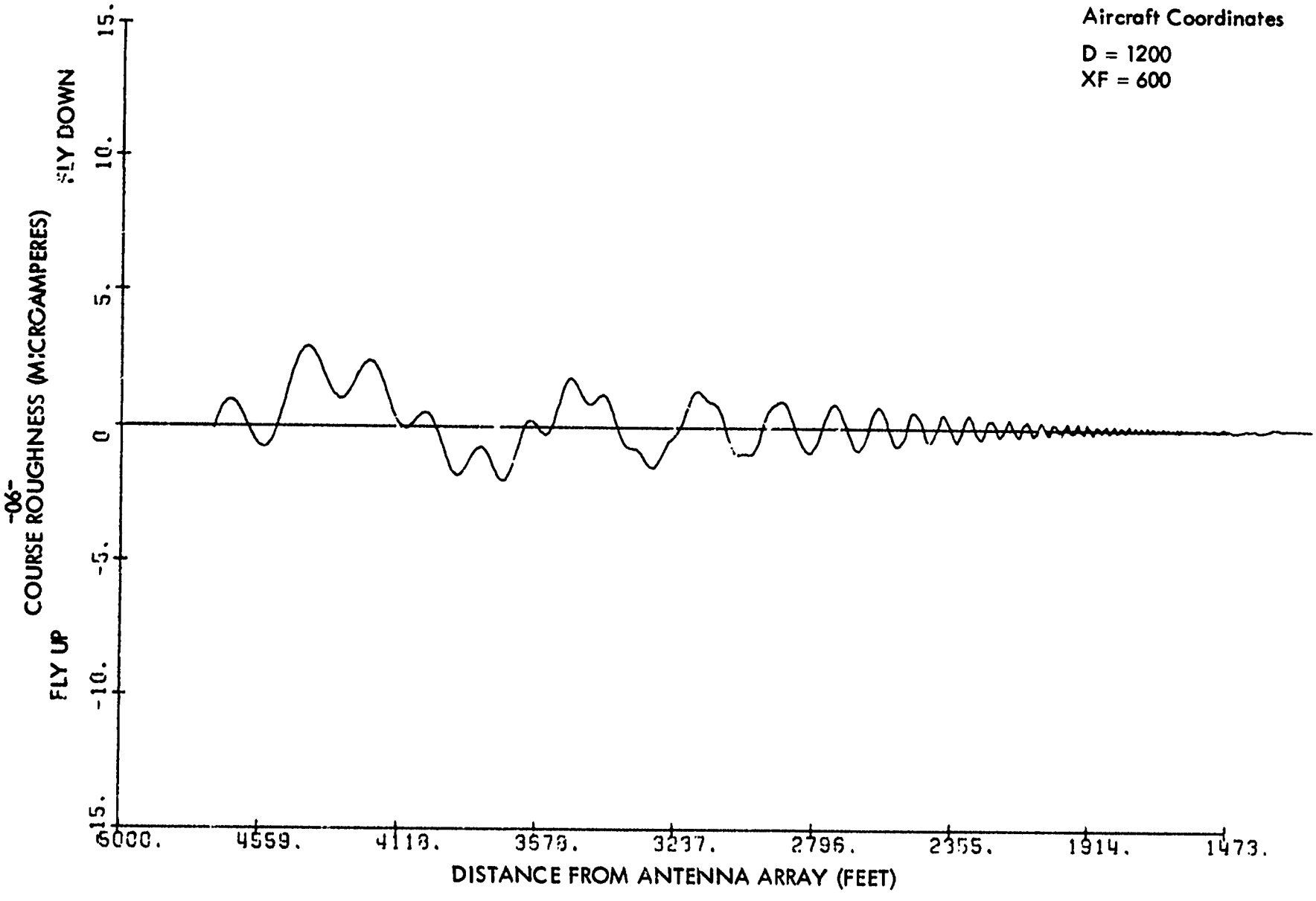

Figure 2-32. Amplitude of Glide Path Roughness for D = 1200 Feet in Figure 2-27. Fuselage is Parked Perpendicular to Centerline.

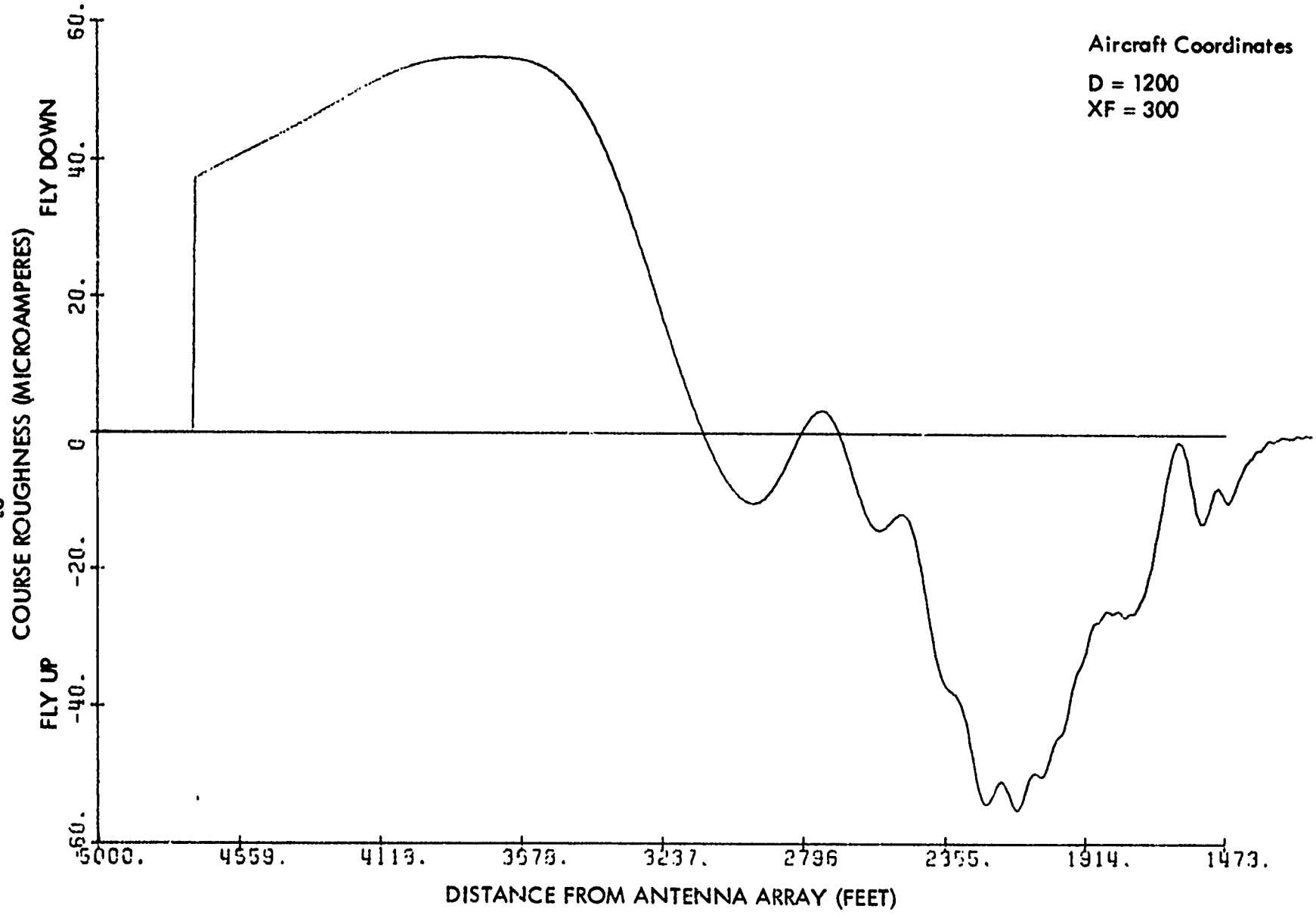

Figure 2-33. Amplitude of Glide Path Roughness for D = 1200 Feet in Figure 2-27. Fuselage is Parked Perpendicular to Centerline.

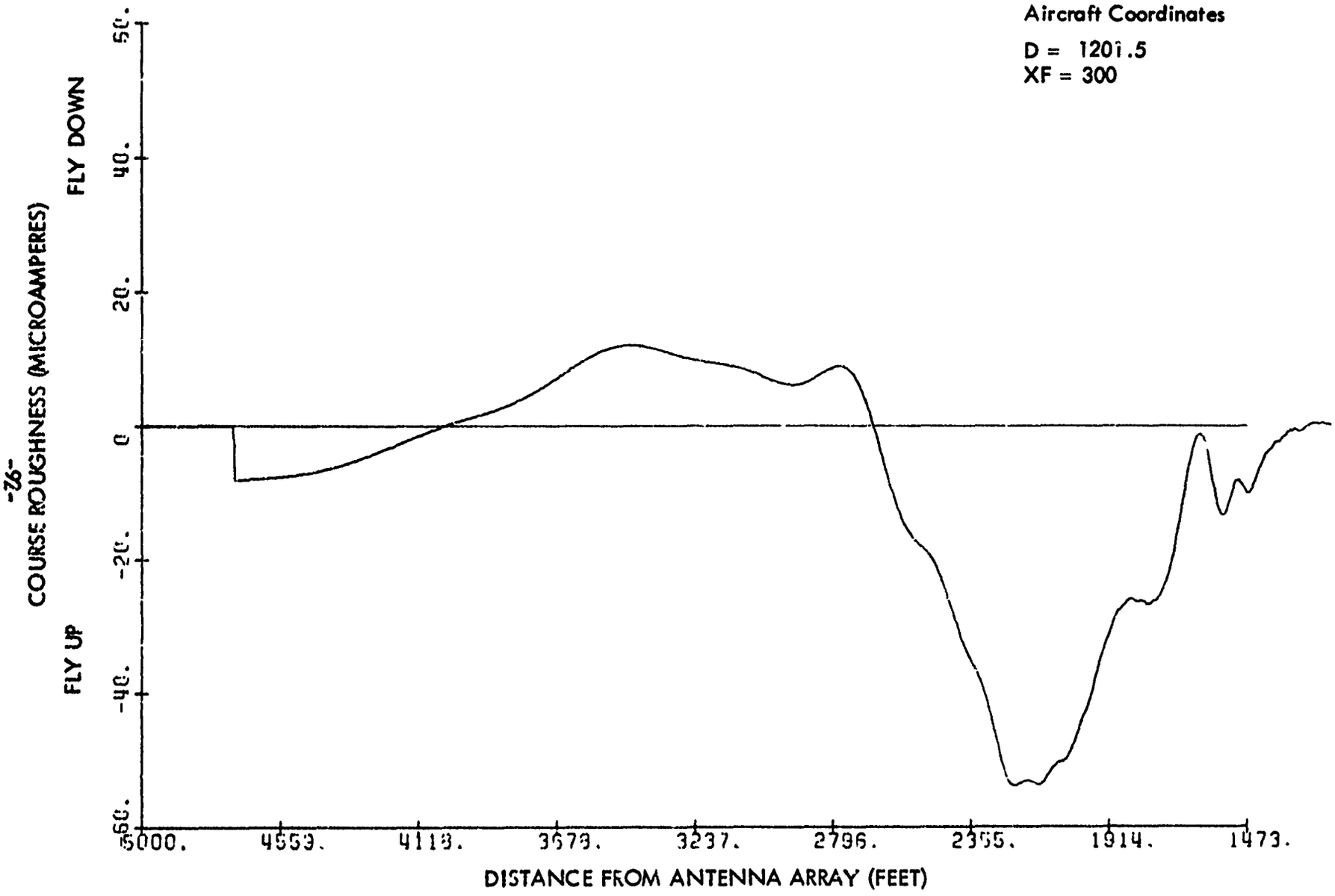

Figure 2-34. Amplitude of Glide Path Roughness for D = 1201.5 Feet in Figure 2-27. Fuselage is Parked Perpendicular to Centerline.

2. Glide Path Derogation Due to Reflections from Aircraft in Selected Location.

This section presents the computed glide path roughness for a number of different positions of a 747 aircraft in the neighborhood of the glide path transmitting antennas. The aircraft positions and the orientation of the fuselage axis with respect to runway centerline were chosen by FAA personnel. The mathematical model used is described in the preceding section.

All the results presented here represent the filtered output of the aircraft receiver for an approach speed of 120 MPH. The 747 is assumed to be taxiing to the approach end of the runway when the fuselage is parallel to runway centerline and toward runway centerline when the fuselage is perpendicular to centerline. The row and column numbers on the plots correspond to the rows and columns designated on Table 2-8. The glide path array positioned 525 feet from centerline is a null reference installation and the sideband antenna is 30 feet above ground plane.

The results show that the largest course bends occur when the 747 is positioned perpendicular to centerline directly in front of the transmitting array. The results marked directional antenna were computed assuming a three-element transmitting antenna is used and the results marked standard antenna are for the bent dipole whose radiation pattern is approximated by a cos θ pattern.

It is seen that the use of the directional antennas provide an improved glide path.

Table 2-8 lists the figures which present these calculations graphically, indicating the 747 locations and orientations used in modeling the situation explored in each computer run, as well as a key to the location as shown in the plan view of Figure 2-35.

Final work during the report period has been to obtain results which are applicable to defining critical areas for use in FAA manuals. The first step in this process has been to compare the available results from the physical scale models reported by J. G. Lucas of the Air Navigation Group at the University of Sydney, Sydney, Australia, with those predicted using the mathematical model reported in preceding pages. Unfortunately only 10 of the points are common to both sets of prediction and a 2.5° angle was used with the physical model and 2.83° with the mathematical model; however, comparison of the results is encouraging.

Presently work is underway to change the path angle with the mathematical model and rerun several points at 2.50° to get a direct comparison. A program is

being prepared which will use a specular point method and will be run on sample points using 2.5° glide path angle for comparison of the results with the analog physical model.

Once these results have been obtained and the degree of correlation between the mathematical and physical model obtained, then predictions will be made for use in the FAA manuals. If a close correlation is obtained a high degree of confidence in the mathematical model will, of course, be justified. Further predictions then can be made for various other locations of the aircraft on the airdrome.

One word should be added concerning the computer running time of the mathematical model. The complete mathematical model requires approximately four hours of computer time to describe the position on the 0 DDM line in space for a given location of a reflecting aircraft on the ground. The new specular point model should permit the identification of critical areas with running times on the order of a few minutes. The obvious economic saving in computer time makes it worthwhile to investigate the capabilities of the specular point method as compared with the complete mathematical model and the physical scale model.

	Figure	Dist. Forward of Array Feet	Dist. From Runway Centerline Feet *	Antenna Pattern	Orientation: Parallel to Centerline	Orientation: Perpendicular to Centerline	Orientation: Angle Between 747 Axis and CL	Point No. (Reference Fig. 2-35)	Coordinates on Chart: Row	Coordinates on Chart: Column	Comments
2-	36	4000	300	STD		X		1	1	6	
	37	2700	750	STD		X		2	2	2	
	38	2700	600	STD		X		3	2	3	
	39	2700	525	STD		X		4	2	4	
	40	2700	450	STD		X		5	2	5	Figs. 37-50
	41	2700	300	STD		X		6	2	6	747
	42	1800	750	STD		X		7	3	2	Taxiing
	43	1800	600	STD		X		8	3	3	Toward
	44	1800	525	STD		X		9	3	4	Runway
	45	1800	450	STD		X		10	3	5	
	46	1800	300	STD		X		11	3	6	
	47	1500	600	STD		X		12	4	3	
	48	1500	525	STD		X		13		4	
	49	1500	450	STD		X		14	4	5	
	50	1500	300	STD		X		15	4	6	
	51	900	900	STD	X			16	6	1	
	52	900	900	DIR	X			17	6	1	
	53	1500	900	STD	X			18	4	1	Figs. 51-63
	54	1500	900	DIR	X			19	4	1	Toward
	55	1800	900	STD	X			20	3	1	Approach
	56	1800	900	DIR	X			21	3	1	End of
	57	2700	900	STD	X			22	2	1	Runway
	58	900	-400	STD	X			23	6	12	
	59	1200	-400	STD	X			24	5	12	
	60	1500	-400	STD	X			25	4	12	
	61	1500	-400	DIR	X			26	4	12	
	62	1800	-400	STD	X			27	3	12	
	63	1800	-400	DIR	X			28	3	12	
	64	1800	-400	STD			20%	29	3	12	20° to CL rwy
2-	65	1200	0	STD	X			30	5	8	Take-off position

* Negative distances opposite side of runway from array.

Table 2-8. Definition of Points of Interest for Boeing 747 Calculation Reference (Figure 2-35).

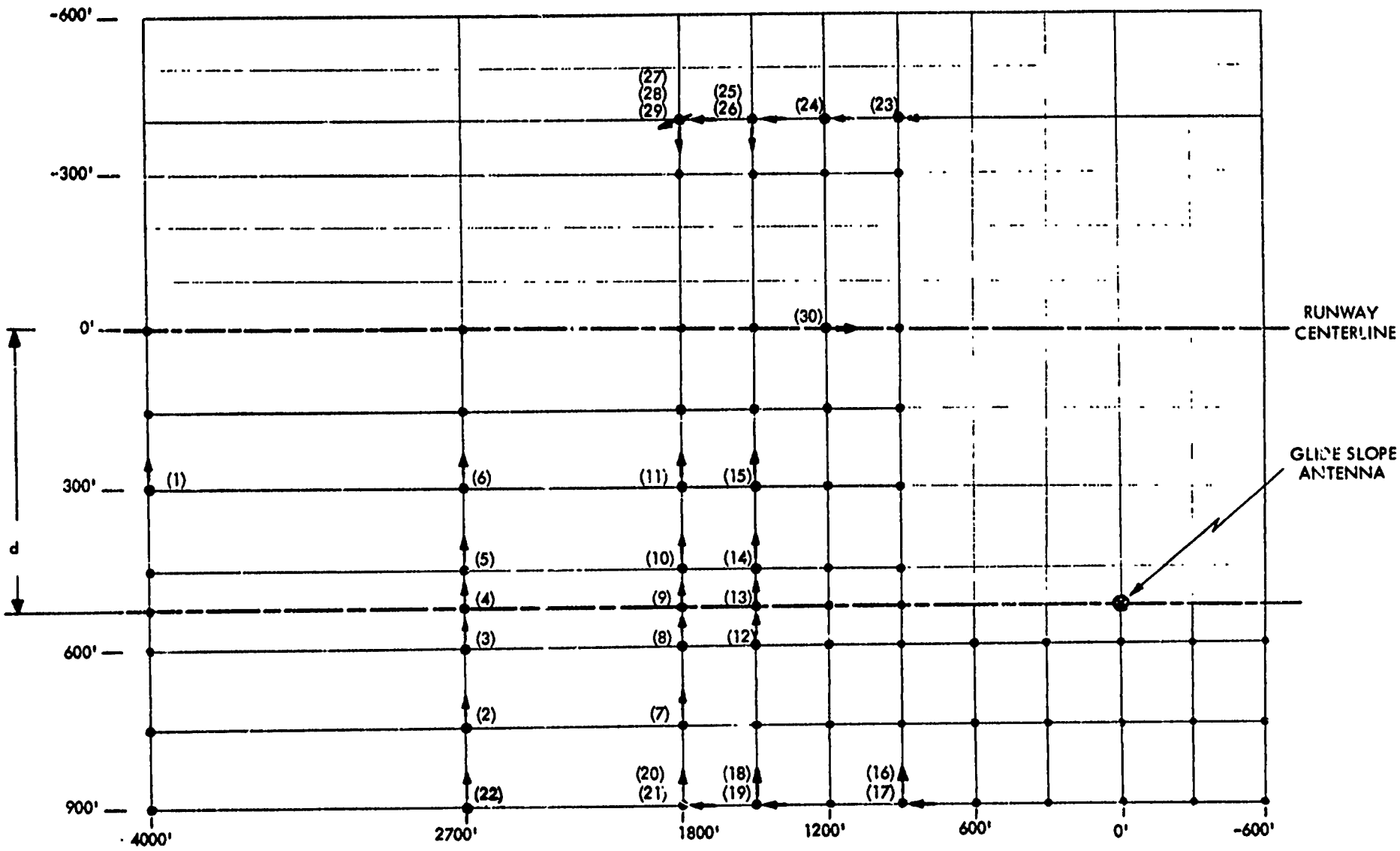

Figure 2-35. Layout of Points of Interest for Calculating Effects of Signals Reflecting From a Boeing 747.

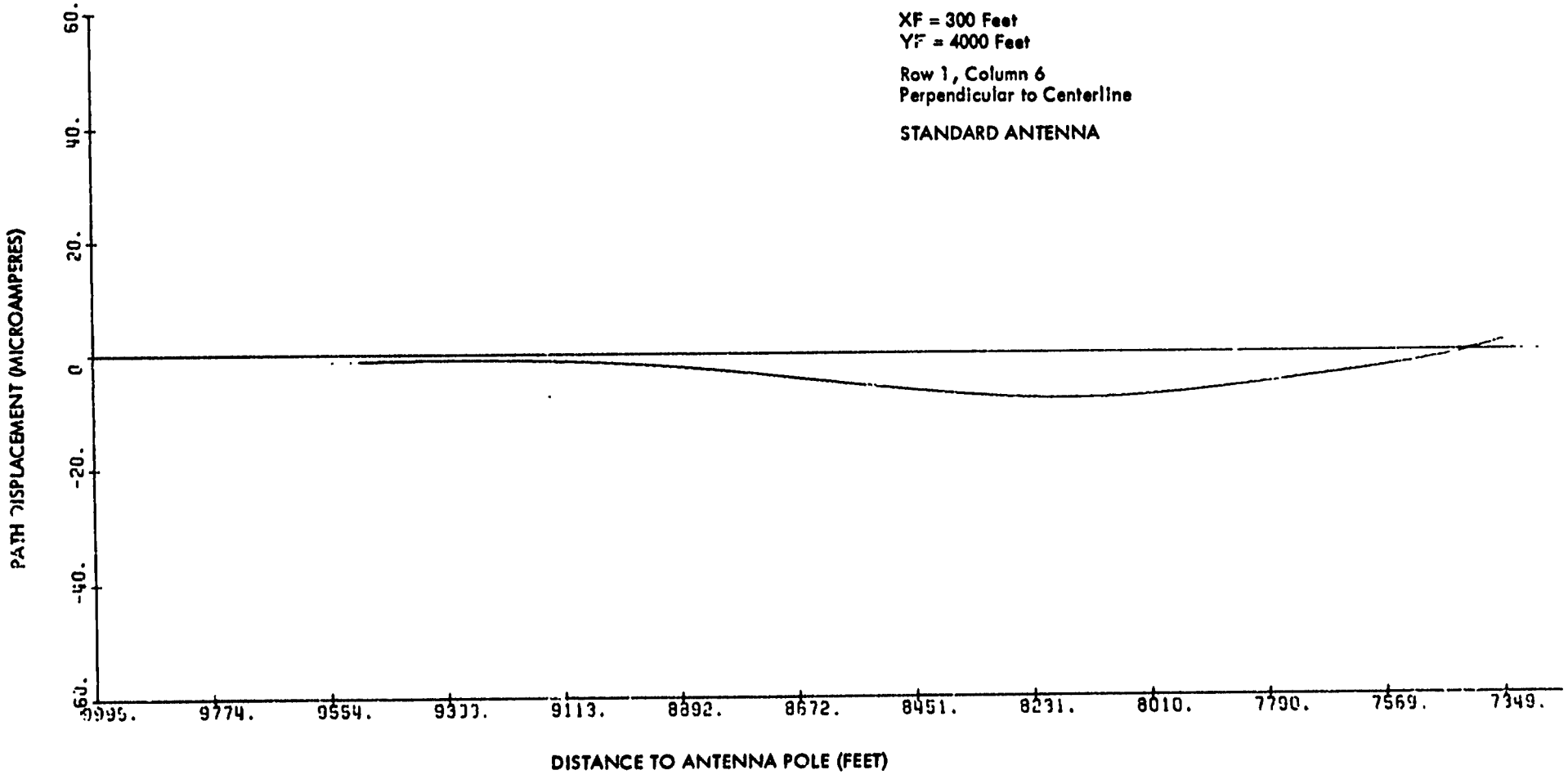
XF = 300 Feet
YF = 4000 Feet
Row 1, Column 6
Perpendicular to Centerline
STANDARD ANTENNA
PATH DISPLACEMENT (MICROAMPERES)
60.
40.
20.
0
-20.
-40.
-60.
9995.
9774.
9554.
9333.
9113.
8892.
8672.
8451.
8231.
8010.
7790.
7569.
7349.
DISTANCE TO ANTENNA POLE (FEET)

Figure 2-36.

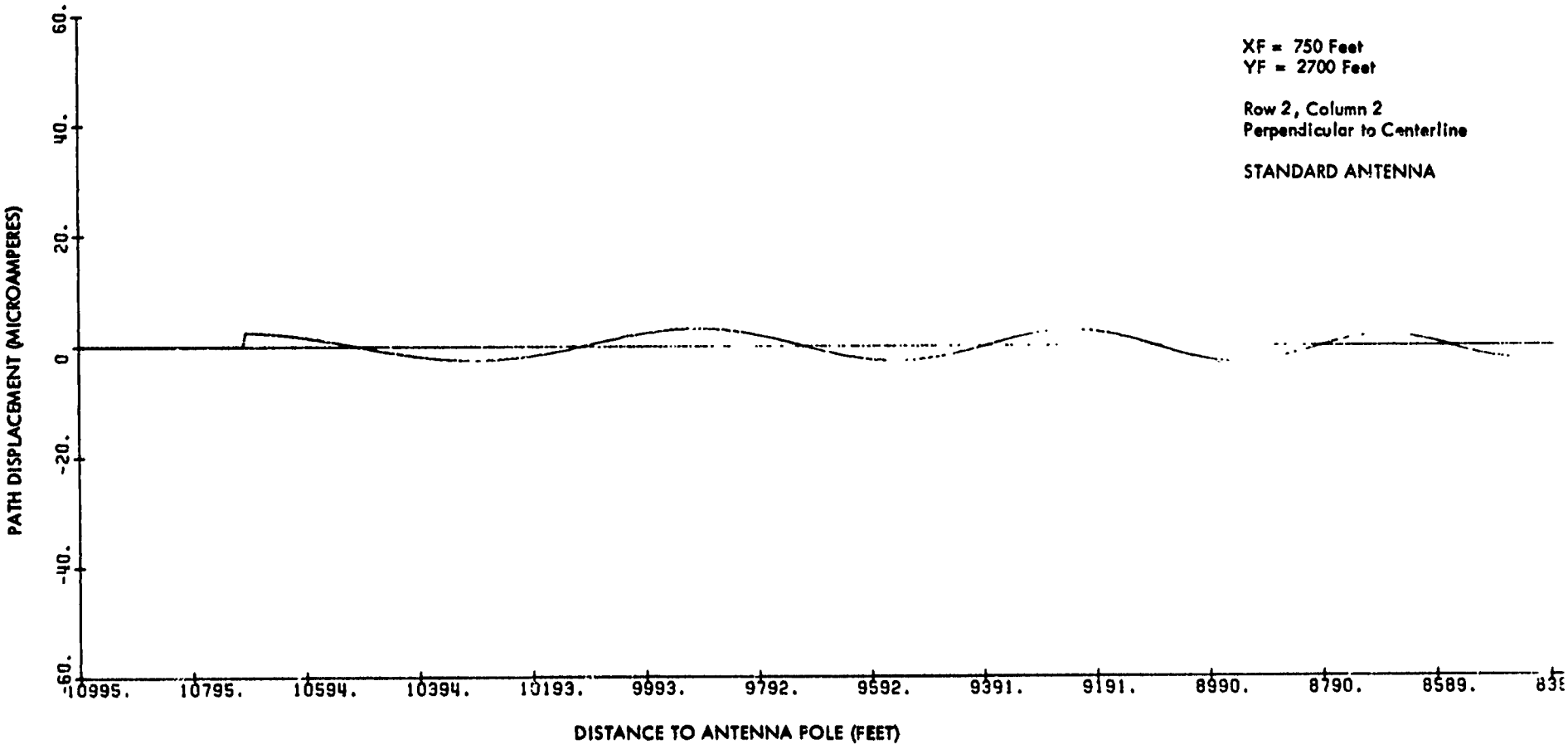
XF = 750 Feet
YF = 2700 Feet
Row 2, Column 2
Perpendicular to Centerline
STANDARD ANTENNA
PATH DISPLACEMENT (MICROAMPERES)
60.
40.
20.
0
-20.
-40.
-60.
10995.
10795.
10594.
10394.
10193.
9993.
9792.
9592.
9391.
9191.
8990.
8790.
8589.
DISTANCE TO ANTENNA POLE (FEET)

Figure 2-37.

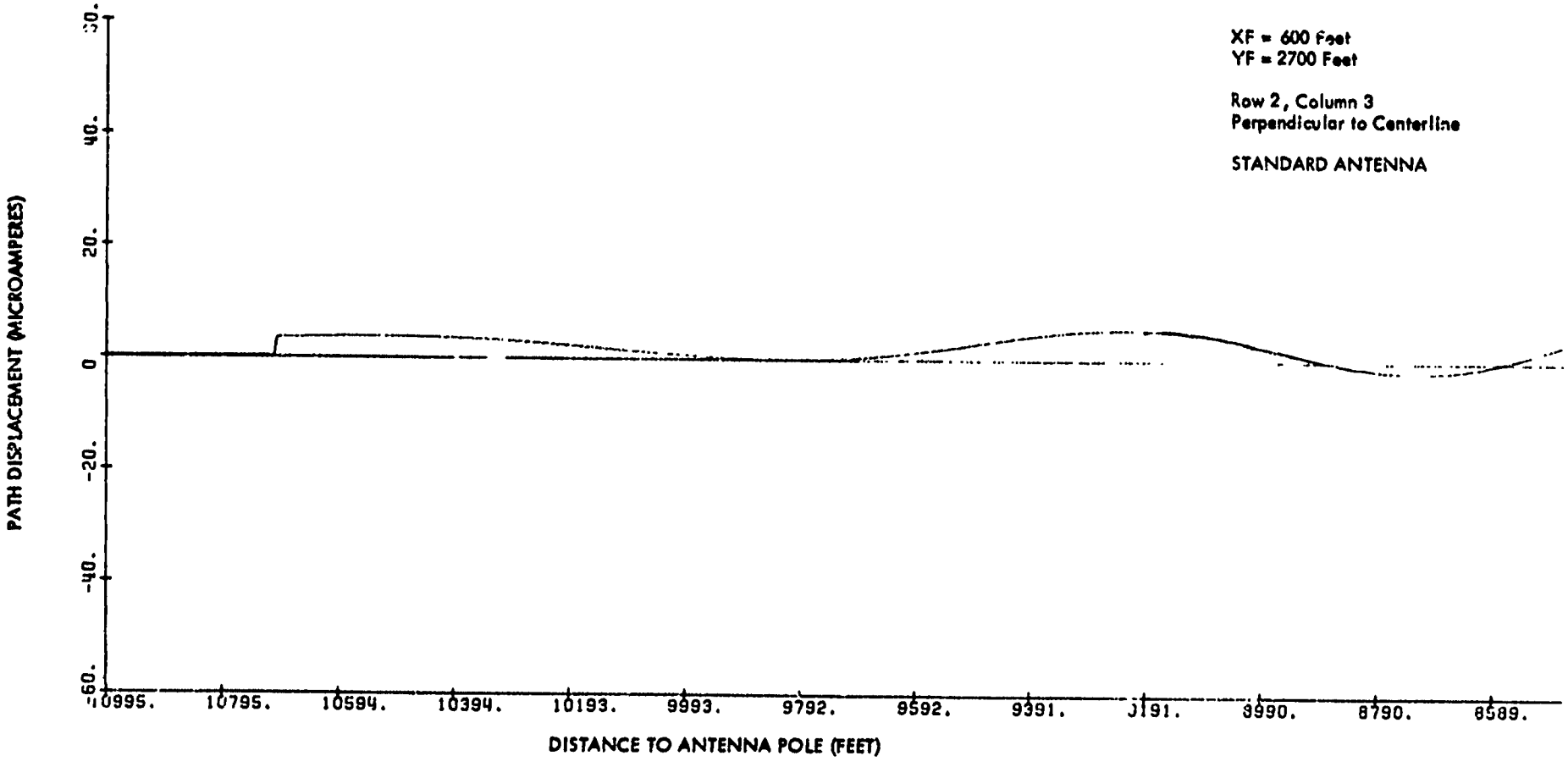
XF = 600 Feet
YF = 2700 Feet
Row 2, Column 3
Perpendicular to Centerline
STANDARD ANTENNA
PATH DISPLACEMENT (MICROAMPERES)
60.
40.
20.
0
-20.
-40.
-60.
10995.
10795.
10594.
10394.
10193.
9993.
9792.
9592.
9391.
9191.
8990.
8790.
8589.
DISTANCE TO ANTENNA POLE (FEET)

Figure 2-38.

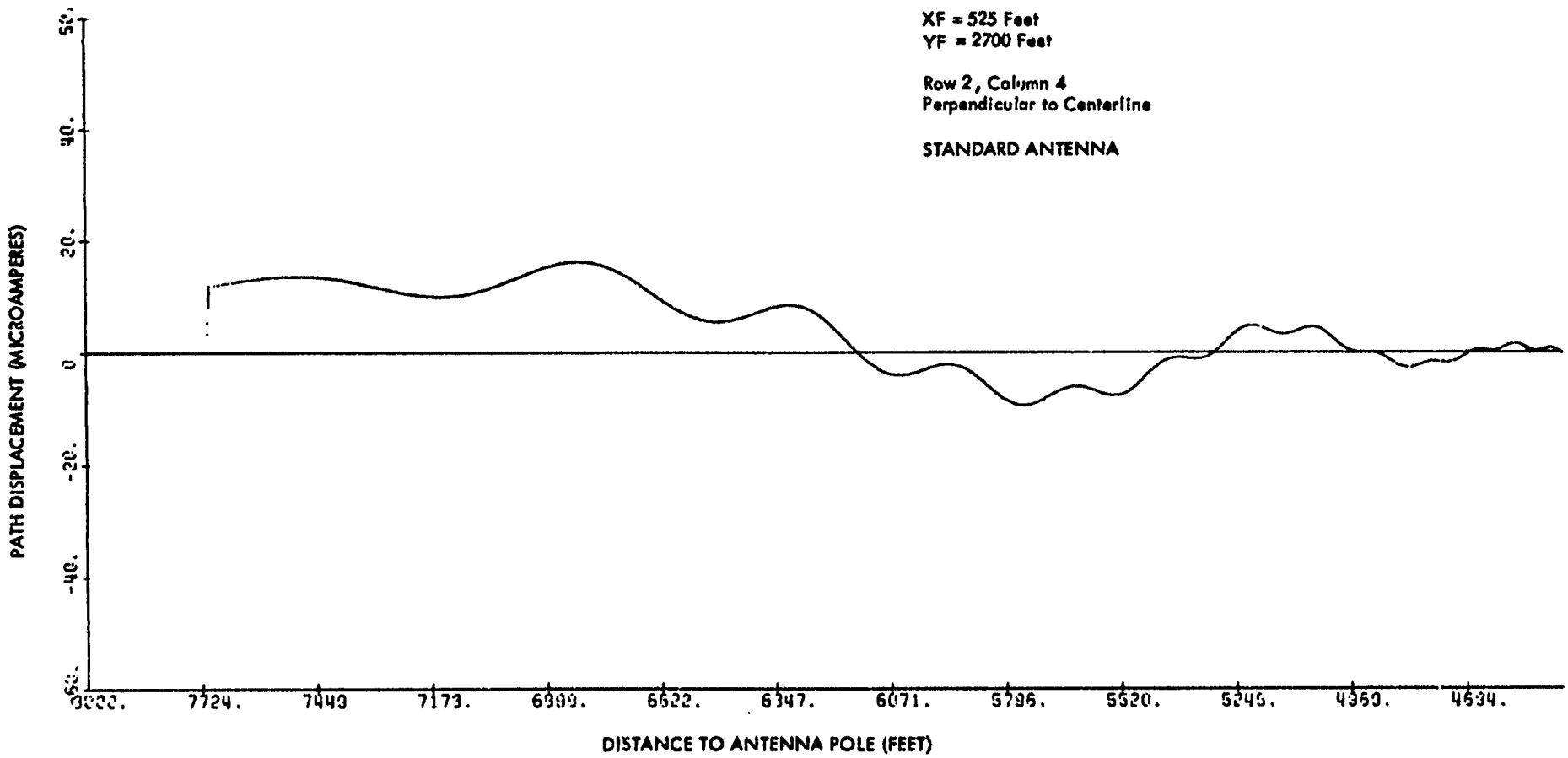
XF = 525 Feet
YF = 2700 Feet
Row 2, Column 4
Perpendicular to Centerline
STANDARD ANTENNA
PATH DISPLACEMENT (MICROAMPERES)
50.
40.
20.
0
-20.
-40.
-60.
7724.
7449
7173.
6347.
6071.
5796.
5520.
5245.
4969.
4694.
DISTANCE TO ANTENNA POLE (FEET)

Figure 2-39.

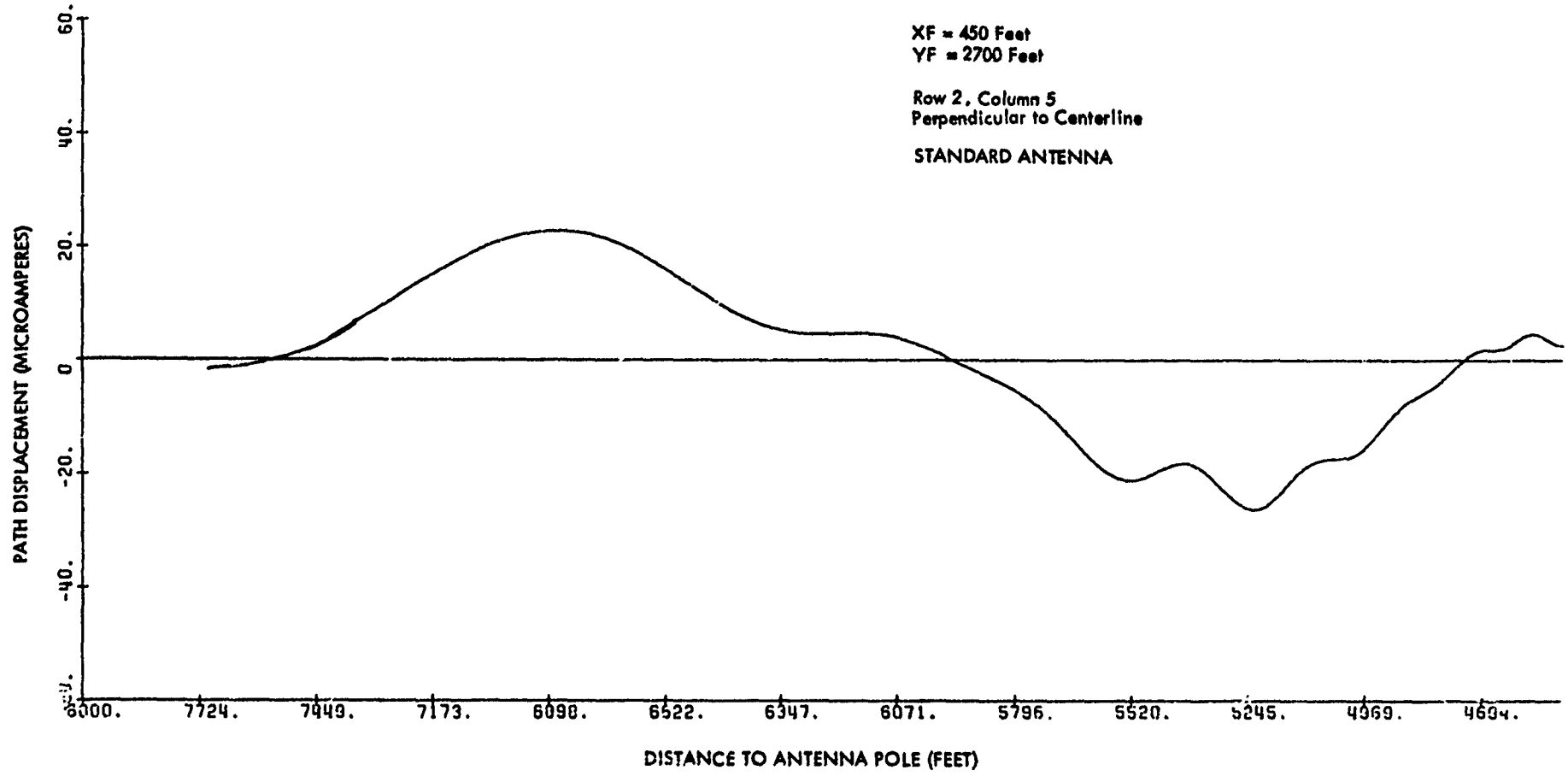
XF = 450 Feet
YF = 2700 Feet
Row 2, Column 5
Perpendicular to Centerline
STANDARD ANTENNA
PATH DISPLACEMENT (MICROAMPERES)
60.
40.
20.
0
-20.
-40.
8000.
7724.
7449.
7173.
6898.
6522.
6347.
6071.
5796.
5520.
5245.
4969.
4694.
DISTANCE TO ANTENNA POLE (FEET)

Figure 2-40.

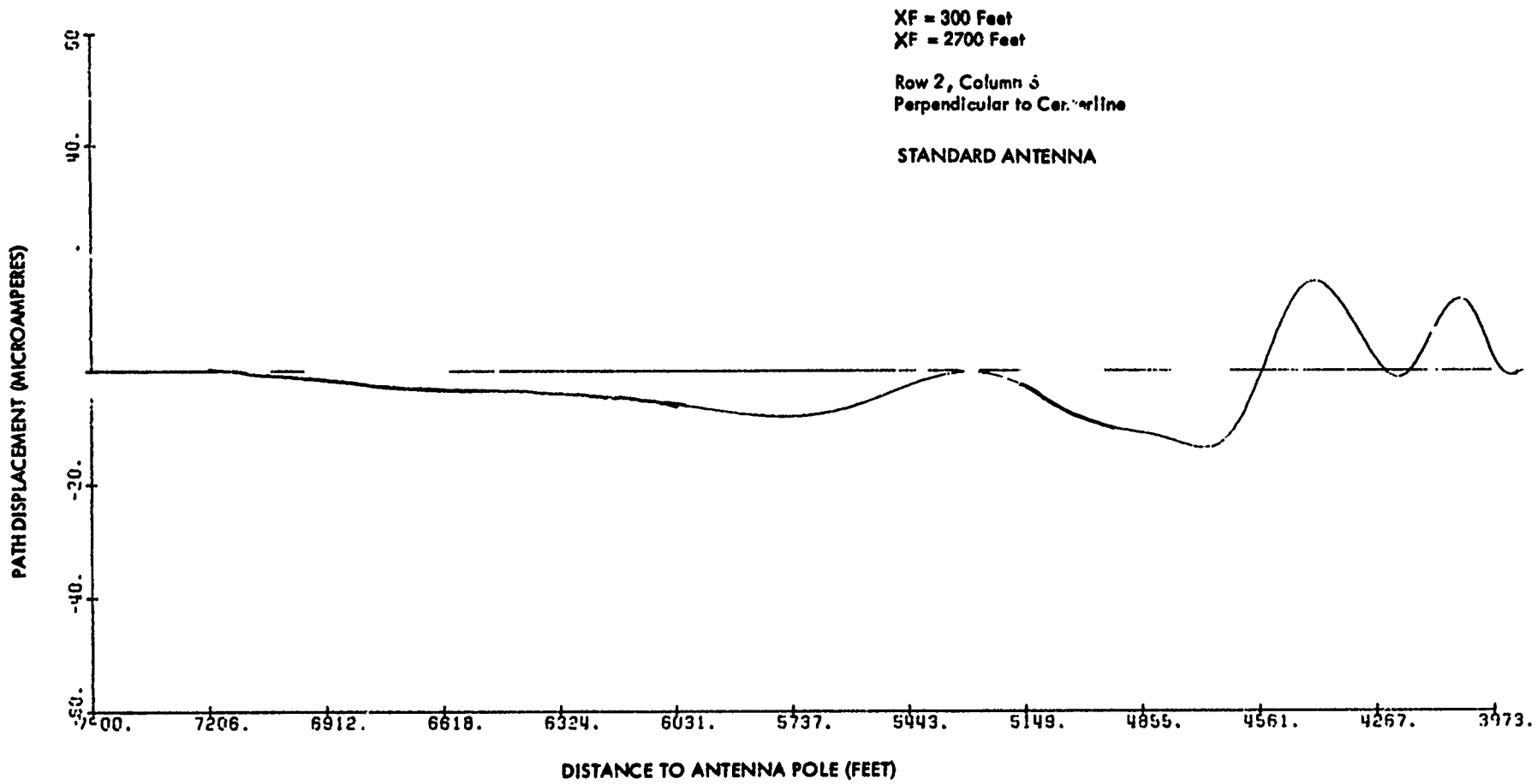
XF = 300 Feet
XF = 2700 Feet
Row 2, Column 6
Perpendicular to Centerline
STANDARD ANTENNA
PATH DISPLACEMENT (MICROAMPERES)
50
40.
-20.
-40.
-50.
7200.
7206.
6912.
6618.
6324.
6031.
5737.
5443.
5149.
4855.
4561.
4267.
3973.
DISTANCE TO ANTENNA POLE (FEET)

Figure 2-41.

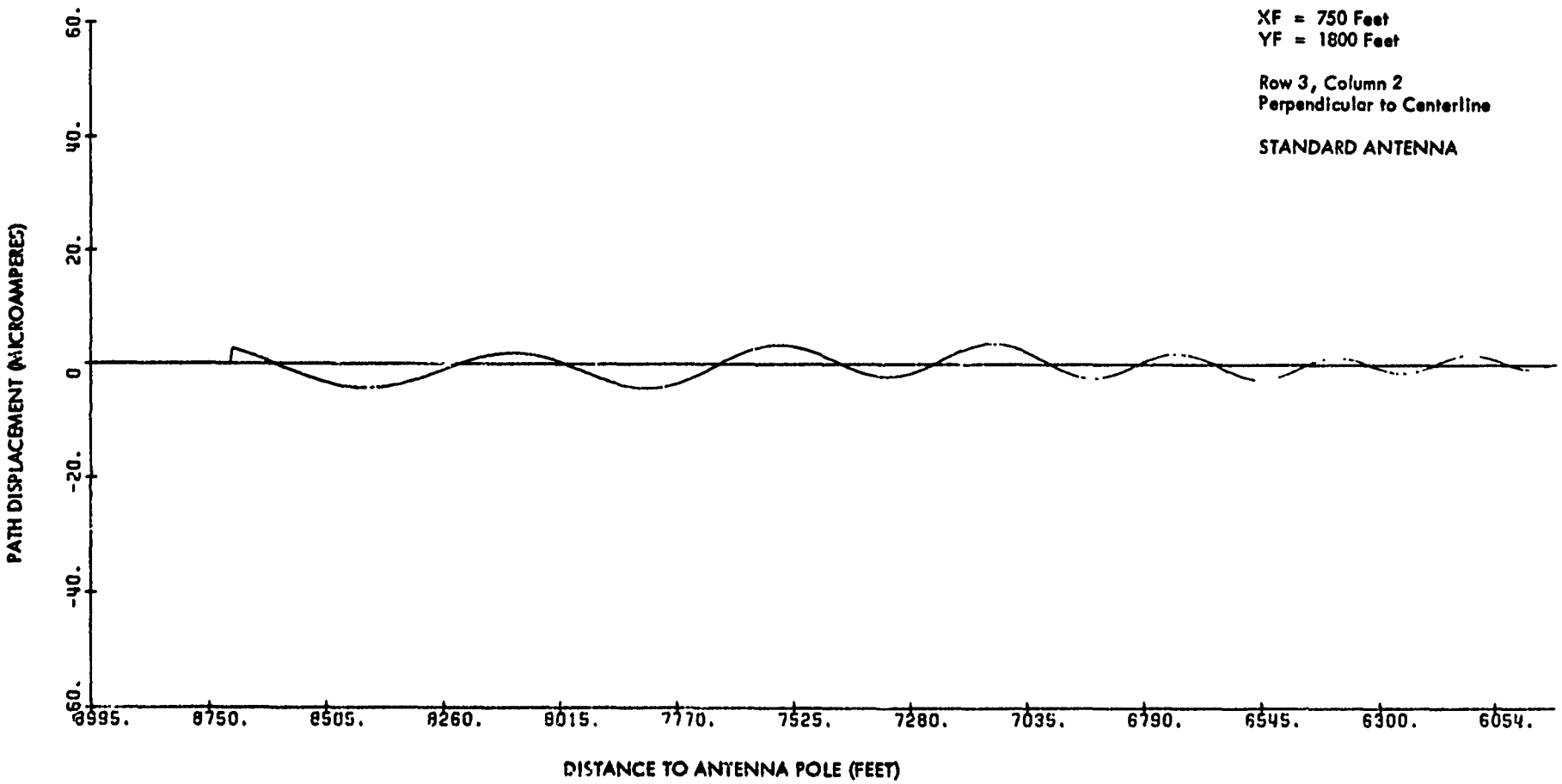
XF = 750 Feet
YF = 1800 Feet
Row 3, Column 2
Perpendicular to Centerline
STANDARD ANTENNA
PATH DISPLACEMENT (MICROAMPERES)
60.
40.
20.
0
-20.
-40.
-60.
9995.
8750.
8505.
8260.
8015.
7770.
7525.
7280.
7035.
6790.
6545.
6300.
6054.
DISTANCE TO ANTENNA POLE (FEET)

Figure 2-42.

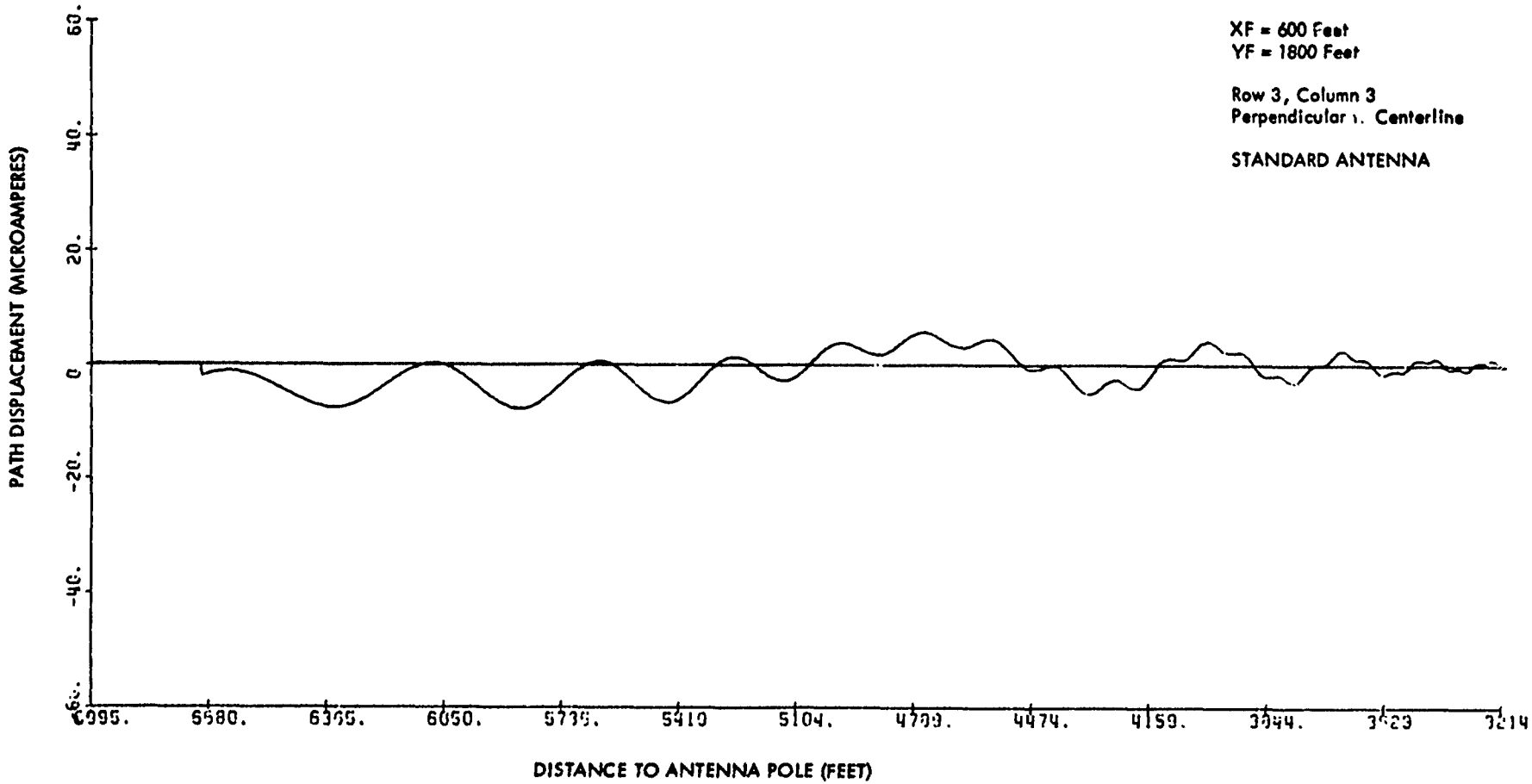
XF = 600 Feet
YF = 1800 Feet
Row 3, Column 3
Perpendicular to Centerline
STANDARD ANTENNA
PATH DISPLACEMENT (MICROAMPERES)
60.
40.
20.
0
-20.
-40.
-60.
6995.
6580.
6365.
6050.
5735.
5410
5104.
4789.
4474.
4159.
3844.
3529
3214
DISTANCE TO ANTENNA POLE (FEET)

Figure 2-43.

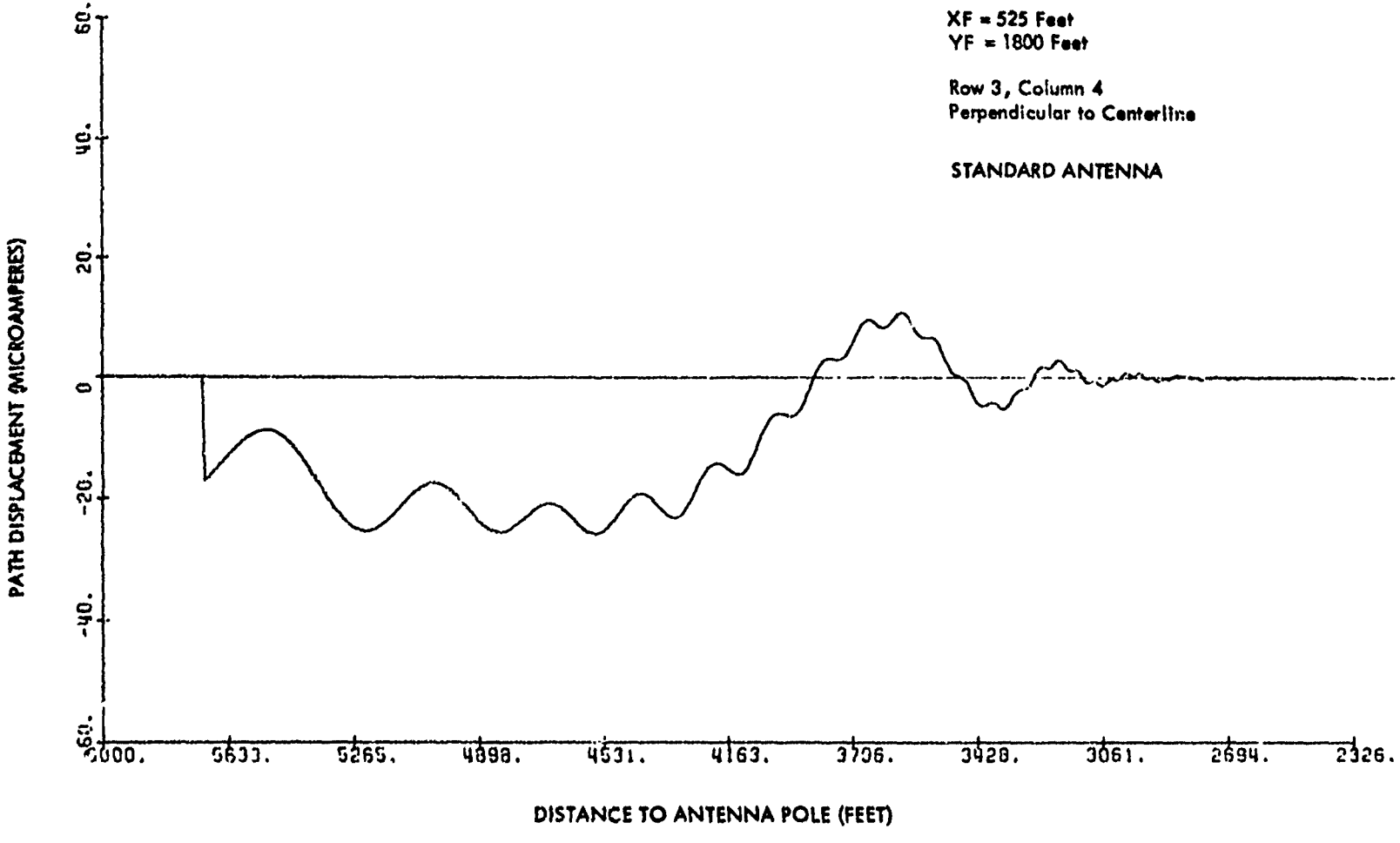
XF = 525 Feet
YF = 1800 Feet
Row 3, Column 4
Perpendicular to Centerline
STANDARD ANTENNA
PATH DISPLACEMENT (MICROAMPERES)
60.
40.
20.
0
-20.
-40.
-60.
6000.
5633.
5265.
4898.
4531.
4163.
3796.
3428.
3061.
2694.
2326.
DISTANCE TO ANTENNA POLE (FEET)

Figure 2-44.

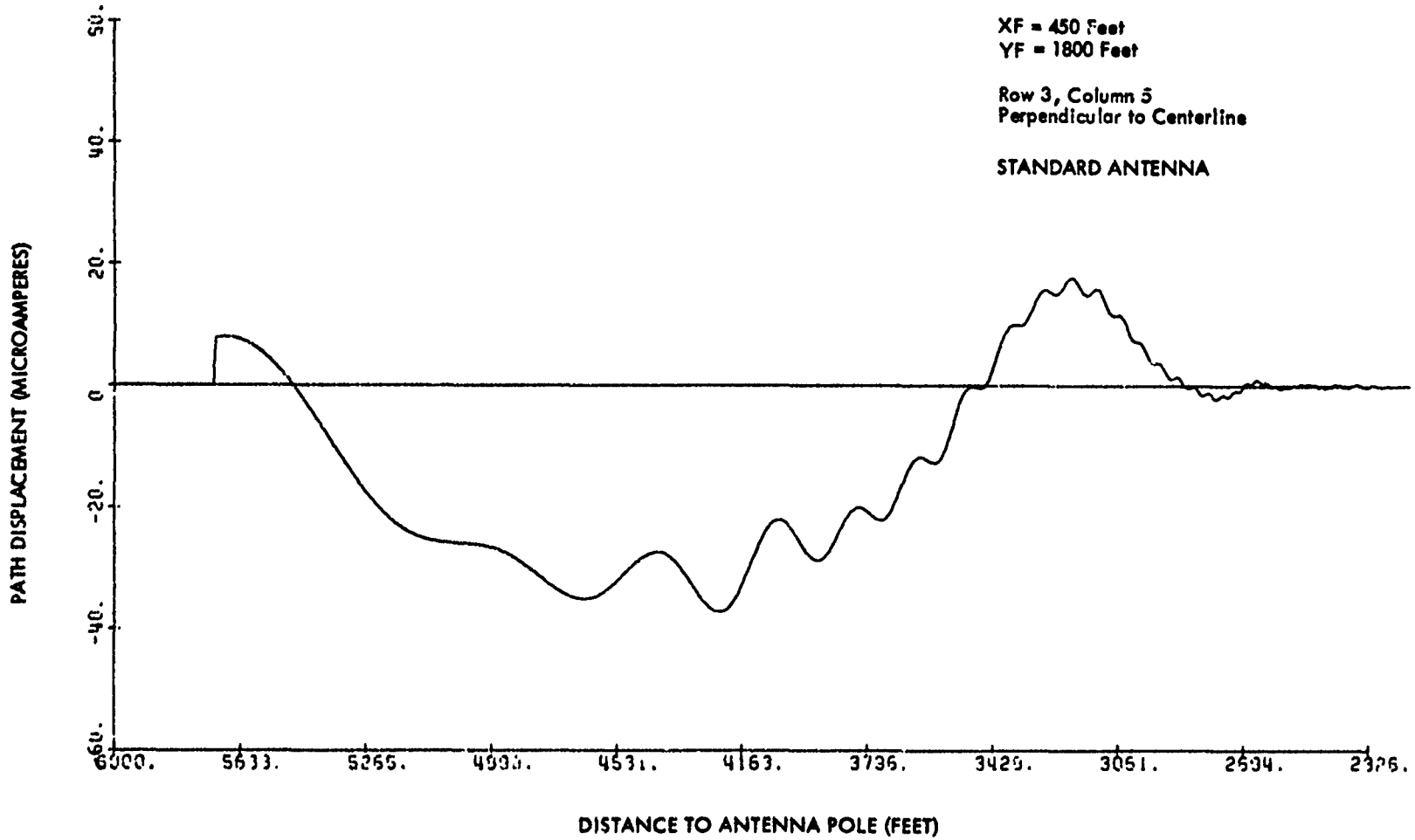
XF = 450 Feet
YF = 1800 Feet
Row 3, Column 5
Perpendicular to Centerline
STANDARD ANTENNA
PATH DISPLACEMENT (MICROAMPERES)
50.
40.
20.
0
-20.
-40.
-60.
6000.
5633.
5265.
4898.
4531.
4163.
3796.
3429.
3061.
2694.
2326.
DISTANCE TO ANTENNA POLE (FEET)

Figure 2-45.

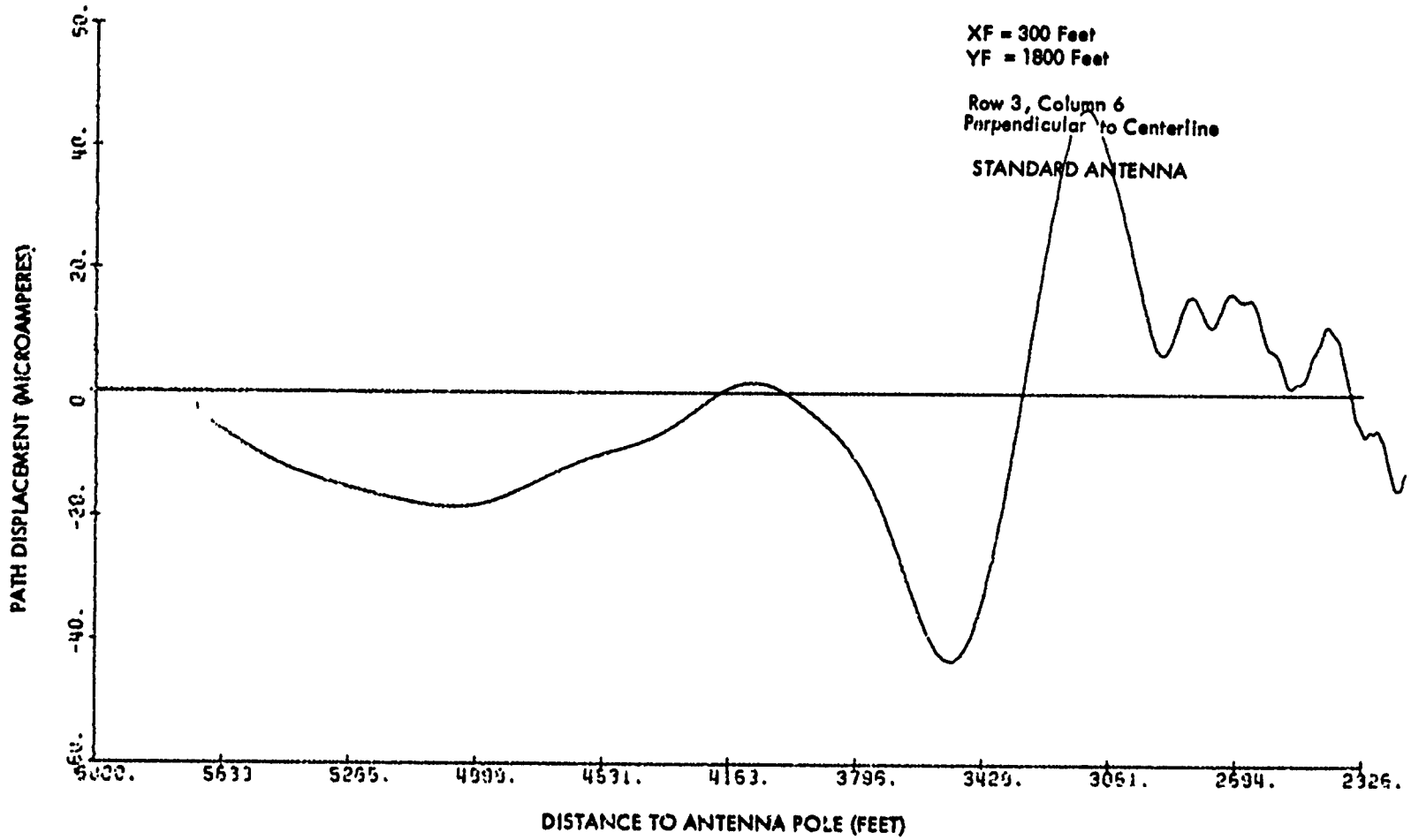
XF = 300 Feet
YF = 1800 Feet
Row 3, Column 6
Perpendicular to Centerline
STANDARD ANTENNA
PATH DISPLACEMENT (MICROAMPERES)
50.
40.
20.
0
-20.
-40.
-60.
5633
5265.
4899.
4531.
4163.
3796.
3428.
3061.
2694.
2326.
DISTANCE TO ANTENNA POLE (FEET)

Figure 2-46.

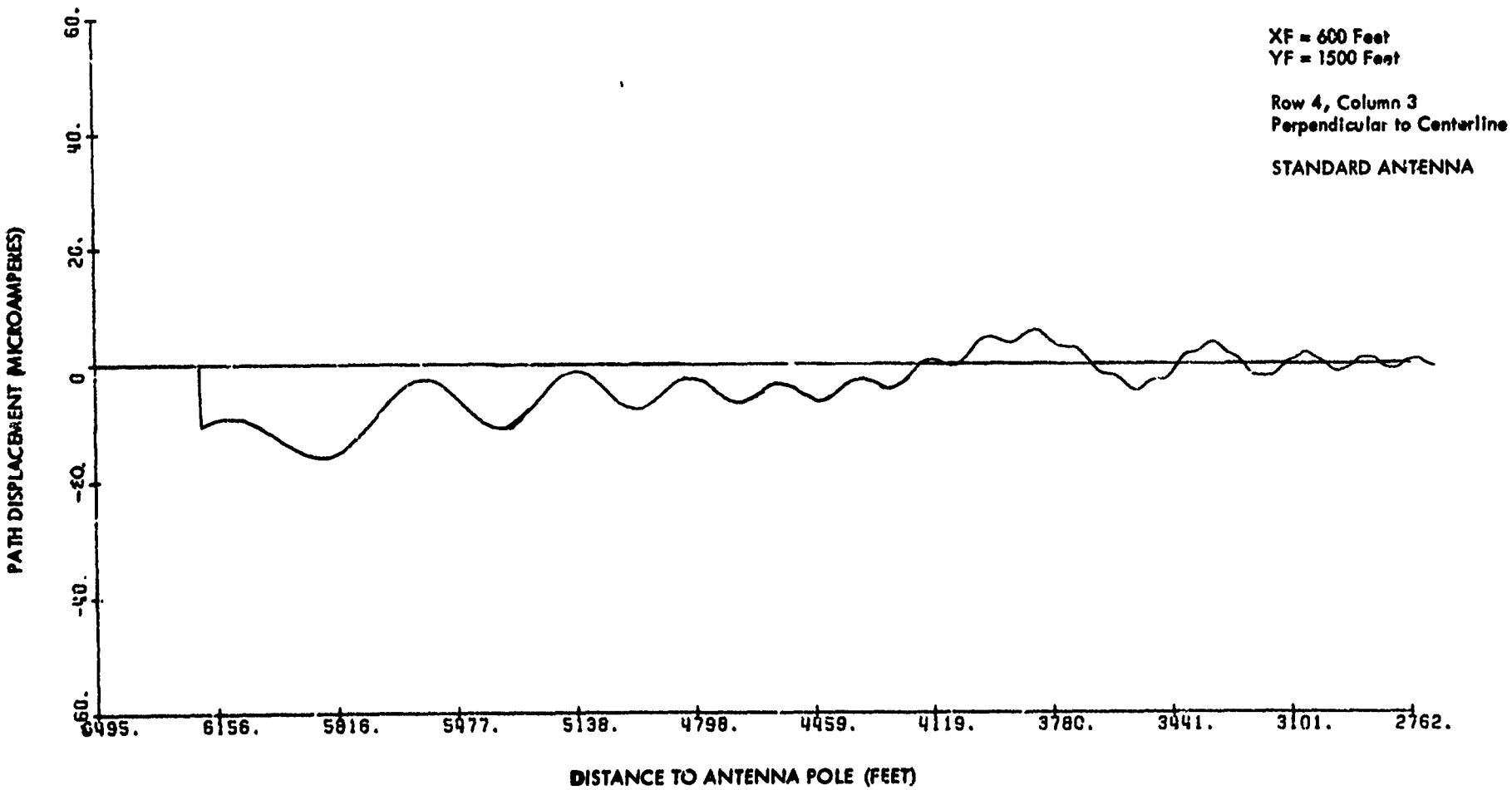
XF = 600 Feet
YF = 1500 Feet
Row 4, Column 3
Perpendicular to Centerline
STANDARD ANTENNA
PATH DISPLACEMENT (MICROAMPERES)
60.
40.
20.
0
-20.
-40.
-60.
6495.
6156.
5816.
5477.
5138.
4798.
4459.
4119.
3780.
3441.
3101.
2762.
DISTANCE TO ANTENNA POLE (FEET)

Figure 2-47.

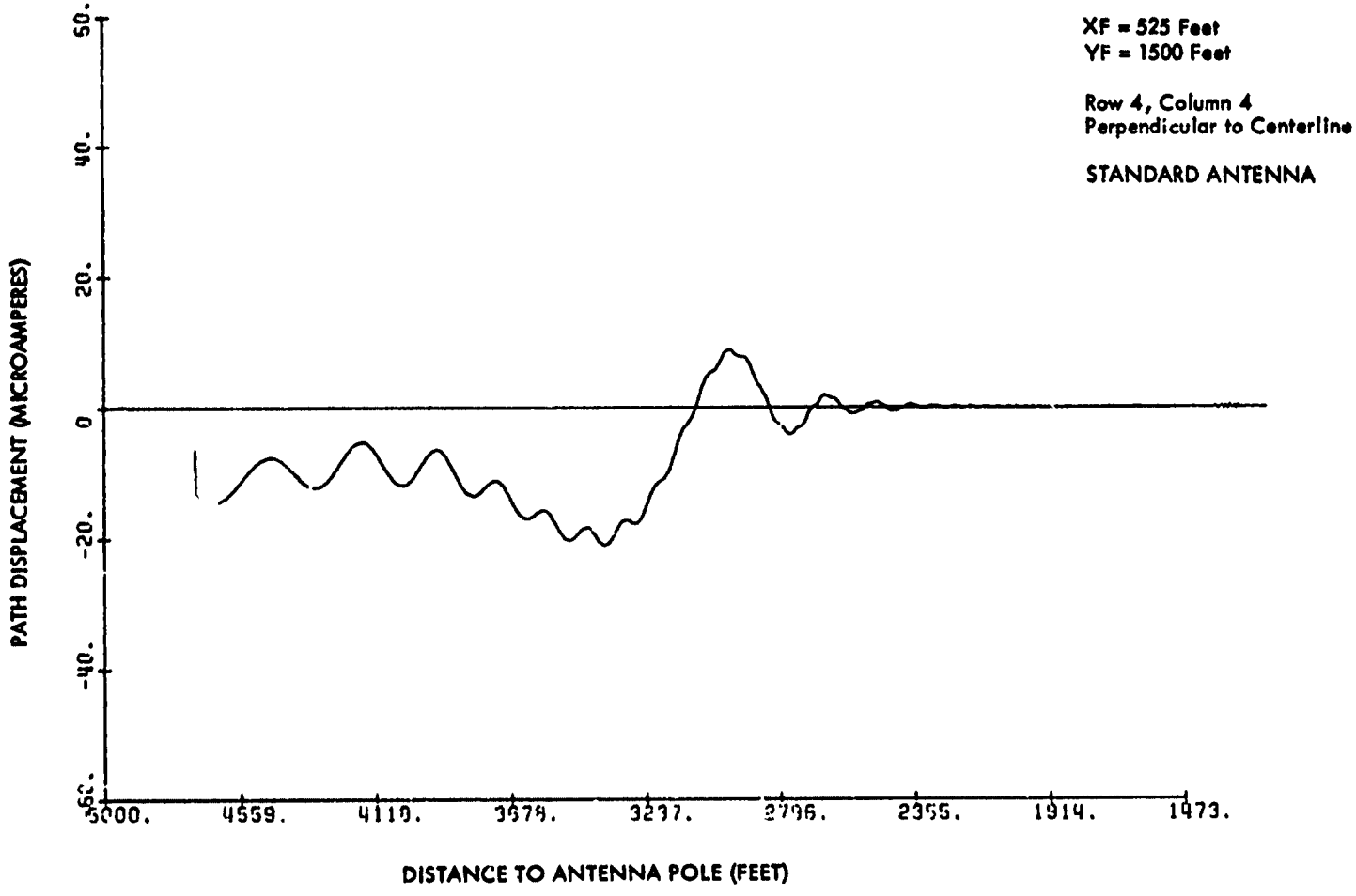
XF = 525 Feet
YF = 1500 Feet
Row 4, Column 4
Perpendicular to Centerline
STANDARD ANTENNA
PATH DISPLACEMENT (MICROAMPERES)
50.
40.
20.
0
-20.
-40.
-60.
5000.
4559.
4119.
3678.
3237.
2796.
2355.
1914.
1473.
DISTANCE TO ANTENNA POLE (FEET)

Figure 2-48.

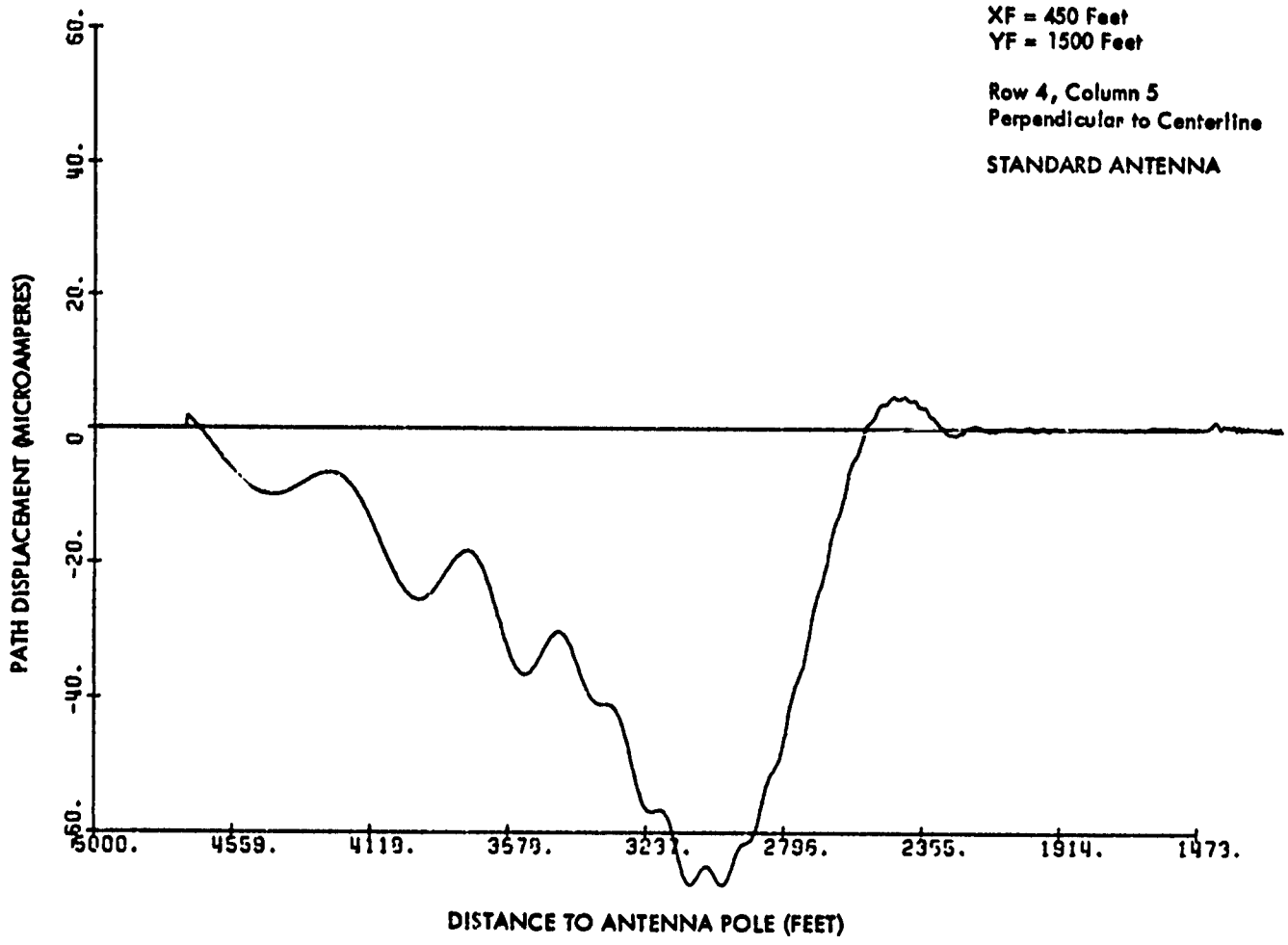
XF = 450 Feet
YF = 1500 Feet
Row 4, Column 5
Perpendicular to Centerline
STANDARD ANTENNA
PATH DISPLACEMENT (MICROAMPERES)
60.
40.
20.
0
-20.
-40.
-60.
5000.
4559.
4119.
3679.
3237.
2796.
2355.
1914.
1473.
DISTANCE TO ANTENNA POLE (FEET)

Figure 2-49.

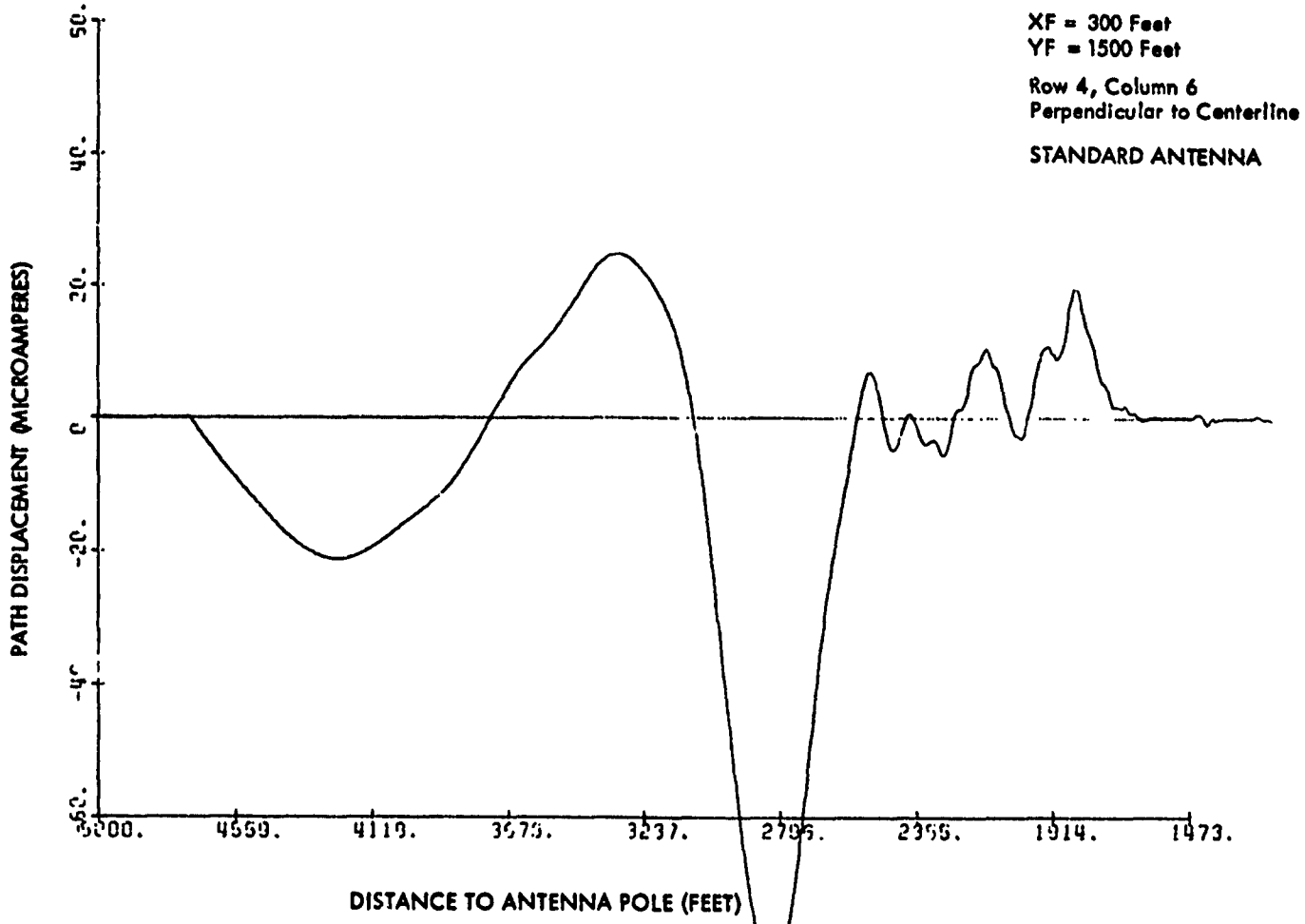
XF = 300 Feet
YF = 1500 Feet
Row 4, Column 6
Perpendicular to Centerline
STANDARD ANTENNA
PATH DISPLACEMENT (MICROAMPERES)
50.
40.
20.
0
-20.
-40
-60.
5000.
4559.
4119.
3678.
3237.
2796.
2355.
1914.
1473.
DISTANCE TO ANTENNA POLE (FEET)

Figure 2-50.

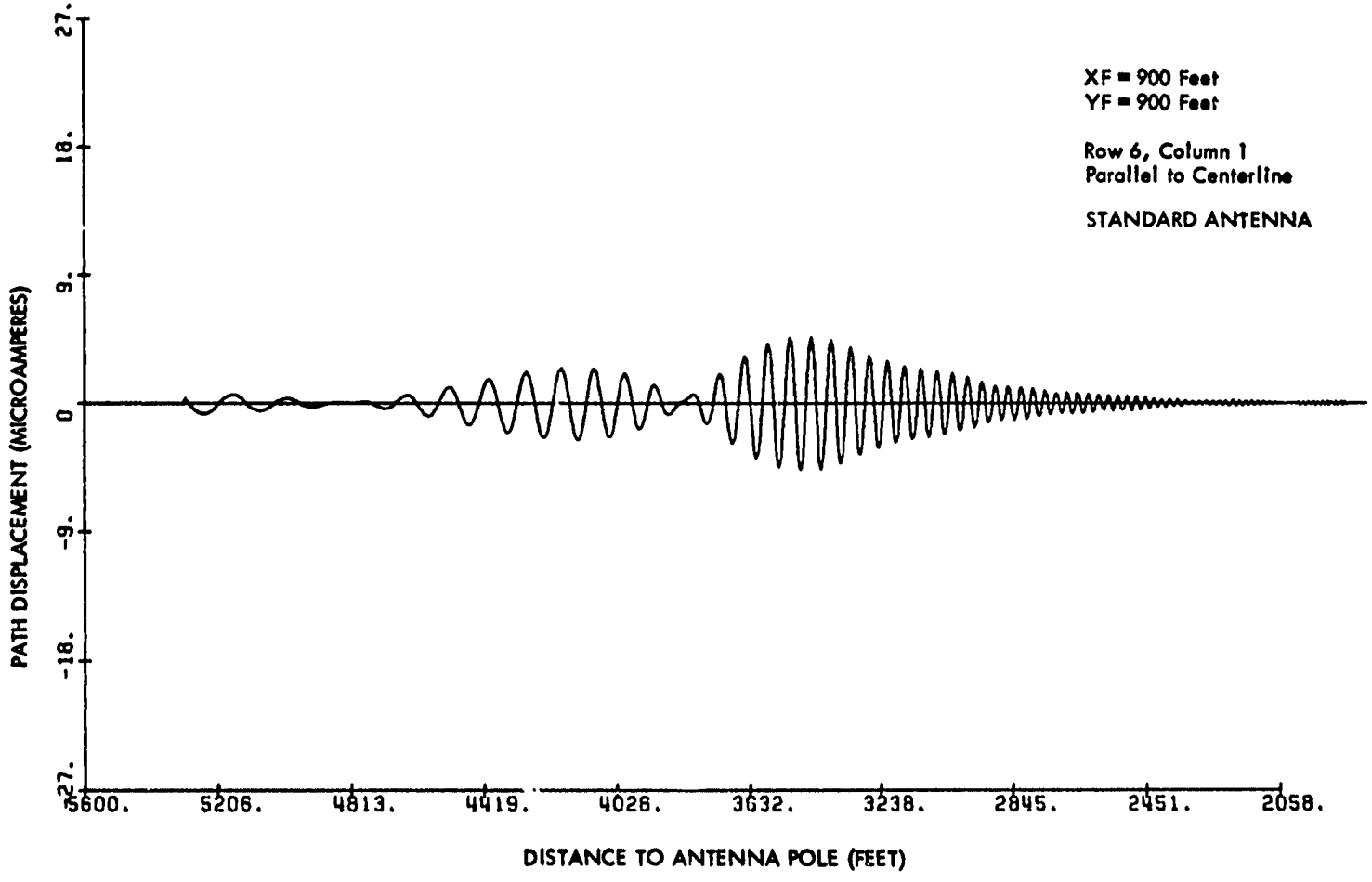
XF = 900 Feet
YF = 900 Feet
Row 6, Column 1
Parallel to Centerline
STANDARD ANTENNA
PATH DISPLACEMENT (MICROAMPERES)
27.
18.
9.
0
-9.
-18.
-27.
5600.
5206.
4813.
4419.
4026.
3632.
3238.
2845.
2451.
2058.
DISTANCE TO ANTENNA POLE (FEET)

Figure 2-51.

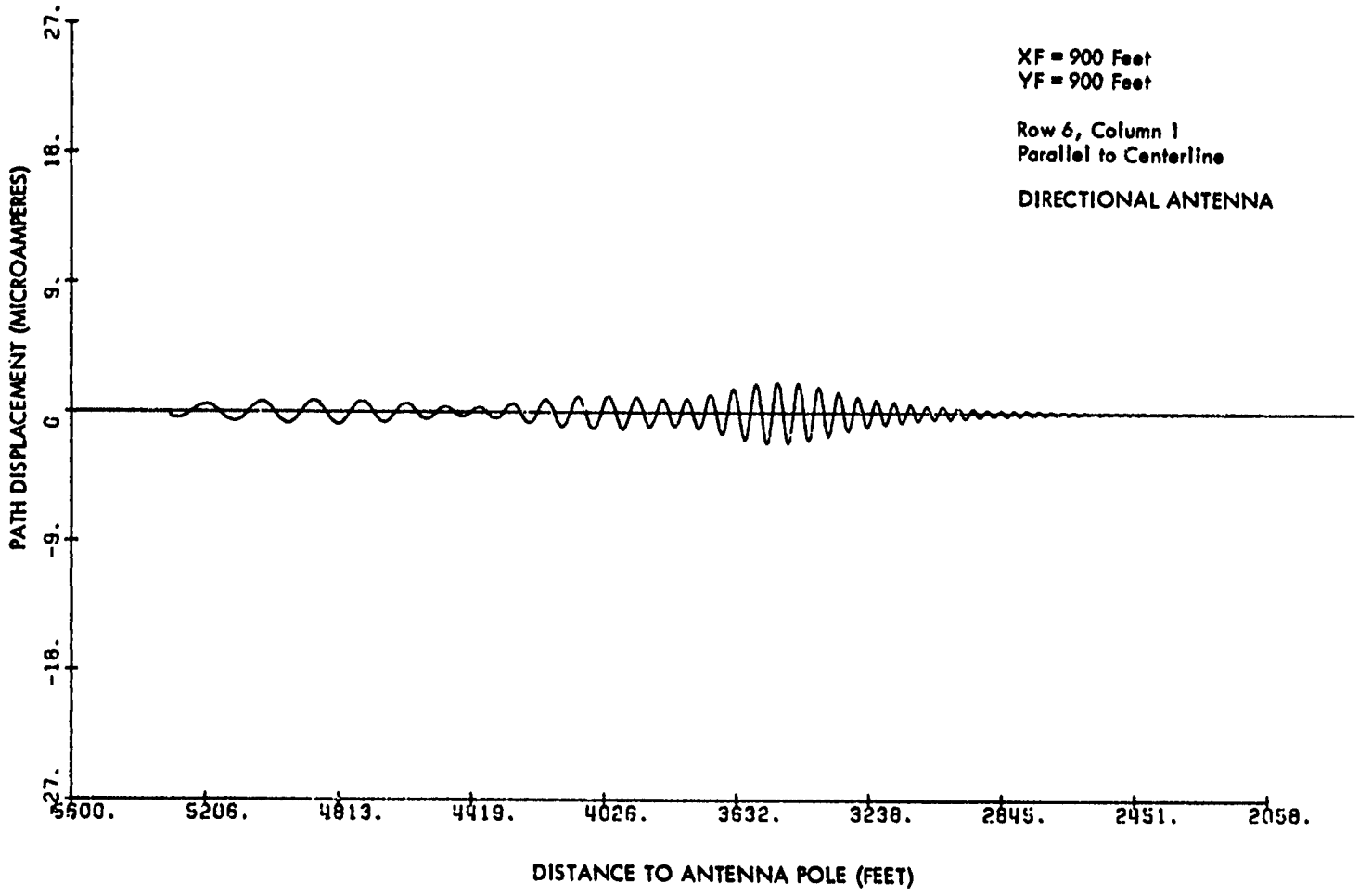
XF = 900 Feet
YF = 900 Feet
Row 6, Column 1
Parallel to Centerline
DIRECTIONAL ANTENNA
PATH DISPLACEMENT (MICROAMPERES)
27.
18.
9.
0
-9.
-18.
-27.
5500.
5206.
4813.
4419.
4026.
3632.
3238.
2845.
2451.
2058.
DISTANCE TO ANTENNA POLE (FEET)

Figure 2-52.

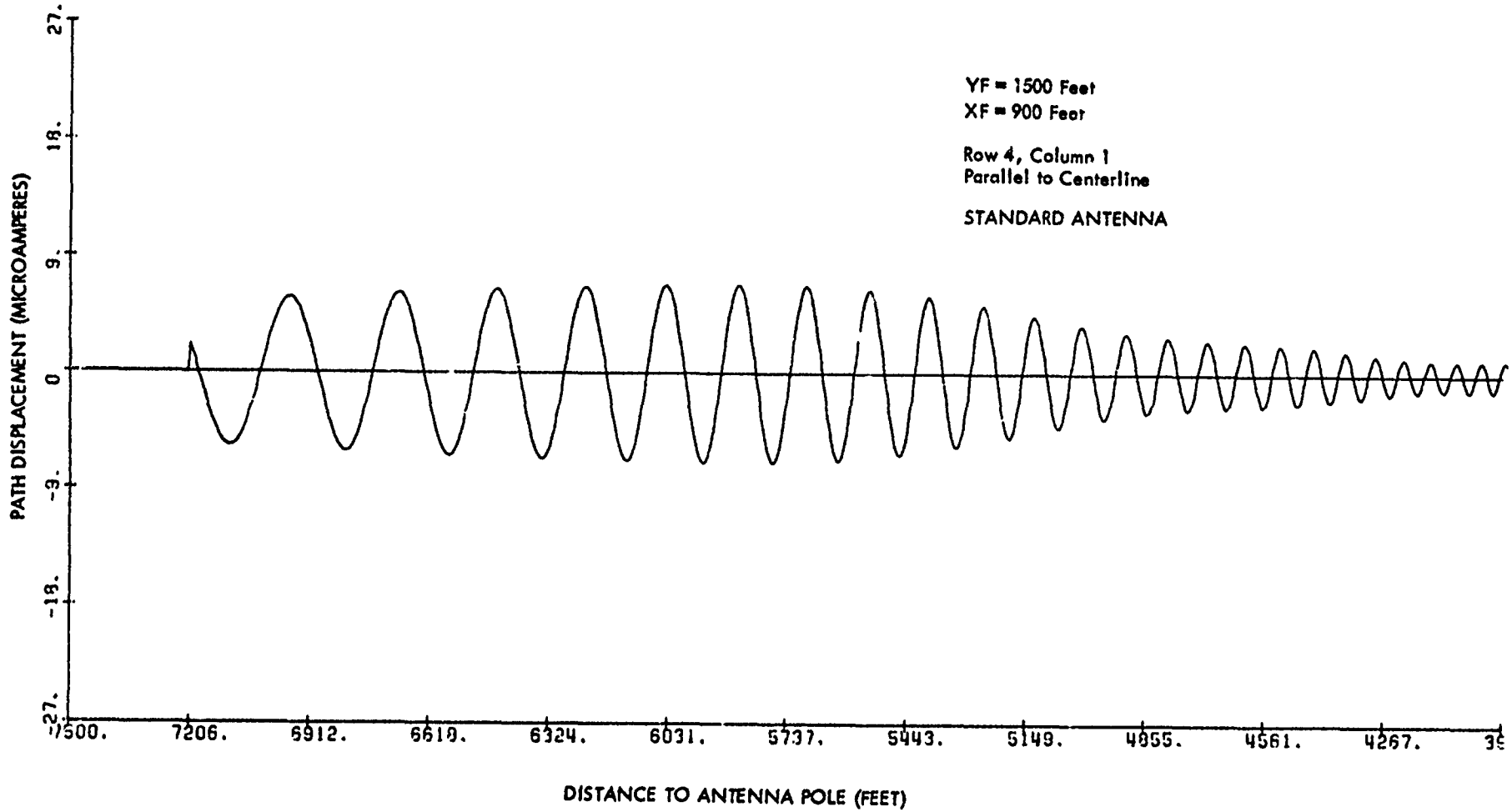
YF = 1500 Feet
XF = 900 Feet
Row 4, Column 1
Parallel to Centerline
STANDARD ANTENNA
PATH DISPLACEMENT (MICROAMPERES)
27.
18.
9.
0
-9.
-18.
-27.
7500.
7206.
6912.
6618.
6324.
6031.
5737.
5443.
5149.
4855.
4561.
4267.
DISTANCE TO ANTENNA POLE (FEET)

Figure 2-53.

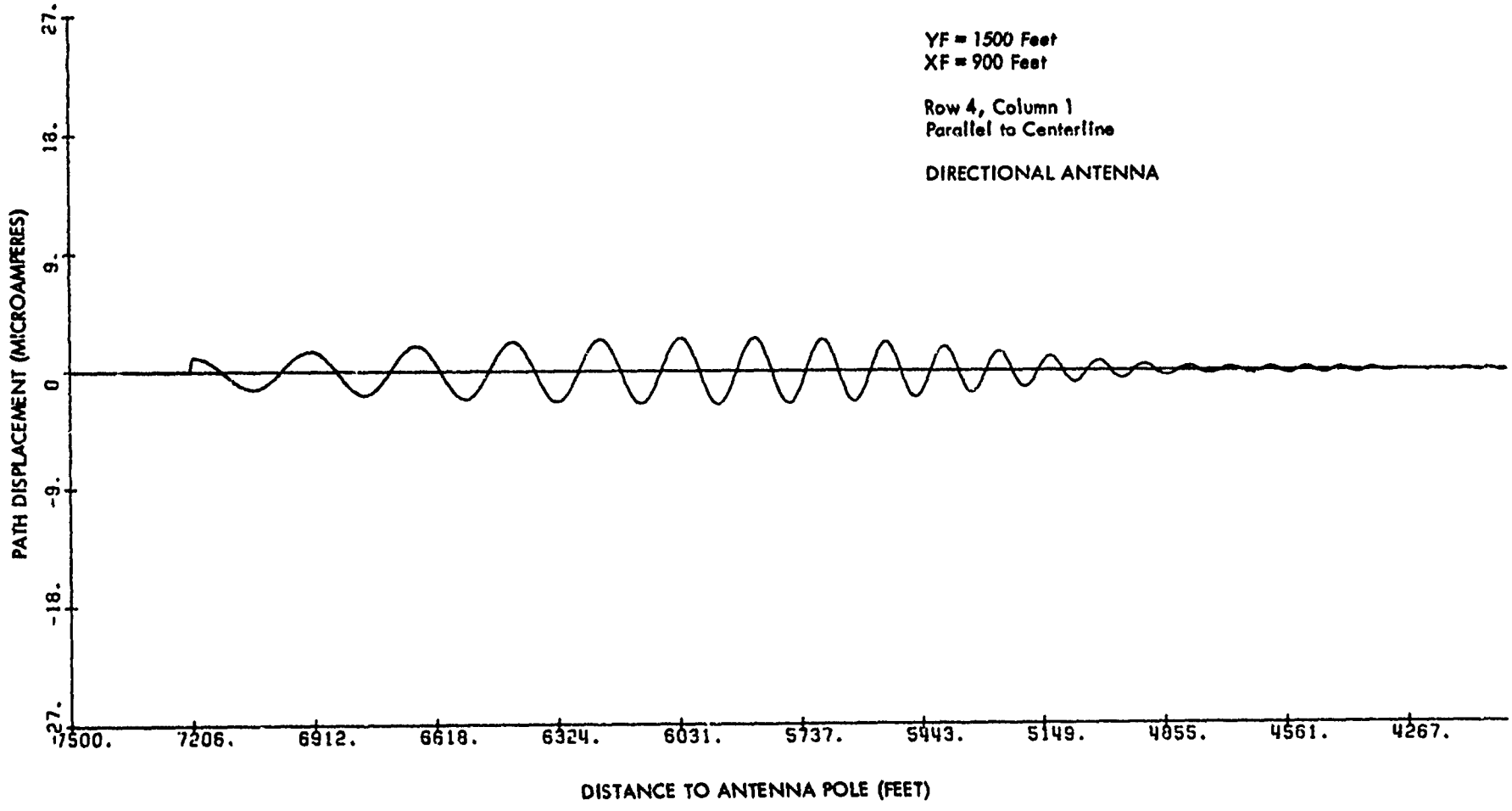
YF = 1500 Feet
XF = 900 Feet
Row 4, Column 1
Parallel to Centerline
DIRECTIONAL ANTENNA
PATH DISPLACEMENT (MICROAMPERES)
27.
18.
9.
0
-9.
-18.
-27.
7500.
7206.
6912.
6618.
6324.
6031.
5737.
5443.
5149.
4855.
4561.
4267.
DISTANCE TO ANTENNA POLE (FEET)

Figure 2-54.

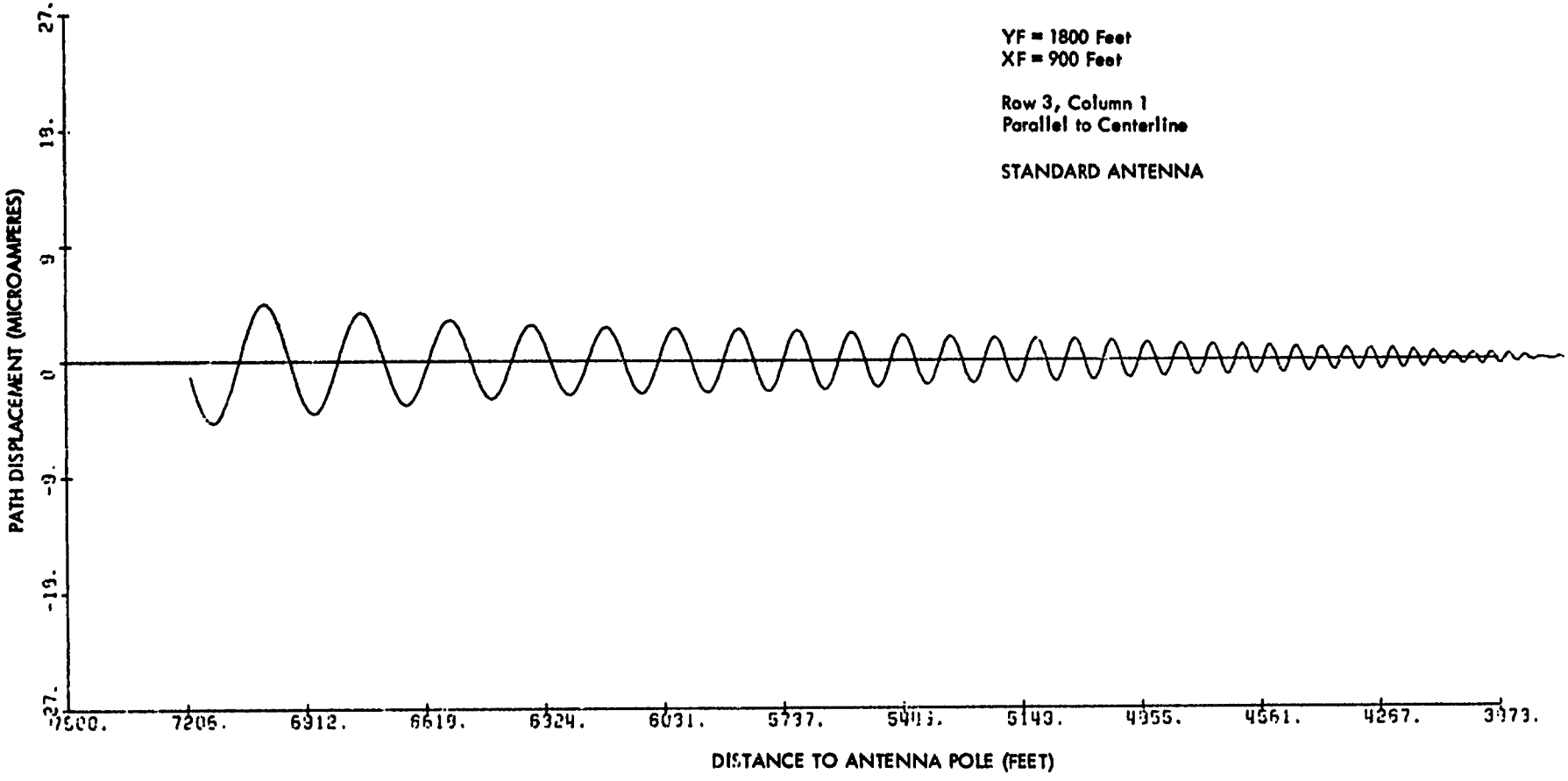
YF = 1800 Feet
XF = 900 Feet
Row 3, Column 1
Parallel to Centerline
STANDARD ANTENNA
PATH DISPLACEMENT (MICROAMPERES)
27.
19.
9
0
-9.
-19.
-27.
7500.
7206.
6912.
6619.
6324.
6031.
5737.
5443.
5149.
4855.
4561.
4267.
3973.
DISTANCE TO ANTENNA POLE (FEET)

Figure 2-55.

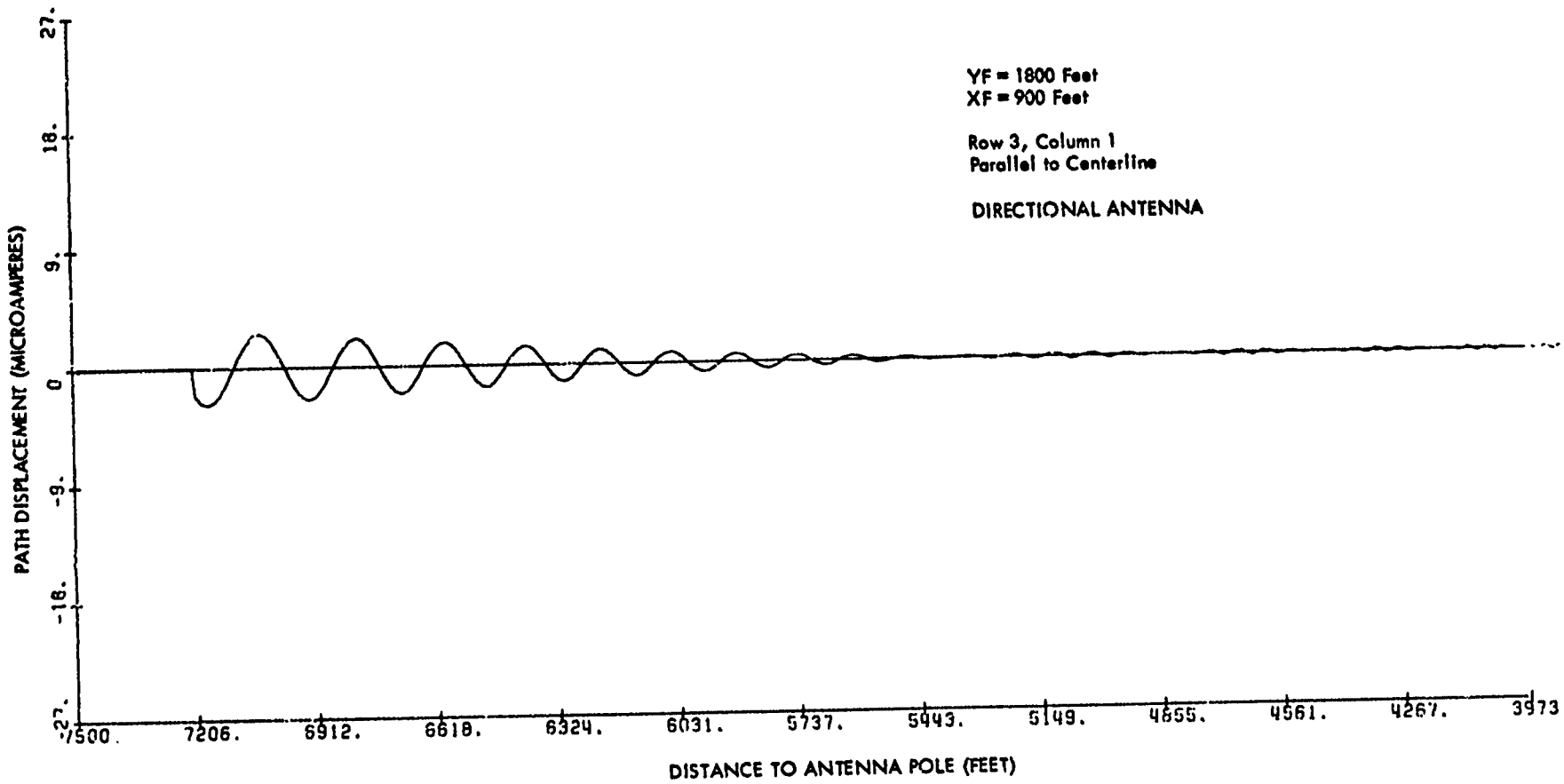
YF = 1800 Feet
XF = 900 Feet
Row 3, Column 1
Parallel to Centerline
DIRECTIONAL ANTENNA
PATH DISPLACEMENT (MICROAMPERES)
27.
18.
9.
0
-9.
-18.
-27.
7500.
7206.
6912.
6618.
6324.
6031.
5737.
5443.
5149.
4855.
4561.
4267.
3973
DISTANCE TO ANTENNA POLE (FEET)

Figure 2-56.

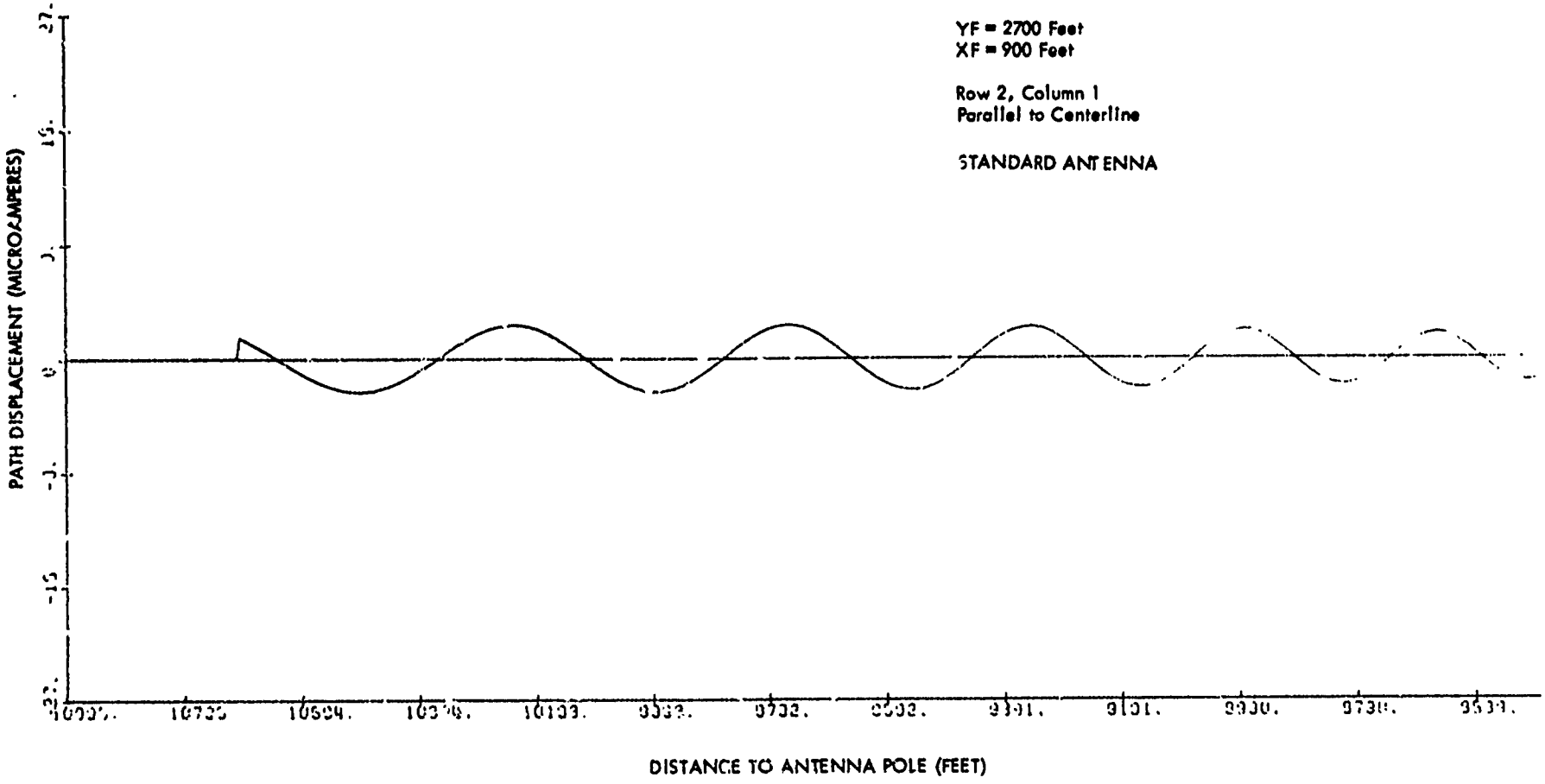
YF = 2700 Feet
XF = 900 Feet
Row 2, Column 1
Parallel to Centerline
STANDARD ANTENNA
PATH DISPLACEMENT (MICROAMPERES)
DISTANCE TO ANTENNA POLE (FEET)

Figure 2-57.

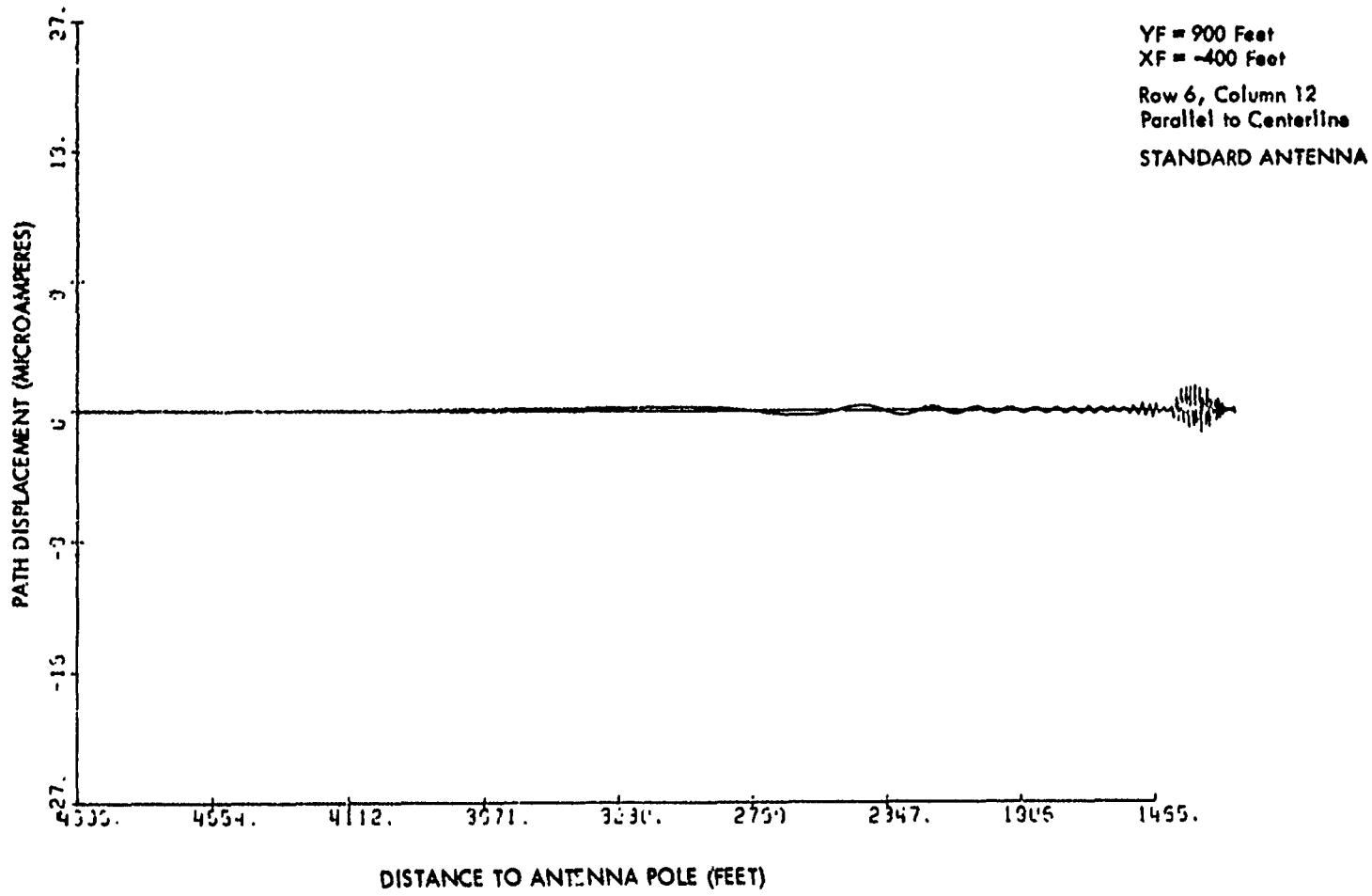
YF = 900 Feet
XF = -400 Feet
Row 6, Column 12
Parallel to Centerline
STANDARD ANTENNA
PATH DISPLACEMENT (MICROAMPERES)
27.
13.
3.
0
-3
-15
-27.
4555.
4554.
4112.
3571.
3330.
2750
2347.
1905
1455.
DISTANCE TO ANTENNA POLE (FEET)

Figure 2-58.

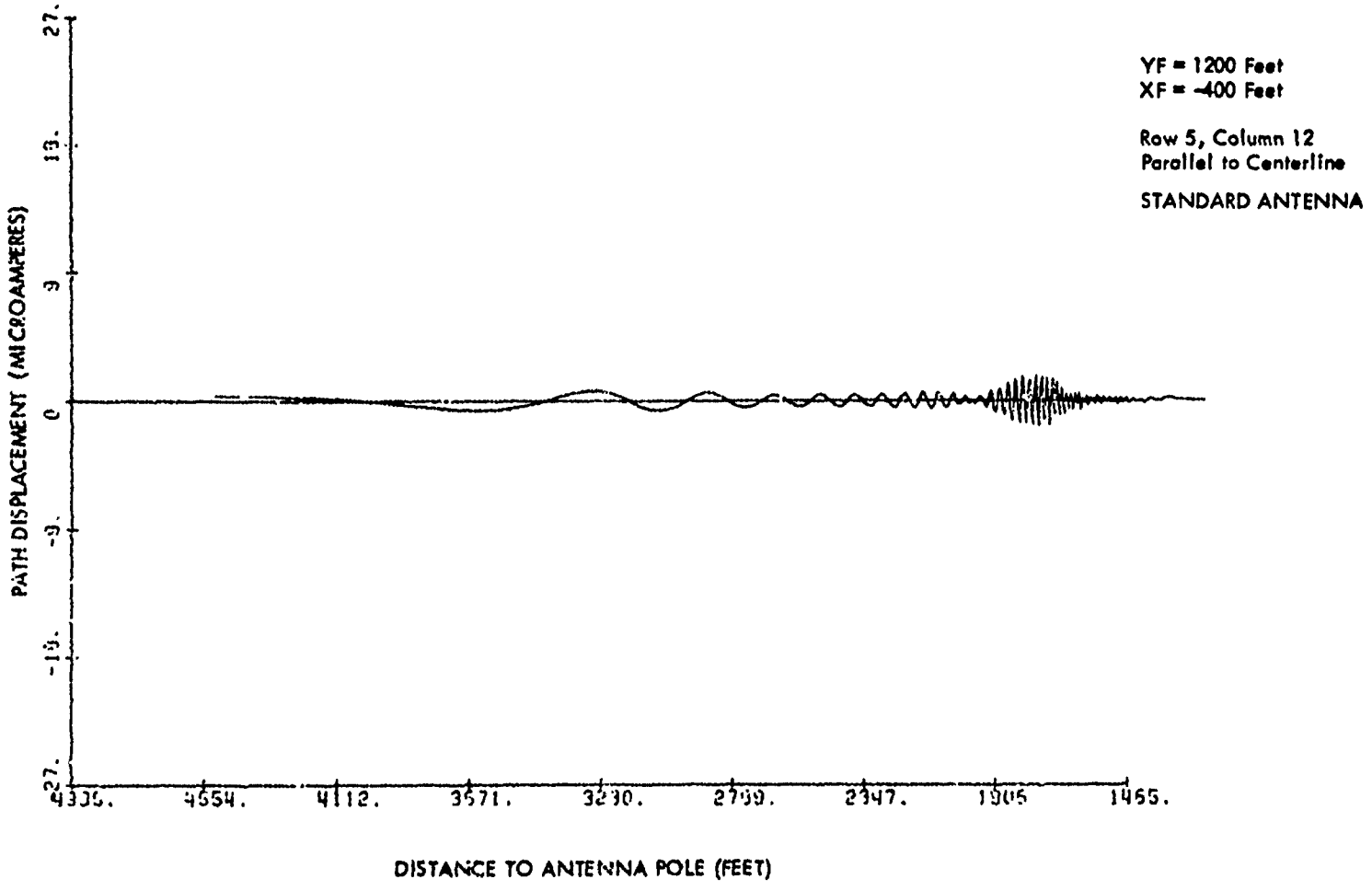
YF = 1200 Feet
XF = -400 Feet
Row 5, Column 12
Parallel to Centerline
STANDARD ANTENNA
PATH DISPLACEMENT (MICROAMPERES)
27.
18.
9
0
-9.
-18.
-27.
4554.
4112.
3671.
3230.
2347.
1905
1465.
DISTANCE TO ANTENNA POLE (FEET)

Figure 2-59.

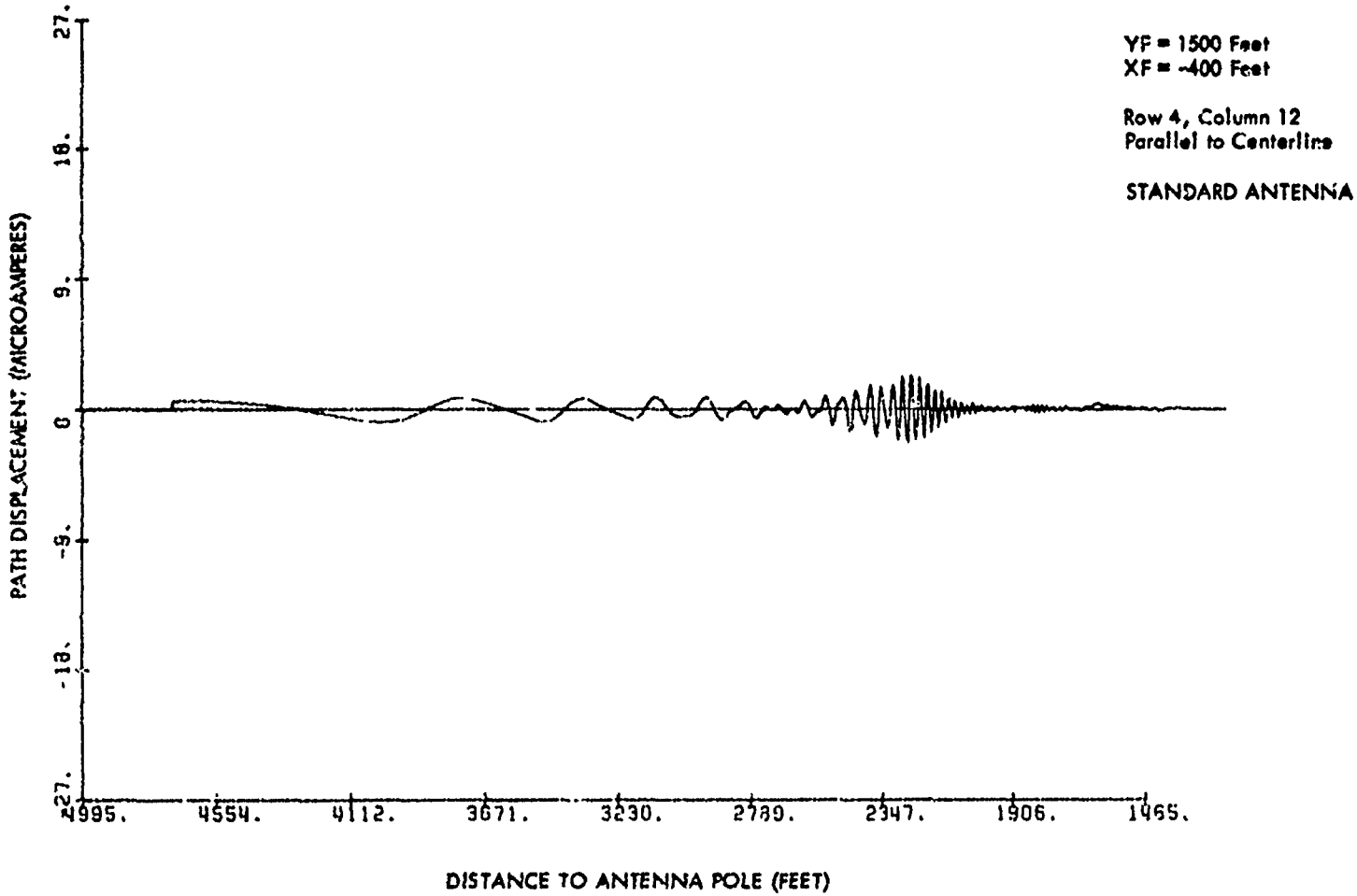
YF = 1500 Feet
XF = -400 Feet
Row 4, Column 12
Parallel to Centerline
STANDARD ANTENNA
PATH DISPLACEMENT (MICROAMPERES)
27.
18.
9.
0
-9.
-18.
-27.
4995.
4554.
4112.
3671.
3230.
2789.
2347.
1906.
1465.
DISTANCE TO ANTENNA POLE (FEET)

Figure 2-60.

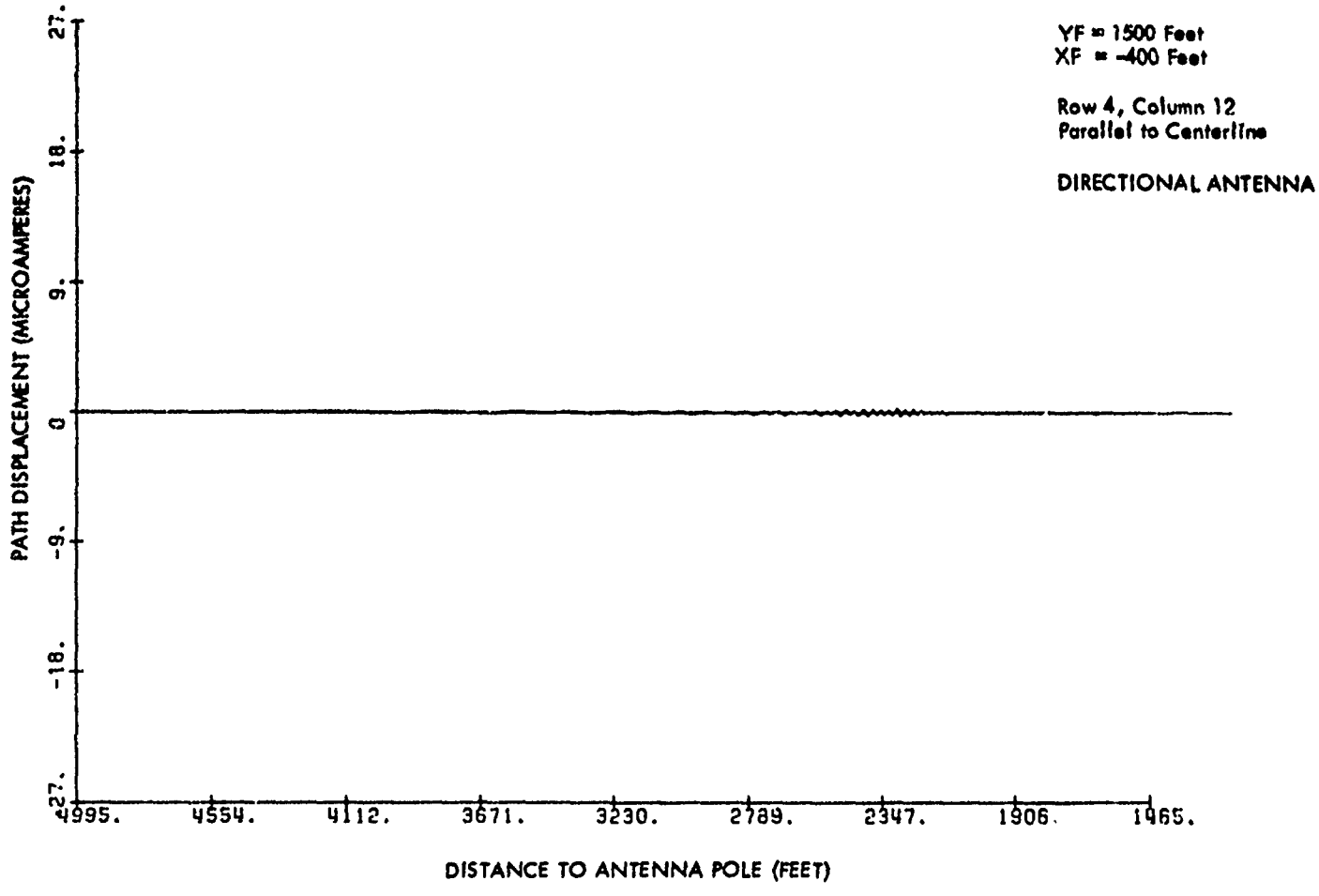
YF = 1500 Feet
XF = -400 Feet
Row 4, Column 12
Parallel to Centerline
DIRECTIONAL ANTENNA
PATH DISPLACEMENT (MICROAMPERES)
27.
18.
9.
0
-9.
-18.
-27.
4995.
4554.
4112.
3671.
3230.
2789.
2347.
1906.
1465.
DISTANCE TO ANTENNA POLE (FEET)

Figure 2-61.

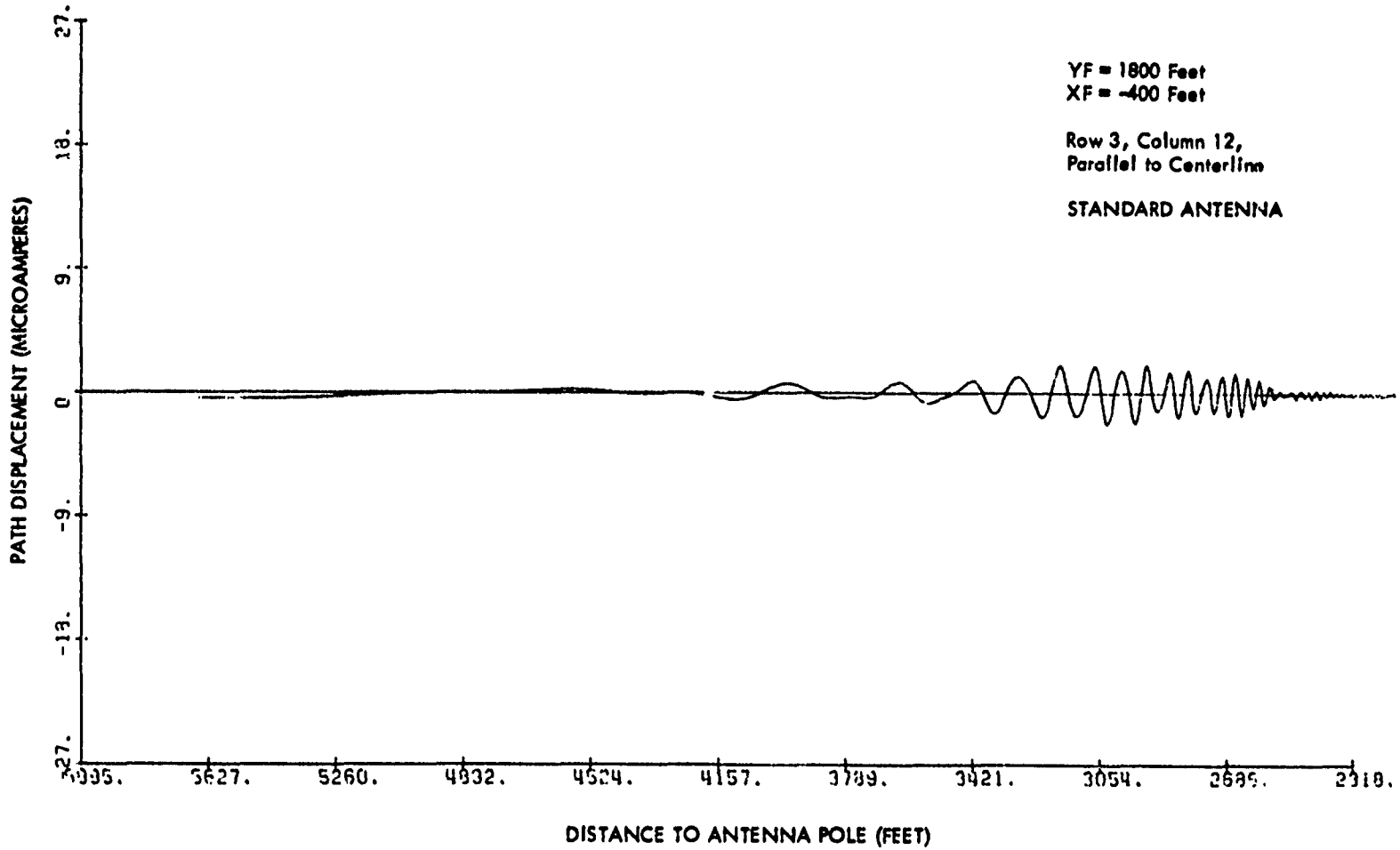
YF = 1800 Feet
XF = -400 Feet
Row 3, Column 12,
Parallel to Centerline
STANDARD ANTENNA
PATH DISPLACEMENT (MICROAMPERES)
27.
18.
9.
0
-9.
-18.
-27.
5627.
5260.
4157.
3421.
3054.
2310.
DISTANCE TO ANTENNA POLE (FEET)

Figure 2-62.

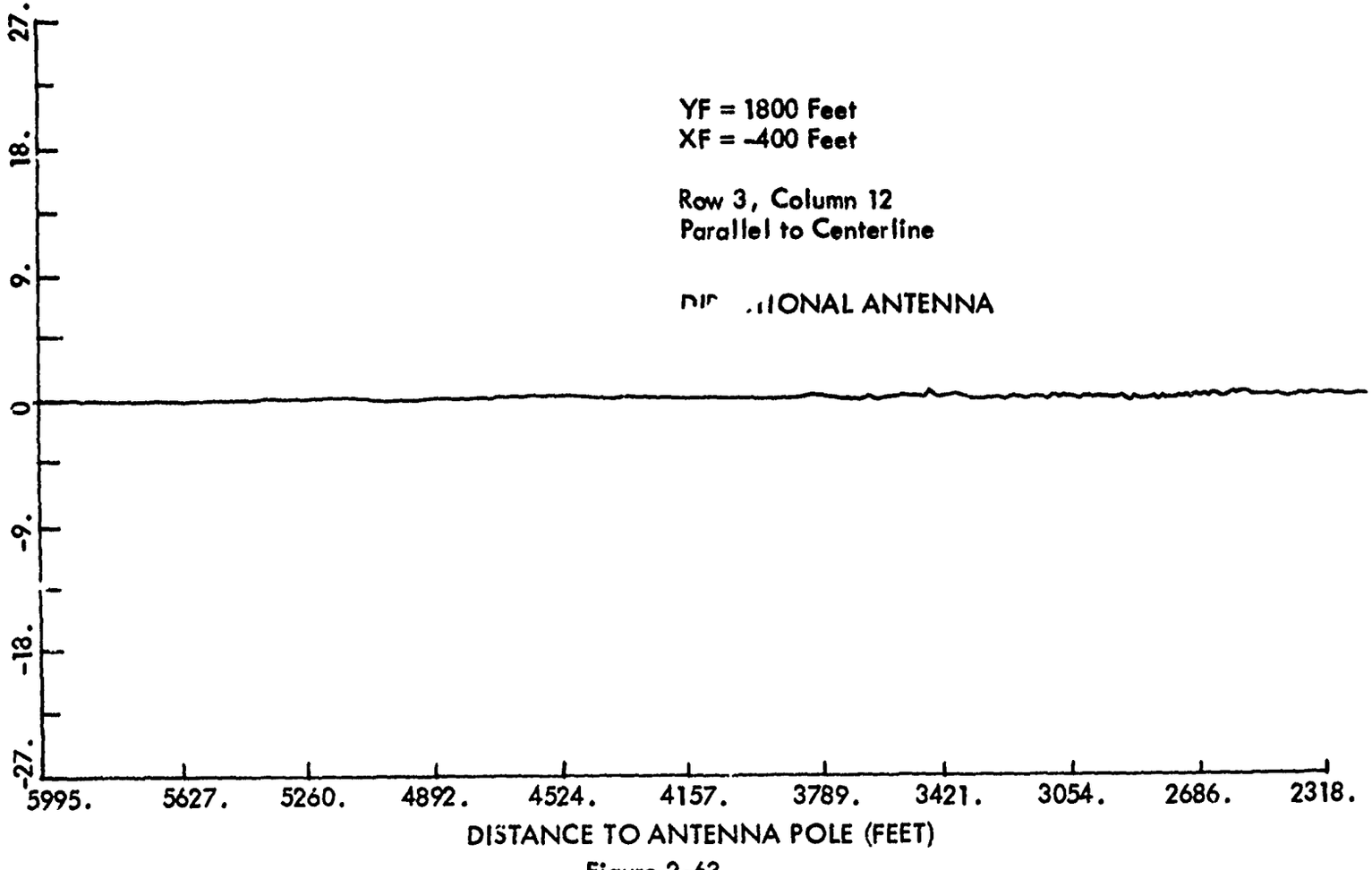
YF = 1800 Feet
XF = -400 Feet
Row 3, Column 12
Parallel to Centerline
DIRECTIONAL ANTENNA
27.
18.
9.
0
-9.
-18.
-27.
5995.
5627.
5260.
4892.
4524.
4157.
3789.
3421.
3054.
2686.
2318.
DISTANCE TO ANTENNA POLE (FEET)

Figure 2-63.

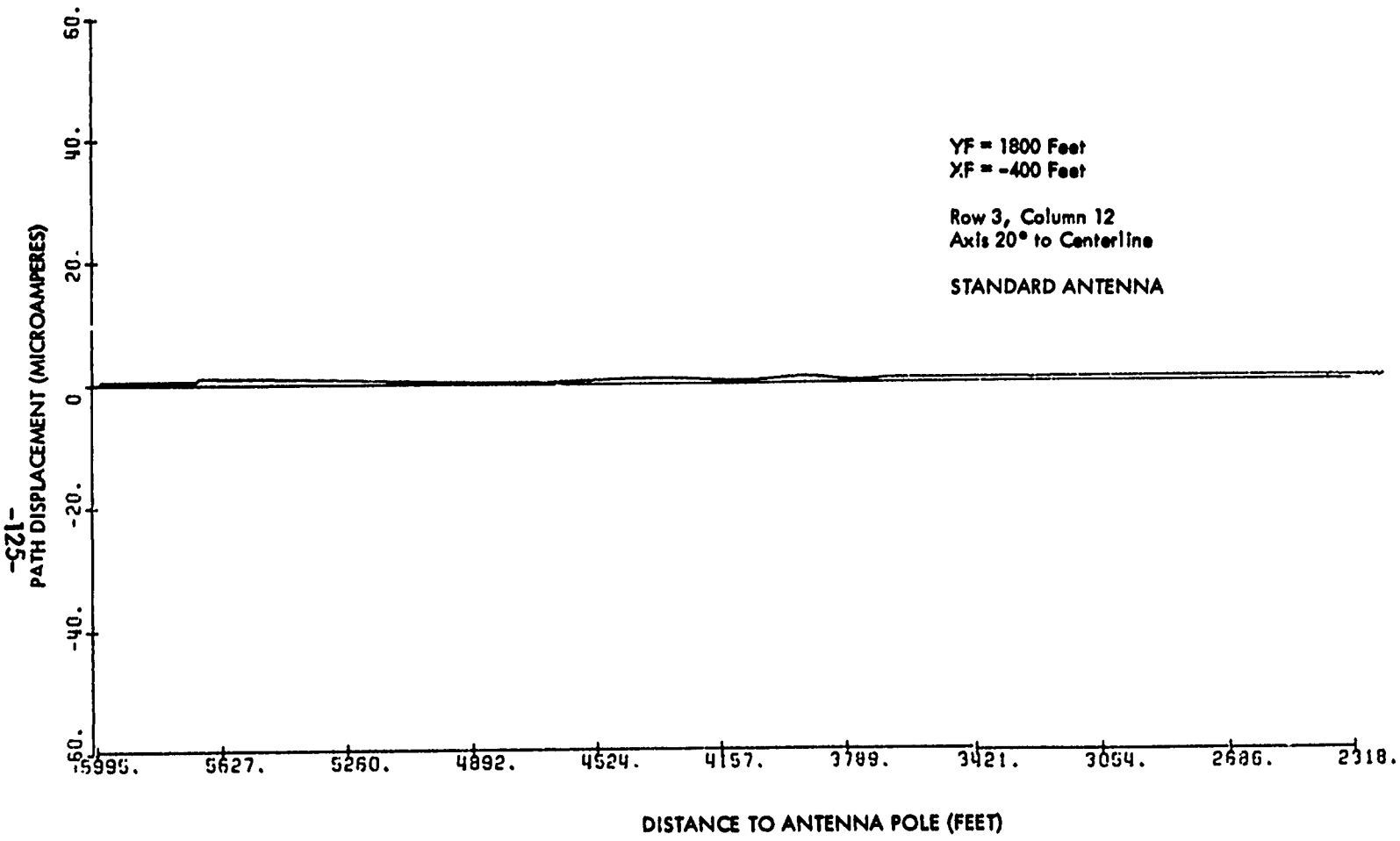
YF = 1800 Feet
XF = -400 Feet
Row 3, Column 12
Axis 20° to Centerline
STANDARD ANTENNA
PATH DISPLACEMENT (MICROAMPERES)
60.
40.
20.
0
-20.
-40.
-60.
-5995.
5627.
5260.
4892.
4524.
4157.
3789.
3421.
3054.
2686.
2318.
DISTANCE TO ANTENNA POLE (FEET)

Figure 2-64.

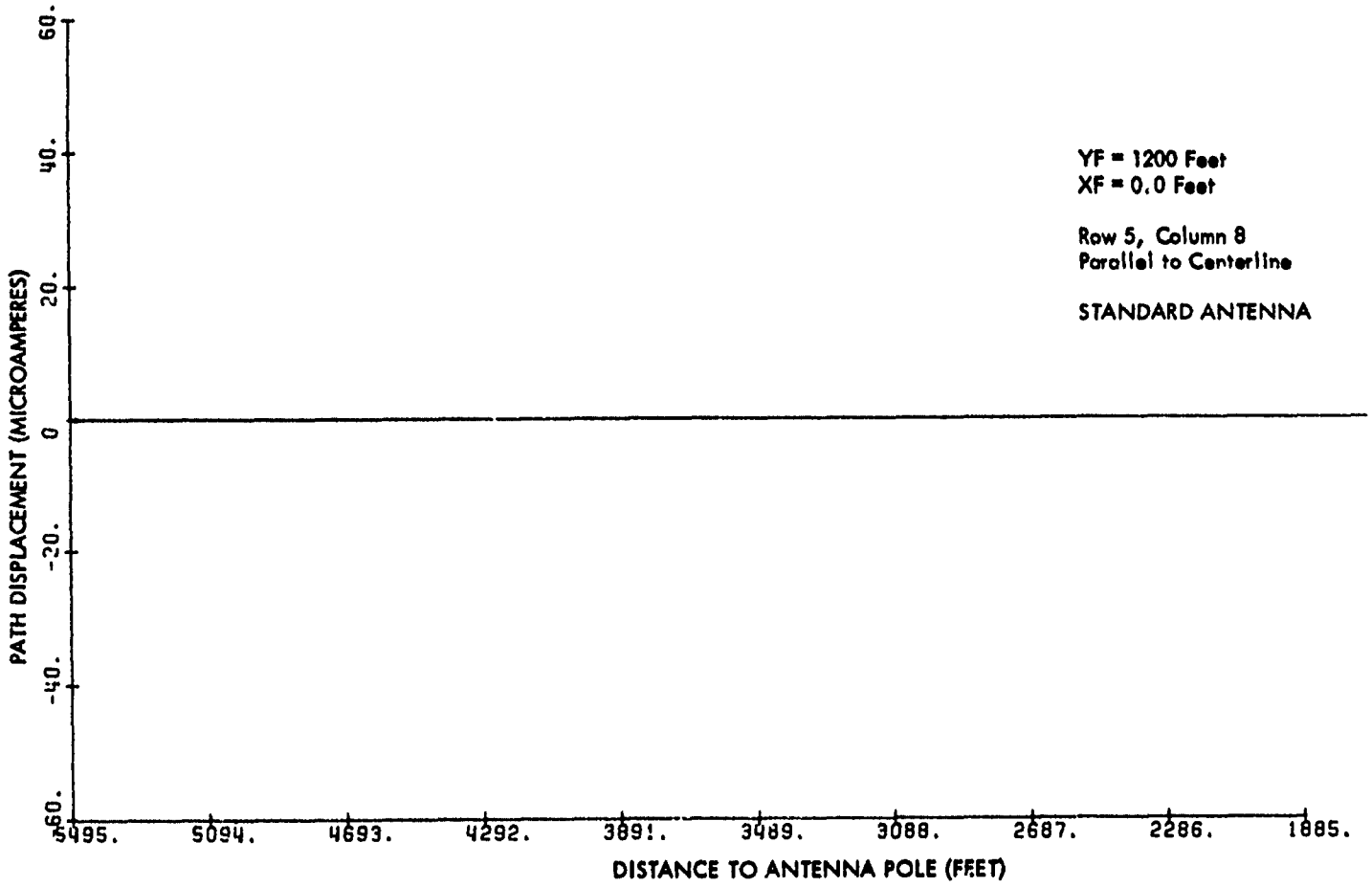
YF = 1200 Feet
XF = 0.0 Feet
Row 5, Column 8
Parallel to Centerline
STANDARD ANTENNA
PATH DISPLACEMENT (MICROAMPERES)
60.
40.
20.
0
-20.
-40.
-60.
5495.
5094.
4693.
4292.
3891.
3489.
3088.
2687.
2286.
1885.
DISTANCE TO ANTENNA POLE (FEET)

Figure 2-65.

3. Comparison of Mathematical and Physical Models for Glide Path Performance in the Presence of Reflections from Aircraft.

The emphasis of this work during the report period has been to obtain results as requested by the COR which are applicable to be included in the FAA manuals defining areas. The physical-model measurement assistance provided by the Air Navigation Group in Sydney, Australia (see page 93) is being utilized fully in determining the credibility of the predictions obtained using the mathematical models. This work has just begun and no conclusions can be stated at this time. Eventually a complete comparison will be available for predictions based on the physical optics, geometrical optics, and physical optics models. As a final check all will be compared with results of field measurements using an actual Boeing 747 aircraft.

E. Snow Cover Effects on Glide Paths

1. A Worst Case Approach to Glide Path Errors Caused by Snow Cover

a. Introduction. In studying the probable effects of a horizontally uniform snow ground cover on ILS glide slope performance, two mathematical models have been used. One the ray optic method [6], and two, transmission line analogy to plane reflection and transmission by dielectric layers [7]. Both methods give similar, but not identical results which can be expected since both methods are admittedly approximations and cannot be expected to give exact quantitative answers. Field experience has pointed to the difficulties involved in obtaining the data necessary for implementation of an exact analysis, and the extreme complexity of that analysis in itself weighs against the use of any such rigorous methods.

The purpose of this section is to report a number of findings using a different model and to suggest an approach to a solution of the monitoring problem bypassing the necessity for determination of the elusive and enigmatic snow parameters.

This discussion will be concerned solely with the null-reference, image, glide-path system.

b. Geometric Analysis. Figure 2-66 indicates the geometry involved. It is assumed that the ground is a perfect reflector and effectively an infinite, horizontal, plane surface. In the following, unless otherwise noted, all distances will be in carrier wavelengths. This will generalize and simplify the equations. It is further assumed that all distances of interest between transmitter and its images and the receiver are so nearly equal that the 1/R term may be neglected without seriously altering the relative field strengths. One may then write:

$$\bar{E}_p = E_a e^{-i\psi} \tag{2.79}$$

where $\bar{E}_p$ is the phasor field component at the receiver, E_a is a relative magnitude term to account for each antenna excitation, and ψ is the delay caused by the distance between antenna and receiver.

Since the DDM is the difference between the sideband components at 150 and 90 projected on the carrier component and taken relative to the carrier magnitude, one can write:

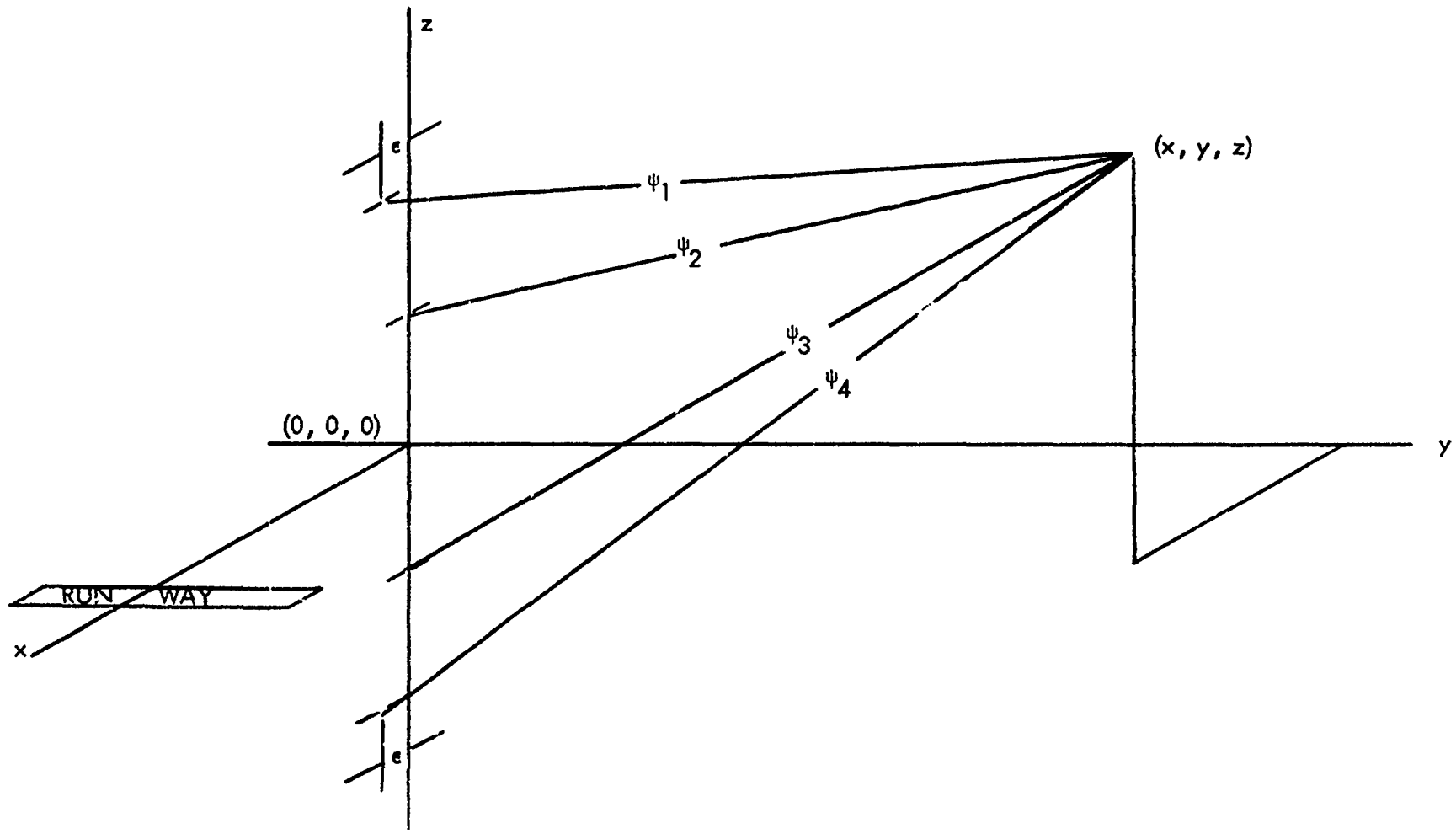

Figure 2-66. Coordinate System for Geometric Analysis.

$$DDM = 2\,Am\,\frac{\sin \pi\,(\psi_4 - \psi_1)}{\sin \pi\,(\psi_3 - \psi_2)}\,\cos \pi\,((\psi_1 + \psi_4) - (\psi_2 + \psi_3)) \qquad (2.80)$$

where m is the modulation factor of the sidebands on the carrier antenna and A is the ratio of the sidebands on the sideband antenna to the sidebands on the carrier antenna

$$\psi_1 = ((x - \epsilon)^2 + y^2 + (z - H)^2)^{\frac{1}{2}} \qquad (2.81)$$

$$\psi_2 = ((x^2 + y^2 + (z - h)^2)^{\frac{1}{2}} \qquad (2.82)$$

$$\psi_3 = ((x^2 + y^2 + (z + h)^2)^{\frac{1}{2}} \qquad (2.83)$$

$$\psi_4 = ((x - \epsilon)^2 + y^2 + (z + H)^2)^{\frac{1}{2}} \qquad (2.84)$$

Here ϵ is the offset of the upper (sideband) antenna toward the runway. H and h are the heights above the surface of the upper and lower antennas respectively.

This formulation can be used for the totally reflecting snow surface by subtracting the snow depth (assumed uniform horizontally) from z, H, and h, and then adding it to any z determined in using the equation which references that altitude to the site elevation level.

Under the current assumption (total reflection, infinite horizontal surfaces, etc.) it is evident that the glide path is represented by:

$$\sin \pi\,(\psi_4 - \psi_1) \simeq 0 \qquad (2.85)$$

or

$$\psi_4 - \psi_1 = 1 \qquad (2.86)$$

thus

$$((x-\epsilon)^2 + y^2 + (z+H)^2)^{\frac{1}{2}} = ((x-\epsilon)^2 + y^2 + (z-H)^2)^{\frac{1}{2}} + 1 \tag{2.87}$$

square both sides

$$(x-\epsilon)^2 + y^2 + (z+H)^2 = (x-\epsilon)^2 + y^2 + (z-H)^2 + 2((x-\epsilon)^2 + y^2 + (z-H)^2)^{\frac{1}{2}} + 1 \tag{2.88}$$

which reduces to

$$4zH - 1 = 2\,((x-\epsilon)^2 + y^2 + (z-H)^2)^{\frac{1}{2}} \tag{2.89}$$

square both sides

$$16z^2H^2 - 8zH + 1 = 4\,((x-\epsilon)^2 + y^2 + (z-H)^2) \tag{2.90}$$

or

$$z^2\,(16H^2 - 4) = 4\,((x-\epsilon)^2 + y^2 + H^2) - 1 \tag{2.91}$$

and

$$z = (((x-\epsilon)^2 + y^2 + H^2 - 0.25)/(4H^2 - 1))^{\frac{1}{2}} \tag{2.92}$$

Note that this gives the height of the glide path as $z = 0.5$ for $x = \epsilon$, $y = 0$ and $(z/y) = 1/(399)^{\frac{1}{2}}$ or approximately 0.05 for large y, or a far-field glide slope of 2.87°, when $h = 5$ and $H = 10$.

The cosine term goes to -1, indicating an inverted glide path at

$$\pi\,((\psi_1 + \psi_4) - (\psi_2 + \psi_3)) = \pi \tag{2.93}$$

more specifically

$$\tfrac{1}{2} < ((\psi_1 + \psi_4) - (\psi_2 + \psi_3)) < \tfrac{3}{2} \tag{2.94}$$

but the value, 1, is of special interest since it gives the so-called 180° point monitor location.

$$((x - \epsilon)^2 + y^2 + (z + H)^2)^{\frac{1}{2}} + ((x - \epsilon)^2 + y^2 + (z - H)^2)^{\frac{1}{2}} \tag{2.95}$$

$$= 1 + (x^2 + y^2 + (z + h)^2)^{\frac{1}{2}} + (x^2 + y^2 + (z - h)^2)^{\frac{1}{2}} \tag{2.96}$$

A simple calculation based on the first three terms of the Taylor series expansion of the radicals gives

$$y((H/y)^2 - (h/y)^2 - (0.75\,(x/y)^2\,((H/y)^2 - (h/y)^2) + 0.25\,((H/y)^4 - (h/y^4))) = 1 \tag{2.97}$$

where x and ϵ have been taken as negligible. For H = 10, h = 5 and $(z/y)^2$ = 1/399 this yields y = 74.44

As a test of the validity of the assumption of total reflection from snow surfaces, angles of incidence versus snow depth are given for this 180° location and for the far-field at y = 1000 and y = 5000. In Table 2-9 below θ_{10} and θ_5 and indicate respectively the incidence angles of rays from antennas at 10 and 5 wavelengths above the ground.

Snow Depth	180° Point		1000		5000	
	θ_{10}	θ_5	θ_{10}	θ_5	θ_{10}	θ_5
0.0	79.53	83.29	86.57	86.85	87.02	87.08
0.1	79.63	83.44	86.58	86.86		
0.2	79.82	83.59	86.59	86.87		
0.3	79.97	83.74	86.60	86.89		
0.4	80.12	83.90	86.61	86.90		
0.5	80.27	84.05	86.62	86.91		
1.0	81.02	84.88	86.68	86.97	87.05	87.10
2.0	82.53	86.34	86.79	97.08	87.07	87.13
3.0	84.05	87.88	86.91	87.19	87.09	

Table 2-9. Ray Incidence Angles for Various Snow Depths (Linear dimensions in wavelengths).

Table 2-10 gives reflection coefficient magnitudes for snow dielectric constants from 1.1 to 10.0 for incidence angles 75° to 89.9°.

It can be seen that in the far-field even with dielectric constants of snow as low as 1.1, the total reflection assumption is very good. The near-field picture, however, is not clear. The dielectric constant may be fairly high and still allow considerable energy to enter the snow, be delayed, reflected from the ground and return to mix with the first surface reflection at almost any electrical angle.

Since there must, however, be some unique value of total field from each antenna at the point of reception, a possible approach is to assume an effective snow surface and effective reflection coefficient and delay which will give the same results as the actual more complex situation. One may then write the direct and reflected signals at the receiver as

$$E_d = Ee^{-i\psi_d 2\pi} \tag{2.98}$$

$$\frac{\cos i - \mathrm{SQRT}((e - 1 + \cos^2 i))}{\cos i + \mathrm{SQRT}((e - 1 + \cos^2 i))} = \rho$$

(Values in the Table are $\rho \times 10^5$.)

Dielectric Constants	INCIDENCE ANGLE															
	75°	76°	77°	78°	79°	80°	81°	82°	83°	84°	85°	86°	87°	88°	89°	89.9°
1.1	22446	22408	26610	29085	31871	35014	38562	42570	47102	52225	50015	64553	71928	80230	89554	98902
1.2	33253	35520	37992	40689	43633	46847	50356	54185	58363	62920	67886	73293	79174	85563	92494	99223
1.4	45060	47355	49800	52405	55179	58132	61276	64621	68179	71960	75977	80240	84763	89556	94631	99450
1.6	51870	54069	56386	58826	61397	64103	66951	69947	73097	76408	79887	83538	87369	91386	95594	
1.8	56499	58592	60784	63077	65476	67985	70607	73348	76210	79199	82318	85571	88962	92495	96173	
2.0	59928	61925	64006	66174	68431	70781	73227	75771	78416	81166	84022	86988	90066	93259	96570	
2.5	65733	67534	69398	71326	73320	75380	77510	79709	81981	84325	86744	89239	91811	94461	97190	
3.0	69488	71143	72847	74604	76412	78273	80189	82160	84186	86270	88411	90610	92867	95185	97562	
4.0	74248	75696	77180	78702	80261	81859	83494	85169	86883	88637	90430	92263	94137	96051	98005	
5.0	77252	78558	79893	81258	82653	84078	85532	87017	88533	90079	91656	93263	94902	96570	98270	
7.5	81653	82738	83842	84966	86110	87274	88458	89662	90886	92129	93393	94676	95978	97299	98640	
10.0	84170	85120	86086	87067	88063	89074	90101	91142	92199	93270	94356	95456	96571	97700	98843	

Table 2-10. Reflection Coefficients for Snow at Incidence Angles of 75° to 89.9° for Relative Dielectric Constant 1.1 to 10.1.

$$E_r = -\rho E e^{-i\psi_r 2\pi} \tag{2.99}$$

where ψ_d is the direct path length in wavelengths, and ψ_r is the equivalent path length for the reflected signal including the delaying effect of the snow and of the possible complex reflection coefficient at the ground, and ρ is the magnitude of the effective reflection coefficient.

Writing these equations for both antennas and combining the fields at the receiver gives (neglecting the small 1/R variation as before)

$$\text{DDM} = 2\,\text{AM}\,\frac{C_{14}}{C_{23}} \cos \tfrac{1}{2}\left(C + (\sin^{-1} \rho_3 S_3 - \sin^{-1} S_3) - (\sin^{-1} \rho_4 S_4 - \sin^{-1} S_4)\right) \tag{2.100}$$

where

$$C_{14} = (1 + \rho_4^2 - 2\rho_4 \cos 2\pi (\psi_4 - \psi_1))^{\frac{1}{2}} \tag{2.101}$$

$$C_{23} = (1 + \rho_3^2 - 2\rho_3 \cos 2\pi (\psi_3 - \psi_2))^{\frac{1}{2}} \tag{2.102}$$

$$S_3 = (\sin 2\pi (\psi_3 - \psi_2))/C_{23} \tag{2.103}$$

$$S_4 = (\sin 2\pi (\psi_4 - \psi_1))/C_{14} \tag{2.104}$$

$$C = 2\pi\,[(\psi_1 + \psi_4) - (\psi_2 + \psi_3)] \tag{2.105}$$

ρ_3 and ρ_4 are the magnitudes of the reflection coefficients at the intersections of ψ_3 and ψ_4 with the effect surface of of the snow.

This equation could be programmed and solved for DDM as a function of position and snow depth for various assumed values of ρ_3 and ρ_4 and ψ_3 and ψ_4 and would give rise to such a confusing plethora of results as to render the game unworthy of the candle.

A rather simple alternative approach is to sketch phasor diagrams of the direct and reflected signals and to make a worst case analysis in terms of reasonable assumptions.

The first of these assumptions is that since the angle of incidence for the signal reflected to the far-field from the surface of the snow is greater than 86.6 degrees, for which a dielectric constant of as little as 1.4 relative will give a reflection coefficient of at least 0.8, a phasor diagram can be constructed fr unaltered direct phasors and corresponding surface reflected phasors of 80% the length of the direct phasors. For this, as yet, incomplete diagram, lengths and angles are perfectly definite calculable functions of geometry.

To complete the diagram, a second assumption is made. Since the analysis has assumed infinite plane surfaces, it does not seem likely that the phasor representing the total reflected signal should be larger than that which would be delivered by 100% reflection. It is therefore assumed that the locus of the tip of the reflected phasor must lie on or within a circle of radius (1 - ρ) whose center is the point of the first surface reflected phasor of length ρ.

The phasor diagram constructed on these assumptions gives rise to a range of carrier phase angles and magnitudes and a multiplicity of sideband phases and magnitudes.

Consider Figure 2-67 where, for simplicity, the direct carrier phasor is shown at -90 and the surface reflected carrier at -45. The resultant may range from -13° to -26.8° with magnitude from 1.465 to 1.865.

Figure 2-68 shows the sideband phasors with the direct signal taken as 0° (diagram reference angle) and the first surface reflected phasor at -30°. The carrier phasors are shown as lines of direction only since only the carrier phase is of interest to this part of the construction. The extreme values of the projections of the sideband phasor on the carrier phasor are A and B. These are the worst case values.

Figure 2-69 illustrates the method of determining the DDM from these points and the carrier phasors.

The length O-C in Figure 2-69 may be chosen so as to provide a convenient scale. From the triangles OCC_a and OAD_a it can be seen that OD_a: OA::OC:OC_a and since OC_a and OA are respectively the carrier and projected sideband magnitudes, OD_a would measure one-half the DDM directly if both magnitudes were to the same scale. The suppression of the modulation index, m, and the relative sideband factor, A, (for convenience in drafting) however, makes the length O-C represent a DDM of 2mA or about 0.24. Thus, in Figure 2-69 the DDM ranges from 0.0026 to 0.062 or from 2.2 to 53 microamperes flydown.

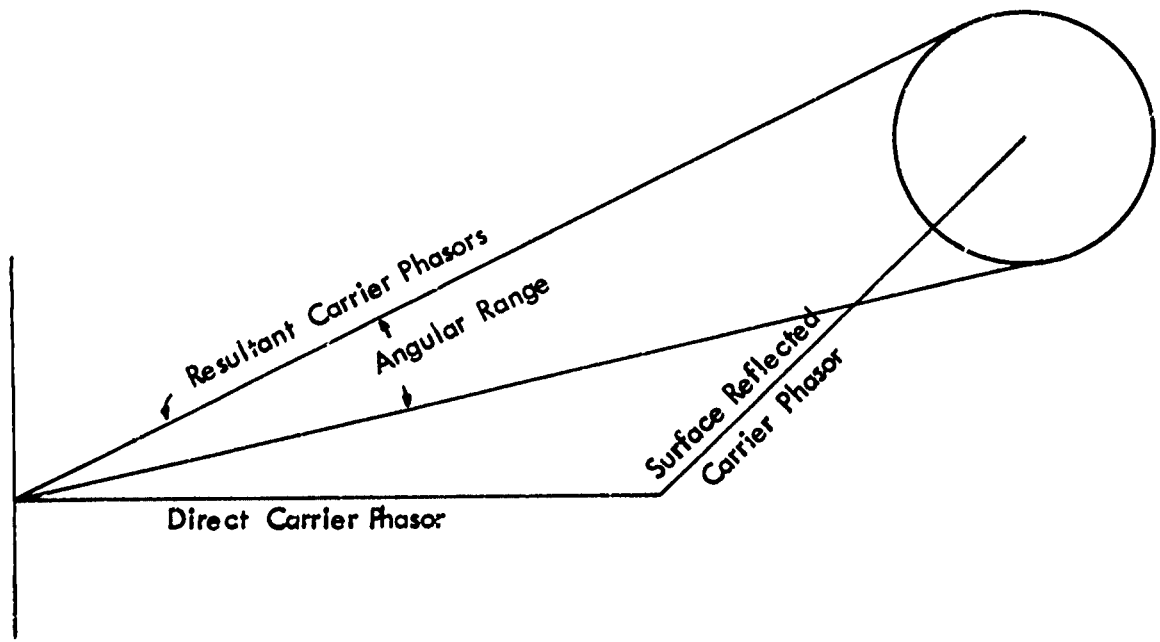

Figure 2-67. Phasor Construct Showing the Range of Carrier Phasors due to 80% Surface Reflection.

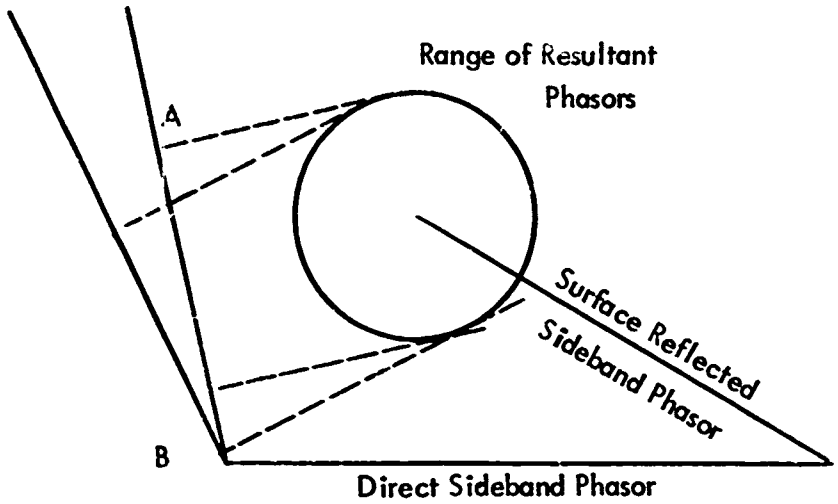

Figure 2-68. Phasor Construct Showing Range of Sideband Phasors due to 80% Surface Reflection.

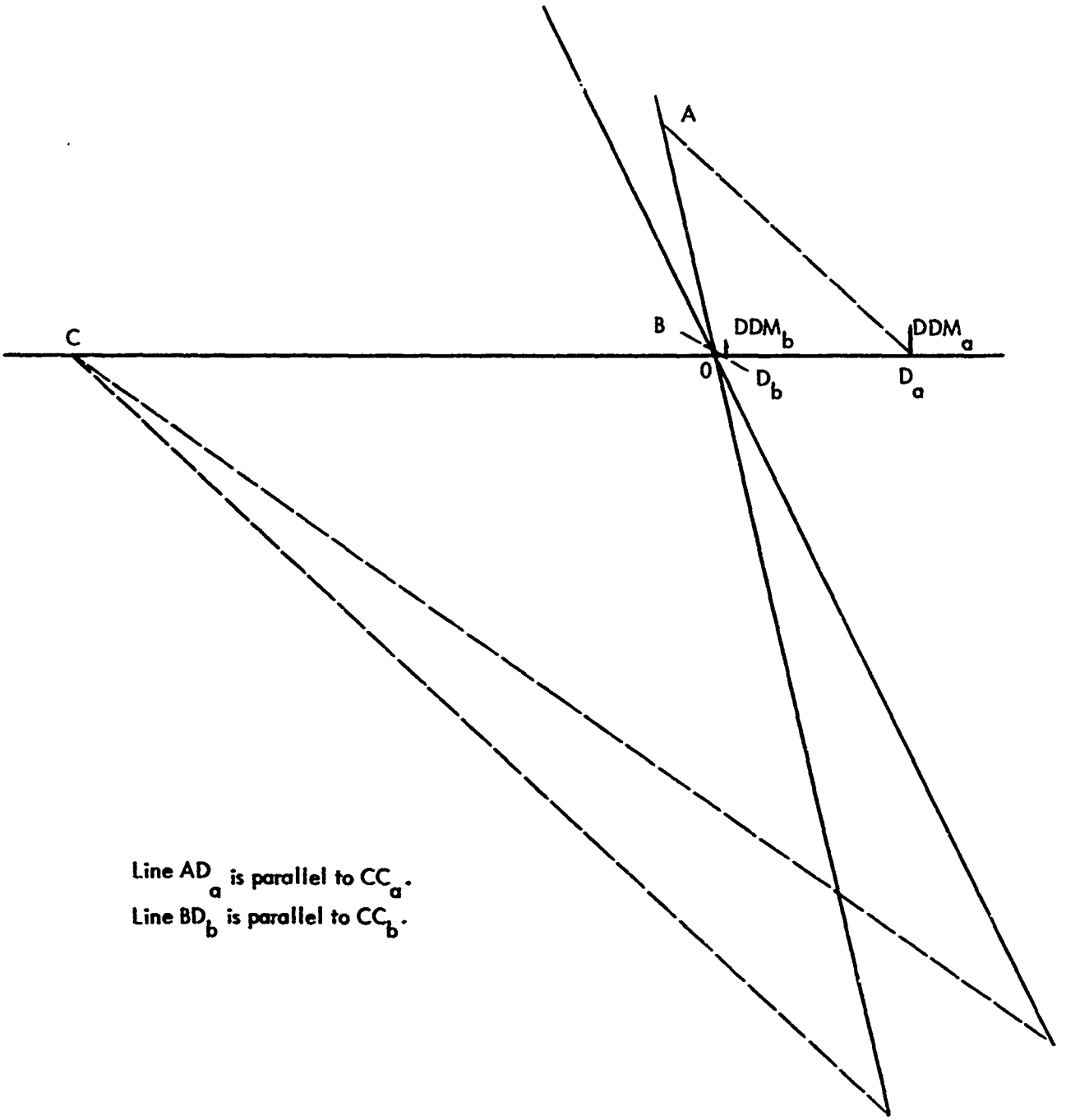

Figure 2-69. Construct for Showing Range of DDM for 80% Surface Reflection.

Figures 2-70 and 2-71 show the worst case phasor construction for the far-field (2000λ) at elevations of 100λ and 110λ respectively. Figures 2-72 and 2-73 present the corresponding total reflection cases.

By a slight simplification of the phasor geometry, one arrives at a manageable formulation based on the fact that, in the region of interest (from about 1.4° to 4.2°) in the far-field, the carrier phasors are reinforcing and thus the circle of uncertainty produces a reasonably small range of carrier phasor angles. In the region of the far-field the resultant of the carrier phasors and the resultant of the sideband phasors are nearly coincident in direction except at the glide path (DDM null) where the sideband phasors must either cancel or reverse direction (thereby cancelling their projection by passing through the normal to the carrier resultant). In either case the following approximations are valid.

Figure 2-74 indicates the geometry involved. Figure 2-74a is drawn for the case of total reflection at the snow surface. This simply projects the resultant of the sideband phasors on its own direction which is nearly that of the carrier, since in the far-field, the argument of the cosine term in Equation (2.106) is nearly zero. Figure 2.74b shows that the term $2 \sin \pi (\psi_4 - \psi_1)$ must be modified to $(1 + \rho) \sin \pi (\psi_4 - \psi_1) \pm (1 - \rho)$. For the worst cases the carrier phasors are similarly modified and lengthened or shortened by $(1 - \rho)$. Thus the worst cases DDM's become

$$2mA \frac{(1 + \rho) \sin \pi (\psi_4 - \psi_1) - (1 - \rho)}{(1 + \rho) \sin \pi (\psi_3 - \psi_2) + (1 - \rho)} \qquad (2.106)$$

and

$$2mA \frac{(1 + \rho) \sin \pi (\psi_4 - \psi_1) + (1 - \rho)}{(1 + \rho) \sin \pi (\psi_4 - \psi_1) - (1 - \rho)} \qquad (2.107)$$

Figures 2-75 to 2-80 are plots of the results obtained with Equations (2.106) and (2.107) in which the binomial approximation of $\psi_4 - \psi_1$ and $\psi_3 - \psi_2$ have been inserted to facilitate computation. ρ has been computed in each case using the usual formula and taking advantage of the small angle approximation, $\sin a \approx a$.

It seems apparent from these plots that the major and expected effect of snow cover is to cause the probable average path angle to rise. The possibility of a lowered path angle in the case of very little snow depth arises from the

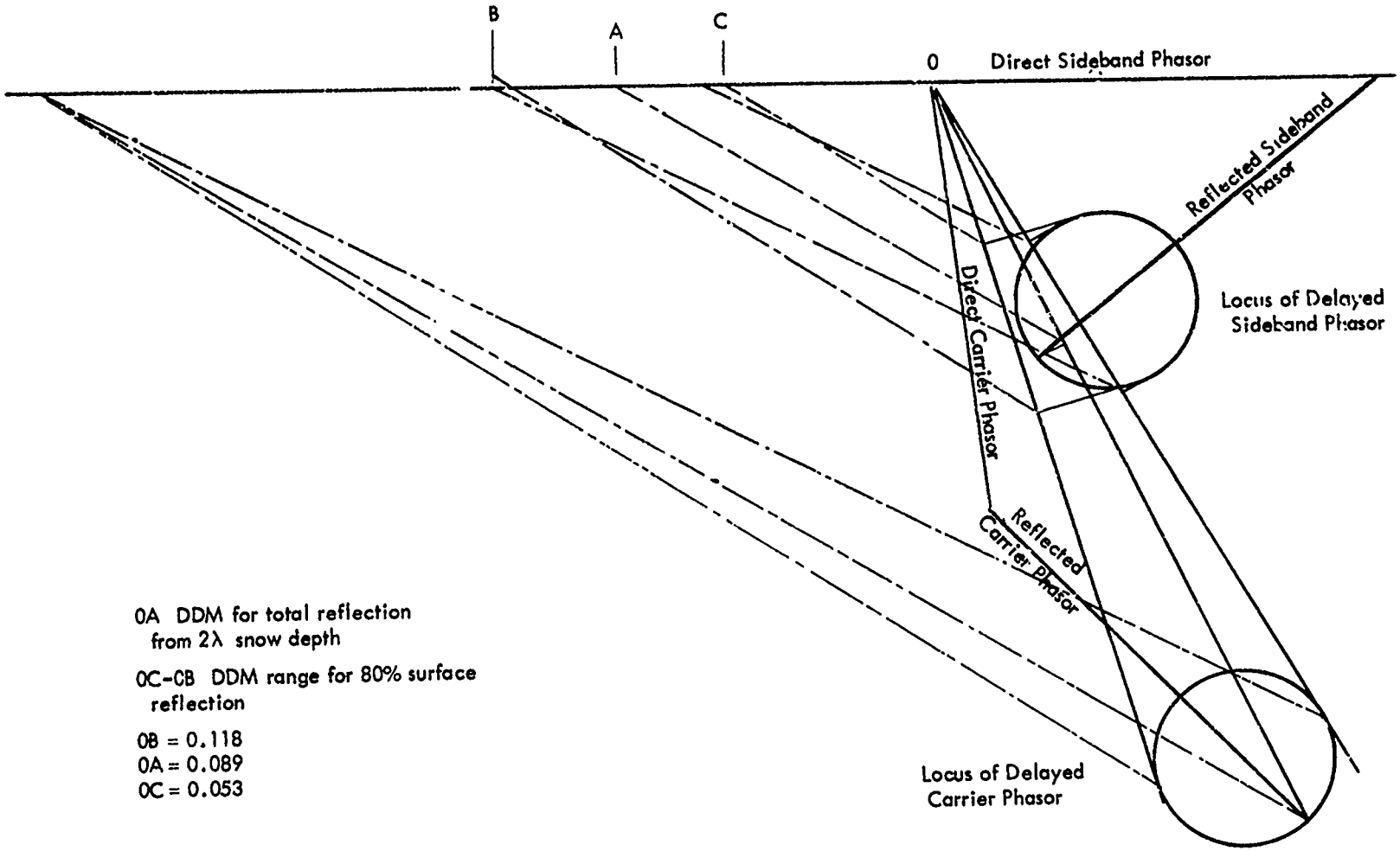

Figure 2-70. Phasor Construct Showing DDM Ranges with 2 λ Snow Depth at 2000 λ (Far-Field) and 100 λ Altitude (on Glide Path).

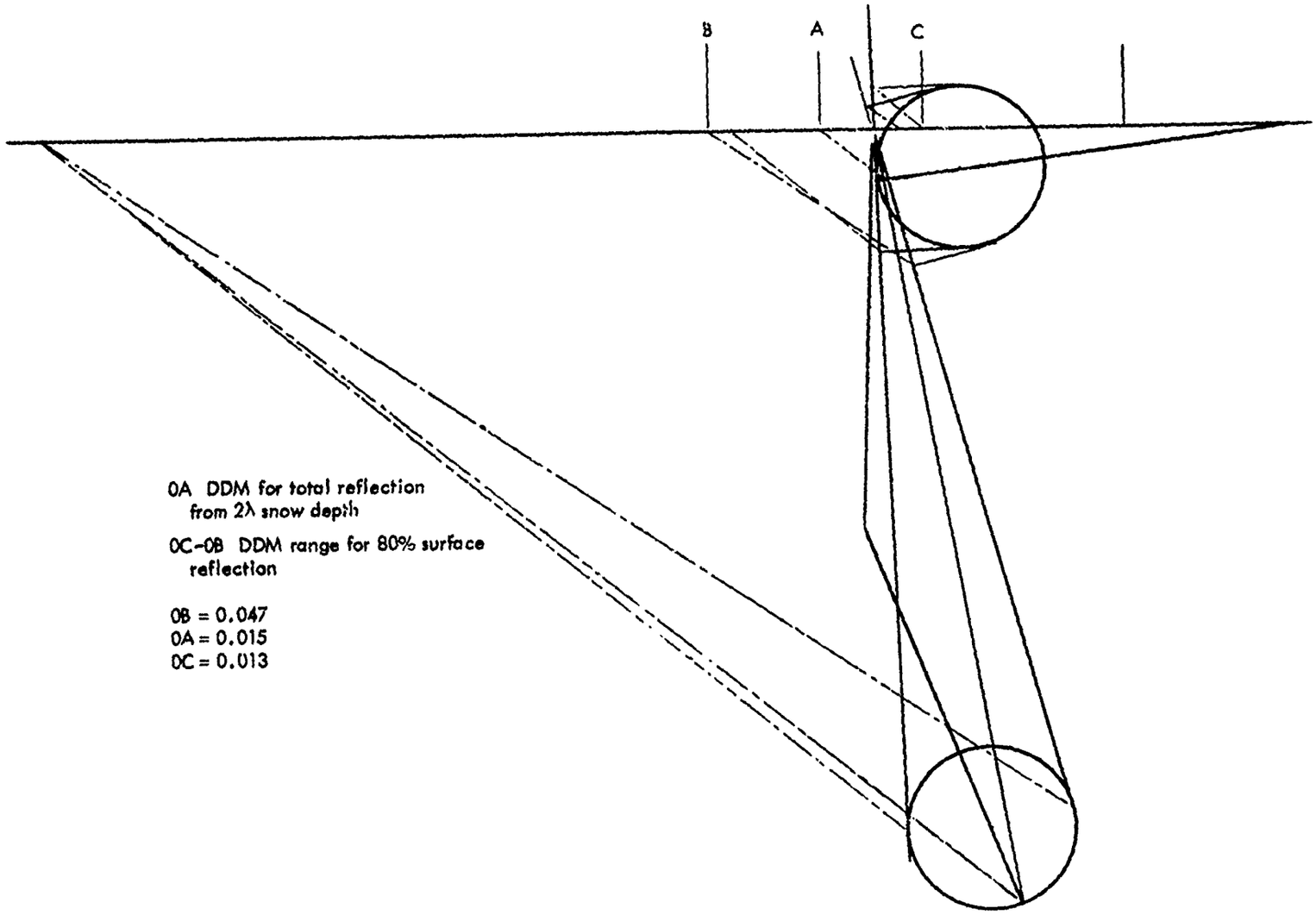

Figure 2-71. Phasor Construct Showing DDM Ranges with 2λ Snow Depth at 2000λ (Far-Field) and 110λ Altitude (.3° above Glide Path).

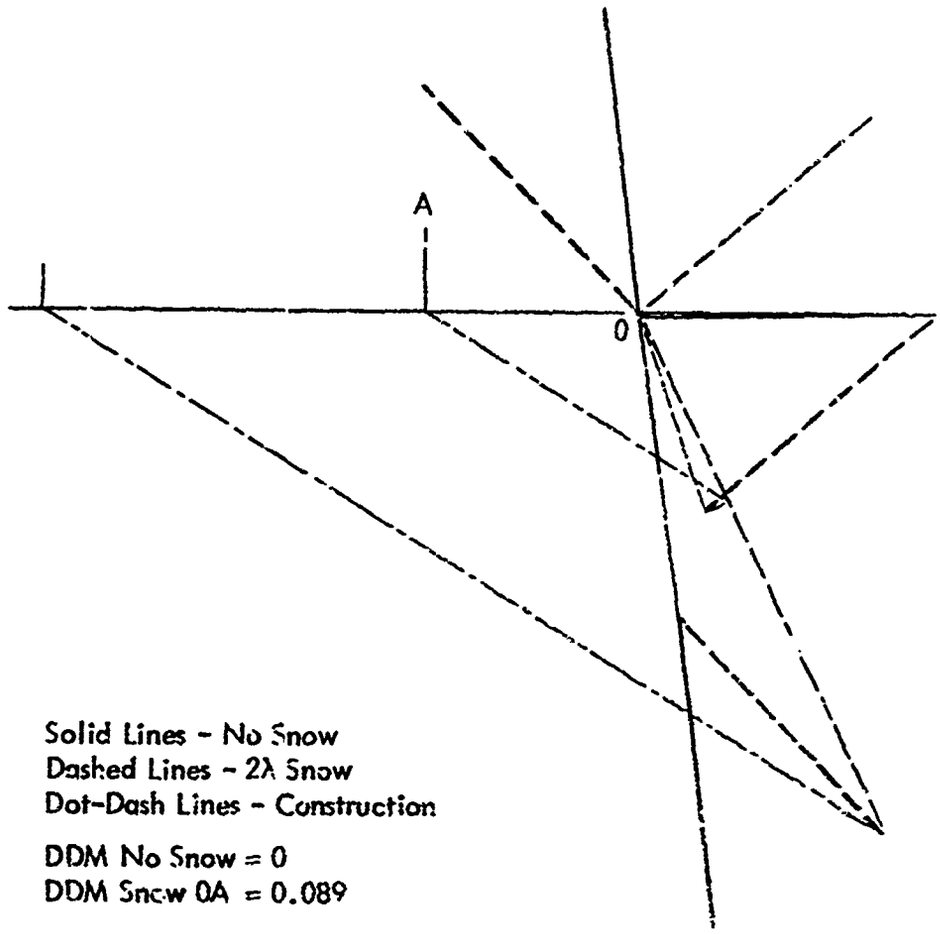

Figure 2-72. Phasor Construct for 2000λ (Far-Field) and 100λ Altitude (no Glide Path) with no Snow and with 2λ Snow Depth.

Solid Lines - No Snow
Dashed Lines - 2λ Snow
Dot-Dash Lines - Construction

CF parallels DE

CG parallels HK

DDM no Snow 0A = -0.071
DDM Snow 0B = 0.015

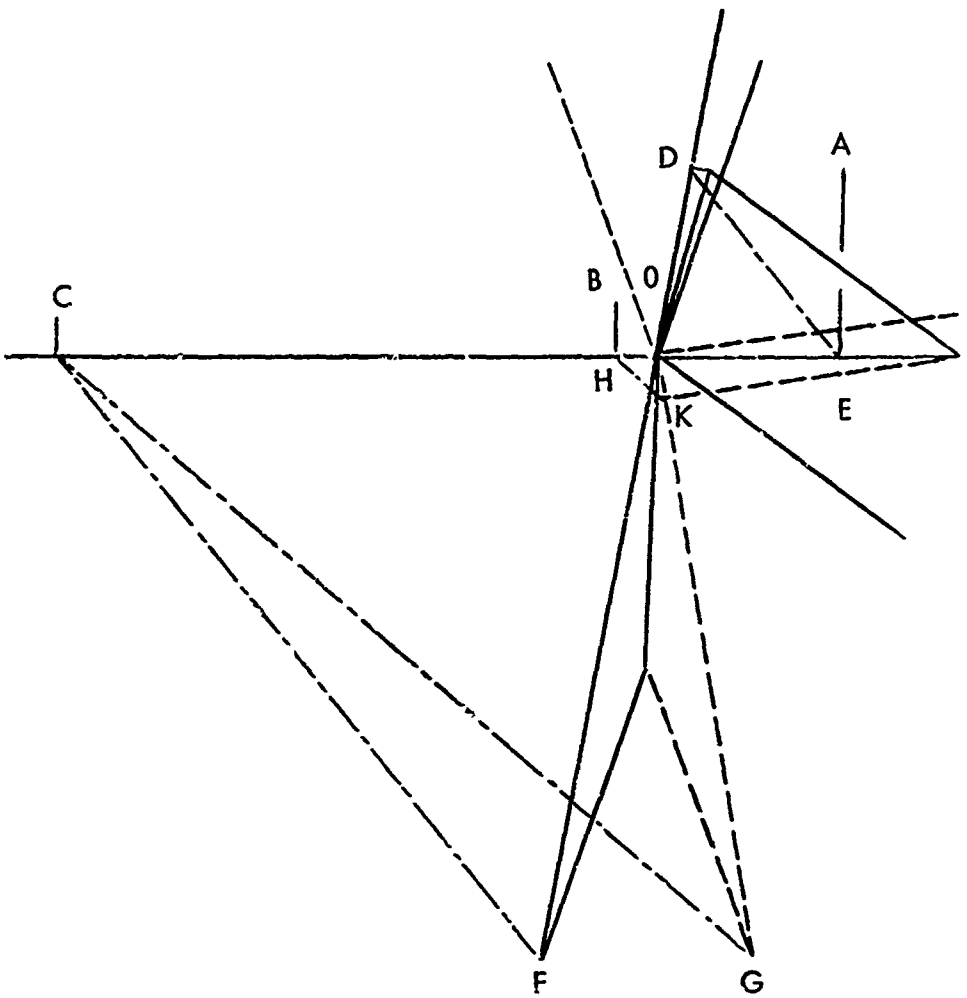

Figure 2-73. Phasor Construct for 2000λ (Far-Field) and 110λ Altitude (.3° above Glide Path) with no Snow and with 2λ Snow Depth.

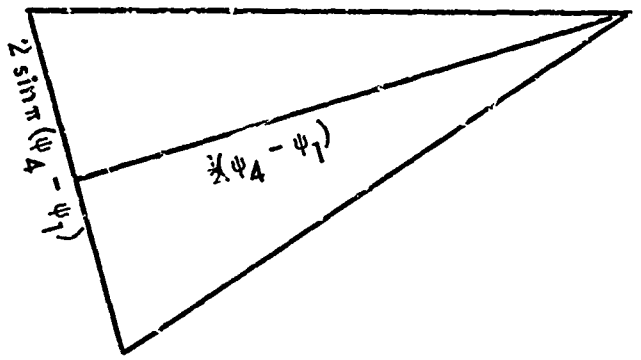

Figure 2-74a.

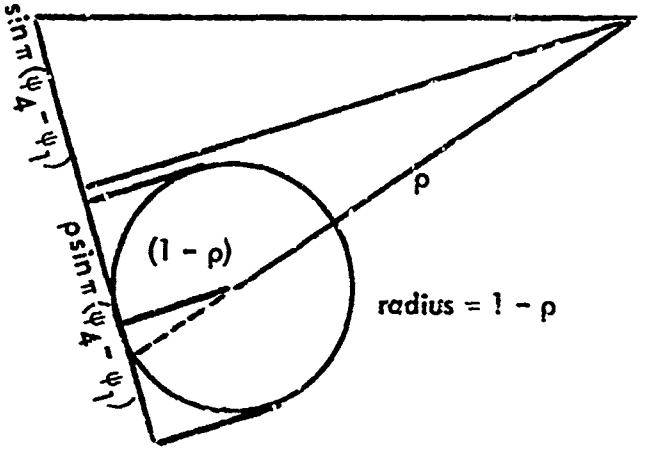

Figure 2-74b.

Figure 2-74. Simplified Sideband Phasor Construct for Worst Case.

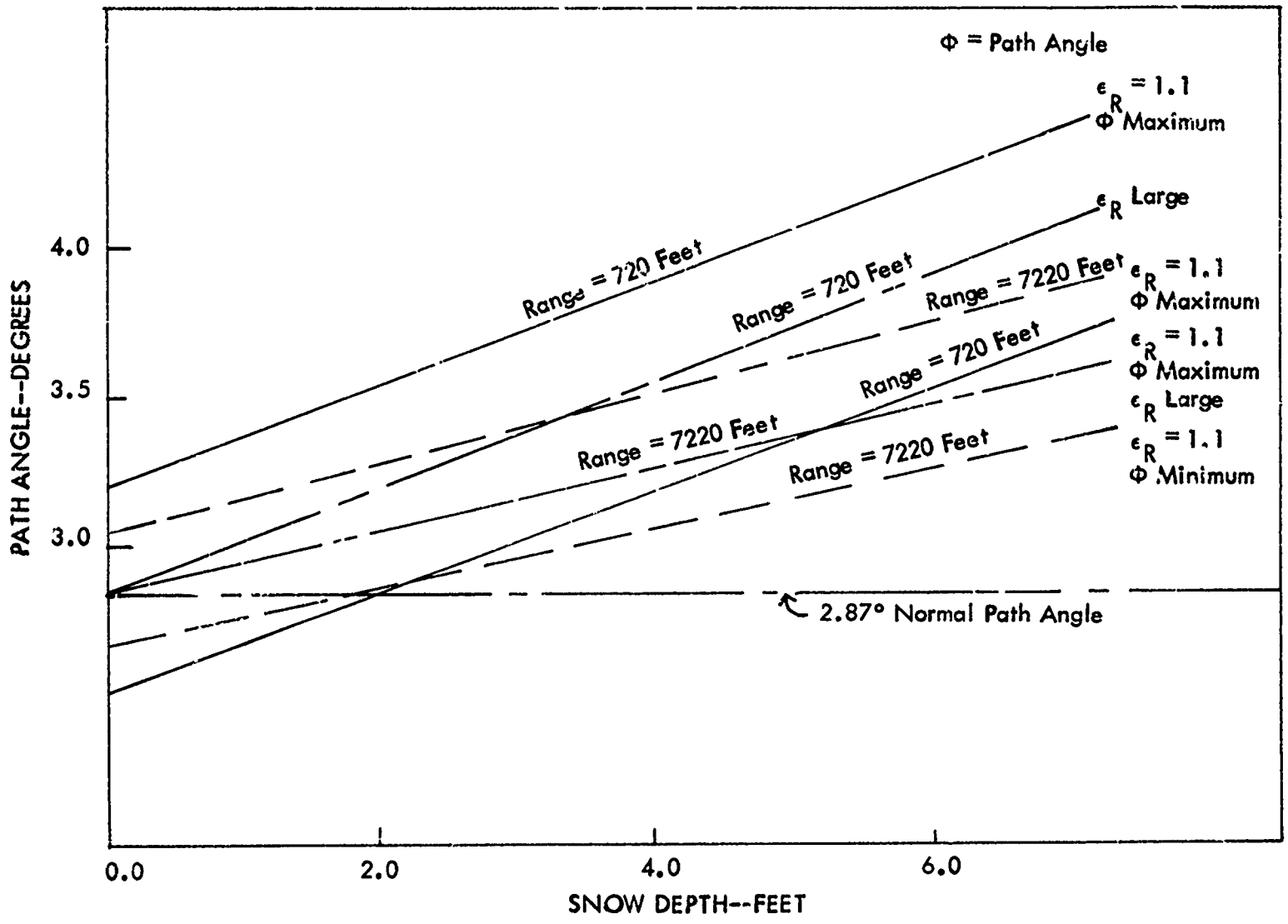

Figure 2-75. Path Angle versus Snow Depth--Worst Cases. $\epsilon_R = 1.1$

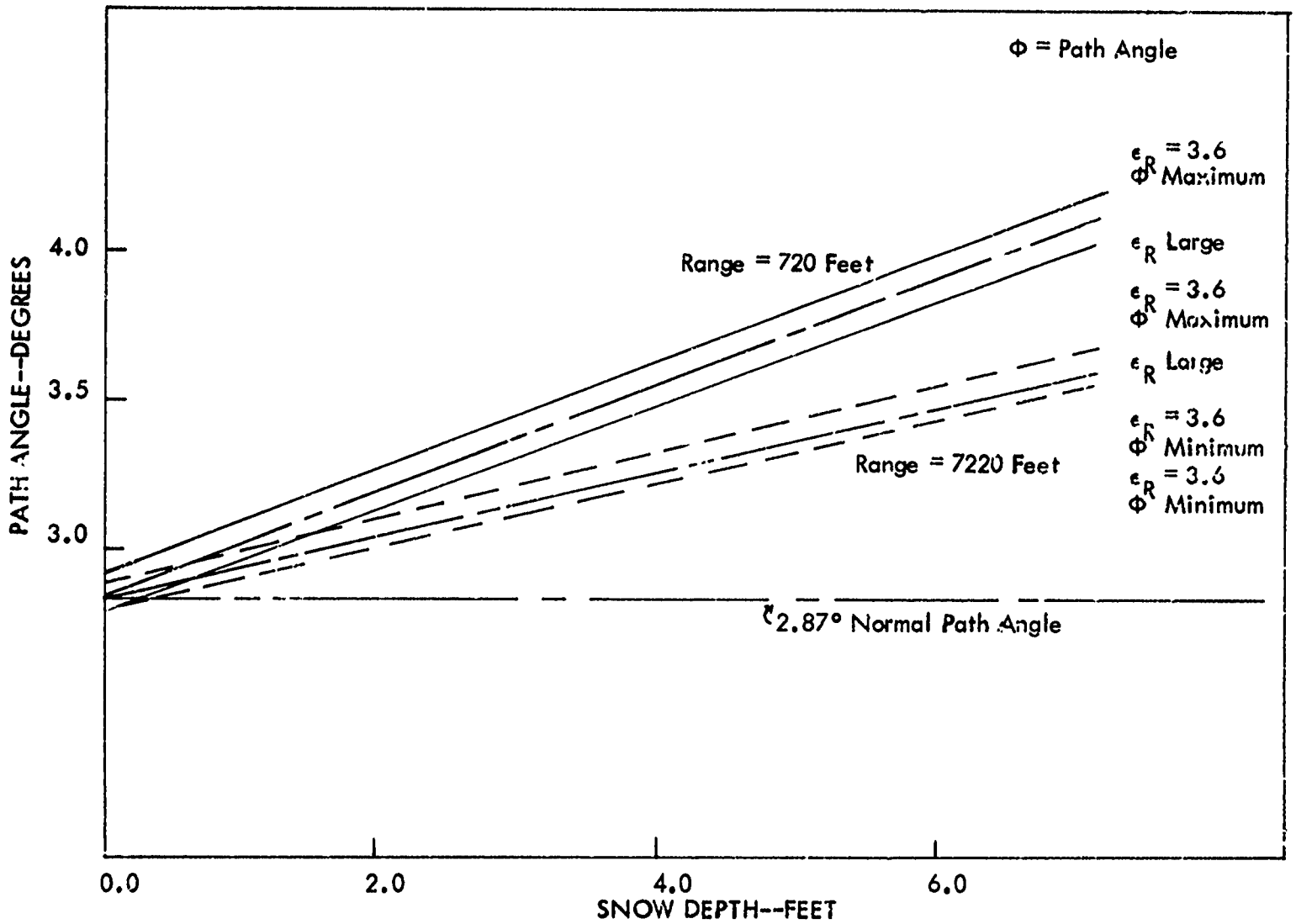

Figure 2-76. Path Angle versus Snow Depth--Worst Cases. ϵ_R = 3.6

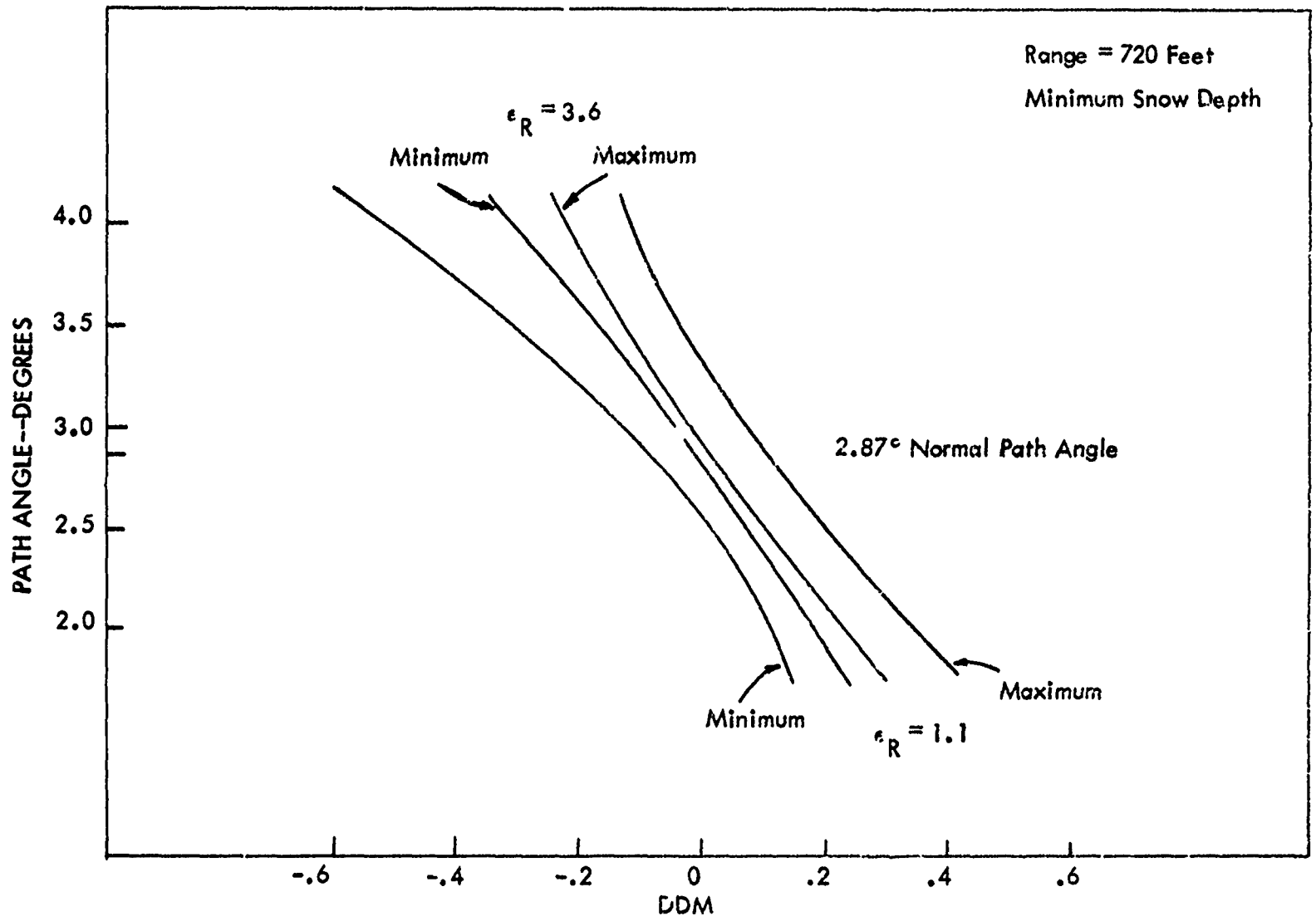

Figure 2-77. Path Angle versus DDM. Range = 720 Feet, Minimum Snow Depth.

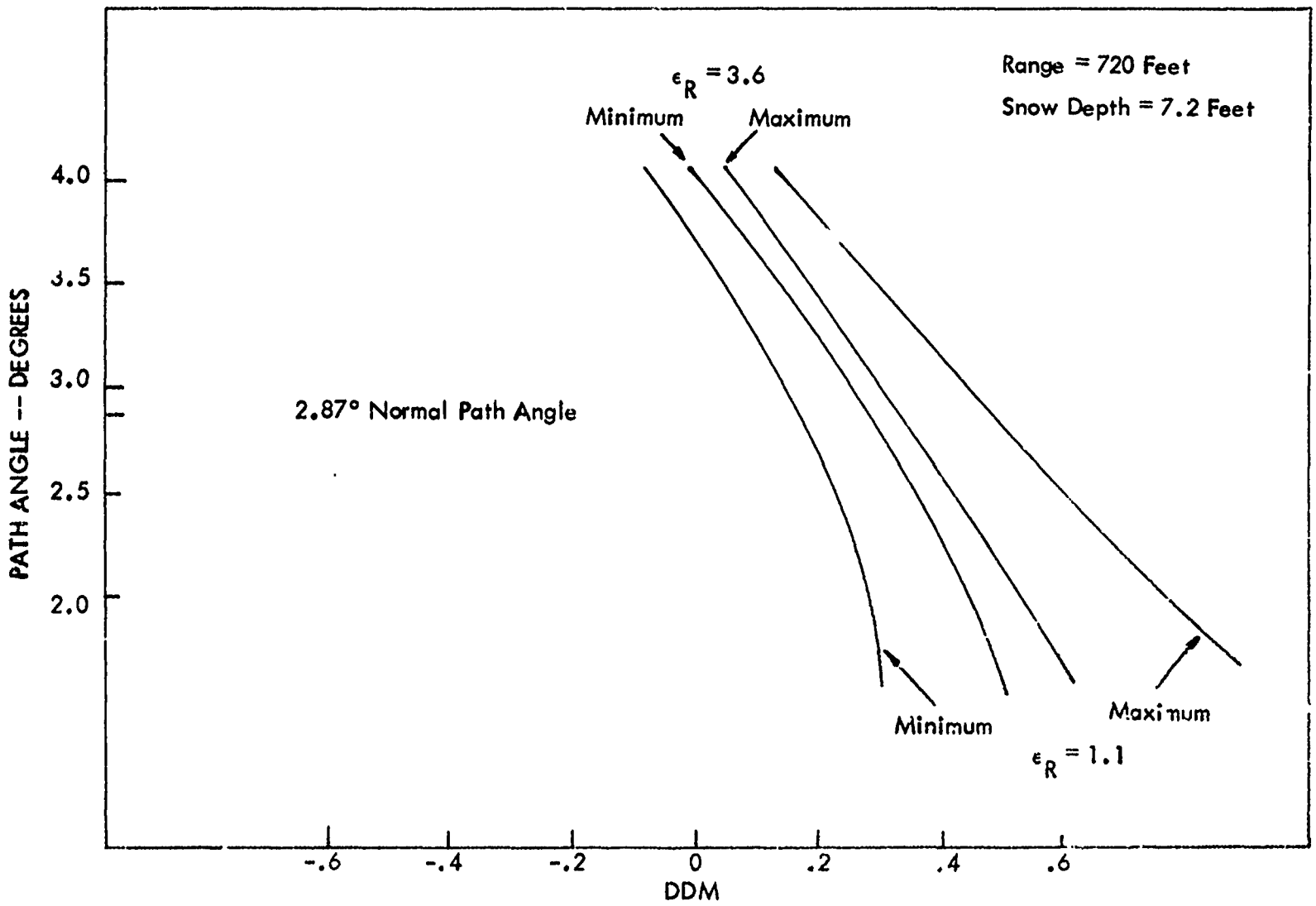

Figure 2-78. Path Angle versus DDM. Range = 720 Feet, Snow Depth = 7.2 Feet.

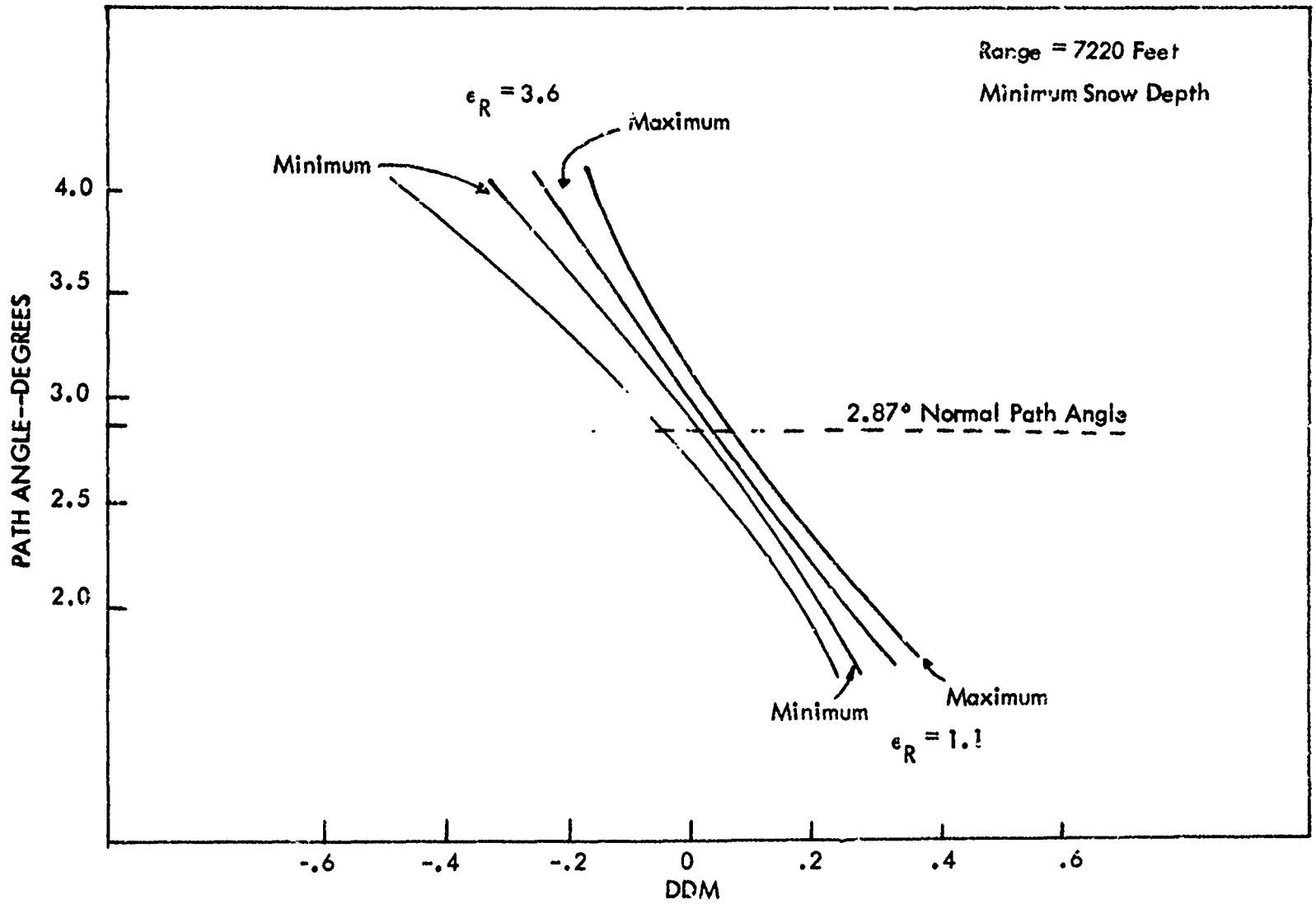

Figure 2-79. Path Angle versus DDM. Range = 7220 Feet, Minimum Snow Depth.

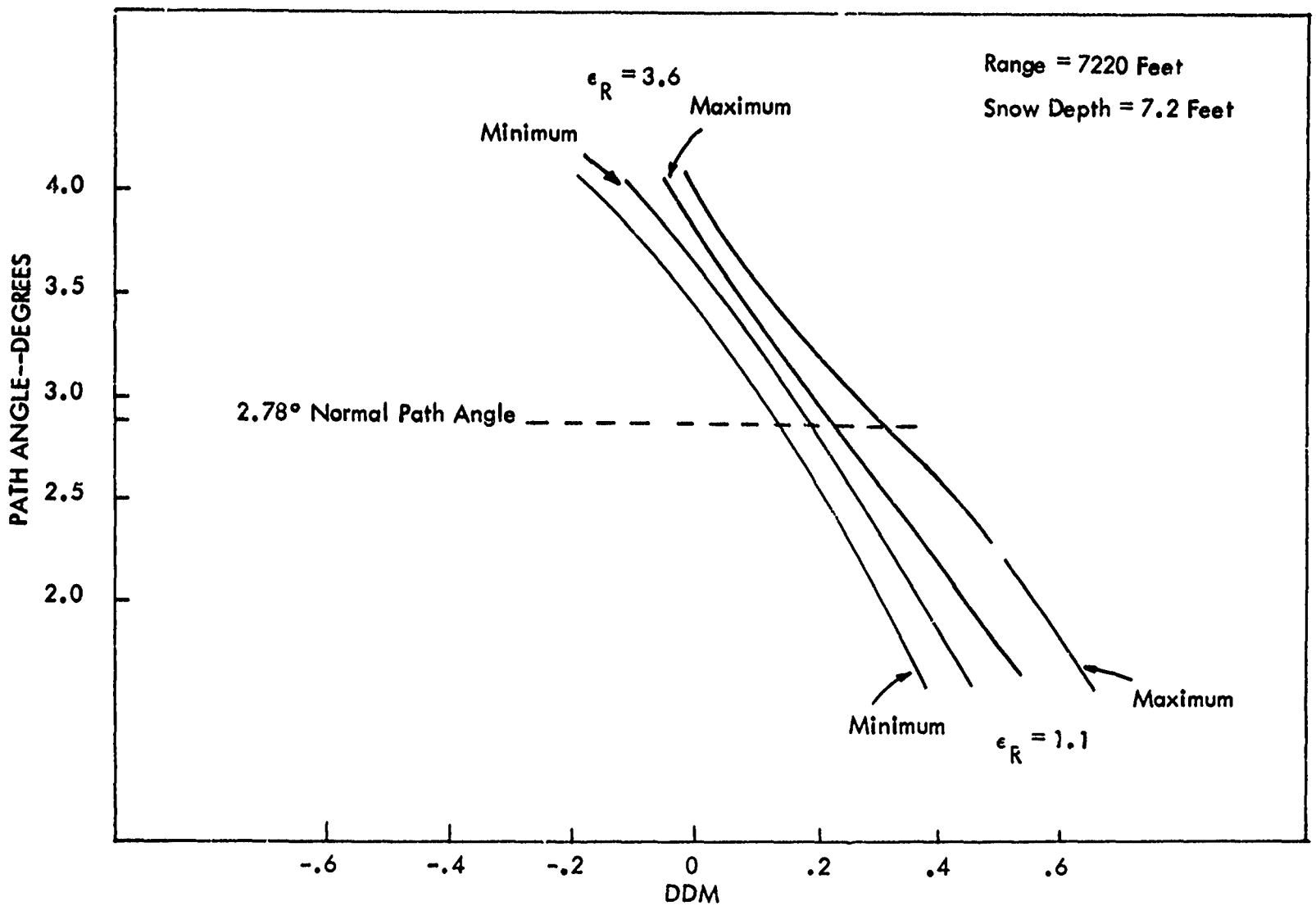

Figure 2-80. Path Angle versus DDM. Range = 7220 Feet, Snow Depth = 7.2 Feet.

mathematical assumption of complete disregard of the ground reflection coefficient under the snow as contrasted to the assumption of perfect reflection in the absence of snow. Actual measurements of ground conductances show quite low values, on the order of 10^{-4} to 10^{-6}, that for copper. From the transmission line analogy viewpoint this is still nea[illegible] a short circuit since the characteristic impedance of the air part of the line [illegible] so quite high, being proportional to the secant of the incidence angle. The plots should be considered of only academic interest in the zero depth limit.

It is evident that the probable effect is much worse at 720-foot range than at 7220-foot range. Because the approximations used were not sufficiently close for calculations at the 180° point they were not carried out for the monitor location, however, other calculations [4, see pp. 21-25] have shown the path angle changes to be more violent at the monitor than in the far-field.

The idea that the snow might act as a quarter wave transmission line, reflecting the short circuit impedance of the conducting ground as an open circuit at the snow surface, has been considered. Probable values of ground impedance (termination of the quarter wave line) are, however, considerably greater than zero and may be quite comparable to the characteristic impedance of the snow. This coupled with the extremely high impedance of the air line ($\eta \sec \theta$) would lead one to discount the possibility of resonant effects, except perhaps with snow overlying salt water. This is clearly an impractical case.

c. Recommendations. Even though calculations and measurements suggest that moderately deep snow of reasonable dielectric constant will not lower the path angle i[illegible] e far-field, simply disregarding the near-field monitor under such conditions is ne[illegible]r a satisfactory nor a satisfying solution. A different system of monitoring more closely related to the far-field condition is needed.

2. Measurements of Far-Field Glide Path Angles at Sites with Heavy Snow Cover

a. Introduction and Background. Acquisition of accurate, meaningful data on ground-plane, snow-cover effects on the glide-path angle in the far field is admittedly expensive and time consuming. Nevertheless the dearth of such data and the critical need for it dictated that an effort be made to acquire some to document quantitatively what effects may be taking place during times when snow covers the ground.

Two approaches have been considered feasible for collecting the needed information. One is through the use of probes mounted on a high tower simulating an aircraft in space. This provides a continuous record of changes which may take place during periods when snow conditions are changing. The second is through the use of an aircraft for making spot checks of path angle.

Although a far-field, high-tower monitoring system has been in operation for five years at Ohio University the limited amounts of snow which accumulate in Athens have provided only one good opportunity to obtain significant data. This was reported in Technical Report EER 5-7. During this reporting period no significant snows fell. In an attempt to collect some data a special series of flights were made into Michigan, Wisconsin, and Minnesota and northern Ohio. A report of these results follows. Plans were also made for installing a far-field tower monitor site in the Michigan snow belt next season.

Results of the measurements indicated that snow effects were negligible at the sites visited. Maximum dispersion from previously recorded FAA data was 0.06 degree and this was an increase in angle. In many cases near-field monitors were approaching or had just returned inside alarm limits. The following Table 2-11. summarizes the data.

FACILITY	GLIDE PATH ANGLES			Average Snow Depth	Specific Volume	% Monitor Alarm Limits
	Published	FAA Measured	Ohio University Measured			
Grand Rapids, Michigan (GRR)	2.50°	----	2.51°	9"	.22	-16% P
Green Bay, Wisconsin (GRB)	2.65°	2.74° LR	2.69°	10"	.29	+16% P
Appleton, Wisconsin (ATW)	2.50°	2.54° LR	2.52°	18"	.38	+80% P
Duluth, Minnesota (DLH)	2.62°	2.62° LR	2.65°	3"	---	0%
Minneapolis, Minnesota (MSP)	2.50°	2.57° RTT	2.55°	2"	---	0%
Minneapolis, Minnesota (APL)	2.50°	2.50° LR	2.50°	10"	.30	0%
Rochester, Minnesota (RST)	2.75°	2.81° LR	2.78°	[illegible]	.34	+64% P
Madison, Wisconsin (MSN)	2.50°	2.57° LR	2.59°	2"	.33	0%
Milwaukee, Wisconsin (GMF)	2.9[illegible]°	2.94° LR	2.99°	8"	.41	+60%
Milwaukee, Wisconsin (MKE)	2.75°	2.71° RTT	2.76°	1"	---	+40% P
Mansfield, Ohio (MFD)	2.73°	----	2.78°	15"	.20	+17% P * +99% W
Akron-Canton, Ohio (CAK)	2.95°	----	2.99°	7"	.23	-17% P
Youngstown, Ohio (YNG)	2.98°	3.05°	3.08°	10"	---	+35% P
Columbus, Ohio (CMH)	3.00°	3.07° RTT	3.13°	1"	.9 Est.	+75% P

NOTES: -P Path Low, +P Path High, -W Path Narrow, +W Path Wide, LR--Level Run, RTT--Radio Theodolite, * Width Monitor on Edge of Alarm. Ohio University measured width by approaches 75 microampere above and below path - .72°.

Table 2-11. Summary of Glide Path Measurements.

On the basis of data obtained from a compilation of glide path monitor data given in Ohio University report EED 1-5, "Glide Path Summary", September 1968, [8] 224 glide path sites in the United States, were placed in one of four groups according to the following criteria:

I Continuous Deep Layers of Snow

II Intermittent Deep Layers of Snow

III Occasional Significant Layers of Snow

IV No Significant Snow Effects

Sites belonging to the above four groups are given in Appendix B.

The basis for assignment to a specific group were the comments made on the monitor data report generated by the facilities personnel and subjective evaluation by the Ohio University and FAA ILS staffs. The groupings are certainly not indisputable for there were many sites which seemed to be borderline cases.

During the month of January 1971 data were obtained concerning existing official snow depths of numerous stations. On the basis of this information ten sites were selected for making measurements of the effect of snow on the glide path angle. These sites were:

1. Battle Creek, Michigan
2. Lansing, Michigan
3. Grand Rapids, Michigan
4. Muskegon, Michigan
5. Green Bay, Wisconsin
6. Duluth, Minnesota
7. Minneapolis, Minnesota
8. Rochester, Minnesota
9. Madison, Wisconsin
10. Milwaukee, Wisconsin

Battle Creek and Lansing were overflown because of the minimal snow depths that existed on the days the measurements were to be made. Muskegon was omitted because weather conditions were below IFR minimums and forecast to remain for some time. Minneapolis and Milwaukee each had two glide slope sites all of which were measured.

Immediately following completion of the first data collection trip a second was made because of a sudden deep snow fall in the Ohio area which alarmed monitors at Mansfield and Akron-Canton. Three glide paths were measured, viz., Mansfield,

Ohio, Akron-Canton, Ohio, and Youngstown, Ohio.

Approximately one week later measurements were made at Columbus, Ohio, after notification was received that the path was at alarm due to slush covering the ground.

A total of eight days was required to collect all of the data on the 14 facilities. This included measurement and travel time. At least one measurement was made each day and on one day in Ohio three measurements were made thus showing the potential efficiency of this type of data collection.

b. Measurement Technique. A Beechcraft Bonanza 35 was selected for use in carrying the airborne probe because of its instrument capability, relatively low cost, maneuverability, personnel and equipment carrying capability, speed and availability. The one-man crew requirement provided further economics during the travel. The stability of the DC-3 flying laboratory which was not critical for the measurements planned was sacrificed.

The measurements were made as follows. Through prior arrangements, personnel from the FAA Airways Facilities Office met the aircraft when it arrived at the respective airports. Through their cooperation transportation of the necessary equipment and the person who operated the theodolite to the glide path site was accomplished where the theodolite and radio equipment were prepared for tracking. Snow samples and depth measurements were obtained.

Simultaneously the aircraft was prepared for measurements. An additional glide path receiver, Narco UGR-2A, was installed temporarily using a separate Aircraft Radio Corporation A-13B antenna and readouts. Course deviation indications (CDI) were presented on a wide-view Model 1329, 4½ inch, 25-0-25 microammeter converted to read 150-0-150 microamperes while presenting a 1000 ohm load to the circuit.

A meter to read flag current was also installed. These meters were mounted on a swivel and pivot to permit positioning to eliminate paralax error. A Wilcox 800A glide path receiver operating with a conventional CDI display was used for cross checking.

Calibration of the glide path receivers was accomplished prior to departure using a Boonton 232A signal generator equating 2db to 78 microamperes. The zero db value was checked using an oscilloscope.

Scale divisions approximately 5/32 inch wide permitted resolving at least two microamperes which under standard conditions represents 0.009° of glide path angle.

A standard ILS approach was flown and when the aircraft was located precisely on course (zero DDM), a tone was transmitted to the theodolite operator.

The theodolite was positioned in accordance with FAA Order 8240.20. This insured compatibility with previous FAA readings and allowed use of a prepared pad at many sites. A Warren-Knight Model WE-83 theodolite commonly used in the FAA radio telemetering theodolite system was used for tracking. Resolution with this instrument is 0.02° with interpolation allowing at least 0.01° to be read. It is fortuitous that the resolving capability of the airborne and ground-based equipment is compatible and that these are very adequate for ascertaining the glide path values.

A Bayside Model 990 portable VHF receiver was used to receive the tones transmitted from the aircraft. When a tone was received the reading of the theodolite position on the aircraft was recorded. The numbers obtained from two to three runs were averaged. Typical dispersions of readings were 0.02°.

Between flight runs the station monitor values were recorded. At some time during the visit to the facility, snow depth measurements were made of the area affecting the far-field. These were taken for the purpose of preparing a map of the snow conditions. Experience has clearly shown that in many instances there are great variations in conditions from one point to another in the reflecting areas. Snow density measurements were made by taking a sample of snow and obtaining a specific volume reading.

Numerical values obtained from these readings are presented next.

c. Discussion of Data . In Table 2-11 a summary of the data obtained from the measurements at the 14 ILS locations is given. The following are discussions of the special cases.

It is important to note the consistency between the Ohio University measured glide path angle and the FAA measured glide path angle. Additionally, at Appleton, Wisconsin; Rochester, Minnesota; Milwaukee, Wisconsin, and Mansfield, Youngstown, and Columbus, Ohio, the following was observed:

Appleton, Wisconsin
18" snow depth in monitor area
Monitor indicating 80% toward alarm--path high
Measured path angle--2.52°
Published path angle--2.50°
FAA measured path angle--2.54°

The facility was out of service for path alarm. As indicated by the above data the path angle is normal and a classic case of monitor sensitivity to snow cover.

Rochester, Minnesota
8" snow depth in monitor area
Monitor indicating 64% toward alarm--path high
Measured path angle--2.78°
Published path angle--2.75°
FAA measured path angle--2.81°

Monitor indicated excessive path high condition.

Milwaukee, Wisconsin (GMF)
8" snow depth
Monitor indicating 66% toward alarm--path high
Measured path angle-2.99°
Published path angle--2.93°
FAA measured path angle--2.94°

Monitor indicated excessive path high condition.

Mansfield, Ohio
18" snow depth
Monitor indicating edge of alarm path width narrow
Measured path angle--2.78°
Measured low 75 μa angle--2.43°
Measured high 75 μa angle--3.15°

Facility out of service for an excessively narrow path. Measured data indicates path width normal. Excessive monitor response to snow.

Youngstown, Ohio	9" snow in monitor area 8-12" snow in Far-Field--level Monitor indicating 35% toward alarm--path high Measured path angle--3.08° Published Path angle--2.98°

Monitor reading 35% high, path 50% high over published angle.

Columbus, Ohio	1" ice and water mixture Monitor indicating 75% toward alarm--path high Measured path angle--3.125° Published path angle--3.00° RTT angle--3.07°

Monitor indicating excessive path high condition.

A graph shown in Figure 2-81 illustrates the great inconsistencies in simply relating path angle with snow depth. The knowledge of the dielectric character and the detailed lateral variations of snow over the reflecting surface is essential for accurate predictions.

The detailed snow data from the sites visited are presented in Apprendix C.

d. Conclusions and Recommendations. Several conclusions on snow effects can be drawn from the measurements made at the 13 ILS glide path sites.

All measured far-field glide path angles were well within tolerance. Monitors are indicating excessive sensitivity to existing snow conditions and in the cases of Appleton, Wisconsin, Mansfield, Ohio and Columbus, Ohio, undoubtedly caused unnecessary facility shut down.

The measurement technique employed for this work proved to be an extremely efficient and accurate method of determining far-field glide path angle. General tolerances can be expected to be 0.02° and under some conditions as small as 0.01°.

The recommendation is that the FAA continue to collect data on far-field path positions. Although a variety of conditions have been measured, caution must be exercised in generalizing from the small amount of data now on hand.

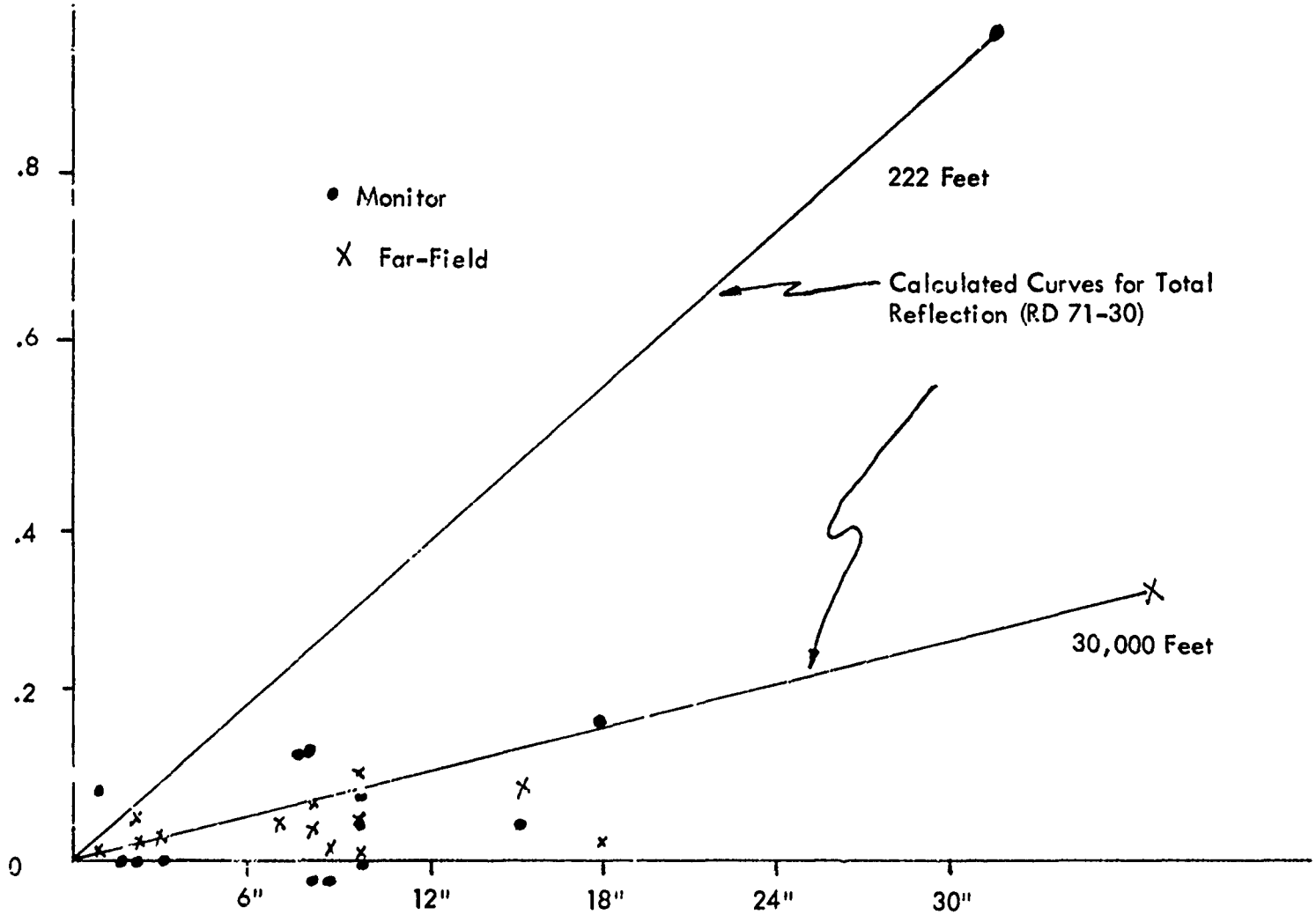

Figure 2-81. Measured Path Indications for Various Snow Depths.

3. Snow Site Implementation with Far-Field Monitoring

In order to collect glide path angle and width data on a continuing basis and with reasonable certainty of existence of significant snow on the ground plane implementation of a special glide path site in Michigan was undertaken. Criteria for site selection were high probability of deep snows, cycling of snow conditions, site to subtend 3.0° angle with tower, flat ground plane, high tower availability, reasonable physical access, and available power. Other factors affecting glide path performance were considered.

A search was made and an excellent location found 20 miles east of Muskegon and 40 miles north of Grand Rapids near Ravenna. A [illegible]-foot tower belonging to WZZM-TV Television Company provided the focus for site selection. WZZM-TV officials graciously offered their tower and building facilities at no charge for use in this project. A further benefit was obtained when a site was selected and the owner of the farm, Mr. Robert Stream, offered the use of it at no charge together with the use of his private air strip. In combination these contributions provided the base for establishing three excellent glide path facilities, viz., capture effect, sideband reference, and capture effect, sideband reference, and capture effect glide path systems.

A well-instrumented van obtained from FAA NAFEC was moved onto the Stream farm which provided 2000 feet of flat ground in front of the array towards the WZZM-TV tower 3 miles distant. Two specially fabricated eight-element yagi antennas, one of which is shown in Figure 2-82, were mounted at 614 feet and 829 feet elevations on the tower to subtend angles from the site of 2.3° and 3.0° respectively. These are to represent the clearance and path angles.

The capability to radiate three different type glide path system signals is provided through the use of two towers spaced approximately 50 feet apart. See Figure 2-83. The capture effect and null reference systems made use of two common antennas and share the same mast. Change over from system to system is accomplished with relays switching the correct transmission lines and antennas into the transmitting system. Two TU-7 transmitters are available, one being on a standby basis.

Each of the systems was flight checked to set parameters and determine if proper path performance was being obtained. The best path performance was obtained from the capture effect system with ± 12 microampere roughness. Difference in path angles measured with the tower and aircraft was found to be 0.03°. Minimum flight checking was required because the high tower was invaluable in setting path width and phasing.

Near-field monitoring is the most involved aspect of the system. The capture effect system has integral, analog monitoring which gives a quantitative

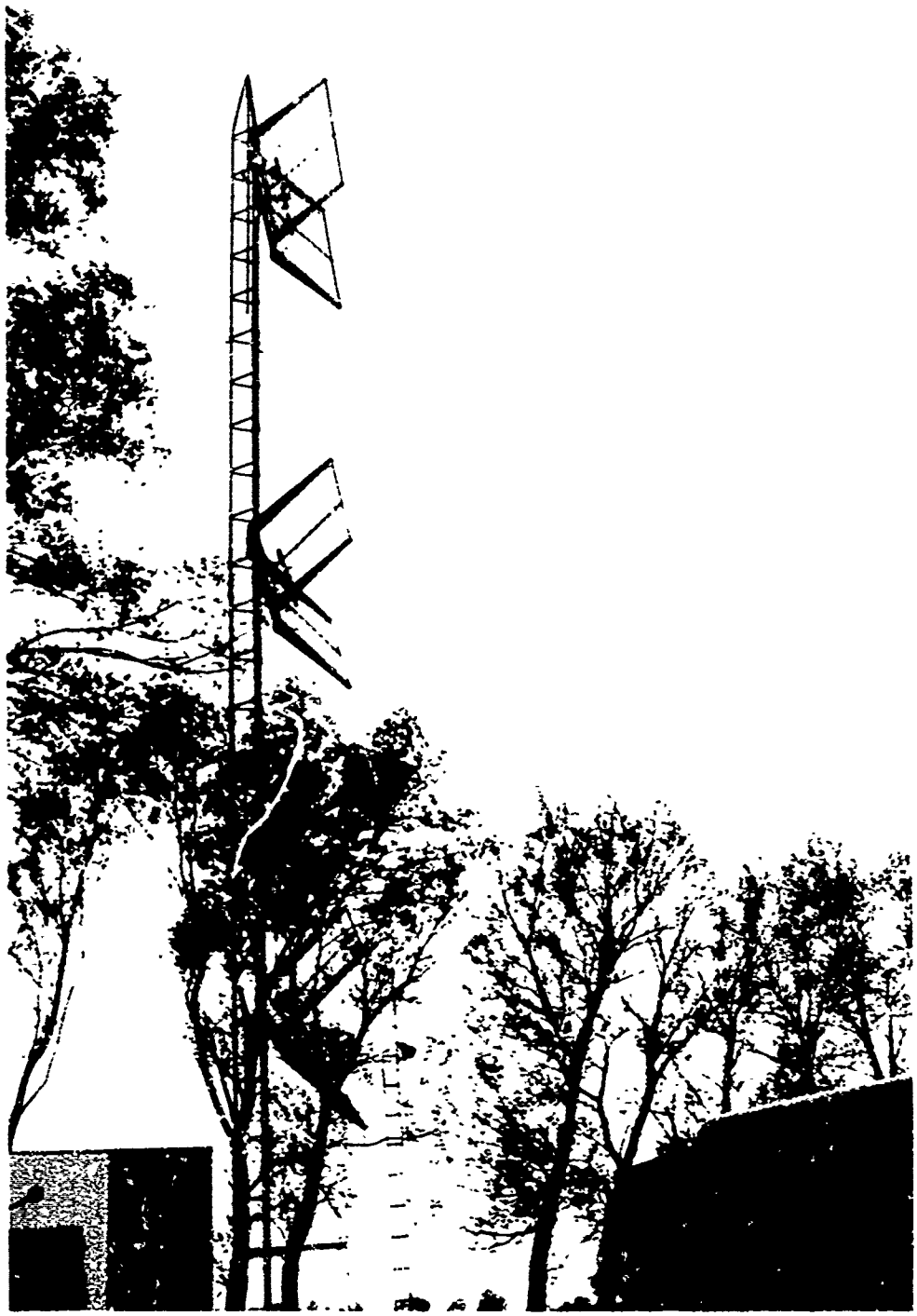

Figure 2-82. Capture Effect Glide Slope Array Used for Environmental Testing at the Michigan Snow Site. Integral Monitoring is Being Effected with the Coupling Probes not Visible in the Corner Reflector Antenna Units. A Sideband Reference Array for Snow Experiments is Visible in the Background.

Figure 2-83. Snow Monitor Site North of Grand Rapids, Michigan. View is Looking out From the Transmitting Arrays, the Sideband Reference Antennas are Shown on the Left. Near-Field Monitors are also Shown. There is Approximately 2,000 Feet of Flat, Unobstructed Terrain in the Direction of the Far-Field Monitor Tower Which has Been Retouched in the Photograph for Clarity. This Tower is 3 Miles Distant and Supports the Far-Field Clearance and Course Monitor Probes.

prediction of path angle and width. In addition, the conventional course monitor 303 feet in front of the array was installed. The null-reference system is monitored by a conventional 180-degree monitor, and the sideband-reference system has the usual near-field monitoring. A total of seven channels of near-field monitor data is available. A photograph of the near-field detectors is shown in Figure 2-84.

All near-field monitors togther with two channels of far-field data are recorded on Honeywell Electronik 17 dual pen machines at the rate of six inches of chart paper per hour. Backup recorders are in place in case of failures. All equipment was either GFE, excess property from GSA or that belonging to Ohio University.

Calibration of the systems is by use of a Boonton 232A referencing 2 db to 78 microamperes.

Receiving equipment used in monitoring is the standardized ARN18/R-322 except where detectors are available in the standard monitor systems.

Monitoring is in progress and during this reporting period the maximum snow depths has been seven inches and no siginificant effects on far-field path angle and widths have been observed.

Reproduced from best available copy.

Figure 2-84. Yagi Probe Antenna Which was Mounted on the 900-Foot WZZM-TV Tower for Monitoring Far-Field Path Angle. A Duplicate Antenna Was Used for Obtaining Path Width Data.

F. Glide Slope Integral Analog Monitor

Continuous measurements of the glide slope integral analog monitor performance are being made at the Grand Rapids, Michigan, snow site. Recordings are being made of the analogs of 3.0° and 2.3° angles and are compared with the recorded path in space. The effect of snow and other weather conditions will be identified using these continuous recordings of monitors. The combining circuits for the integral monitoring are shown in Figure 2-85. All coaxial cables feeding the combining hybrids are of equal electrical length within ± 2°.

The far-field monitors give an excellent opportunity for observing the characteristics of this integral monitor and soon specific faults will be introduced in the system and a comparison made between the high tower readings and the integral monitor response. Ultimately the complete list of faults suggested by the FAA (listed below) will be checked.

Fault List for Integral Monitor--Glide Path--Capture Effect

Fault # 1	Open Middle Antenna.
Fault # 2	Open Upper Antenna.
Fault # 3	Open Lower Antenna.
Fault # 4	Open Middle Antenna and Short APCU Port.
Fault # 5	Open Upper Antenna and Short APCU Port.
Fault # 6	Open Lower Antenna and Short APCU Port.
Fault # 7	Continuously Vary Phase to Middle Antenna. Record Far-Field and Integral Monitor Response every 1° with Airborne Verification every 15° to 45°. Take Far-Field and Integral data to 90°.
Fault # 8	Continuously Vary Phase to Upper Antenna. Record Far-Field and Integral Monitor Response every 1° with Airborne Verification every 15° to 45°. Take Far-Field and Integral data to 90°.
Fault # 9	Continuously Vary Phase to Lower Antenna. Record Far-Field and Integral Monitor Response every 1° with Airborne Verification every 15° to 45°. Take Far-Field and Integral data to 90°.
Fault #10	Vary Attenuation to Middle Antenna in one DB steps to 5 DB.
Fault #11	Vary Attenuation to Upper Antenna in one DB steps to 5 DB.
Fault #12	Vary Attenuation to Lower Antenna in one DB steps to 5 DB.
Fault #13	Remove Clearance Transmitter from APCU Port.
Fault #14	Short Clearance Transmitter APCU Port.
Fault #15	Reduce Sideband Power 3 DB.
Fault #16	Repeat Faults # 1 through # 12 with Clearance Transmitter Removed and APCU Port Terminated

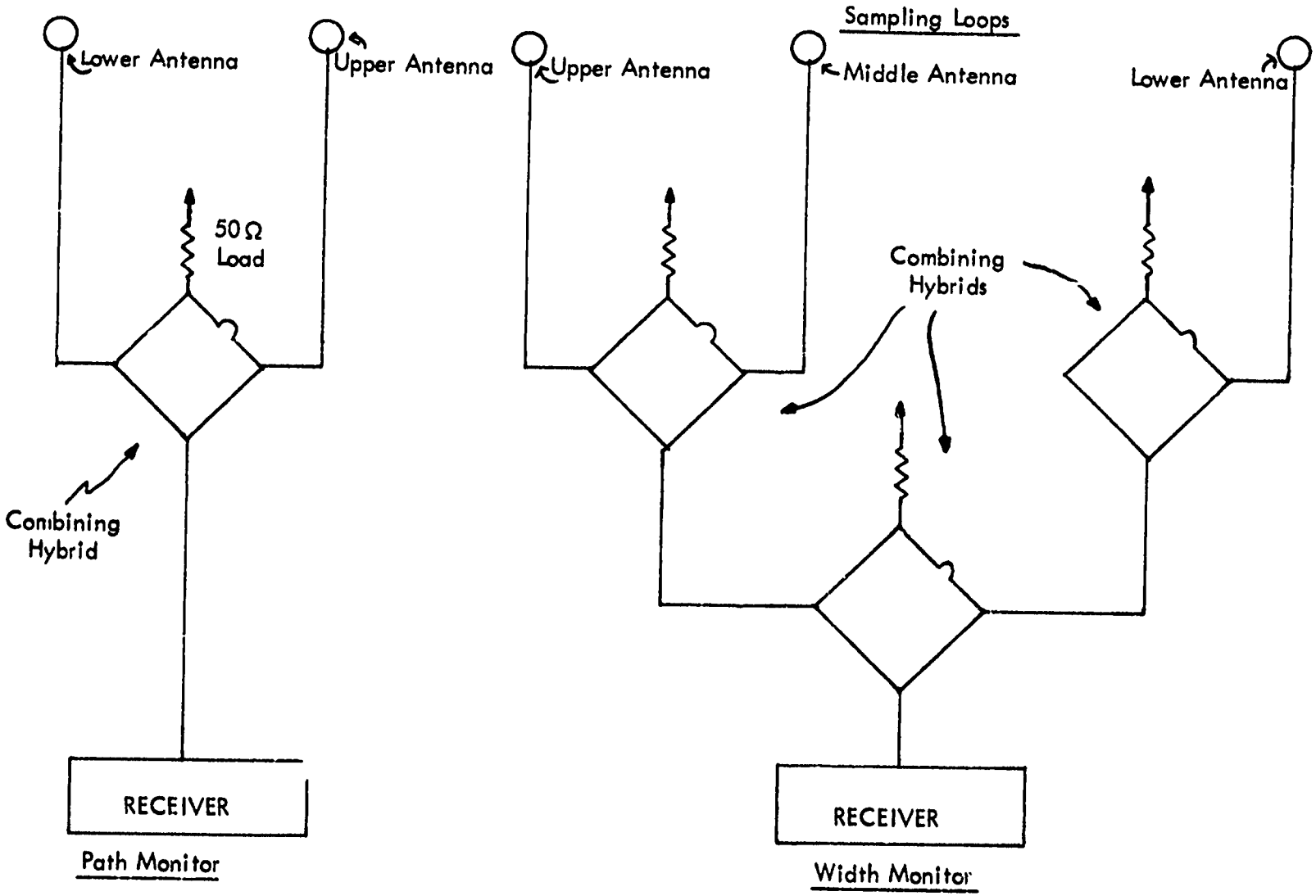

Figure 2-85. Combining Circuits for Integral Monitor.

All indications at this time are that the integral monitor is performing in a faithful and reliable manner. Initially some problems were encountered with some spurious phase shifts in some faulty connectors but these have been corrected and proper performance is now being obtained.

A good indication of the integrity of the integral monitor has been obtained by varying transmitter parameters and observing the simultaneous responses of the far-field and integral monitors. To summarize these results the curves in Figure 2-86 have been plotted and these show the error between the far-field (used as a reference) and the integral monitor and the standard near-field monitor. The errors are given in microamperes and the evidence is clear that the integral monitor is responding in a much more representative manner than is the conventional near-field detector.

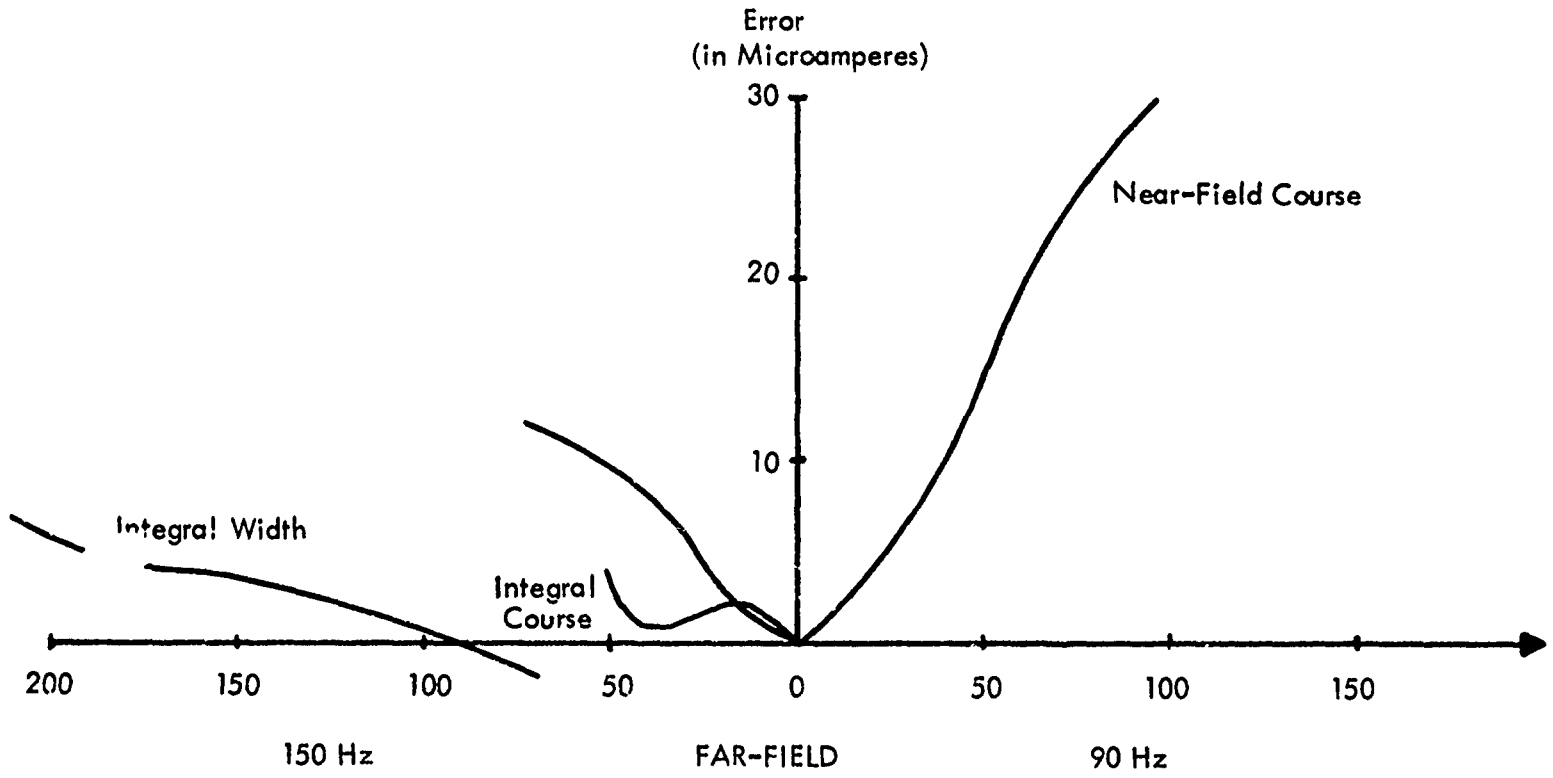

Figure 2-86. Grant, Michigan, Snow Site. Error in Readings of Integral or Near-Field Monitors. December 1971.

G. Effects of Truncated Ground on Image Glide Paths

1. Performance of Glide-Slope Arrays on Sites with Limited Ground Planes

a. Introduction. An ILS glide-slope array is inevitably sited over some sort of terrain, reflections from which must be accounted for since they enter the approach region. Although special arrays [9] can be designed to suppress ground illumination, the most widely used designs [10], [11], assume image theory, i. e., the ground plane is idealized as infinite, flat, and perfectly conducting. Many actual and prospective sites consist of a relatively short, flat ground plane terminated in a precipitous drop or in rough terrain which might be expected to reflect so diffusely that, as far as the glide slope region is concerned, it can be considered to supply negligible specular reflected signal.

The performance of glide slope arrays on such sites is of considerable practical interest. It can reasonably be approximated by considering the ground plane as a one-dimensional, perfectly conducting strip in free space [12]. In the following discussions the null-reference array, capture effect array, and a sideband reference glide-slope array, are treated by using the approximation. Details of the theory are presented in reference [12]. Equations used in the computation of radiation patterns are given in Appendix A.

b. Results of the Analysis.

1) Null Reference. Sideband and DDM patterns for various truncated ground plane lengths have been calculated for a null-reference array with the sideband and carrier antenna heights 10 λ and 5 λ respectively. Results are shown in Figures 2-87 and 2-88. Examination of these figures show the general effects of reducing the size of ground plane are: increase in sideband signal near the horizon, lowering of the path angle, and reduction of DDM slope on path (path softening). The computations indicate that a path can be formed with as little as 250 feet of ground plane, but such a path would probably be very rough. This is because of strong signals near the horizon, which in the presence of low hills or other foreground obstacles, will be scattered into the approach region.

2) Capture Effect. Figures 2-89, 2-90, 2-91, and 2-92 contain computed sideband, carrier, clearance, and DDM curves for various values of ground plane length L in front of a capture effect array with antennas at 5λ, 10λ and 15λ. Figure 2-89 clearly shows how the performance of a capture effect system will be

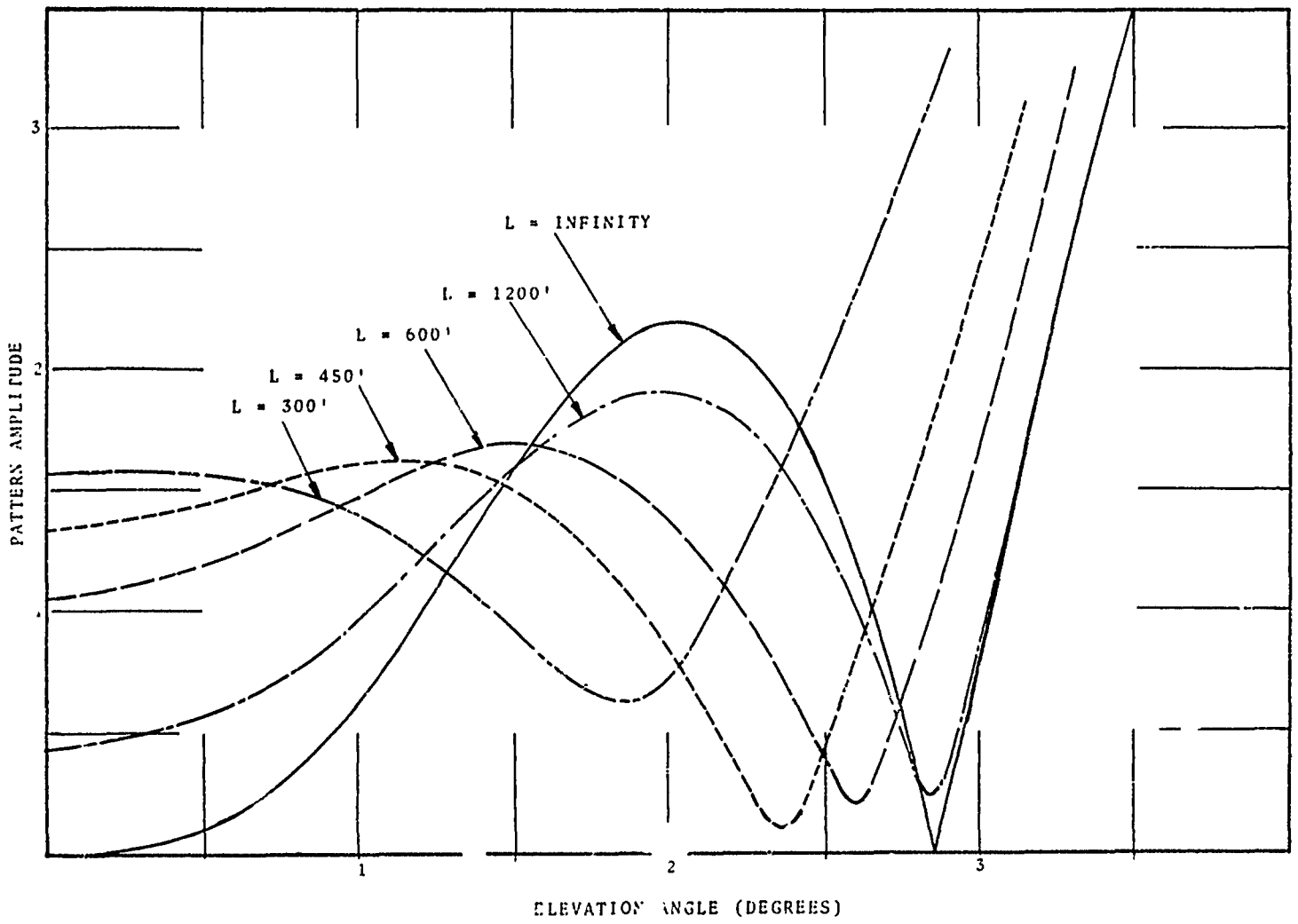

Figure 2-87. Computed Sideband Patterns of Null Reference Array Over Ground Planes of Several Lengths.

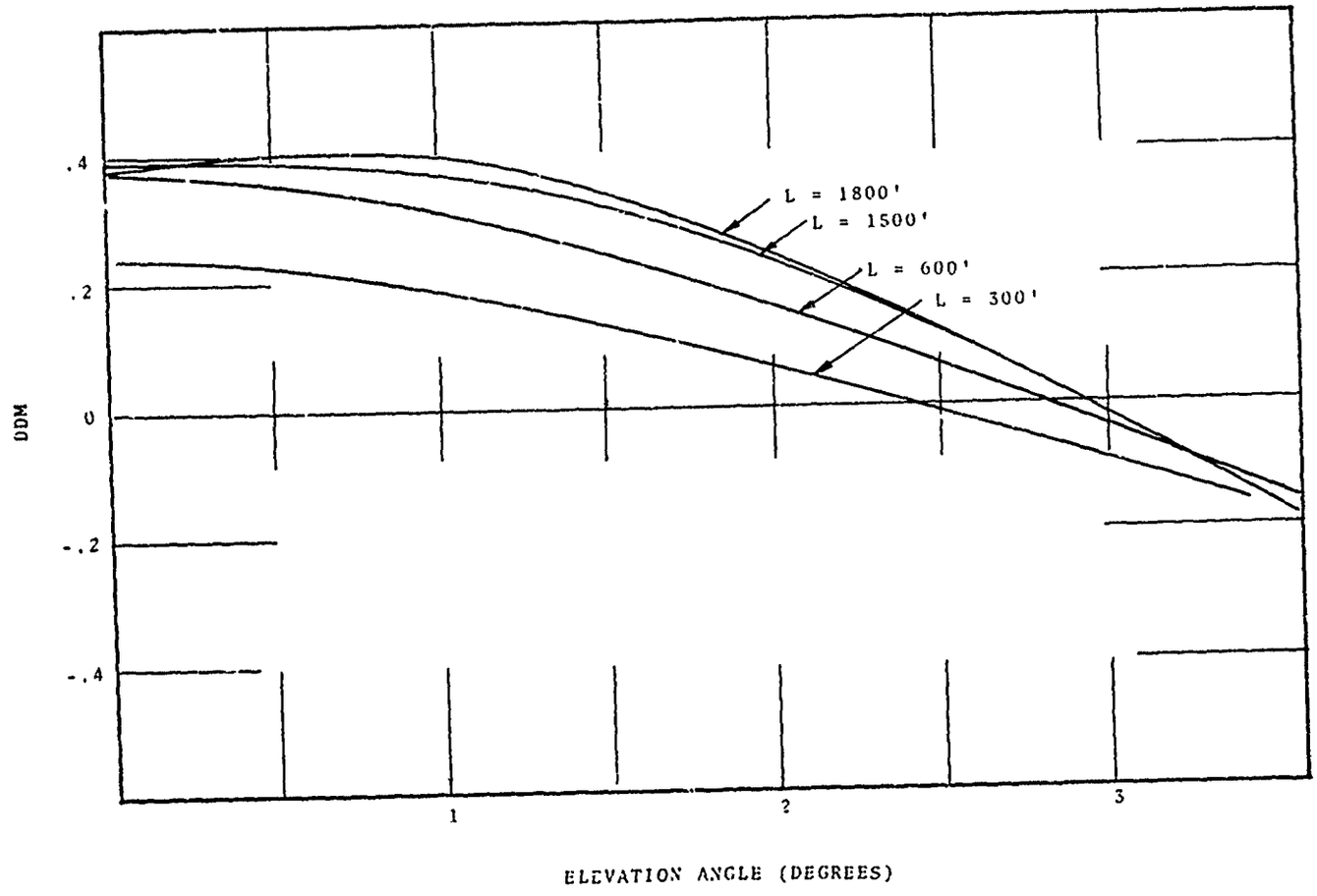

Figure 2-88. Computed DDM Generated by Null Reference Array Over Ground Planes of Several Lengths.

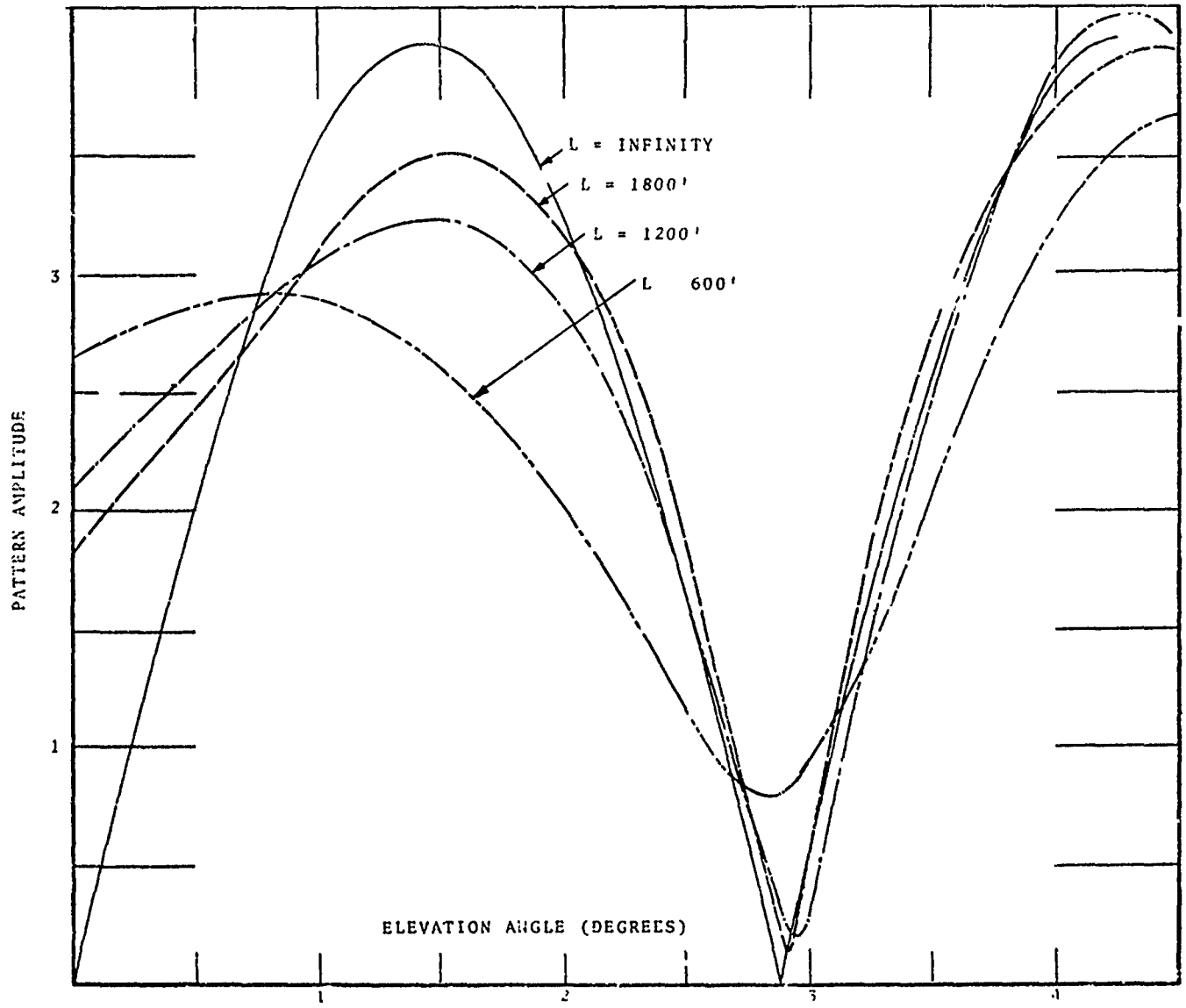

Figure 2-89. Computed Sideband Patterns of Capture Effect Array Over Ground Planes of Several Lengths.

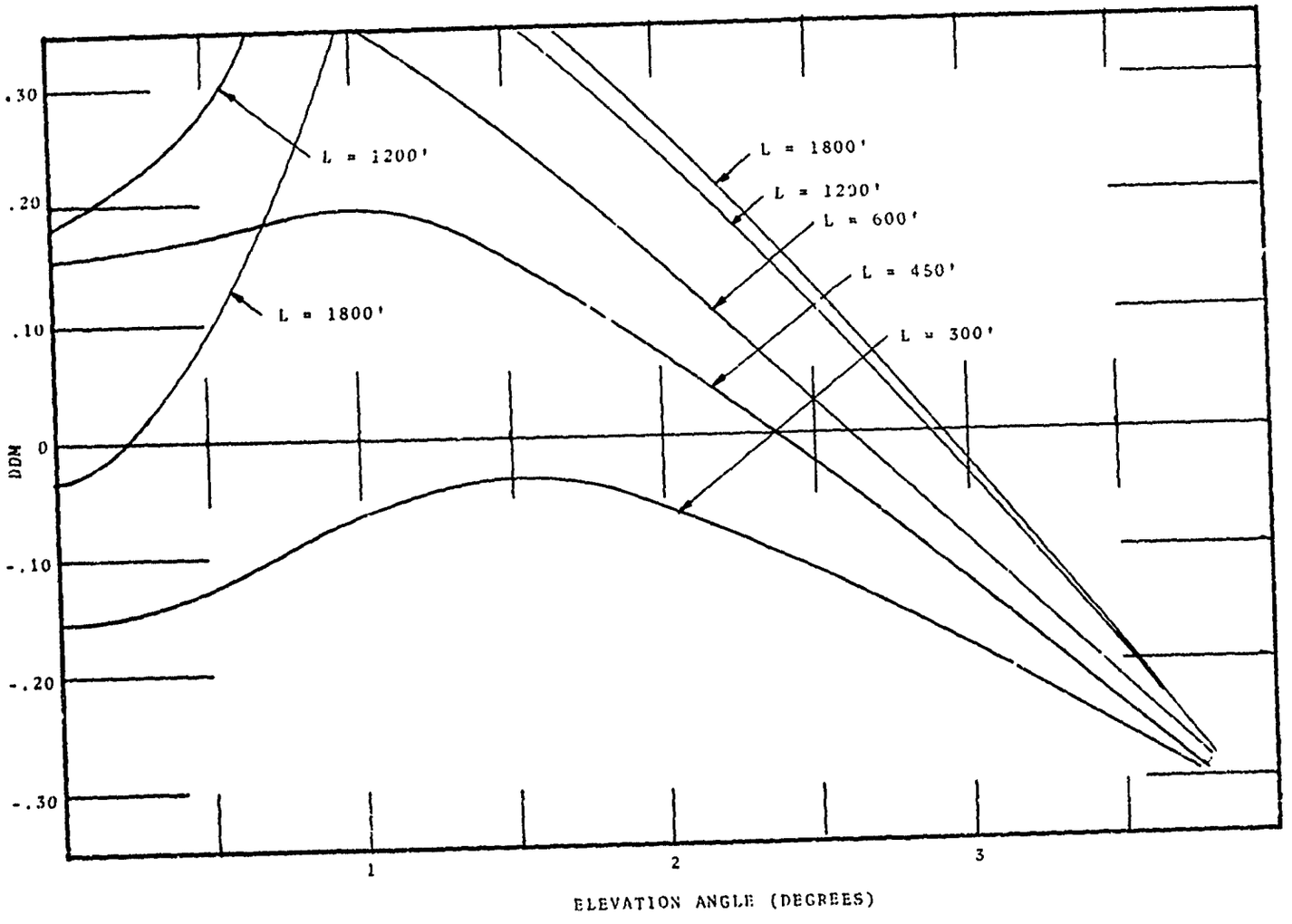

Figure 2-90. Computed Carrier Patterns of Capture Effect Array Over Ground Planes of Several Lengths.

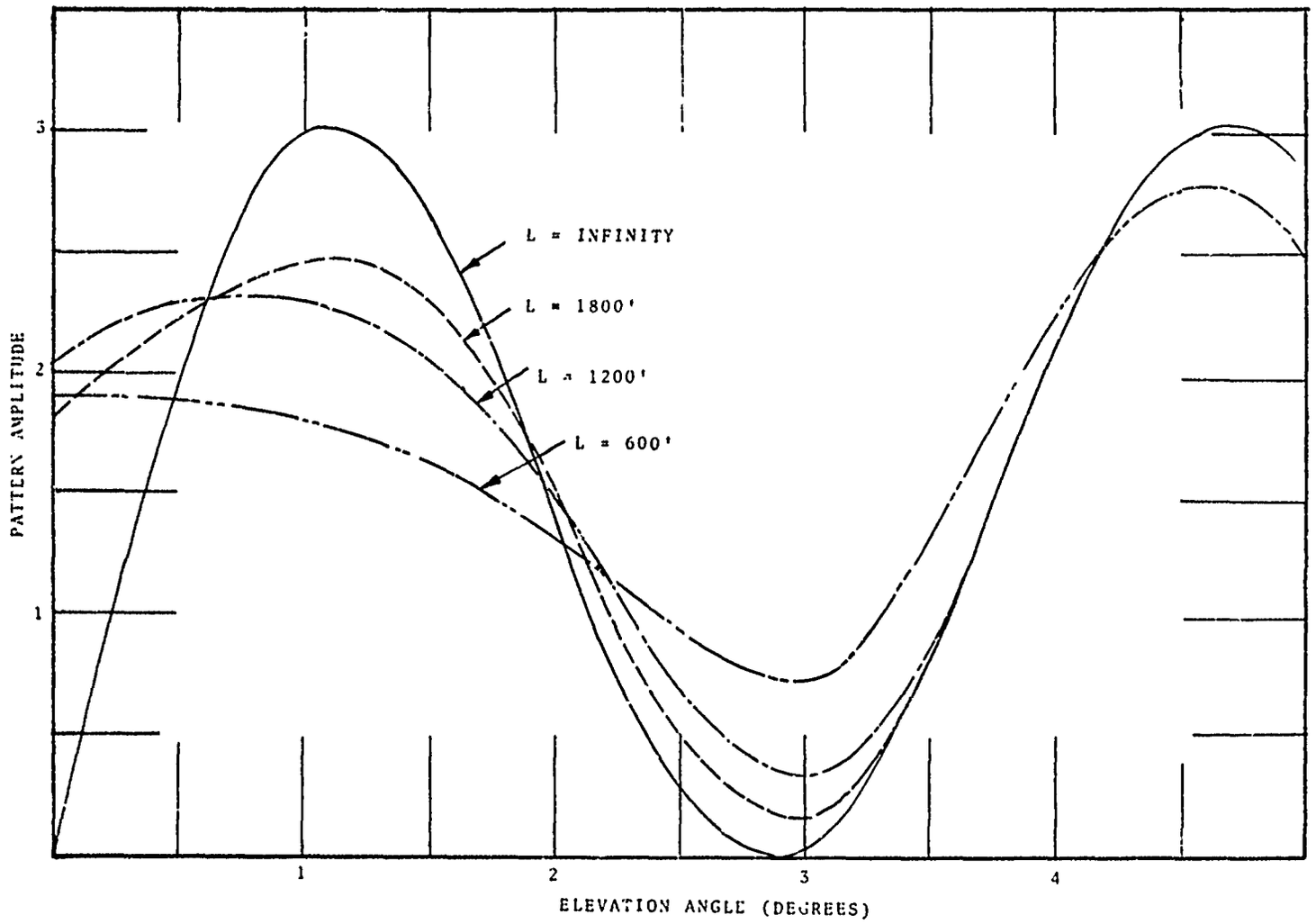

Figure 2-91. Computed Clearance Signal Pattern of Capture Effect Array Over Finite Ground Planes of Several Lengths.

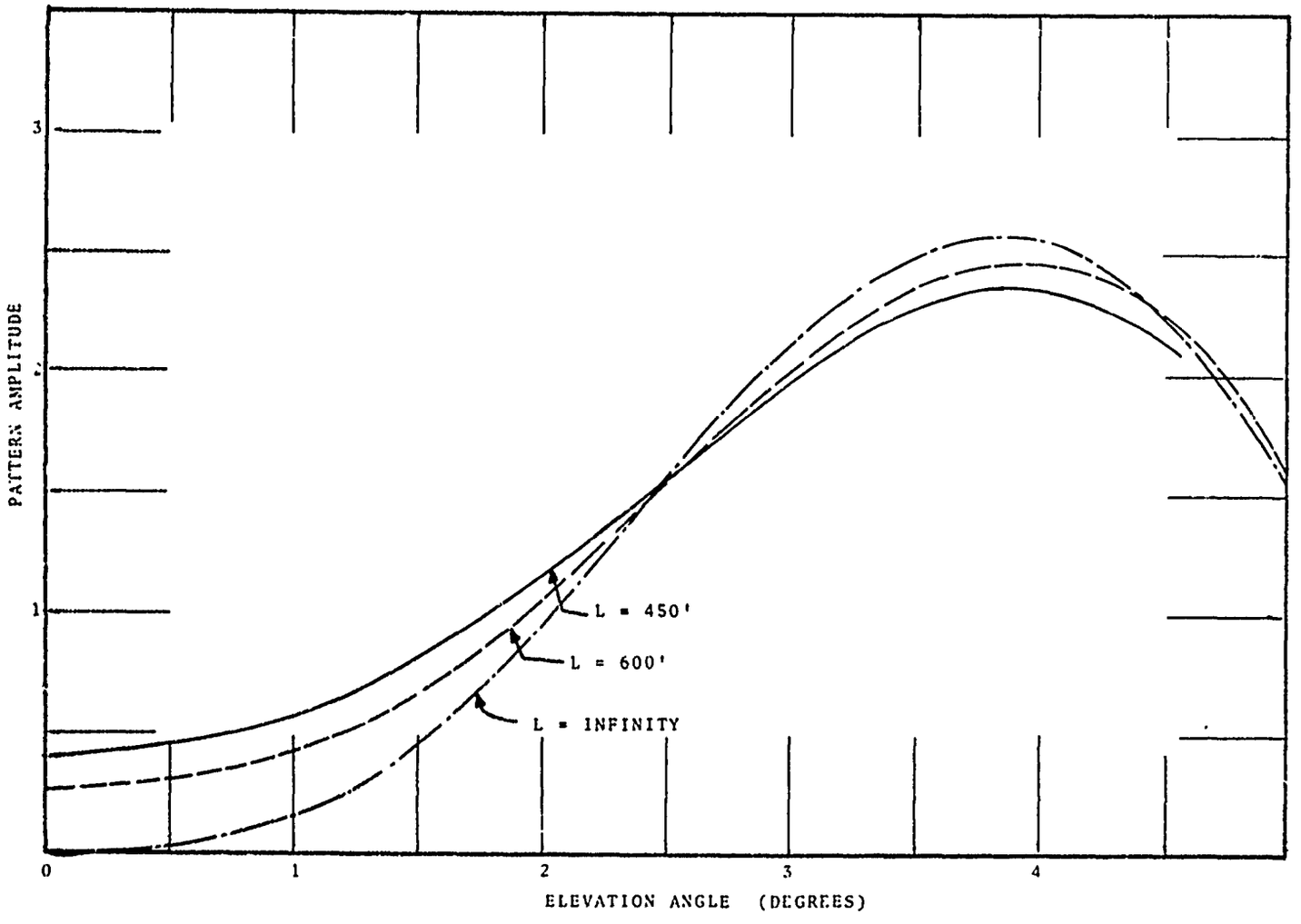

Figure 2-92. Computed DDM Generated by Capture Effect Array, Without Clearance Signal, Over Ground Planes of Various Lengths.

degraded by reduction in ground plane size, which has the effect of increasing signal strength near the horizon and consequently increasing roughness. Also evident from Figure 2-89 is a lowering of elevation angle at minimum sideband signal which suggests that the glide slope angle will be lowered as L is reduced. Figure 2-92 verifies this, and also shows that a path will be formed with L as small as 450 feet, and that the path softens with reduced L.

c. Sideband-Reference, Glide-Slope Array. Figures 2-93 and 2-94 show computed sideband and carrier patterns for various lengths of ground plane with a sideband-reference system. Figure 2-95 shows computed DDM vs. elevation angle also for several lengths of ground plane. Again sideband signal near the horizon increases as ground plane length is reduced.

d. Figure of Merit. As a measure of path roughness likely to be generated by scattering from low hills or other foreground obstacles, a "figure of merit", F, was computed from

$$F = \frac{\text{sideband signal at } 0.5^\circ}{\text{sideband signal } 0.5^\circ \text{ below path}} \qquad (2.108)$$

The numerator of the above equation (2.108) measures the illumination of low angle scatterers, while the denominator measures the sideband signal derivative with respect to elevation angle, near the path angle. For a particular L, comparison of F for various arrays will indicate how much roughness a given scatterer will generate. Figure 2-96 shows computed curves of F versus L, for the three arrays considered. The capture effect deteriorates as L is reduced, but is superior to the null-reference for all L. Sideband-reference glide-slope array is better than the null reference system, but not as good as capture effect.

An unexpected result of the sideband-reference, glide-slope array was a low value of computed fly-up clearance signal near the horizon for quite long ground planes (1800' and 1200'). Clearance below about 1.2° with finite ground planes of all lengths treated is considerably less than would exist with an infinite ground plane.

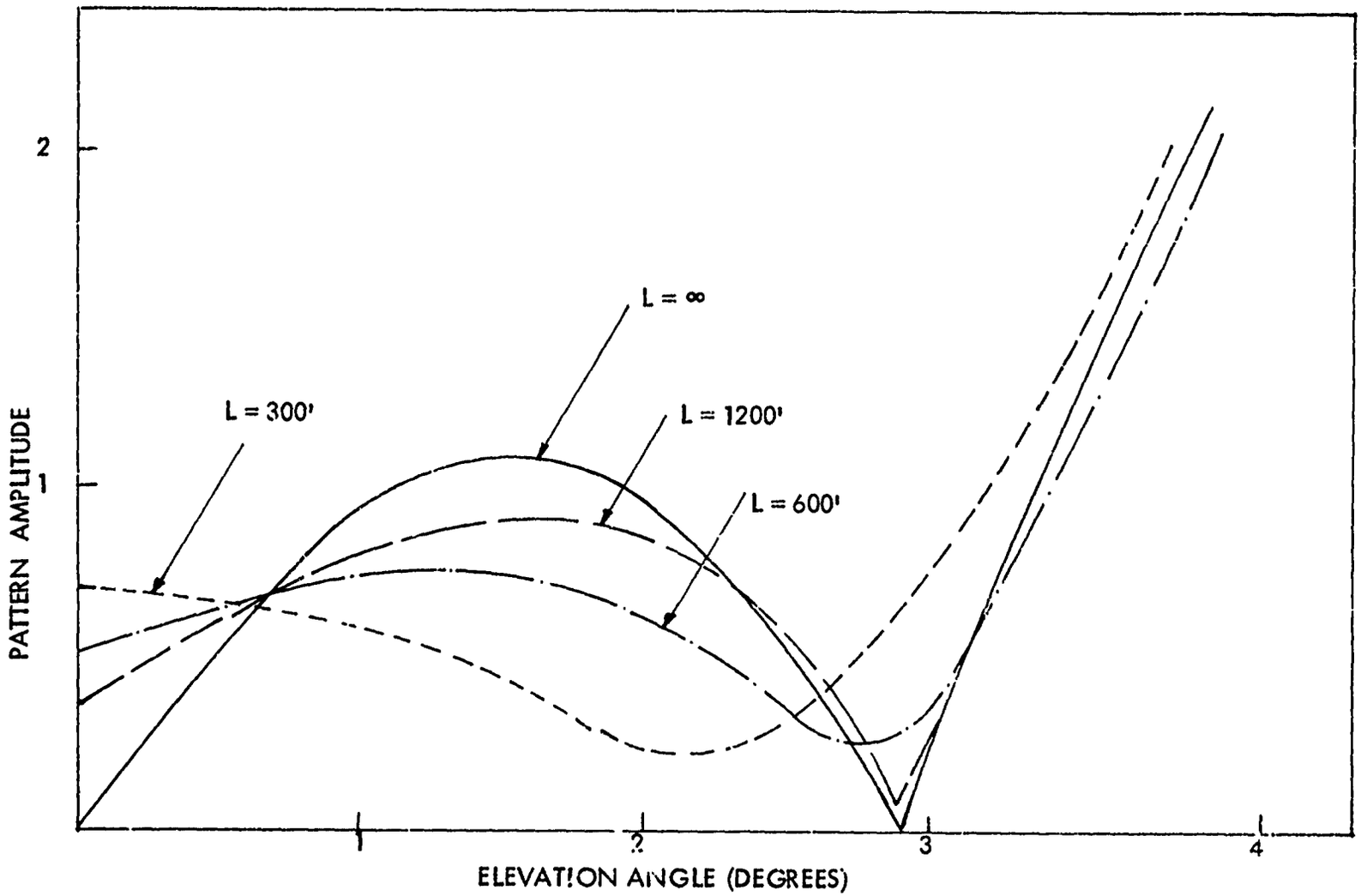

Figure 2-93. Sideband Pattern of Sideband Reference Antenna for Several Lengths of Ground Plane.

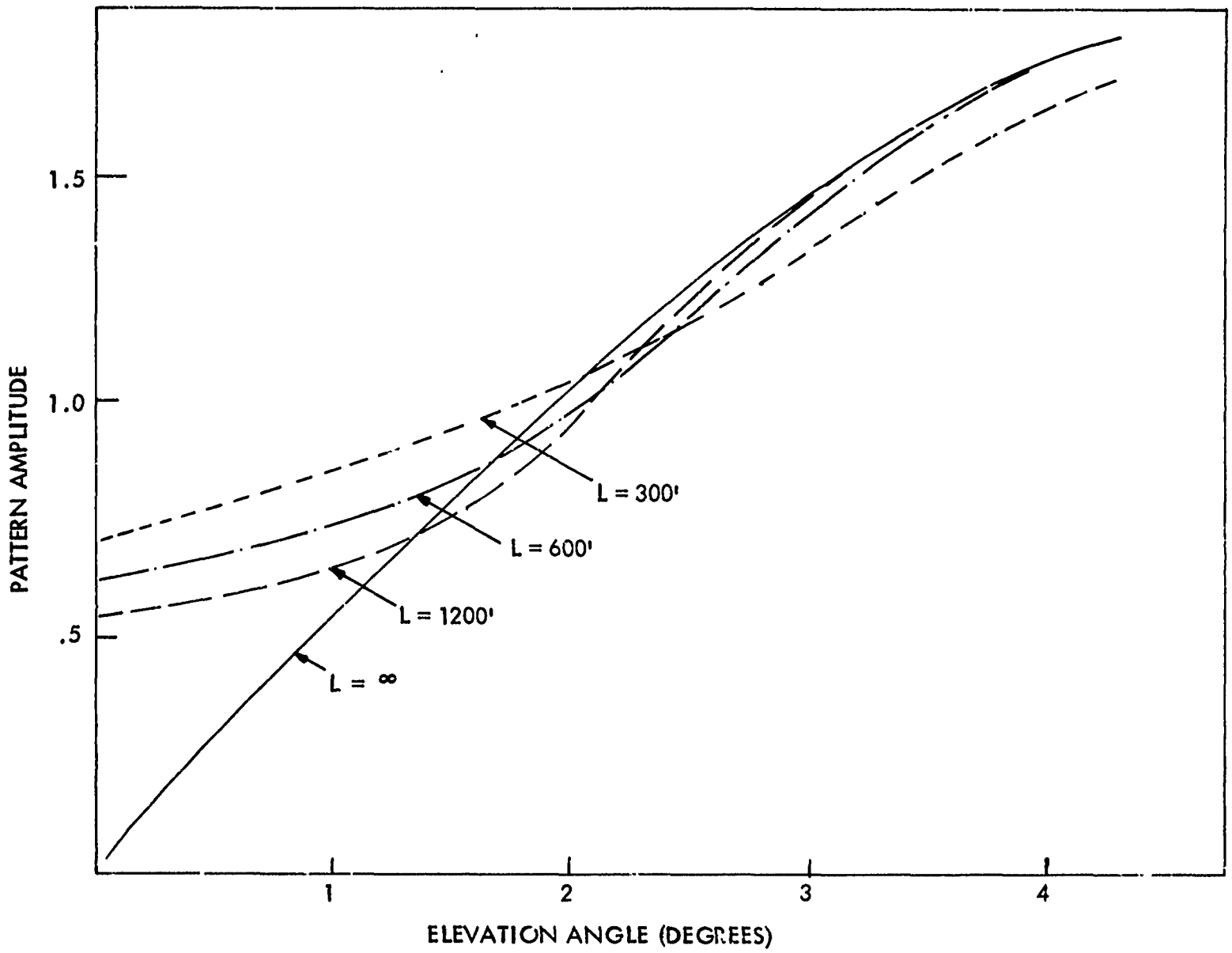

Figure 2-94. Carrier Pattern of Sideband Reference Antenna for Several Lengths of Ground Plane.

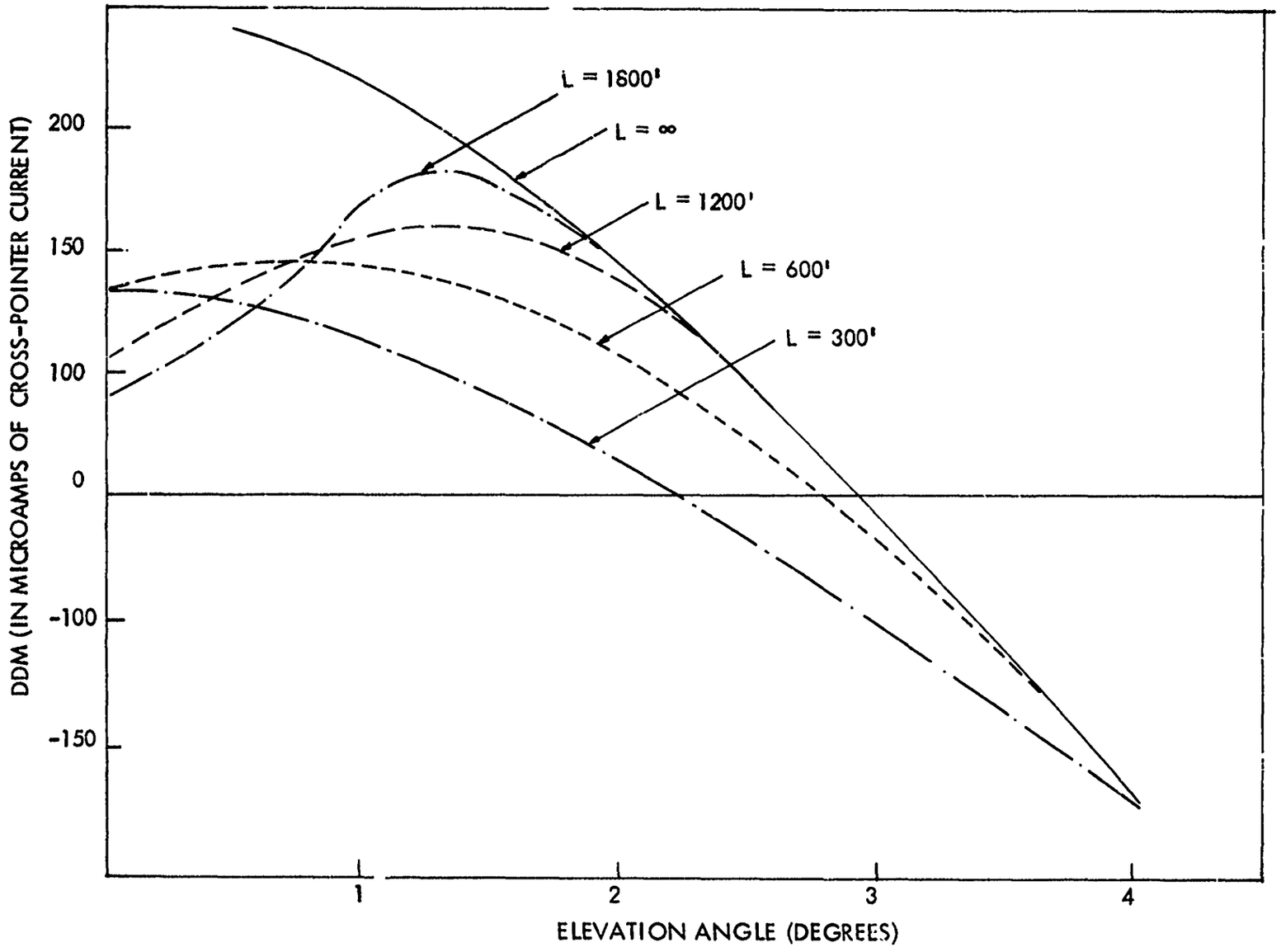

Figure 2-95. DDM Generated by Sideband Reference Antenna for Several Lengths of Ground Plane.

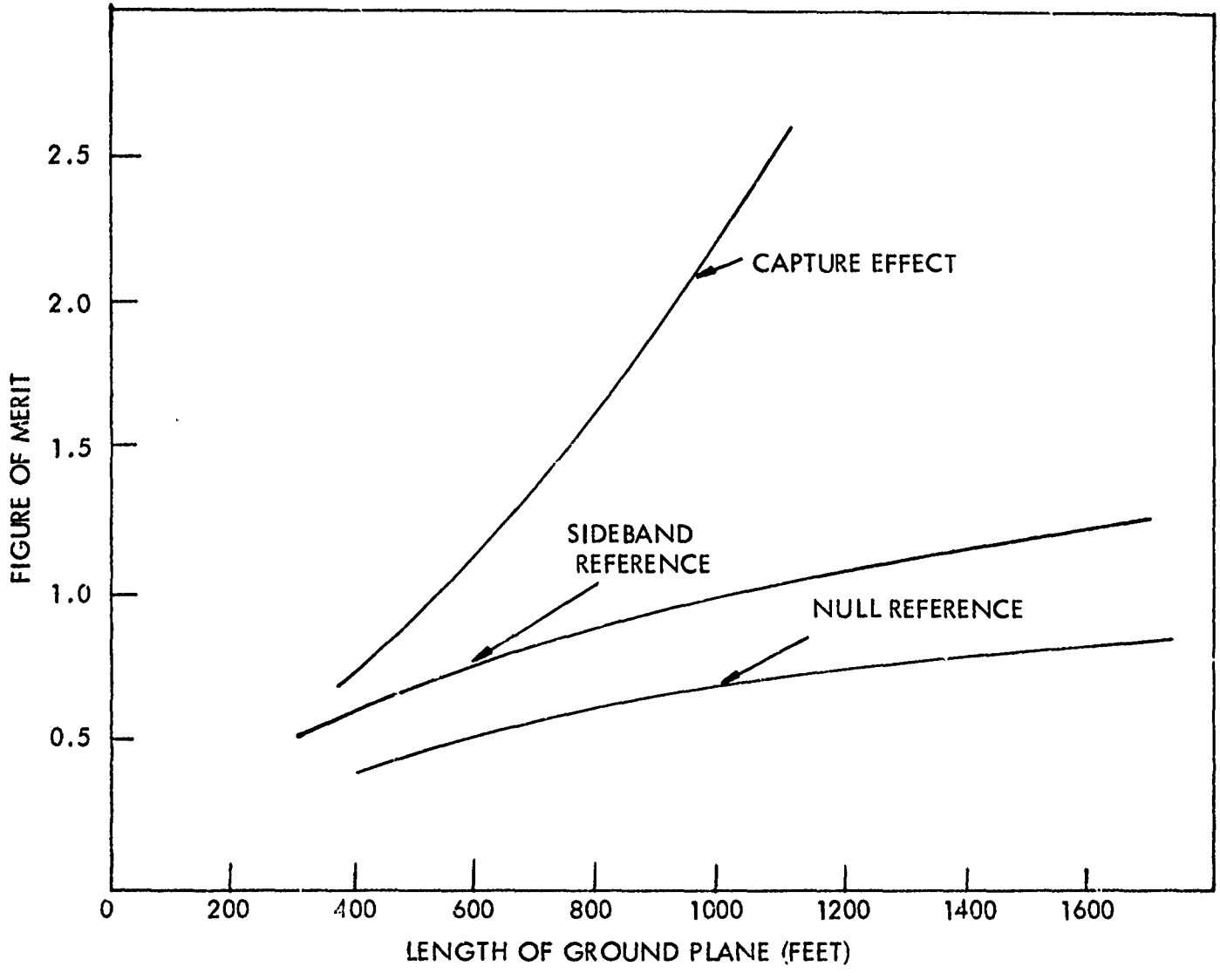

Figure 2-96. Figure of Merit of Several Glide Path Arrays vs. Length of Ground Plane.

2. Additional Study of Capture-Effect Glide Slope

a. Introduction. The results of the preceding section have shown that a limited ground plane lowers and softens a capture-effect glide slope. This section extends the analysis to include antenna offset. Results are that the harmful effects of limited ground plane are aggravated, when approaching off-localizer on the glide path tower side. The radiation patterns of the individual capture effect antennas have been computed and are presented as are graphs of SB-CSB phase with limited ground plane. The computed results suggest three ways to improve capture effect performance on sites with limited ground plane. Capture effect systems incorporating the indicated changes have been analyzed and the results are presented.

b. SB to CSB Phase Difference with Limited Ground Plane. Figures 2-89, 2-90 and 2-[illegible] show computed SB amplitude, CSB amplitude, and DDM for various ground plane lengths. These figures show high SB amplitude below path, but low DDM, thus suggesting large phase anomalies below path. This hypothesis was verified by computations, the results of which are shown in Figure 2-97. The general effect of limited ground plane is to cause SB signal to lag CSB signal. This effect increases as ground-plane size is reduced and as elevation angle is decreased.

The computed phase anomaly suggests that performance below path can be improved by introducing a deliberate leading phase shift in the main sideband feeder to compensate for the anomalous lag due to limited ground plane. To check this, a 30° SB lead was inserted in the computations, yielding computed DDM curves of Figure 2-98 which show considerable increase in below path DDM as a result of deliberate SB lead. Above path, where site induced dephasing is less, deliberate lead reduces DDM. For longer ground planes, site induced dephasing is reduced and computations (not illustrated) indicate little improvement from deliberate SB dephasing.

c. Radiation from individual Antennas of Capture-Effect Array. The amplitude pattern of the center antenna was shown in Figure 2-87 (SB pattern of null reference). Results of additional computation of amplitude radiated by the top element is shown in Figure 2-99 and of phase of radiation from each antenna in Figures 2-100, 2-101 and 2-102. Figures 2-99 and 2-102 indicate that for short ground planes, radiation from the top element is severely disturbed in amplitude and phase. If the ground plane is less than about 600' in length, a free space (no ground plane) approximation is more realistic for the top element than an infinite ground plane approximation.

Figure 2-102 suggests another way of increasing below path DDM and of increasing DDM slope on path. The figure shows that the top element signal leads just above path, lags from 2/3 of path elevation to the path, and leads from 1/3

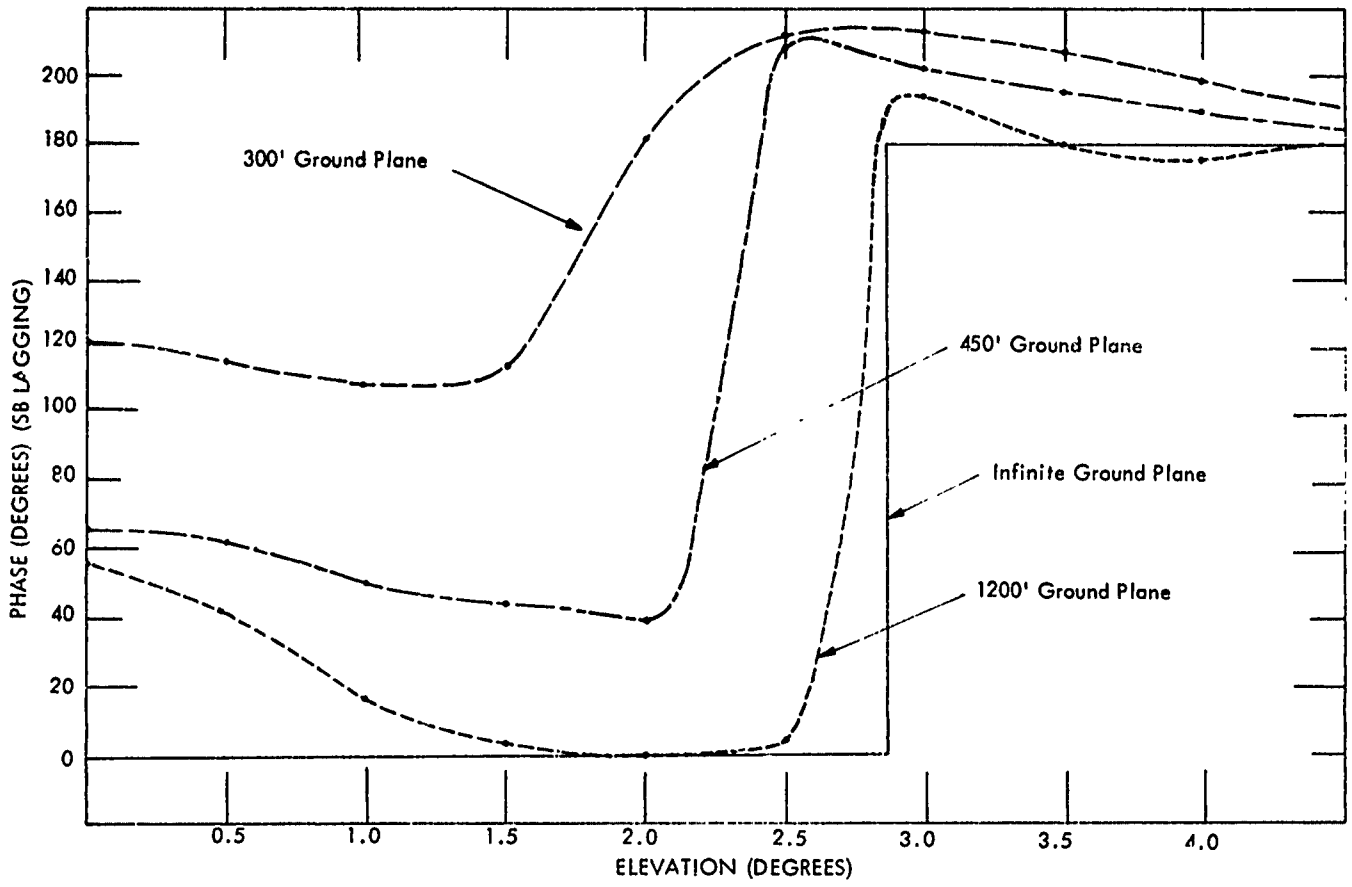

Figure 2-97. Computed Phase Difference Between SB and SCB Signals--Capture Effect Glide Slope.

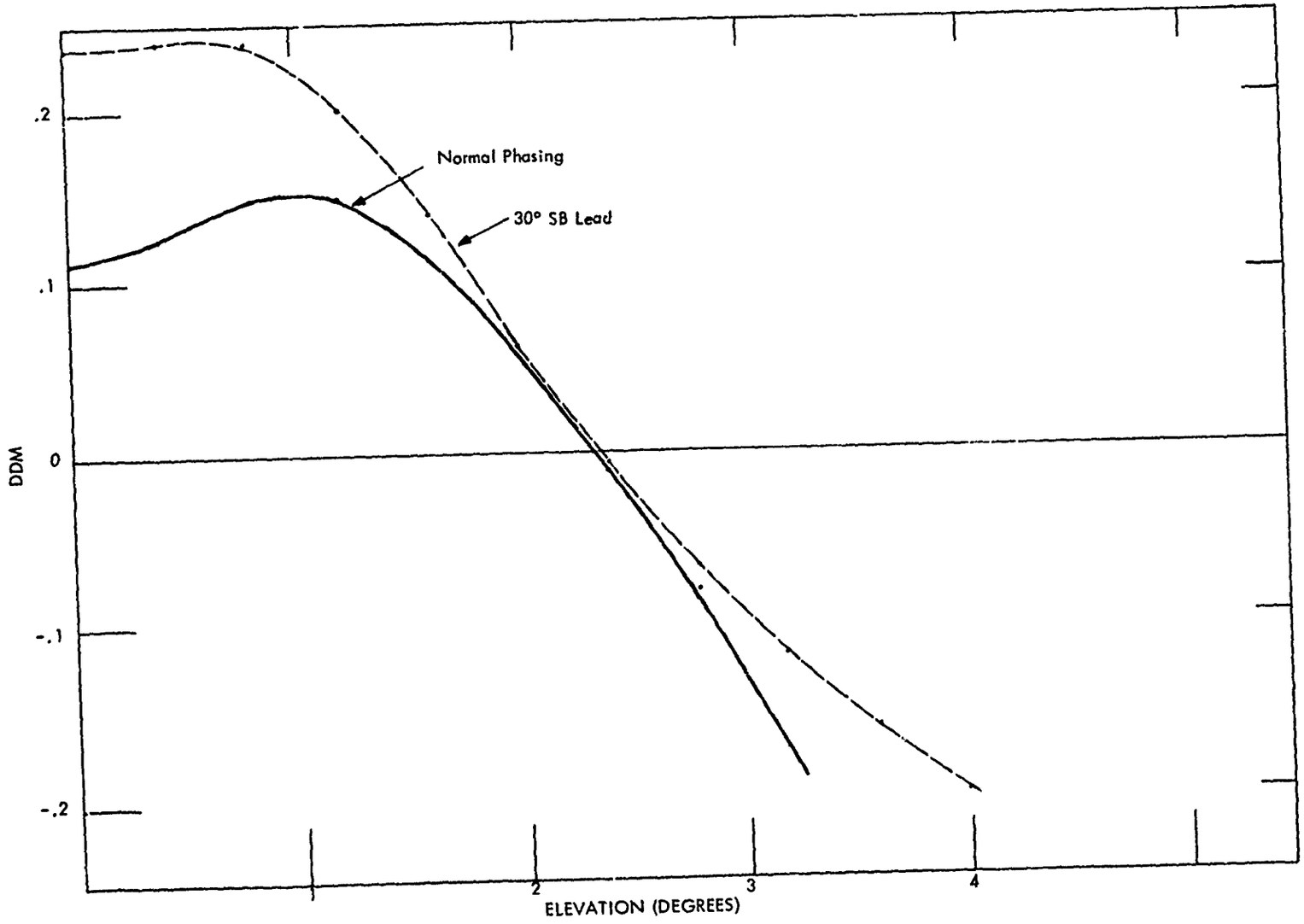

Figure 2-98. Capture Effect DDM Over 450' Ground Plane --With and Without SB Lead.

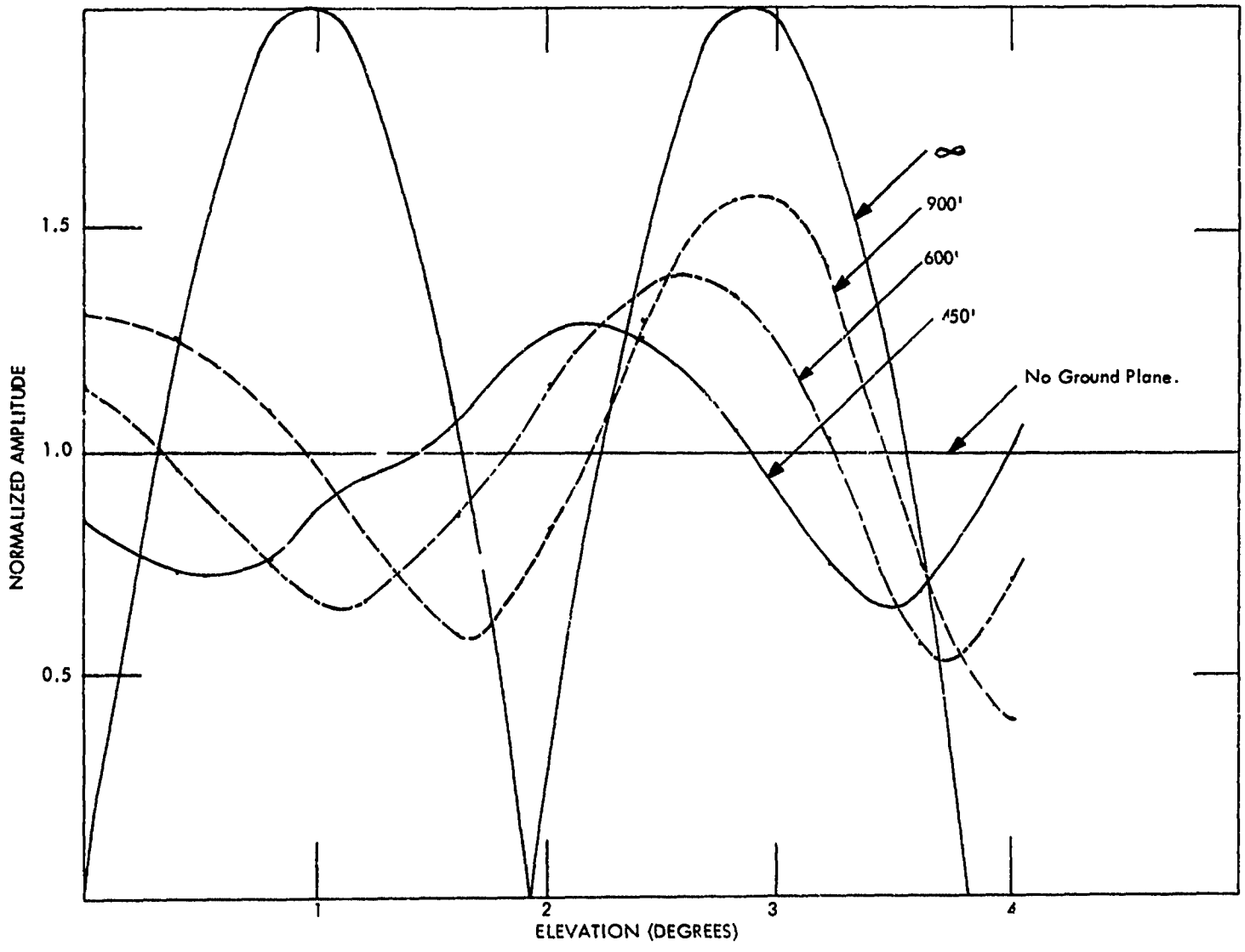

Figure 2-99. Amplitude of Radiation from Top Antenna of Capture Effect System for Several Ground Plane Lengths.

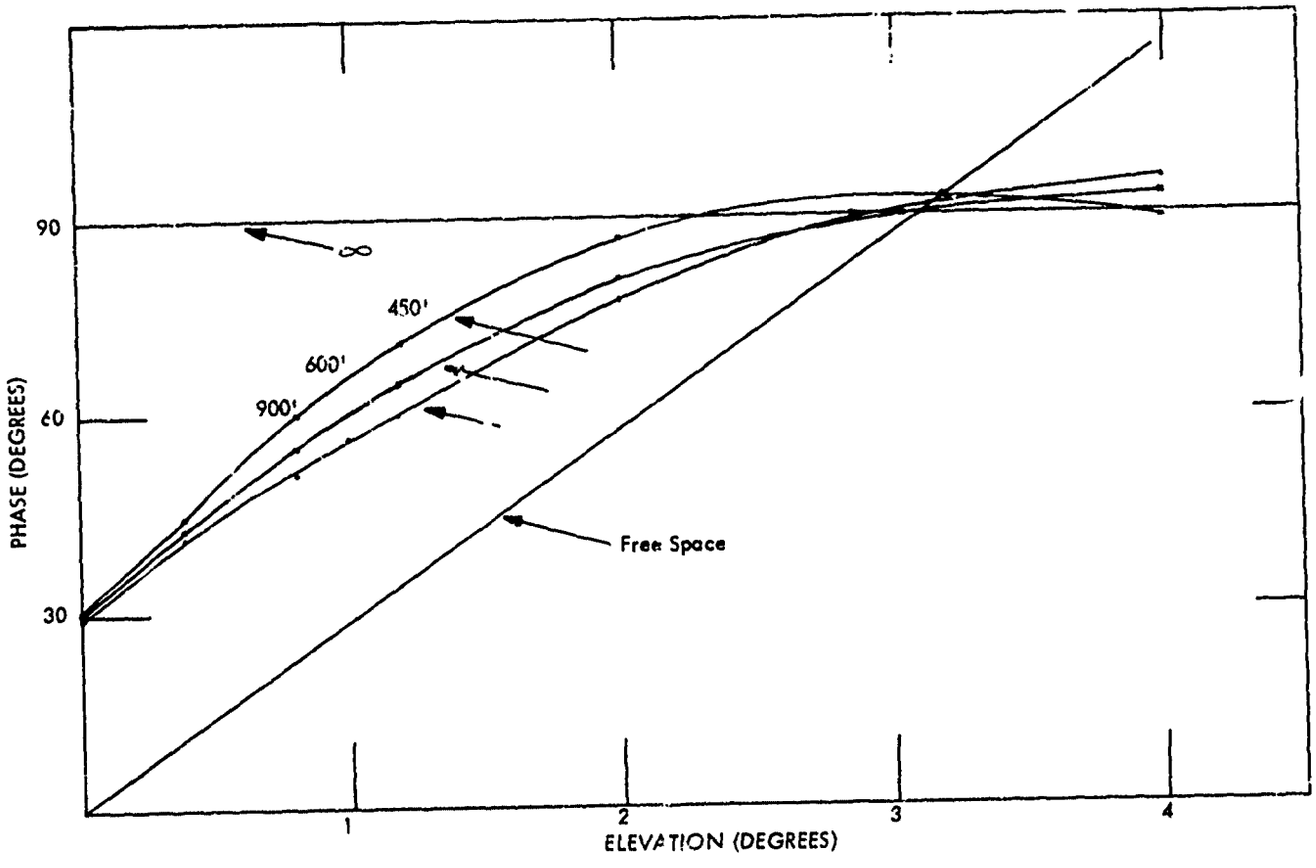

Figure 2-100. Phase of Radiation from Bottom Element of Capture Effect Glide Slope, for Several Lengths of Ground Plane.

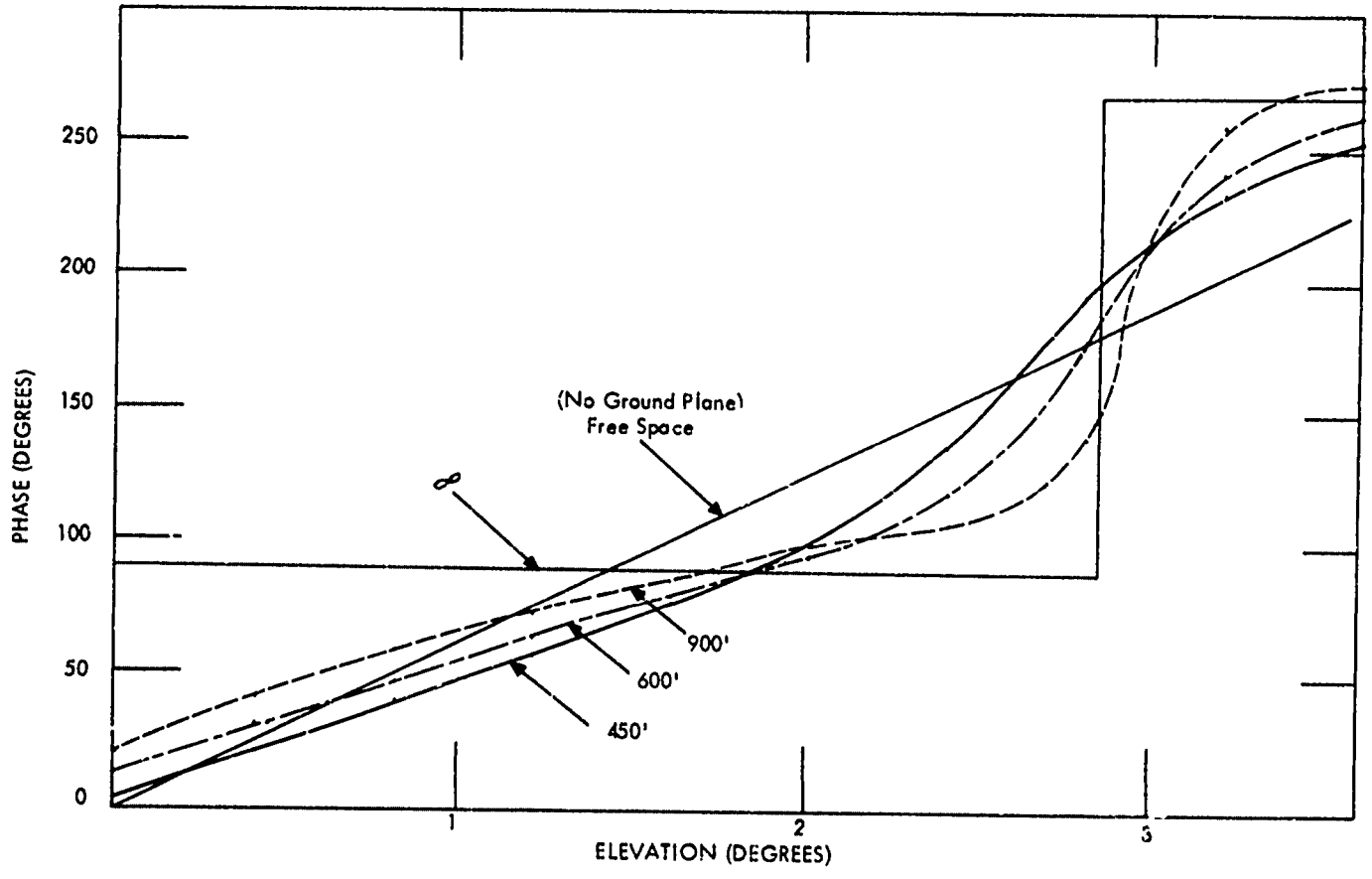

Figure 2-101. Phase of Radiation from Center Element of Capture Effect Glide Slope, for Several Lengths of Ground Plane.

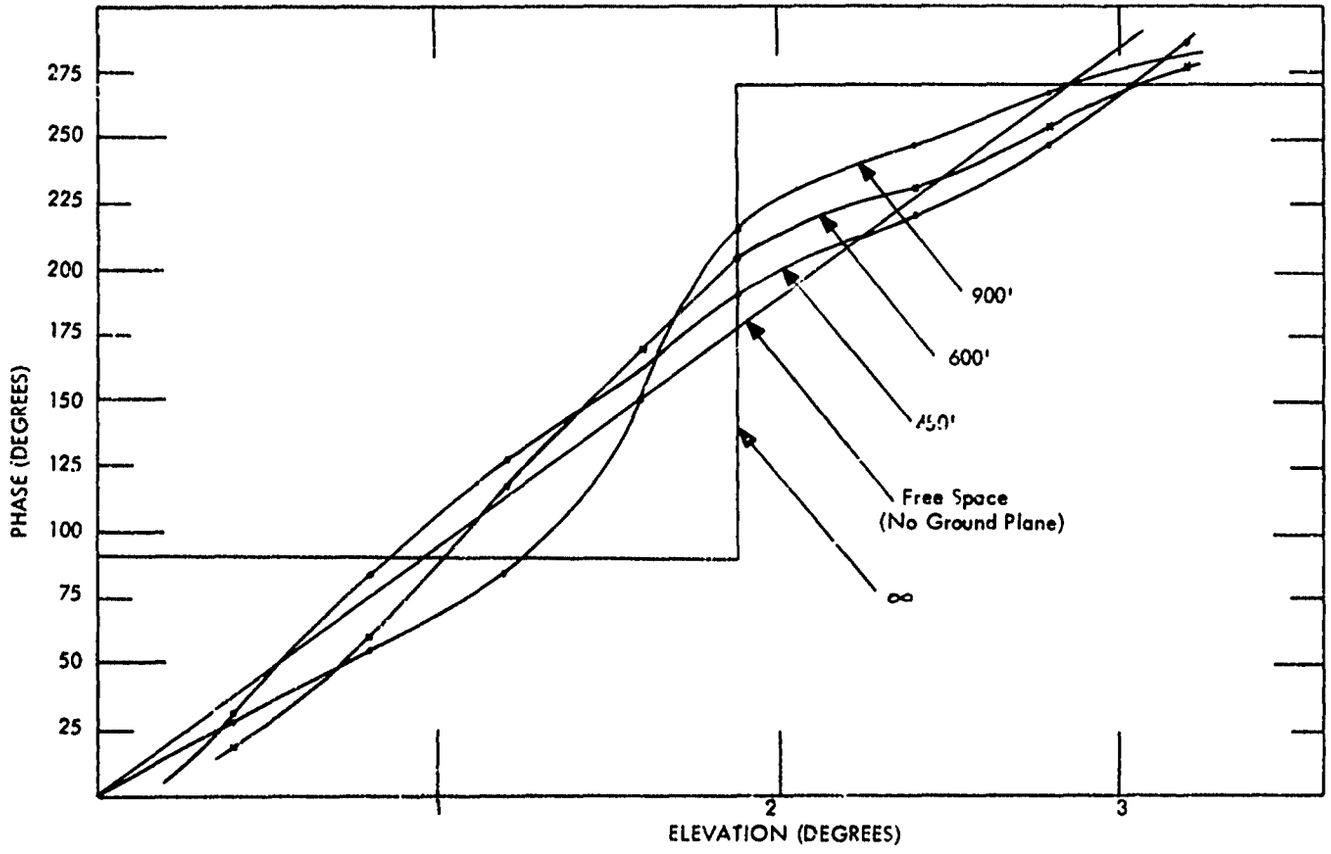

Figure 2-102. Phase of Radiation from Top Element of Capture Effect Glide Slope, For Several Lengths of Ground Plane.

to 2/3 (roughly) of path angle, with reference to an infinite ground plane signal. One may note that the nominal SB signal from the top antenna augments the nominal SB resultant sideband from 2/3 of path elevation to the path, detracts from nominal resultant SB from the horizon to 2/3 of path angle, and detracts from nominal SB just above the path. Consequently with a limited ground plane, a deliberate lead in the top element feeder should augment DDM, except from the horizon to 1/3 of path angle. This supposition was checked by inserting a 30° top element lead in the computation parameters. Results shown in Figure 2-103 indicate a significant increase in below path clearance except from the horizon to about 0.6°.

d. Effects of Antenna Offset. Antenna offset introduces a phase lag when approaching off localizer on the glide path tower side, and thus may be expected to exaggerate the effects of insufficient ground plane, in view of the two preceding sections. To check this supposition, phase lags appropriate to an approach 8° off localizer and a tower offset of 400' from runway centerline were introduced in the computation parameters. The results of the computations shown in Figures 2-104 and 2-105 point to a complete loss of clearance DDM as a result of offset for a 450' ground plane, and a less dramatic but significant reduction of clearance for a 600' ground plane.

The following can be concluded from the foregoing study:

1) On sites with limited ground plane, DDM below path will be reduced by dephasing of SB relative to CSB, even though SB signal is higher than would exist over an infinite ground plane.

2) For off-localizer approaches on the glide slope tower side, antenna offset acts to exaggerate the effects of site induced dephasing, thus further reducing below-path clearance.

3) Radiation from the top antenna is severely disturbed in amplitude and phase by limitation of ground plane.

Future plans are being made for establishing an experimental site involving a truncated ground plane, where practical measurements can be made. A thorough investigation will be made including a complete set of flight measurements.

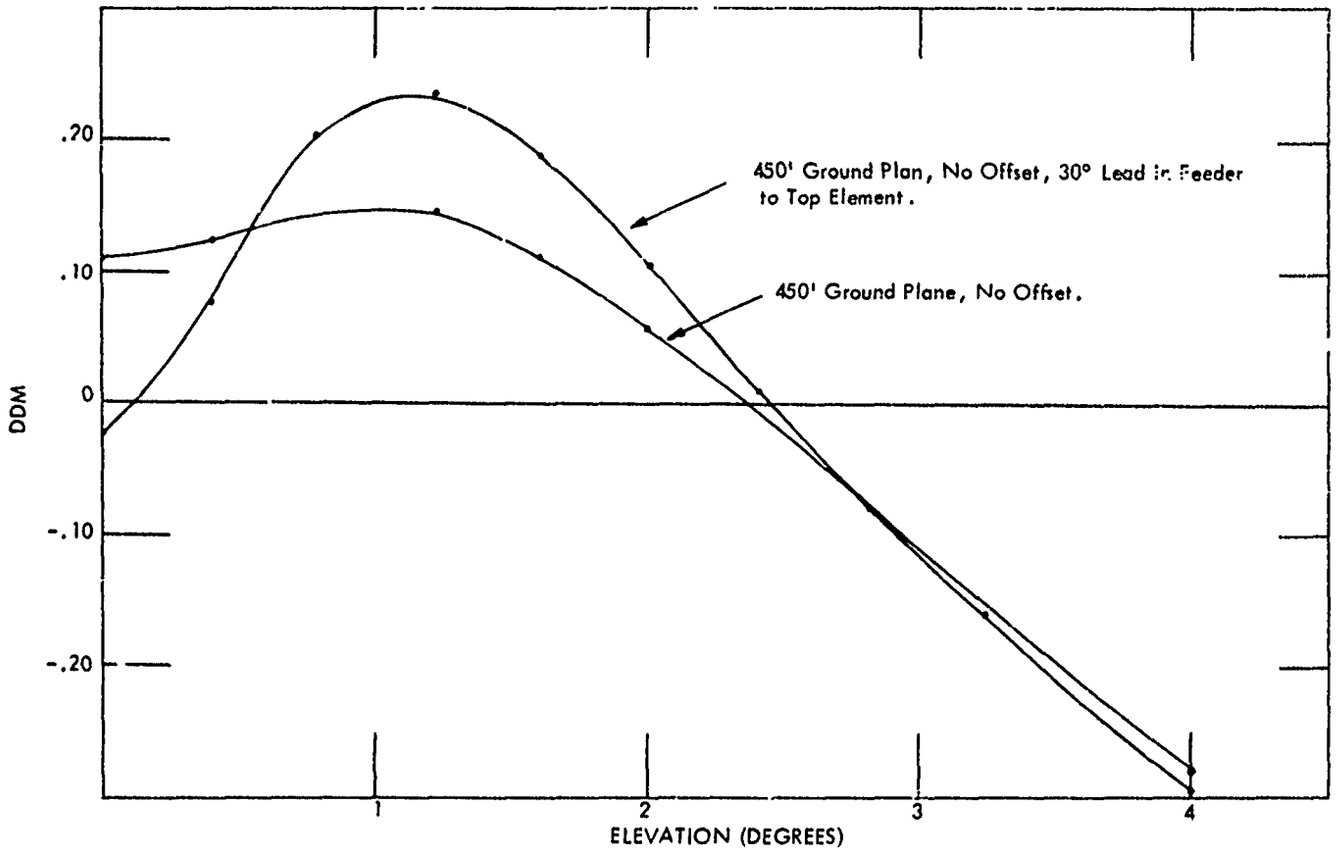

Figure 2-103. Effect of 30° Lead in Top Element on DDM Generated by a Capture Effect System Over a 450' Ground Plane.

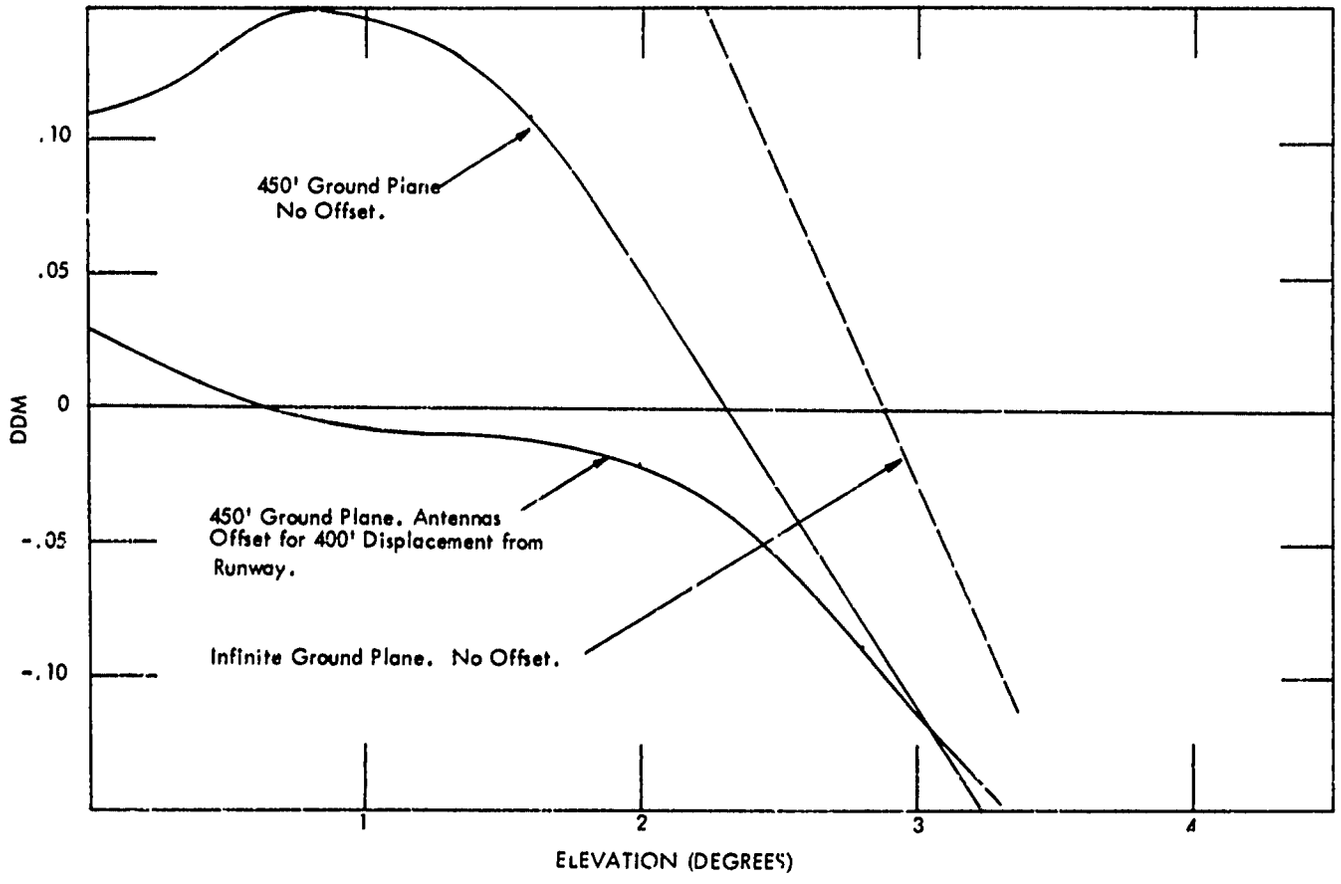

Figure 2-104. DDM Generated by a Capture Effect System Over a 450' Ground Plane at 8° Off Localizer (G. P. Tower Side)--With and Without Offset.

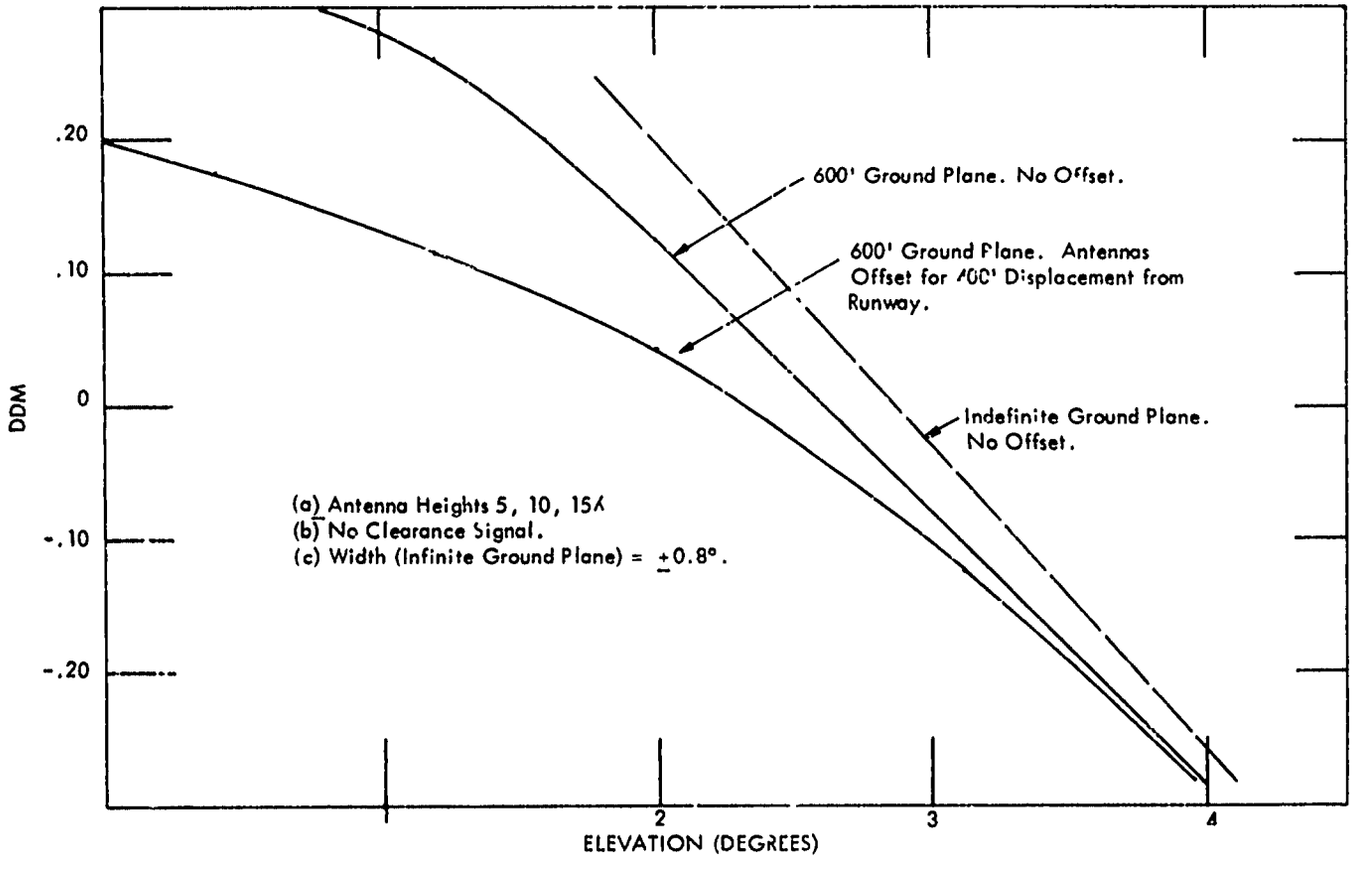

Figure 2-105. DDM Generated by a Capture Effect System Over a 600' Ground Plane at 8° Off Localizer (G. P. Tower Side), With and Without Antenna Offset.

3. Extension of Ground Plane of an ILS Glide Slope by Horizontal, Parallel Wires

a. Introduction. It is possible to extend the ground plane of an ILS Glide Slope by means of a number of horizontal parallel wires. The maximum wire spacing and minimum wire diameter that will suitably reflect waves at angles near grazing are of practical interest. In this section, an expression for the reflection coefficient (in terms of wire diameter, wire spacing, and incident angle) is derived and computed results are presented.

b. Theory. The sketch in Figure 2-106 shows the assumed configuration.

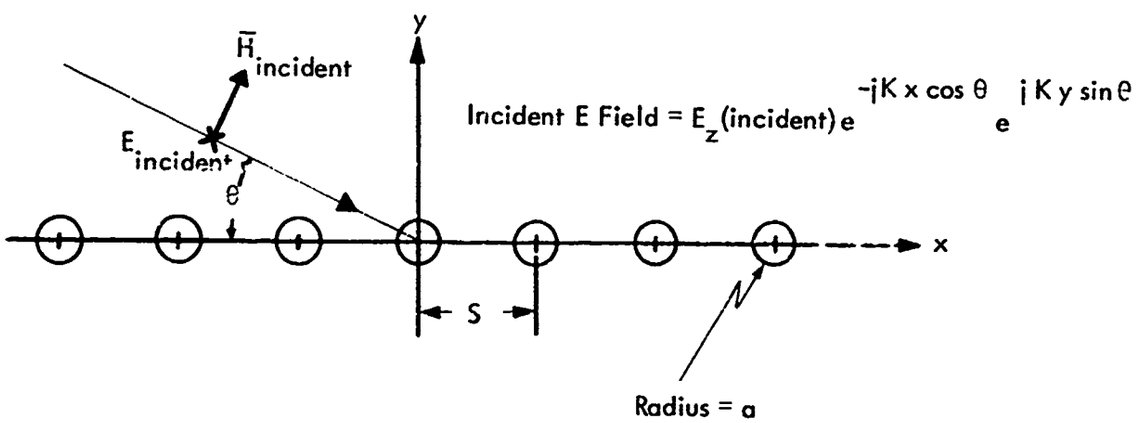

Figure 2-106. Assumed Configuration.

The parallel wire ground plane is assumed to extend at $x = \pm\infty$.

The wires are taken as perfect conductors, hence the tangential electric field at their surface is zero. The z-directed electric field generated by the wire currents must cancel the incident z-directed electric field. It will be assumed that the wire diameter is sufficiently small that the surface current in the wire is constant around the periphery of the wire. Let the total current carried by the wire located a $x = 0$ be I.

Then the z-directed electric field generated by the wire located at $x = 0$ at its own surface is [13]:

$$- \frac{I \eta k}{4} H_o^{(2)} (k a) \tag{2.109}$$

where $\eta = 377$ ohms, $k = 2\pi/\lambda$, and $H_o^{(2)}$ is a zero order Hankel function of the second kind.

The wire at $x = 0$ is also in the field of the remaining wires. A wire at $x = nS$ carries total current

$$I e^{-j n k_x S}$$

where $k_x = k \cos \theta$. Hence it generates a field at the center of the wire located at $x = 0$ that is given by

$$- \frac{I \eta k}{4} e^{-j n k_x S} H_o^{(2)} (n k S) \tag{2.110}$$

Equation 2.110 will henceforth be used to approximate the field generated at the surface of the wire at $x = 0$ by the wire at $x = nS$. The approximation will be accurate provided ka is small and $S >> a$. Summing the incident field at the field of the wires, and setting the result equal to zero, gives

$$I = \frac{4 E_z \text{ (incident)}}{\eta k \left(H_o^{(2)} (k a) + 2 \sum_{n=1}^{\infty} \cos (n k_x S) H_o^{(2)} (n k S) \right)} \tag{2.111}$$

Equation (2.111) will now be used to determine the reradiation from the wires. Considering the current distribution in the $y = 0$ plane as a succession of current filaments separated by S and carrying current of magnitude I and phase $-k_x x$ leads to the following expansion in terms of current waves:

$$I(x) = \frac{I}{S} e^{-jk_x k} \left(1 + e^{-j \frac{2\pi x}{S}} + e^{+j \frac{2\pi x}{S}} + e^{-j \frac{4\pi x}{S}} + e^{+j \frac{4\pi x}{S}} + \text{-----} \right) \tag{2.112}$$

In Equation (2.112) the bracketed series is the Fourier expansion of a train of impulses separated by S. With the notation $k_S = \frac{2\pi}{S}$, the spatial frequency spectrum of Equation (2.112) is

$$-k_x$$

$$-k_x \pm k_S$$

$$-k_x \pm 2k_S$$

etc.

For incident angles close to grazing, $k_x \sim k$. Therefore, if $k_s > 2k$, the amplitude of all spatial frequency components other than k_x exceeds k. These other components are then slow waves and do not radiate. Hence, for angles near grazing, reradiation from the wire ground plane will be observed only in the direction that would be expected if the wire grid was a solid sheet, if $S < \lambda/2$. The current wave that excites this reradiation is

$$\frac{I}{S} e^{-j k_x x} \tag{2.113}$$

The plane wave excited by the current wave (Equation 2.113) in the region $y > 0$ has field components

$$H_x = -\frac{I}{2S} e^{-j k (x \cos\theta + y \sin\theta)} \tag{2.114}$$

$$H_y = +\frac{k_x}{2k_y} \frac{I}{S} e^{-j k (x \cos\theta + y \sin\theta)} \tag{2.115}$$

$$E_z = -\frac{\eta I}{2S \sin\theta} e^{-j k (x \cos\theta + y \sin\theta)} \tag{2.116}$$

Substitution of (2.111) in (2.116) gives the following for the reflection coefficient ρ:

$$\rho = -\frac{2}{k S \sin\theta \left(H_o^{(2)}(k a) + 2 \sum_{n=1}^{\infty} \cos(n k_x S) H_o^{(2)}(n k S)\right)} \tag{2.117}$$

The validity of (2.117) and an estimate of the departure of ρ from -1 may be established by the use of the following identity [14]:

$$\int H_o^{(2)}(x) \cos b x \, d x = \frac{1}{\sqrt{1 - b^2}} \tag{2.118}$$

With the identifications

$$x \longrightarrow k x$$

$$b \longrightarrow \cos \theta$$

Equation (2.118) becomes

$$\sin \theta \int_o^{\infty} H_o^{(2)}(k x) \cos (k_x x) \, d (k x) = 1 \tag{2.119}$$

Examining (2.117) shows its denominator to be a rectangular approximation to the left side of (2.119). Therefore, as S and a approach zero, ρ as given by (2.117) approaches -1 as it should. For finite S and a, the largest difference between the summation in (2.117) and unit will be due to the rectangular approximation of the integral from x = 0 to x = S by

$$\frac{k S}{2} H_o^{(2)}(k a) \tag{2.120}$$

If k a is small, $H_o^{(2)} \longrightarrow -j \ln (k a)$, thus leading to an excessively large, positive, imaginary component of x, the denominator of (2.117). Therefore, one may expect that, for very small wire diameters, or large spacings, the reflection coefficient will have lagging phase and be considerably less than unity. As θ decreases, the magnitude of the difference between the rectangular approximation between x = 0 and x = S and the exact integral decreases because of the sin (θ) term; hence, it is to be expected that the reflection coefficient will increase in magnitude and approach zero phase as $\theta \longrightarrow 0$.

c. Computations. Equation (2.117) was programmed for machine computation for a set of wire diameters ranging from 1/16" to 1/4", a range of wire spacings from .1λ to .4λ, and for θ = 5°. A program listing and printout is given in Figures 2-107, 2-108, and 2-109. Generally, results were as expected. Reflection coefficient was found to decrease in magnitude and lag in phase as spacing was increased for a given wire diameter. For a given spacing, reflection coefficient increased and phase lag decreased as wire size increased. An anomalous result was

the indication of reflection coefficients slightly exceeding unity for the smaller spacings. This result is unquestionably due to the approximations mentioned in the theory section, which become poorer for small spacings. For relatively large spacings and small wire diameters, which are of practical interest, the approximations are good and the results given in the printout are believed accurate.

In summary, this study has revealed the following:

1) Results indicate that a wire diameter of 1/16" with spacing .4λ will give a reflection coefficient of .94 $\angle$ 16.5° for an incidence angle of 5°. For smaller incidence angles, smaller spacings or thicker wire, the reflection coefficient is closer to unity.

2) If wire spacing exceeds one-half wavelength, spurious reflections will appear at angles other than the optical angle.

PROGRAMMER REGION		ACCURACY FIXED	INPUT	TIME 1500	ACCORDS [illegible]	CMAP F	LIST Y	EXEC F	OBJ	CMAP Y	LMAP Y	DUMP	SERIAL 26310

```
/*                    [illegible]
0001                  PRINT 10
0002          10      FORMAT(35X,*D[illegible]*,[illegible],*Z-A[illegible]*, X,*AM2, RHO*,2X,*PHASE RHO*,
                    X ///)
0003          21      PI=3.141593
0004          22      PI2=2.*PI
0005          23      TH=(PI/180.)**2
0006                  CT=COS(TH)
0007                  DO [illegible] N=1,4
0008                  D=.[illegible]
0009                  AK=(2.*N*PI)/([illegible]*36.)
0010          20      X=AK
0011                  CALL [illegible](X,0.,0.,[illegible],1,[illegible])
0012                  IY=FLOAT(AK)
0013          [illegible]  [illegible]
0014          [illegible]  Y=[illegible]
0015                  DO [illegible] M=1,7,2
0016                  MM=M-1
0017                  [illegible]
0018                  SK=2.*PI*[illegible]
0019          32      [illegible]
0020                  AM=[illegible]
0021          33      SUMR=0
0022          34      SUMI=0
0023                  DO [illegible] J=1,44
0024          36      AAJ=J*AK
0025          37      X=AA
0026                  AB=AA**T
0027                  CF=COS(AB)
0028                  IF (AA-[illegible]) [illegible]
0029          4       CALL [illegible](X,[illegible],[illegible],[illegible])
0030          41      CALL [illegible](X,0.,Y,IER)
0031                  ADD=[illegible]*C
0032                  ADD=DY*2.*C
0033          44      GO TO [illegible]
0034          5       ZZZ=([illegible]((CF/AA))**2.*C
0035          45      ZZ=AA-PI/4.
0036          53      ADD=ZZZ*COS(ZZ)
0037          52      ADD=ZZZ*SIN(ZZ)
0038          9       SUMR=SUMR+ADD
0039          3       SUMI=SUMI+ADD
0040          53      DENR=SUMR**2
0041          61      DENI=SUMI**2
0042          63      AR=1./SQRT(DENR*D+DENI*D**2)
0043          65      PH=-(180./PI)*(ATAN(SUMI/SUMR))
0044          1       WRITE(3,20)D,AK,AR,PH
0045          20      FORMAT(30X,4F12.3)
0046          2       WRITE(3,80)
0047          80      FORMAT(///)
0048                  STOP
0049                  END
```

SCALAR MAP

SYMBOL	LOCATION	SYMBOL	LOCATION	SYMBOL	LOCATION	SYMBOL	LOCATION	SYMBOL	LOCATION
PI	000094	FF	000094	TH	000090	CT	000090	N	0000C4
D	0000C8	AK	000[illegible]CC	X	000000	BJ	0000D4	IER	0000D8

Figure 2-107. Program for Calculating Reflection Coefficients.

```
OHIO UNIVERSITY  O U I J I  SYSTEM   FORTRAN IV  G-LEVEL COMPILER                    JULY 1, 1971              PAGE     0002

BY        0000DC    R         0000E0    Y         0000E4    M         0000E8    MN        0000EC
S         0000F0    SK        0000F4    F         0000F8    MM        0000FC    SUMR      000100
SUMI      000104    J         000108    AA        00010C    AB        000110    C         000114
ADDR      000118    ADDI      00011C    ZZZ       000120    ZZ        000124    DENR      000128
DENI      00012C    AR        000130    PR        000134
                                   SUBPROGRAMS CALLED

SYMBOL    LOCATION  SYMBOL    LOCATION  SYMBOL    LOCATION  SYMBOL    LOCATION  SYMBOL    LOCATION
IBCOM#    000138    BESJ      00013C    BESY      000140    COS       000144    ALOG      000148
SIN       00014C    SQRT      000150    ATAN      000154
                                   LABEL MAP

LABEL     LOCATION  LABEL     LOCATION  LABEL     LOCATION  LABEL     LOCATION  LABEL     LOCATION
   14     0001F0       21     00021E       22     00022A       23     000236       26     000286
   29     0002DA       30     0002E2       32     000354       33     00037A       34     000382
   36     000392       37     00030A        4     0003EC       41     0003F6       44     000424
    5     00042A       46     000450       50     000462       52     000474        8     000486
    3     000492       60     000494       61     000400       63     0004CC       65     0004F6
    1     000522       70     00056E        2     000580       80     0005A6 *
  TOTAL MEMORY REQUIREMENTS 00063C BYTES      MAIN44
  /DA1\

                                                                                                          PAGE     0003
MODULE   ADDR  LENGTH          ENTRY POINTS (E), EXTERNAL (X) AND COMMON (C) REFERENCES
MAIN44#  0F000          F-MAIN44  0F000     X-IBCOM#          X-BESJ            X-BESY
                        X-COS               X-ALOG            X-SIN             X-SQRT
                 00630  X-ATAN

  MODULES LOADED FROM REQUEST - CALL LIBRARY

BESJ     0F640 002E8
BESY#    0F928          E-BESY    0F929     X-SQRT            X-SIN             X-COS
                 00868  X-ALOG

  MODULES LOADED FROM AUTO - CALL LIBRARY

BOASSCN  10190 00100    X-IBCOM#          E-SIN     101AC     E-COS     10194
BOASLOG  10290 00108    X-IBCOM#          E-ALOG    102AE     E-ALOG10  10298
BOASSQRT 10398 000A8    X-IBCOM#          E-SQRT    1039E
BOASATN2 10440 00170    X-IBCOM#          E-ATAN    1045C     E-ATAN2   10446
  MODULE SUCCESSFULLY LOADED --- EXECUTION BEGUN AT 0F000 / 2FA08 BYTES OF STORAGE REMAINING

                                DIAMETER  S/LAMBDA  AMP. RHO  PHASE RHO
```

Figure 2-108. Continuations of Programs for Calculating Reflection Coefficients.

Diameter in Inches	Spacing in Inches	Reflection Coefficient Magnitude	Phase
0.063	0.100	1.042	-4.274
0.063	0.200	1.043	5.824
0.063	0.300	0.994	10.270
0.063	0.400	0.936	16.516
0.125	0.100	1.042	3.572
0.125	0.200	1.046	4.391
0.125	0.300	1.000	8.228
0.125	0.400	0.948	14.000
0.188	0.100	1.043	3.162
0.188	0.200	1.047	3.559
0.188	0.300	1.002	7.024
0.188	0.400	0.954	12.501
0.250	0.100	1.043	2.871
0.250	0.200	1.047	2.967

Figure 2-109. Reflection Coefficients for Various Wire Sizes and Spacings.

H. L-Band Glide Path Investigation

Consideration is being given to techniques for mixing in the airborne signals which can be transmitted from the glide path array when operating at L-Band. In addition to the pure glide path signal the anticipation is that a local oscillator signal may also be radiated so that a difference frequency would be obtained which would be in the present glide path frequency band.

A method that can be used to derive a standard 330 MHz glide path signal from an L-Band glide path is shown in Figure 2-110.

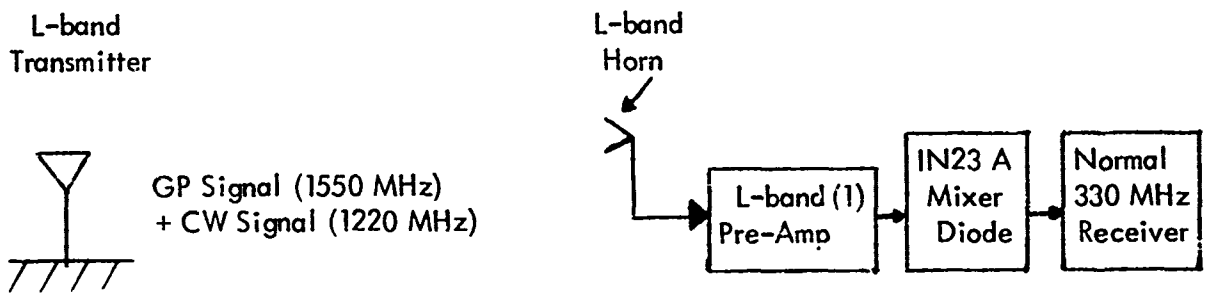

(1) HP 35005A--Cost $1,500

(2) IN23 A Diode--Cost $3

Figure 2-110. Suggested Laboratory Implementation of L-Band Glide Path.

Note that this scheme requires a continuous wave signal at 1220 MHz to be transmitted in addition to the normal L-Band information. The 1220 MHZ signal is amplified along with the 1550 MHz signal and the two spectra are mixed by a diode to provide the glide path receiver with a difference signal in the 330 MHz band.

This airborne add-on device can be used to make a standard glide path receiver compatible with an L-Band facility. The items shown in the figure are standard off-the-shelf hardware. Typical prices are given in the figure. Plans include purchase of these items and flight measurements to demonstrate feasibility of the L-Band compatibility pending availability of ground-based equipment presently at NAFEC. Ground-based equipment presently being shipped by the FAA to Ohio will be used in the experiments.

III ILS LOCALIZER

A. Design of a Localizer Array

1. Design and Flight Testing of a Localizer Array That Provides Clearance Signal Only Within ± 35° of Center Line.

a. Introduction. If operations require localizer clearance only within ± 35° from centerline, any sideband signal outside of the ± 35° sector is of no value and is a potential source of path roughness if reflecting obstacles exist outside the required clearance sector. This section describes the design and testing of a 15-element localizer array which generates sufficient sideband signal within ± 35° to produce clearance, and low sideband signal outside ± 35°. The aperture of the prototype is 88 feet, and the elements employed are Scanwell V-Ring loops. The choice of element was dictated by availability of the Scanwell antennas, see Figure 3-1, but dipoles or omnidirectional loops could have been used with no essential change in design or performance. The array described is not claimed to be broad-band in that precise adjustment of feeder line length is required. Also, it is clear that numerous other combinations as to number of elements and element spacing are possible.

b. Array Design. A uniformly spaced array is unsuitable for the application at hand, since the element-to-element spacing would have to exceed 180° in order to keep the number of elements reasonably low, and to avoid large mutual coupling between elements. Therefore, at some azimuth angle θ_o the element-to-element phase shift would become 180°, and the sideband pattern $P_s(\theta)$ for angles exceeding θ_o could not be independently specified but would be determined from

$$P_s(\theta_o + \psi) = -P_s(\theta - \psi) \tag{3.1}$$

Similarly, the carrier pattern $P_c(\theta)$ for angles exceeding θ_o would be determined by

$$P_c(\theta_o + \psi) = P_c(\theta_o - \psi) \tag{3.2}$$

Hence a non-uniformly spaced array was necessary, and such an array was synthesized by least squares matching to a specified sideband pattern P_{ss}. Designating the distance between the center of the array and the Nth element by S_n, and the sideband drive to the Nth element by A_n, the integrated squared difference between the generated pattern and the specified pattern is given by

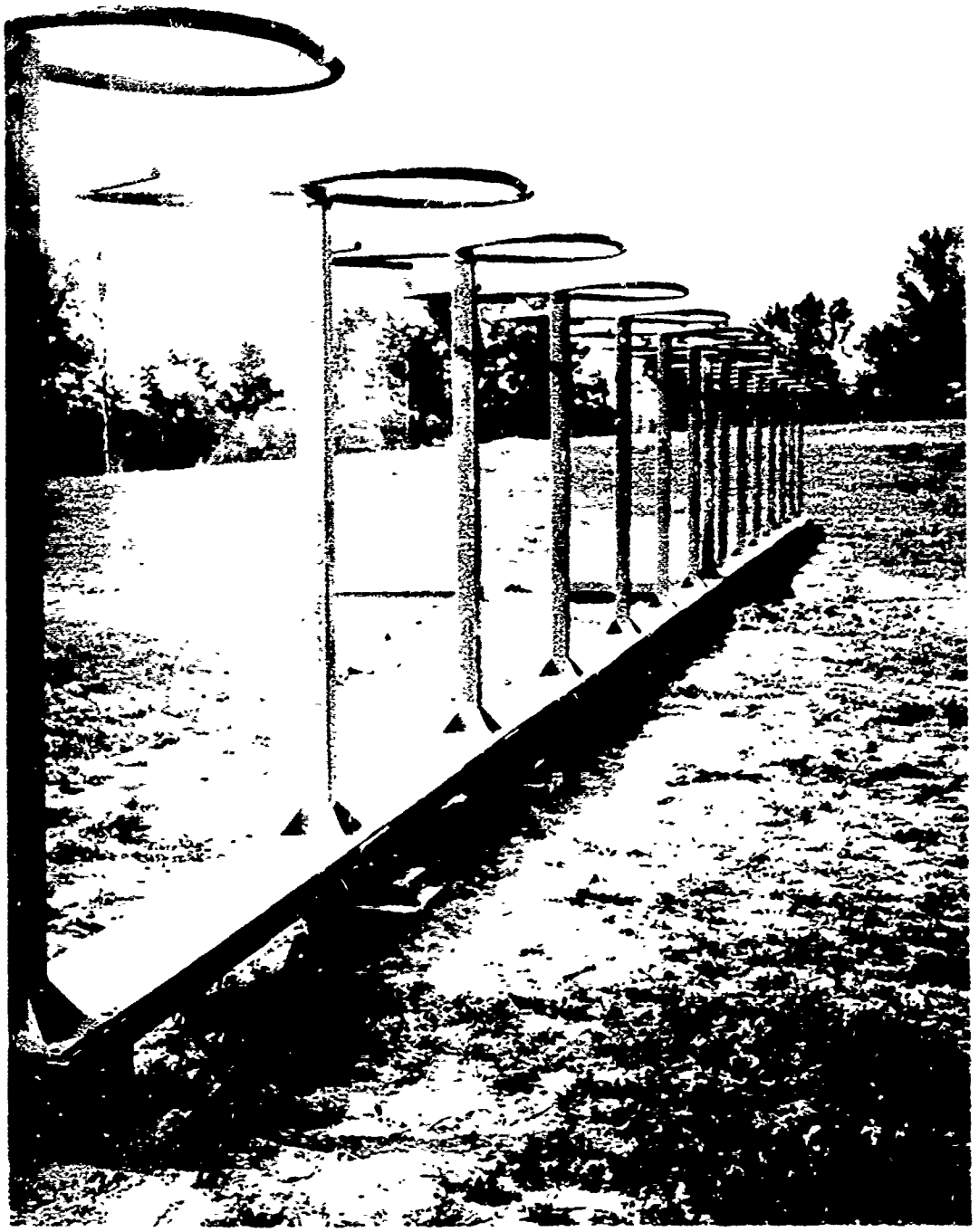

Figure 3-1. V-Ring Array at Ohio University Test Site Used for Testing the Special Configuration to Provide Localizer Coverage only Within ± 35°. Careful Inspection of the Picture Will Reveal a White Radome on Top of Each Pedestal. These Radomes House the Integral Monitor Coupling Probes.

$$E = \int_0^1 (P_{ss} - \Sigma A_n \sin(S_n \alpha))^2 \, d\alpha \tag{3.3}$$

where $\alpha = \sin\theta$

If S_n are specified, E can be minimized by setting

$$\frac{\partial E}{\partial A_n} = 0 \tag{3.4}$$

Applying 3.4 to 3.3 leads to the following set of linear equations in which A_n are the unknowns:

$$\sum_n A_n \int_0 \sin(S_n \alpha) \sin(S_p \alpha) \, d\alpha = \int_0^1 P_{ss} \sin(S_p \alpha), \; p = 1, N \tag{3.5}$$

Using (3.5) and assumed values for N and S_n, A_n, were computed and the resulting fit between P_{ss} and the generated pattern noted. Trials showed that $N<7$ was incapable of producing an acceptable fit, and that with $N = 7$, a good fit was generated by the following spacings (in radians) and amplitudes.

$$\begin{aligned} S_1 &= 4.0 & A_1 &= 1.00 \\ S_2 &= 8.4 & A_2 &= .700 \\ S_3 &= 13.0 & A_3 &= .665 \\ S_4 &= 17.2 & A_4 &= .570 \\ S_5 &= 22.0 & A_5 &= .449 \\ S_6 &= 26.3 & A_6 &= .286 \\ S_7 &= 30.5 & A_7 &= .105 \end{aligned} \tag{3.6}$$

In the foregoing, P_{ss} was specified as

$$P_{ss} = \frac{1 - \cos(26\alpha)}{18.7\alpha}, \quad 0 < \theta < 9° \tag{3.7a}$$

$$P_{ss} = .2 + \frac{.0114}{\alpha - .123}, \quad 9° < \theta < 32° \tag{3.7b}$$

$$P_{ss} = .2189^{-56.5(\alpha - .53)^2}, \quad 32° < \theta < 90° \tag{3.7c}$$

Considerations dictating the choice (3.7) were: (a) sideband signal between 9° and 35° specified as minimum value required to maintain coverage. SB in this range exceeds .20 of peak SB; (b) negligible sideband signal between about 38° and 90°; (c) continuity in amplitude and approximate continuity in slope; (d) peak sideband value of 1.0 for convenient normalization; and (e) "natural" shape of central peak, i. e., higher slope on centerline side of peak than on the other side.

Figure 3-2 shows the sideband pattern generated by an array of V-Rings with spacings and amplitudes given in Equation (3.6). The pattern would be substantially identical for dipole elements. If omnidirectional elements were used, an amplitude rise to 0.09 of peak would occur between 70° and 90°.

The required carrier pattern is determined from the generated sideband pattern by the required DDM, which is proportional to (sidebands/carrier). Designating the sideband pattern generated by an array with spacings and amplitudes (3.6) by P_{gs}, the required carrier pattern P_c was taken as

$$P_c = .0610\,(P_{gs}/\alpha) \qquad 0 < \theta < 4.2° \tag{3.8a}$$

$$P_c = (P_{gs}/1.2) \qquad 4.2° < \theta < 40° \tag{3.8b}$$

$$P_c = 0 \qquad \theta > 40° \tag{3.8c}$$

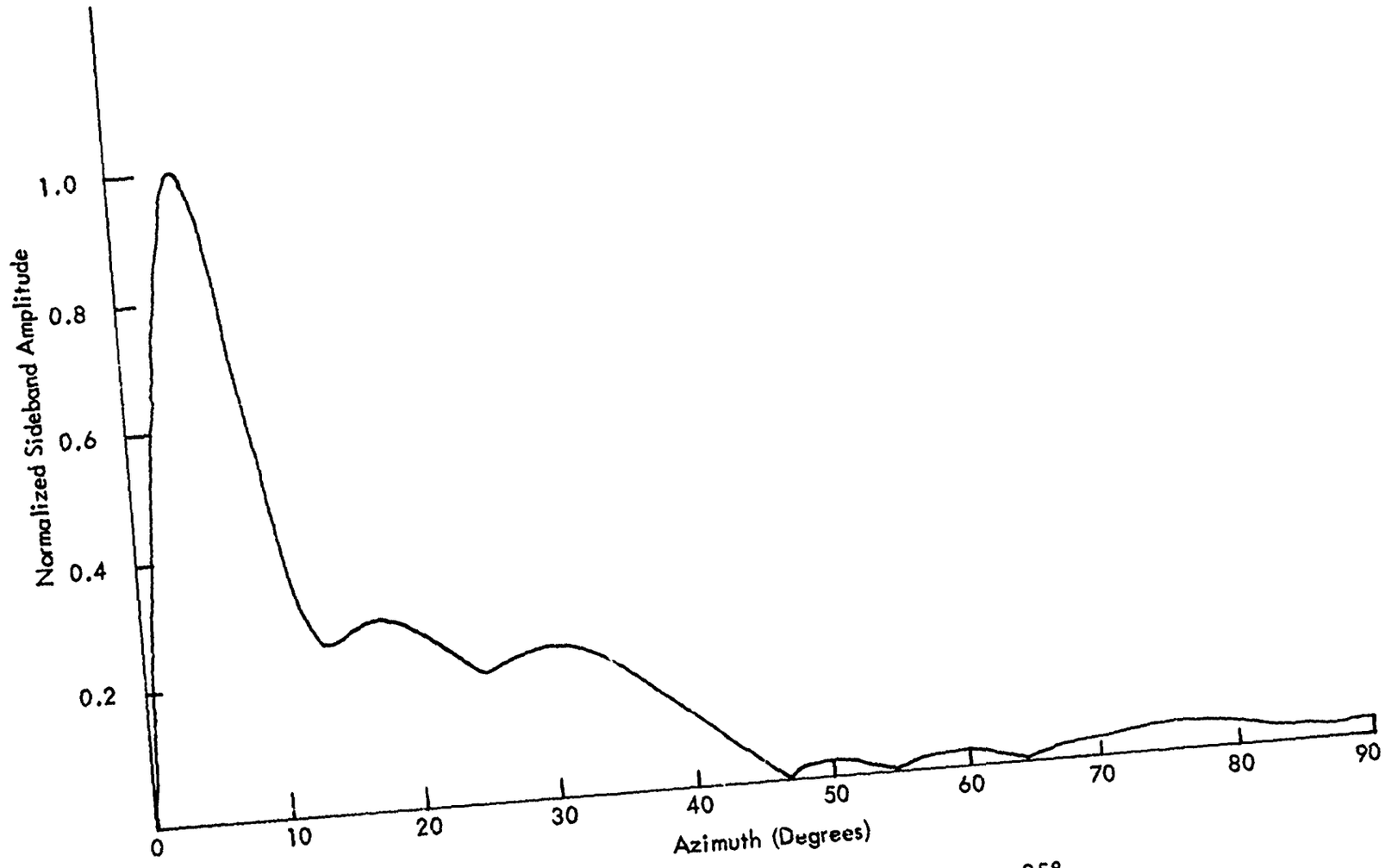

Figure 3-2. Design Sideband Pattern -- 35°.

Equation (3.8a) specifies linear DDM between 0° and 4.2°, the constant .0610 being chosen to give equality of P_c and P_{gs} at 3.5°. Inspection of (3.8b) shows that, if (3.8a) is fulfilled, 180 microamps of clearance at a course width of ±3.5° (7° total width) is specified by (3.8b).

Synthesis of the carrier array was carried out by least squares matching to (3.8). Since the spacings S_n had already been determined from the synthesis of the sideband array, they were not available as parameters in the carrier synthesis. The carrier amplitudes B_n obtained by least squares are

$$
\begin{aligned}
B_0 &= 1.0 \text{ (center element)} \\
B_1 &= .478 \\
B_2 &= .292 \\
B_3 &= .195 \\
B_4 &= .106 \\
B_5 &= .031 \\
B_6 &\quad \text{Negligible} \\
B_7 &\quad \text{Negligible}
\end{aligned}
\tag{3.9}
$$

The carrier pattern generated by an array of V-Rings having the amplitudes (3.9) and the spacings (3.6) is shown in Figure 3-3. DDM generated by the array specified by (3.9) and (3.6), at a course width of 7°, is shown in Figure 3-4. Although the fit between the generated and specified carrier patterns is not as good as for the sideband pattern (due to non-availability of S_n as parameters), it was accepted, as clearance DDM was adequate, and the presence of carrier signal outside 35° could have only a second order effect on scalloping.

c. Distributor and Suppression of Parasitics. Suppression of parasitics is essential to the operation of the array described here, as relatively small amplitude and phase errors caused by parasitics can lead to low clearances in the 10°- 35° region, where design signals are low. The type of distributor employed makes possible suppression of parasitics to a degree limited only by losses in the feeder cable (20 db suppression for 60 foot RG-8 feeders). The distributor consists of 50 ohm shorted stubs, $\lambda/4$ long, tapped at points computed to give the desired division ratios and connected to the feeder through 50 ohm lines whose lengths compensate for the phase shift through the divider. A divider section is illustrated in Figure 3-5.

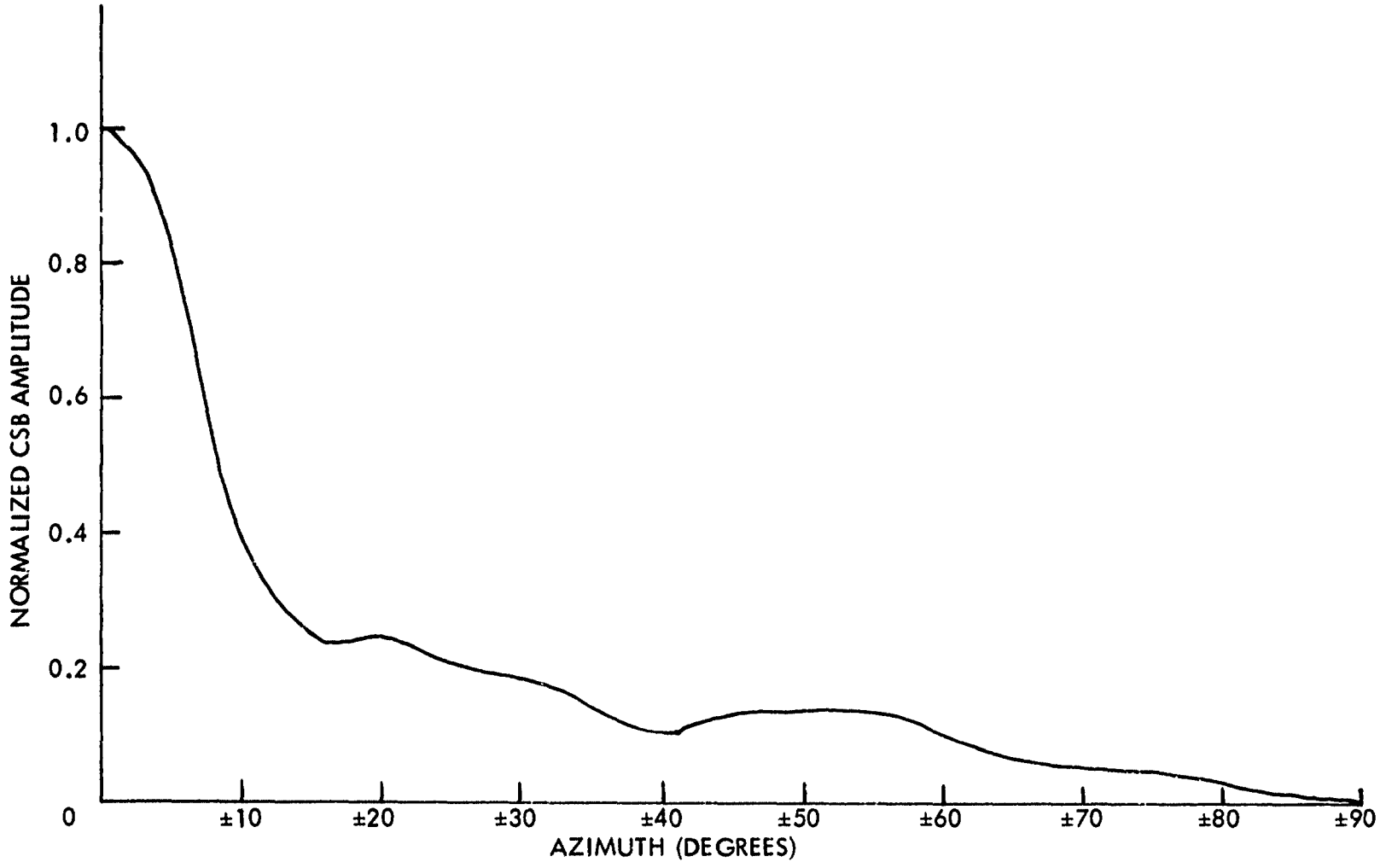

Figure 3-3. Design CSB Pattern -- 35° Localizer.

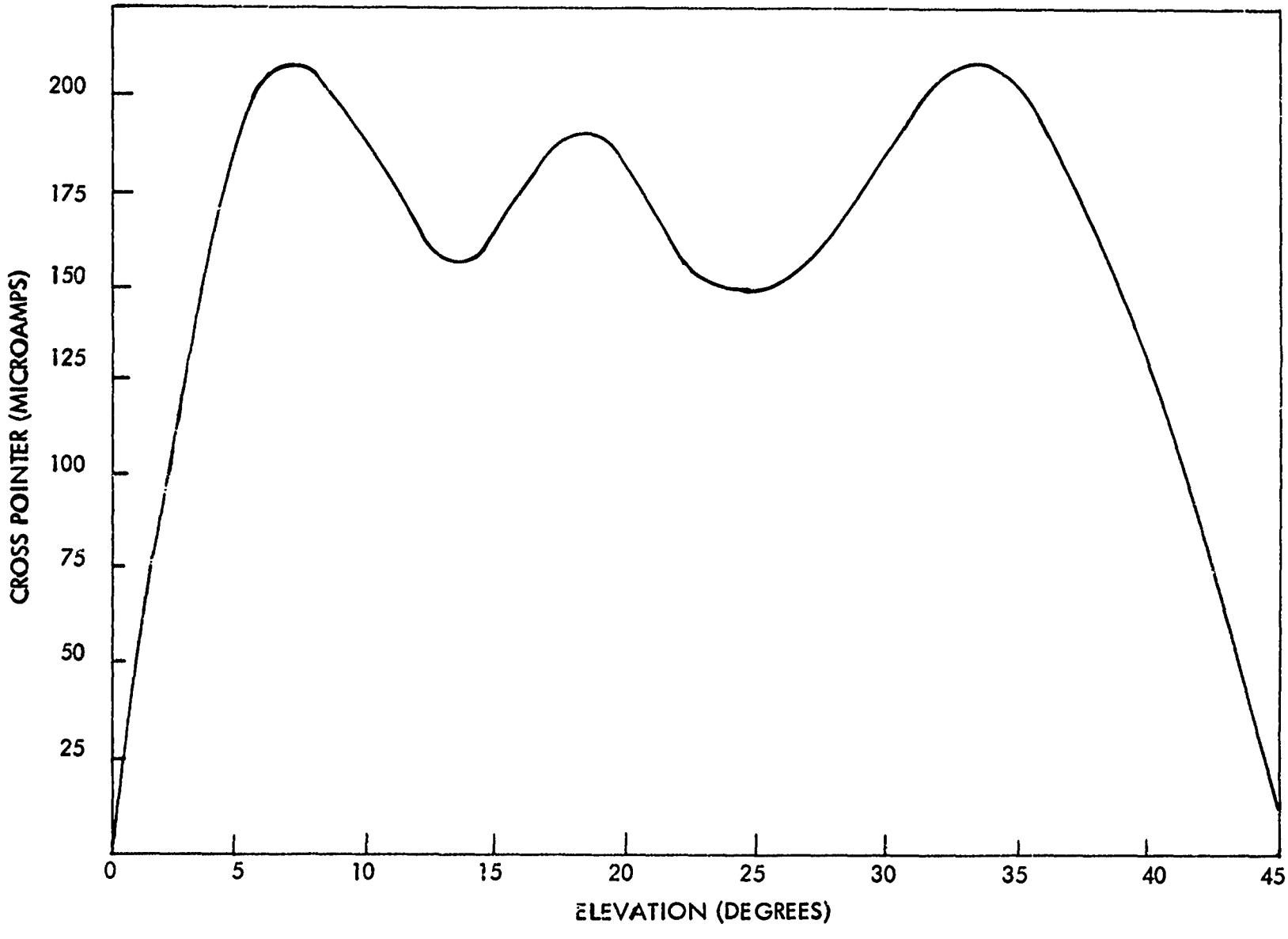

Figure 3-4. Computed DDM Width = 7.0°.

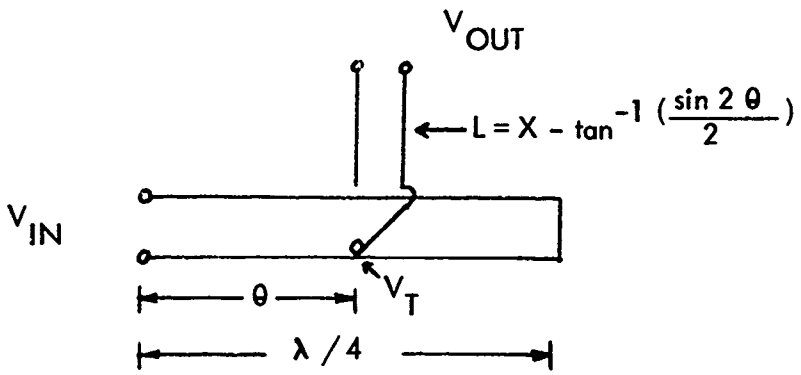

Figure 3-5. Divider Section.

It can be shown that, if a matched load is connected across the output terminals

$$\frac{V_T}{V_{IN}} = \frac{\cos\theta}{1 + j\,\frac{\sin 2\theta}{2}} \tag{3.10}$$

Thus, $0 < \left|V_T / V_{IN}\right| < 1$. Phase shift between V_T and V_{IN} is $-\tan^{-1}((\sin 2\theta)/2)$, and is compensated for by using the line of length L in the diagram. The properties of the distributor which make possible parasitic suppression are: (a) input admittance looking into the output terminal, with the input terminal shorted, is reactive and independent of the position of the tap point; and (b) if a number of dividers are connected to a common input node, the mutual admittance between any two output nodes is zero.

Property (a) can be verified by the use of elementary transmission line theory, or can be deduced from general network theory as follows. Suppose a two port reactive network containing an adjustable parameter has the property that, when a resistive load is connected across its output port, the phase of the voltage appearing across the load is independent of the adjustable parameter. Numbering the input port 1 and the output 2 and applying general network theory gives

$$I_2 = Y_{12} V_1 + Y_{22} R I_2$$

or

$$\frac{I_2}{V_1} = \frac{Y_{12}}{1 - Y_{22} R} \qquad \text{(R = load resistance)} \tag{3.11}$$

Since Y_{12} is reactive and the phase of (I_2 / V_1) is independent of parameter change, Y_{22} must be independent of parcmeter change.

Property (b) follows immediately from the definition of mutual admittance. The mutual admittance between two output nodes is defined as the radio of the current in one to the voltage in the other with all other nodes, including the input node, shorted. But, with the input node shorted, all output nodes are completely decoupled and $Y_{mn} = 0, \ m \neq n$.

From property (b), the distributor can be described by an abbreviated set of admittance parameters, as follows:

(0th node = input)

$$I_1 = Y_{10} V_0 + Y_{11} V_1$$

$$I_2 = Y_{20} V_0 + Y_{22} V_2$$

etc., N equations (3.12)

The system of N antennas to which the distributor characterized by (3.12) is connected can be described by a set of impedance parameters as follows:

$$V_n = \sum_{m=1}^{n} Z_{nm} I_m \qquad n \sigma 1, 2 \ldots N \tag{3.13}$$

Solving (3.12) and (3.13) for I_n gives

$$I_n = \frac{Y_{no} V_o}{1 - Y_{nn} Z_{nn}} + \frac{Y_{nn} \Sigma Z_{nm} I_m}{1 - Y_{nn} Z_{nn}} \tag{3.14}$$

If the distributor is designed on the basis of isolated loads of magnitude Z_{nn} then the current in a mutually coupled antenna system will differ from the design currents by the second term in (3.14). If Y_{nn} can be made zero for all n, then mutual coupling disturbances can be suppressed. Y_{nn} is the input admittance looking into the nth feeder, with the input node shorted. For a distributor as described in the foregoing, it is equal for all n and reactive, by virtue of property (b). Hence, by adjustment of feeder length, Y_{nn} can be made zero for all n, since a reactive load can always be transformed to an open circuit by transformation through a length of transmission line.

Feeder length for maximum parasitic suppression was determined experimentally by the following procedure: (a) short the carrier input node of the distributor; (b) excite the center element of the array with CW; (c) connect elements 1 left and 1 right to the distributor through equal length feeder cables, each in series with a line stretcher; (d) mount a current measuring pickup on 1 left (or 1 right) and connect it to an RF voltmeter; and (e) adjust the line stretchers symmetrically for minimum parasitic current in the no. 1 elements.

Table 3-1 shows experimental antenna current distribution, with feeders cut as above, in comparison with design currents and currents generated by the distributor working into dummy loads.

d. Flight Testing. CW sideband and carrier patterns were measured in orbital flight through ± 90° from centerline. A 51R-3 receiver with AGC disabled and a diode detector added to the last IF was used to amplify and detect the receiver signal. The orbit was flown at an elevation of 15° to minimize site effects. Results are shown in Figures 3-6 and 3-7, which may be compared with Figures 3-2 and 3-3. It will be noted that the signal strength scale of Figures 3-6 and 3-7 is non-linear.

Following CW measurements, the array was connected as a localizer and orbital DDM measurements were made through ± 90°, at measured widths of 4.68° and 7.0° successively. Results are shown in Figures 3-8, and 3-9. Figure 3-9 may be compared with Figure 3-4.

SIDEBAND				
Element Number	Design	Distributor Into Dummy Loads	Antenna with Feeders Cut to Suppress Parasitics	
			Left	Right
1	1.0 ∠ 0°	1.0 ∠ 2°	1.04 ∠ 0°	1.04 ∠ 0°
2	.70 ∠ 0°	.70 ∠ -1°	.70 ∠ -5°	.67 ∠ -9°
3	.67 ∠ 0°	.65 ∠ +1°	.67 ∠ -3°	.67 ∠ +3°
4	.57 ∠ 0°	.55 ∠ 0°	.56 ∠ -4°	.56 ∠ -8°
5	.45 ∠ 0°	.44 ∠ 0°	.46 ∠ +2°	.45 ∠ -3°
6	.29 ∠ 0°	.29 ∠ +1°	.27 ∠ +1°	.30 ∠ -2°
7	.11 ∠ 0°	.12 ∠ -1°	.11 ∠ +5°	.12 ∠ -5°
CARRIER				
Center	1.0 ∠ 0°	1.0 ∠ 0°	.92 ∠ -5°	.92 ∠ -5°
1	.48 ∠ 0°	.48 ∠ 0°	.48 ∠ +4°	.48 ∠ +2°
2	.29 ∠ 0°	.29 ∠ +1°	.29 ∠ -2°	.28 ∠ -6°
3	.20 ∠ 0°	.20 ∠ 0°	.20 ∠ -1°	.20 ∠ +4°
4	.11 ∠ 0°	.11 ∠ 0°	.11 ∠ -1°	.11 ∠ -5°
5	.03 ∠ 0°	.04 ∠ 0°	.04 ∠ +3°	.04 ∠ -3°
6 and 7	Negligible	---------	---------	---------

Table 3-1. 35° Localizer SB and CSB Currents at 110.5 MHz.

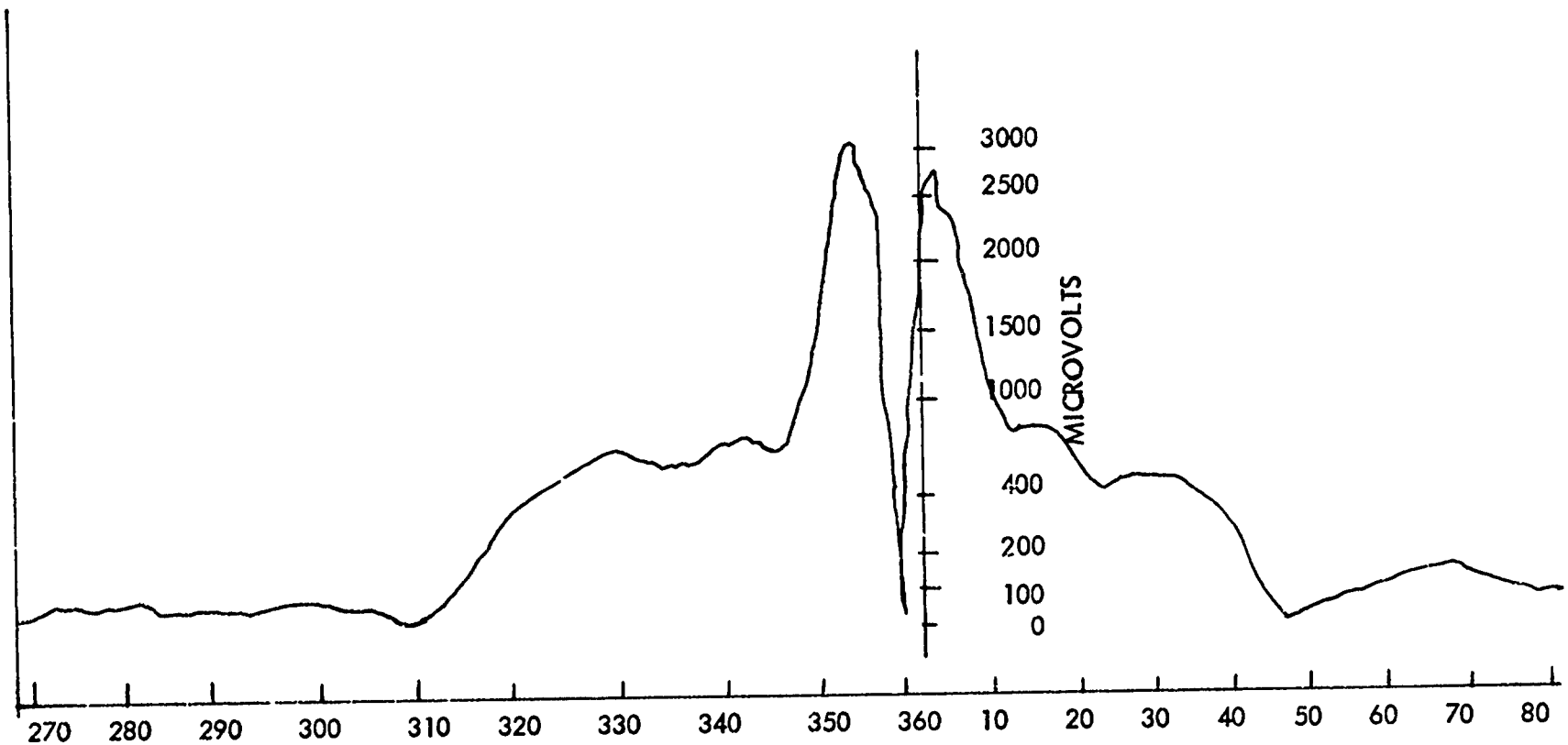

Figure 3-6. Measured SB Pattern -- 35° Localizer.

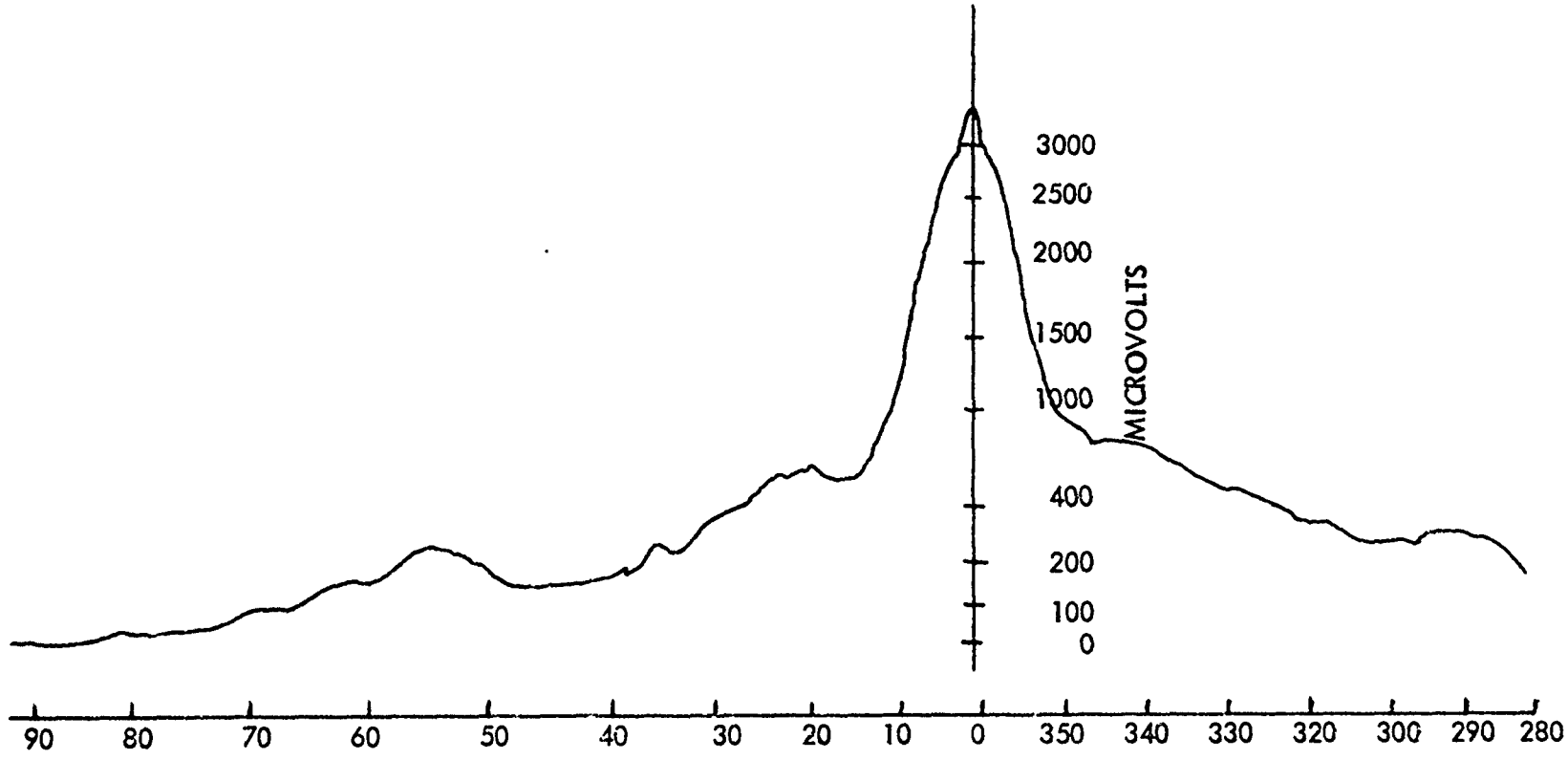

Figure 3-7. Measured CSB Pattern -- 35° Localizer.

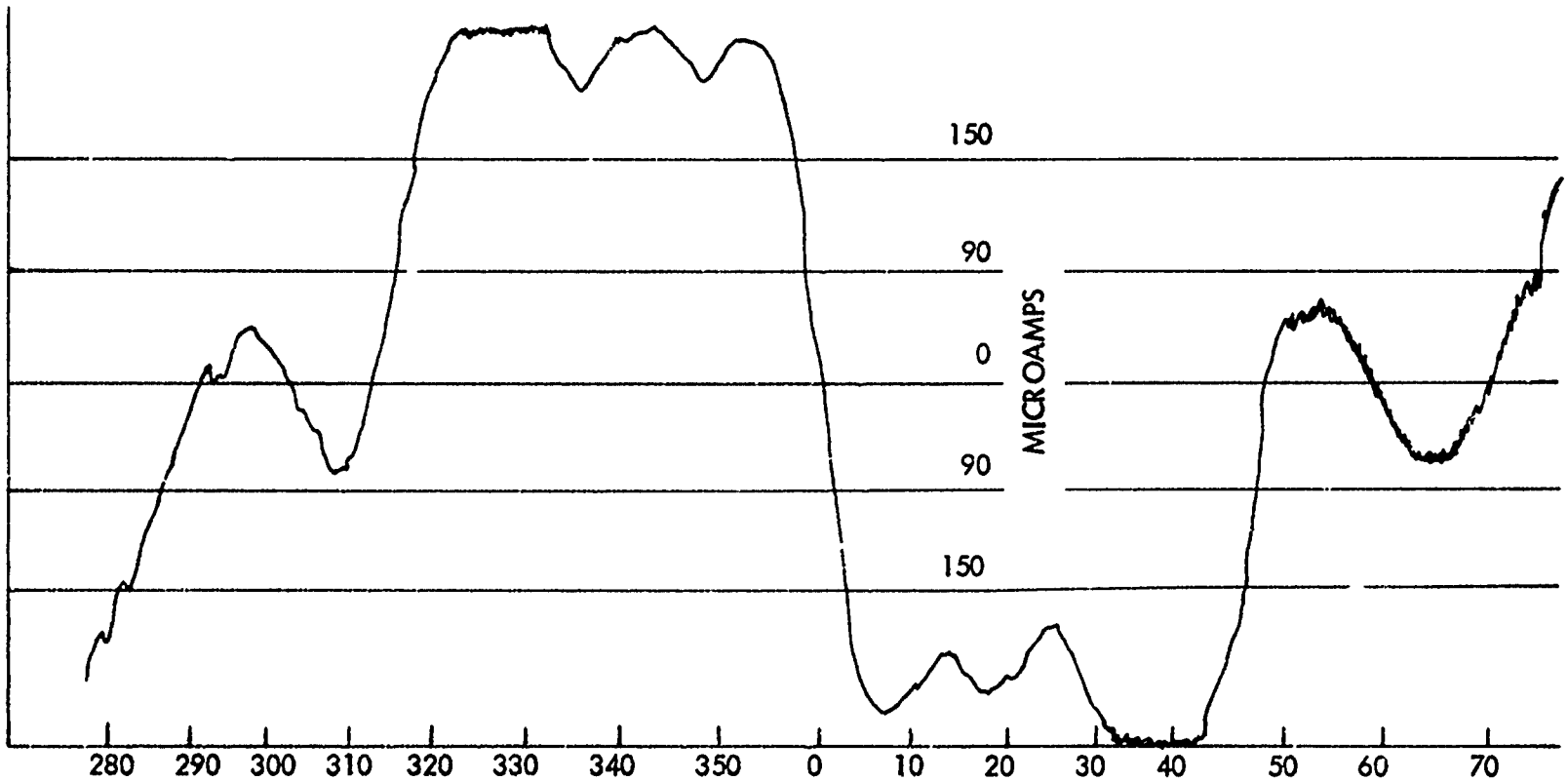

Figure 3-8. Measured DDM - 35° Localizer Width = 4.68°.

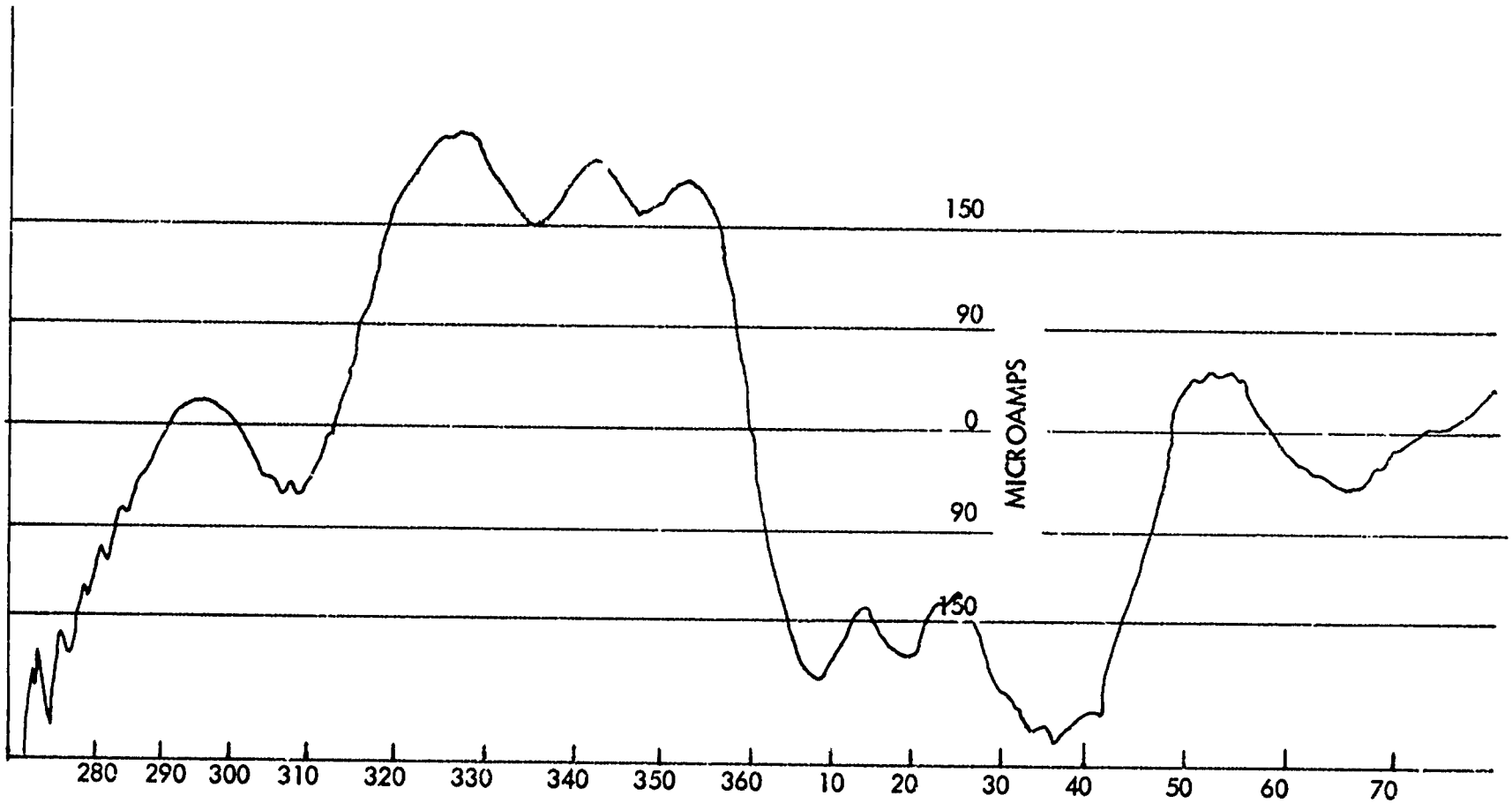

Figure 3-9. Measured DDM - 35° Localizer Width = 7.0°.

e. Computed Comparison of Scalloping Generated by 35° Localizer and Other Localizer Arrays. The scalloping caused by reflection from a single obstacle can be expressed as

$$K \times \frac{\text{SB Signal Incident on Obstacle}}{\dfrac{d\,(SB)}{d\,\theta}} \quad \text{on centerline} \tag{3.15}$$

where K is a complex constant characteristic of the scattering properties of the obstacle. When the ratio of scalloping produced by a particular obstacle illuminated by the 35° localizer to the scattering produced by the same obstacle when illuminated by another type of localizer is taken, K cancels and the ratio is a function only of the sideband patterns of the two arrays.

The ratio R is given by (3.16)

$$R(\theta) = \frac{\text{35° Localizer SB at Azimuth } \theta}{\text{Other localizer SB at Azimuth } \theta} \times \frac{\left(\dfrac{d(SB)}{d\,\theta}\right)_{\theta = 0,\ \text{other loc.}}}{\left(\dfrac{d\,(SB)}{d\,\theta}\right)_{\theta = 0,\ 35°\ \text{loc.}}}$$

R is plotted in Figure3-10 foran 8-loop and for a 105-foot aperture Type 3 Scanwell Localizer.

f. Conclusions. The following can be concluded from this investigation:

(1) The 35° localizer is capable of producing substantial reductions in scalloping caused by obstacles in the range 35° to 90°.

(2) Precise antenna currents, hence precise radiation patterns (exclusive of site effects), can be achieved by adjustment of feeder length according to a straight-forward procedure. This results in an array that is not broad-band.

(3) Theoretical minimum clearance at 7.0° width is 149 microamps at ± 24°. Flight checks at 7.0° width showed minimums of 148 microamps at - 24°, 32 microamps at ± 24°.

(3) Theoretical minimum clearance at 7.0° width is 149 microamps at ± 24°. Flight checks at 7.0° width showed minimums of 148 microamps at - 24°, 132 microamps at ± 24°. Lower than design clearance at + 24° was almost certainly a site effect (See Figure 3-6 which shows low SB amplitude at + 24°) hence no attempt at correction was made, even though means were available to reduce CSB drive to the center element and thus increase clearance signal.

(4) This task points to the need for further in-depth engineering effort to arrive at the optimum means of modifying V-Ring arrays in the field. (Examples of unresolved areas are described under 2. Data for Implementation, Page 225).

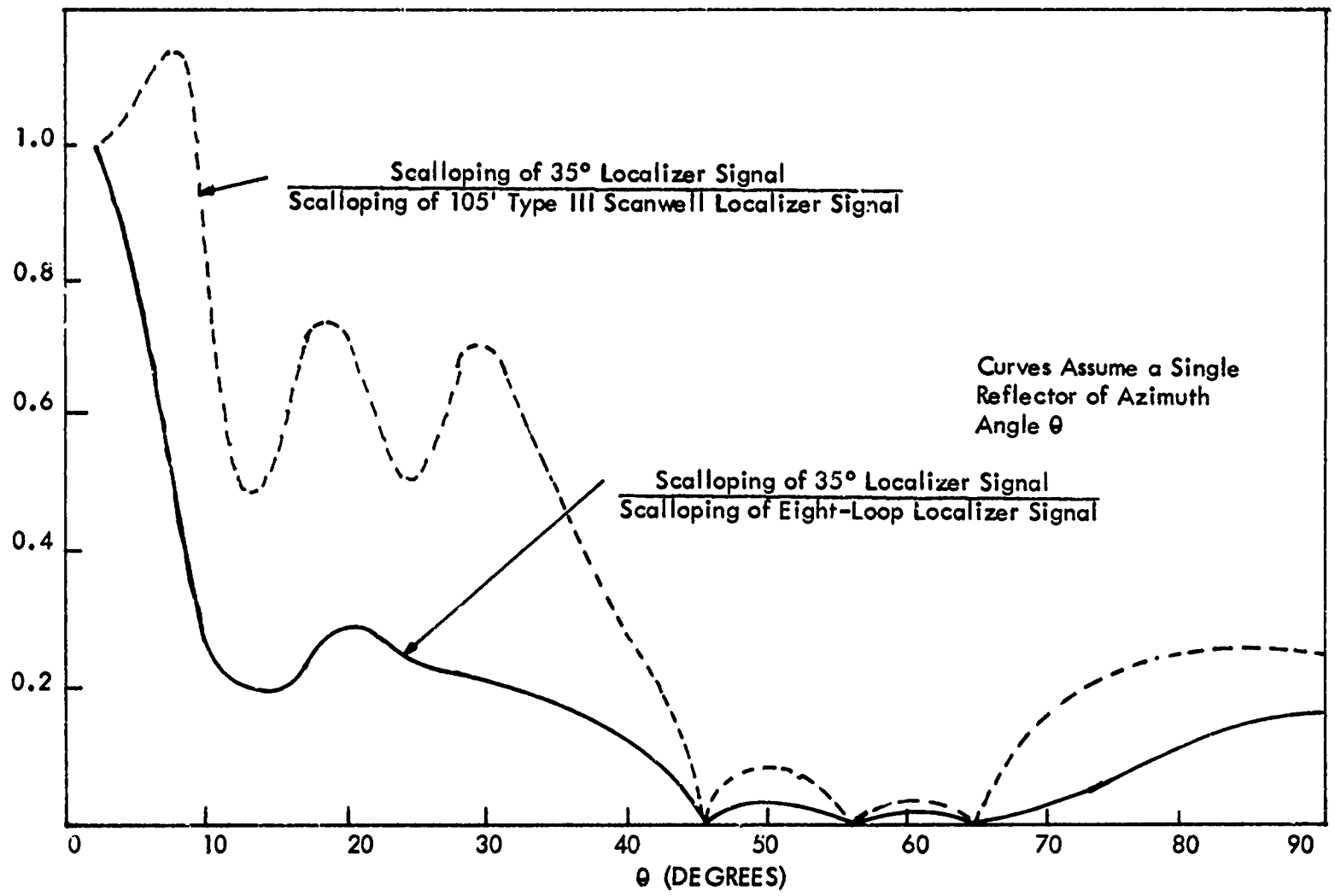

Figure 3-10. Measured DDM -- 35° Localizer Width = 7.0°.

B. Localizer Monitors

1. Results of Flight Tests of Integral and Seven-Element Near-Field Localizer Monitors

a. Summary. The attached data summarizes the results of tests performed concurrently on an integral localizer monitor and on a seven-element near-field localizer monitor, while both were monitoring the performance of a V-Ring localizer redesigned to give coverage in a ± 35° sector as reported in the preceding section.

The general procedure was to introduce a fault in the localizer, read the DDM indicated by the centerline and width channels of each monitor, and measure, with an airborne receiver, the far-field DDM on geometric centerline and 2.34° right of geometric centerline. The position of the test aircraft was referenced using a theodolite.

Two different classes of faults were introduced, one which should in principle have been correctly monitored by both monitors (in the sense that both monitors should correctly predict far-field DDM). The other class of faults was such that a correct prediction could only have been expected from the seven-element monitor.

Excellent agreement exists between the integral monitor and the far-field aircraft measurements. A total of 15 fault checks were conducted and the average difference between aircraft and integral monitor readings were 3 μa course and 6 μa width. This represents excellent correlation with the airborne monitor and is within the expected accuracy of the experiment.

b. Test Arrangement and Fault Description. A modified V-Ring localizer array, described in section III A 1, is located 1500 feet from the southwest end of the Ohio University Airport runway at Albany, Ohio. The localizer has been modified to provide clearances in a 70° sector centered on the centerline. As previously reported, this modification increased the spacing between elements and the distribution of current among the elements. Clearly the modification should decrease mutual coupling between elements with the result of increased accuracy for an integral type monitor using loop-type coupling probes, an example of which is shown in Figure 3-11. Previous tests of an integral monitor [1] resulted in average differences between monitor readings and aircraft readings of 11.38 μa for course and 8 μa for width. The rather large difference in course readings was considered to be due to mutual coupling between antenna elements. The results of these experiments substantiate that assumption.

For the measurement program a repeat of portions of the tests conducted in 1969 were made to ascertain the effects of decreased mutual coupling on the accuracy

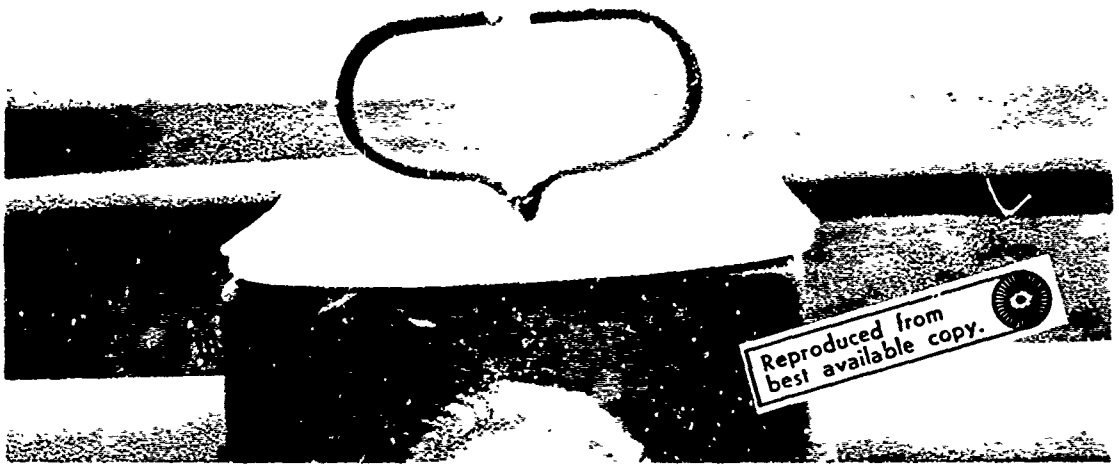
Reproduced from best available copy.

Figure 3-11. Close-up View of Coupling Probe Used to Sample the Current in a V-Ring Localizer Element. Fifteen such Loops are Used in the Integral Monitoring Scheme.

of the integral monitor.

Fault List for Integral Monitor Flight Tests

1. Disconnect feeder to 1L.
2. Disconnect feeders to 1L and 2L.
3. Disconnect feeders to 1L, 2L and 3L.
4. With 1L, 2L, and 3L feeders disconnected, short the 1L, 2L and 3L ports of the divider.
5. Insert a 180° line in 1L.
6. Disconnect feeders to 5R, 6R and 7R.
7. With 5R, 6R and 7R disconnected, short the 5R, 6R and 7R ports of the divider.
8. Insert a 180° line in 2R.
9. Unbalance tones at transmitter.
10. Misphase sidebands at transmitter by 60°.
11. With 2 L remaining disconnected, connect a dummy load to the 2 L distributor terminal.
12. Disconnect feeder to 5L and connect a dummy load to 5L distributor terminal.
13. Disconnect 7L and connect dummy load to 7L distributor terminal.
14. Parasitic elemenrs on 1L and 2L.
15. Parasitic elements on 1R and 2 R.

of the integral monitor.

Fault List for Integral Monitor Flight Tests

1. Disconnect feeder to 1L.
2. Disconnect feeders to 1L and 2L.
3. Disconnect feeders to 1L, 2L and 3L.
4. With 1L, 2L, and 3L feeders disconnected, short the 1L, 2L and 3L ports of the divider.
5. Insert a 180° line in 1L.
6. Disconnect feeders to 5R, 6R and 7R.
7. With 5R, 6R and 7R disconnected, short the 5R, 6R and 7R ports of the divider.
8. Insert a 180° line in 2R.
9. Unbalance tones at transmitter.
10. Misphase sidebands at transmitter by 60°.
11. With 2 L remaining disconnected, connect a dummy load to the 2 L distributor terminal.
12. Disconnect feeder to 5L and connect a dummy load to 5L distributor terminal.
13. Disconnect 7L and connect dummy load to 7L distributor terminal.
14. Parasitic elements on 1L and 2L.
15. Parasitic elements on 1R and 2R.

c. Test Results.

FAULT NO.	CENTERLINE MONITOR			WIDTH MONITOR		
	Seven-Element DDM (μa)	Integral DDM (μa)	Measured by Aircraft on ℄ DDM (μa)	Seven-Element DDM (μa)	Integral DDM (μa)	Measured by Aircraft 2.34° Right of ℄ DDM μa
No Fault	+1	+3	+3	-150	-147	-150
1	+26	+25	+28	-140	-145	-135
2	+46	+50	+51	-140	-130	-128
3	+52	+54	+57	-125	-102	-114
4	+25	+26	+26	-170	-130	-124
5	-6	-12	-13	-215	-210	-192
6	-7	-6	-12	-125	-125	-123
7	+12	+14	+14	-105	-100	-96
8	-18	-18	-9	-172	-165	-167
9	-39	-34	-32	-175	-165	-170
10	+2	+7	+15	-60	-25	-27
11	+12	+24	+15	-150	-125	-136
12	+12	+24	+15	-140	-125	-124
13	+3	+9	+4	-150	-135	-135
14 *	+24	+6	+25	-148	-145	-129
15 *	-50	-6	-41	-247	-190	-226

* Nature of fault such that it should be correctly monitored by 7-element monitor, but not necessarily by integral monitor. See fault list for description of faults. Data not included in averages.

Table 3-2. Summary of Monitor Test Results.

Excluding conditions of the environment affecting the localizer performance it is clear that this analog, integral monitor provides representative monitoring superior to that presently in the field.

2. Data for Implementation

In general, three areas are currently being pursued in this study which are intended to supply specific pieces of information to the FAA for decision making regarding the applicability of the integral monitor and associated 35° localizer array. First, the broadband characteristics of both the array and the monitoring system are being ascertained. The plan is to provide quantitative data concerning the capability to operate over the band without major adjustments in the lines or associated components. It must be kept in mind that the original design of the integral monitor for the 35° array was such as to minimize component costs and as a result special inexpensive transmission section lines were fabricated in lieu of purchasing the more expensive, broadband, ferrite, hybrid units.

Another aspect to be determined will be the amount of decoupling that can be obtained using various techniques such as the screens for selected transmission line lengths. Also, the possibility of using a different element for the center antenna is being considered. For example, a dipole would provide for less coupling. Finally, design data is being prepared in order that evaluation of the design procedures and the selection of the particular array spacing and currents for the ± 35° localizer design may be made by the FAA. This will reveal the need for the number of elements that are being used and the particular spacing which has been applied. Also the requirements for the use of a center or odd-numbered element will be identified.

Preliminary results of measurements of the effectiveness of variable height ground-plane screens for decoupling the V-Ring antennas have been obtained. For reference, in the preceding section III A 1 on the ± 35° V-Ring array redesign the voltage induced in the pickup loop was 110 mv. After the line stretchers were adjusted for a minimum parasitic current in the No. 1 element, the voltage measured was 6 mv. This indicated a suppression of greater than 18:1.

The present modification consisted of readjusting the line structures identified in section III B 2 and setting them for a maximum parasitic current as noted in the No. 1 element. The 3-foot by 20-foot copper screens were placed directly below the center element in the localizer array. The elevation of these screens was varied until a minimum induced voltage in the pickup loop was noted. A minimum of 45.5 mv was measured. This is a suppression ratio of 2.3:1. Further experiments are planned.

3. A Method for Minimizing the Effects of Overflights on the Localizer Monitors

A method to provide for the relief of the false alarms due to aircraft overflights of the ILS localizer is described in this section. A block diagram of the overflight system is shown in Figure 3-12.

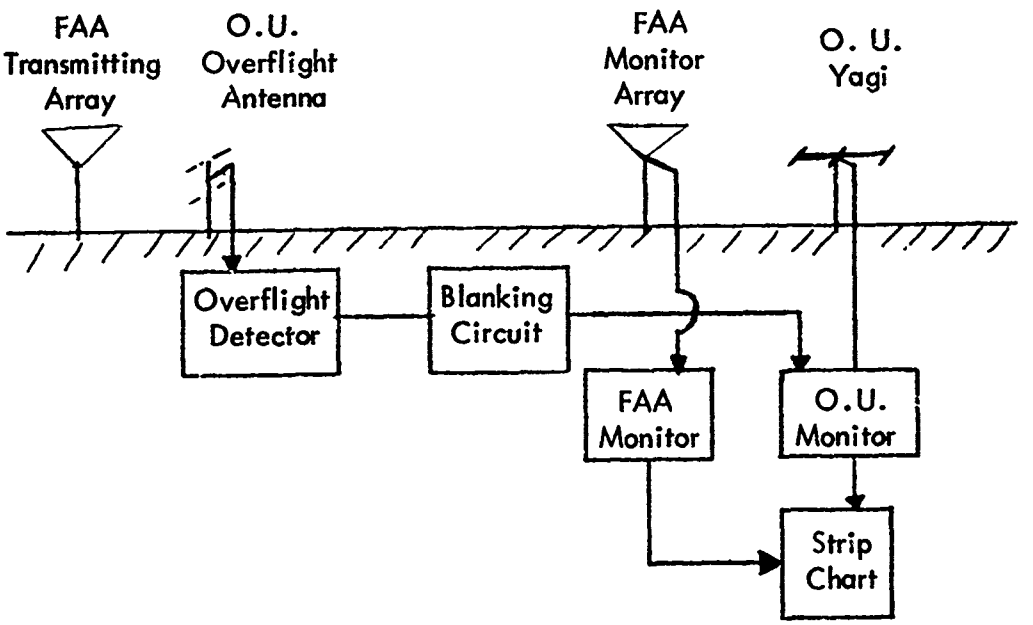

Figure 3-12. Block Diagram of Overflight System.

The proposed monitor uses a narrow beam width Yagi antenna mounted one-half wavelength above the ground connected to a standard FAA monitor receiver. (Figure 3-12). Receiver modifications are made, as necessary, in the low-pass filter circuitry following the 90 Hz and 150 Hz envelope detectors. In addition a directional overflight antenna is used as a sensor in front of the transmitting antenna and oriented in the vertical direction. This sensor antenna consists of two half-wave length dipoles mounted on a vertical mast one quarter and one-half wave-length above the ground. The signals from the dipoles will be combined in the ratio of one to one-half by a transmission line summing network.

The combining ratio causes the blanking antenna pattern to be maximum in the vertical direction and minimum in the horizontal direction. Because of this a direct signal from the transmitting array will be minimized while any signals reflected from overhead will be maximized. This permits the identification of the overflight and allows blanking to be initiated.

The electronics necessary for this has been completed. The localizer monitor for use in the overflight experiments in Athens are being obtained from the FAA.

After preliminary tests in Athens, the system will be taken to Port Columbus International Airport where frequent problems of overflight exist and there recordings taken to indicate the efficacy of the blanking technique. The plan is to completely separate the test equipment from the operational equipment installed at Columbus in order not to disturb the present operational monitoring system.

a. Past Investigations. The following tutorial section discusses some past investigations of the monitor system and its relation to overflight alarms. A brief explanation is given in Appendix F of the nature of the doppler shifted interferences encountered during overflights. From Appendix F it is clear that an ideal monitor antenna would have a radiation pattern that is very narrow and directional. No interfering reflections from overflying aircraft would be detected by this antenna except during the time the aircraft is very near the transmitting array. Monitor arrays should be (and generally are) mounted one-half wavelength above ground in order to generate null in the antenna pattern in the vertical direction. Simple dipoles are used in some installations are not directional and sense equally well in the forward and reverse directions. Two element arrays (i. e., a dipole and a parasitic element) are only slightly better for monitoring than the dipole. A monitor array should have a front to back ratio of 20 db or more and a vertical antenna pattern with a 3 db beam width of 20° to 30°. Consequently the monitor antenna should consist of an array containing three or more elements.

The effects of the localizer signal reflected from the overflying aircraft on the monitor receiver is analyzed in Appendix G. A comparison is made between a coherent detector and an envelope detector for use as a detector involving the 90 Hz and 150 Hz signals. The theoretical results show that the two detectors produce identical responses during overflight conditions. This derivation, however, was based on an assumed model for the coherent interference and some questions as to the validity of the model existed. For clarification the 90 Hz and 150 Hz coherent detectors were constructed and an experimental comparison was made between them and the normally-used envelope detectors (see Figure 3-13). For this comparison bandwidths of the low pass filters following the detectors were identical. The 90 Hz and 150 Hz signals from the monitor receiver were tape recorded during the overflight test for future laboratory use. Experimental responses of two detectors (i. e., envelope and coherent) were identical. (see Appendix G). This is then verification of the mathematical model used.

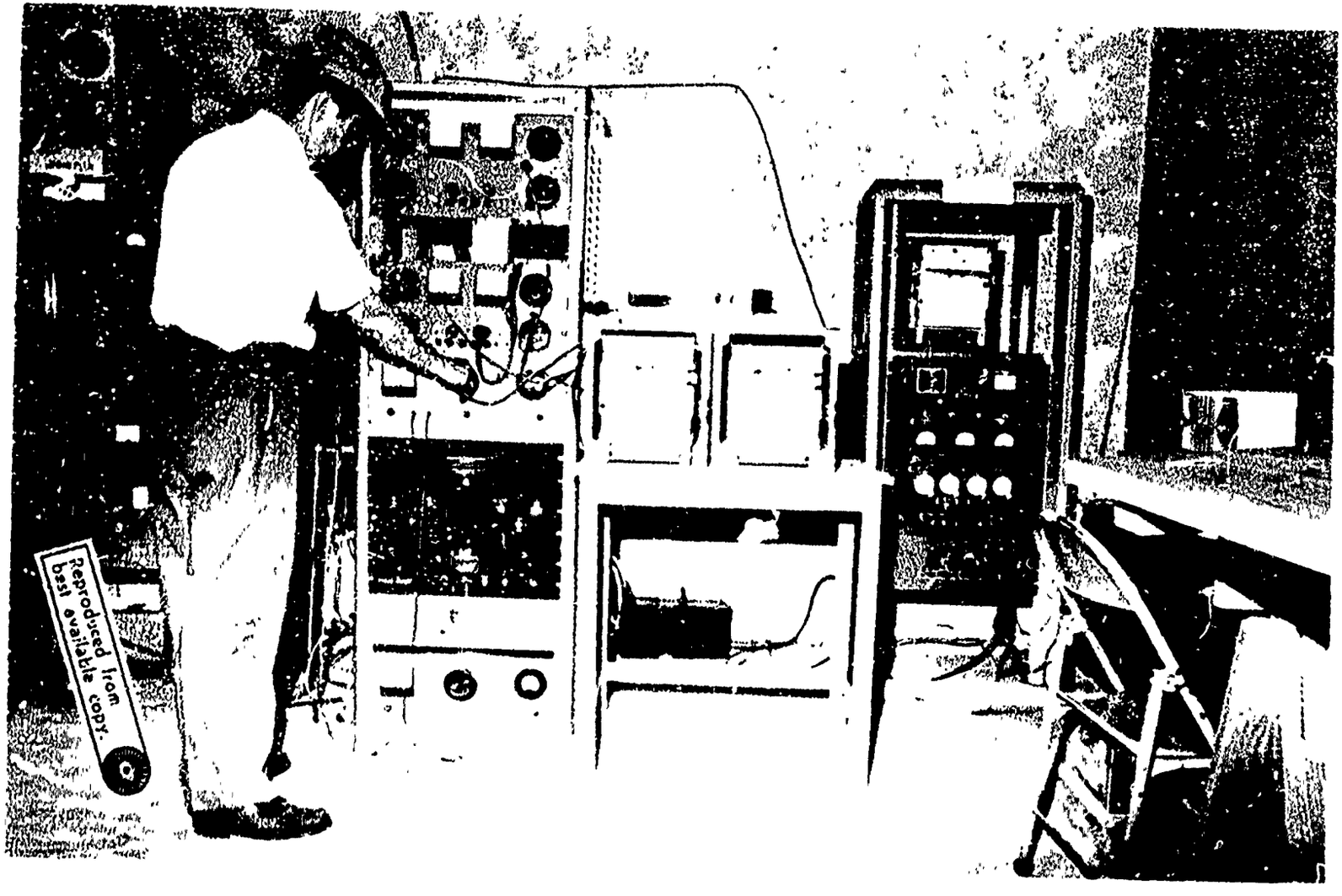

Reproduced from best available copy.

Figure 3-13. Over Flight Monitoring and Recording Setup for the Localizer.

Some improvement could be expected if the first detector were coherent. The magnitude of the improvement in the DC component of the 90 Hz and 150 Hz signals is at most 25 percent. This was not verified experimentally because it was felt that the expected improvement was too small to be detected.

Laboratory tests using the tape recorded overflight signals previously mentioned show that the low pass filters following the 90 Hz and 150 Hz envelope detectors should have bandwidths of 3 Hz. This will allow the disturbance caused by overflights to dissipate in the shortest time.

Experimental tests were made using a 7-element Yagi as a monitor antenna, and an envelope detector with a bandwidth (simple RC filter) of 1.5 Hz. The maximum out-of-tolerance time for any case with DC-3 type aircraft was 2 seconds. This is well within the allocated time before shut-down for most monitor systems.

IV ILS MODULATOR TOLERANCE STUDY

A. Summary

Currently there is some difficulty in maintaining modulator bridge tolerances in certain localizer and glide slope transmitters. A test and evaluation program was conducted by Ohio University to ascertain the effects of modulator output waveform distortion on the signal in space and how typical ILS receivers would process the signal.

Digital computer programs were developed to model the localizer and glide slope signals as a function of modulator bridge distortion. Laboratory tests were conducted with a Collins 51R-3 receiver to measure its responses to harmonically related signals, Fourier analysis of existing modulator bridge outputs were conducted, and comparisons were made with orbital information to validate the theoretical models.

Based on the work described above it is concluded that the mechanical modulator tolerances remain essentially as before. The present tolerances can be expected to consume 61.5 percent of the present clearance limit for a 7.2 degree width localizer course and 35 percent of the glide path width tolerance.

The 270, 300 and 450 Hz tolerances can be relaxed from 5 percent to 10 percent, but the 90, 150 and 180 Hz tolerances must remain the same.

B. Introduction

Reports indicate that the FAA field personnel are having difficulty in maintaining modulator bridge tolerances on certain types of localizer and glide slope transmitters. In addition, during the fault analysis program [15] conducted at Ohio University on the V-Ring localizer, it was recognized that modulator output waveshape had a fundamental effect on array clearance signals.

A four-part test and evaluation program was initiated to ascertain the effect of modulator output waveform distortion on the signal in space and how typical localizer and glide slope receivers would process the signal. During the first part several computer programs were developed to provide a graphical as well as a tabular listing of the V-Ring signal in space as a function of angle from the centerline for any harmonic desired.

The second part of the program consisted of laboratory tests of a Collins 51R-3 VHF navigation receiver to determine its characteristic bandpass response and its response to the harmonics listed in SM P 6750-2, Chg 8, dated 5/8/68. Given the receiver response as determined by laboratory experiment and the signal in space as computed by the digital programs the receiver response to an arbitrary radiated signal can be predicted.

For the third phase of the program waveforms of the Ohio University operated V-Ring modulator were recorded, the Fourier coefficients determined, and the predicted localizer pattern compared to the actual pattern as determined by airborne measurements.

Part four of the program was the development of the appropriate computer program to ascertain the effect of modulator output waveform distortion on the glide path signal in space.

C. Digital Modeling of Localizer Signals in Space

Several computer programs were written to provide the tools necessary to compute the field of harmonics or signal at a desired point in space relative to the center of the array and the inbound courseline. These programs are described below.

1. Program No. 113

This program is designed to compute and plot the field of several pairs of antenna elements and add them to give the field of the entire array. In particular this program computes and plots the field of an 8-loop ILS localizer which is made up of three pairs of elements that transmit the 90 and 150 sidebands.

Use is made of the perpendicular bisector of the line of elements that make up the array as the angular reference. The angular error is measured in the conventional counter-clockwise direction. The program computes the relative far-field strength along a concentric circle about the center of the array. The field is computed for the desired number of points for each pair of elements making up the array; then, the total field is summed for each pair's contribution at a particular point.

The computation of electric field is done by mechanizing the equation

$$E = 2\,E_o \sin\left[\,(D_r/2)\sin\theta\,\right] \qquad (4.1)$$

where

E_o = electric field produced by each antenna

D_r = distance between antenna elements in electrical degrees

θ = angular deviation from reference line

2. Program No. 114

This program is designed to compute the field for each degree around a pair of V-Ring element antennas. The V-Ring elements are directional and the total field will deviate correspondingly from an isotropic pattern. The "E" variable is used to store the relative field strength for each degree around a single V-Ring element. These values were read from a polar-plot such as that shown in Figure 4-1 which is typical for a V-Ring element. The field strength for pairs of elements is computed with the "E" factor applied to each point computed.

3. Program No. 116

This program computes and plots a series of patterns, one for each set of descriptive data added to the program. This program is used to determine the patterns from the seven pairs of antennas making up the V-Ring array. This program can also be used to determine the effects of varying the element spacing on the pattern shape of an array.

4. Program No. 117

After the configuration and current feet parameters are decided this program computes and plots the total field of the array. The "E" variable is used to store the non-isotropic qualities of the V-Ring element.

This is the working program for modeling of the transmitted signal. The various harmonics under consideration can be introduced as data with appropriate relative amplitudes and phase differences. The total effect on the array's pattern can then be found by comparing these results with the ideal output.

5. Subroutine No. 113

This subroutine is used in all four of the programs described by this report and is especially designed to plot on a broadly expanded scale a field pattern as computed by the main program. It automatically scales the plot within the limits

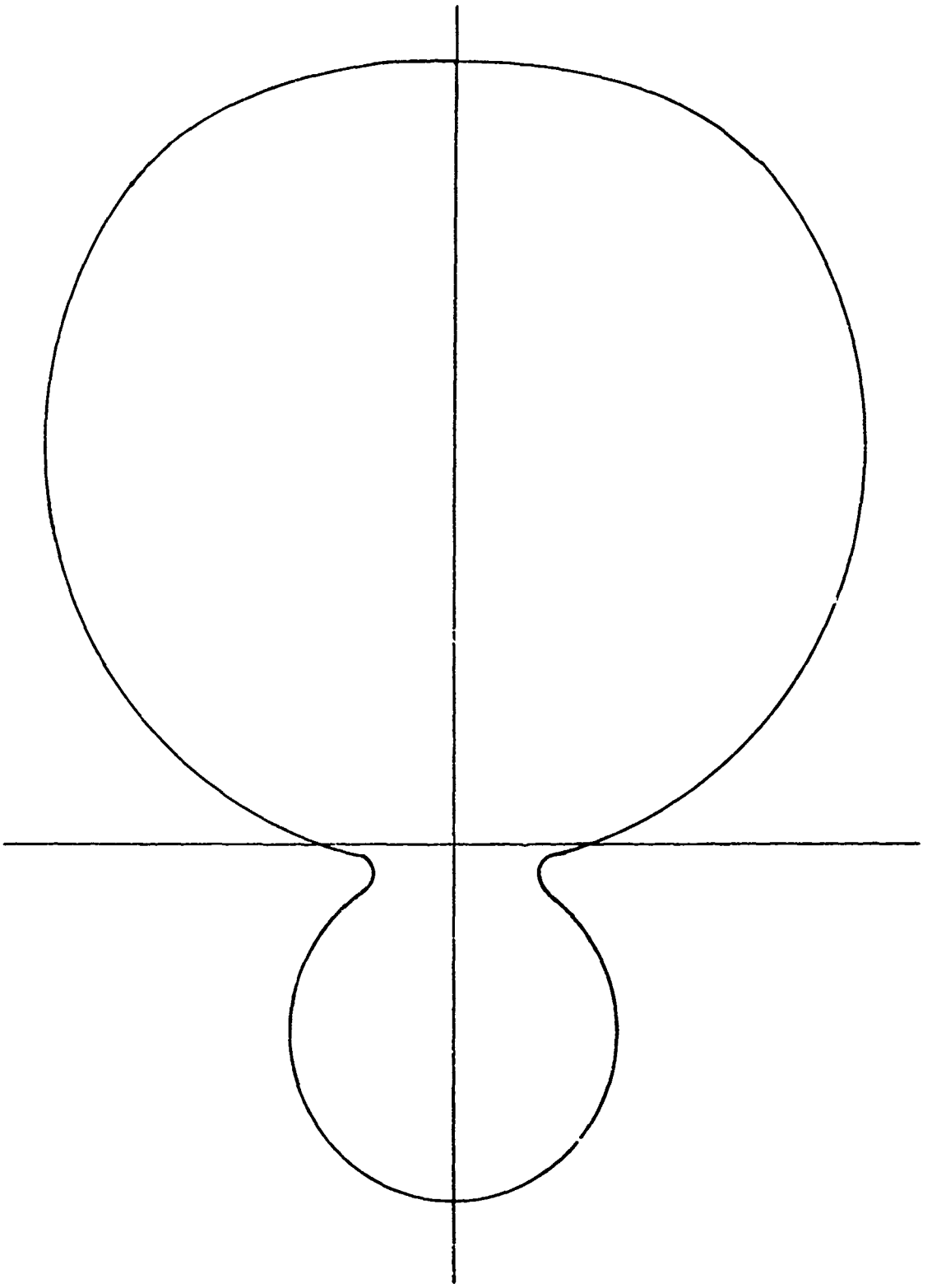

Figure 4-1. Radiation Pattern--Single V-Ring Antenna, Type FA-S549X.

described at the beginning of the program. Its main feature is that the pattern can be expanded to plot a point for each 0.1 degree or less. This would be desirable to see visually and fairly accurately the steep slopes of the field pattern in the first few degrees on either side of the on-course reference. The number and range of the points to be plotted can also be specified.

6. "E" Variable Data Deck

The relative field strength along a circle centered on a V-Ring antenna element is described by Figure 4-1. This polar plot was the result of a previous computation of the field expected from the V-Ring antenna. The "E" variable data needed for all V-Ring antenna computations has been read from Figure 4-1 for each degree from 0-360. These 361 values are punched on 37 cards in a 10F7.2 format.

D. Results of the Digital Modeling of the Signal in Space

The following is a list of the harmonics that were investigated. This list is that published in SM P 6750.2 CHG 8 dated 5/8/68.

Item	Reference Paragraph	Standard	Initial Tolerance	Operating Tolerances
MECHANICAL MODULATOR TOLERANCES	143,109	----	----	----
a. 90 Hz in 150 Hz		0%	2%	3%
b. 300 Hz in 150 Hz		0%	5%	7.5%
c. 450 Hz in 150 Hz		0%	3%	5%
d. 150 Hz in 90 Hz		0%	2%	3%
e. 180 Hz in 90 Hz		0%	5%	7.5%
f. 270 Hz in 90 Hz		0%	3%	5%

Table 4-1. Present Allowable Modulator Tolerances.

The harmonics specified above were used in the programs to generate the signals in space for each harmonic considered. The total signal in space is then the sum of each harmonic as the propagation path, antennas and array antenna bridge are considered linear. Results of these investigations are given as tabulations and digital plots.

Once the signal in space is known, the receiver response to this signal must be ascertained. A laboratory test of a typical navigation receiver was instituted to determine its response to the harmonics listed above.

E. 51R-3 VHF Navigation Receiver Tests

In order to ascertain the receivers response to the signal in space its response to the various harmonics present in the signal was measured. First the receivers 90 and 150 Hz bandpass characteristics were determined and then the response to the various harmonics was measured.

1. 51R-3 Bandpass Characteristics

As shown in Figure 4-2, the modulated Rf output of a Boonton211-A signal generator is fed to the receiver under test. Modulation is accomplished by a Wavetek III function generator connected to the external modulation port of the Boonton. The output of the receiver was measured by a center scale microammeter with a choice of two scales, ± 250 μa and ± 50 μa. The microammeter presents a standard load to the receiver, i. e., a total input impedance of 333 ohms.

To initialize the set-up the Wavetek III was adjusted in frequency to a maximum reading on the 150 Hz side of the microammeter. The amplitude of the modulating signal was then adjusted for a reading of 125 μa for a low level test and 250 μu for a high level test. Two levels were used to insure that the test was conducted in the linear operating range of the receiver and to ascertain what the effects of receiver non-linearity might be on the receiver bandpass characteristics. The frequency of the Wavetek was then varied over the range of 75 to 185 Hz taking care that the modulation percentage remained constant throughout the test.

The data obtained from the test is presented in Tables 4-2 and 4-3 and the receivers normalized bandpass characteristics are shown in Figures 4-3 and 4-4.

Bandwidth of the filters remained constant for the high and low level tests and are 20 Hz for the 90 Hz filter and 30 Hz for the 150 Hz filter.

2. 51R-3 Response to a Signal Containing Harmonics

The 51R-3 receiver response to the harmonics listed in SM P 6750-2 CHG 8, paragraph 124 was tested in the laboratory to ascertain if there were any anomalous responses not predictable by the bandpass characteristics. Because the harmonics generated by the mechanical modulator will have a unique phase relationship to the fundamental frequency a method of generating harmonics with a unique phase relationship to the fundamental was required. The following procedure was evolved.

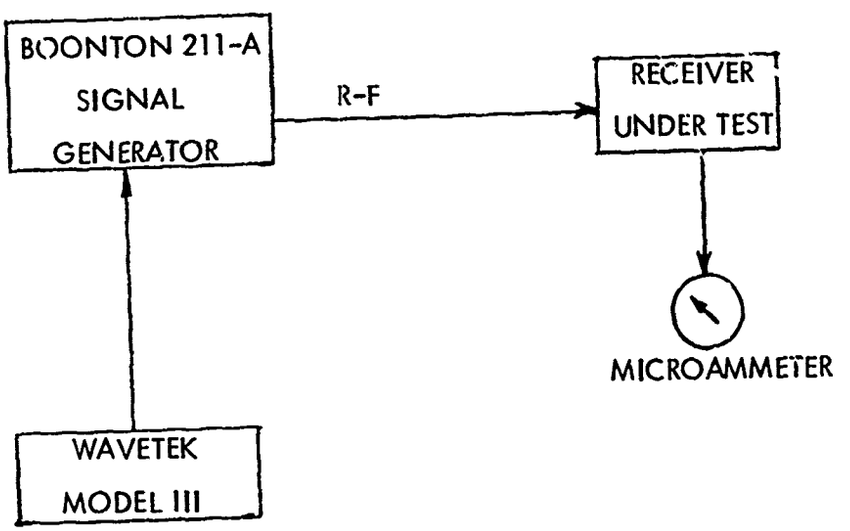

Figure 4-2 Bandpass Characteristic Test Arrangement.

a. Laboratory Test Arrangement. A model 116 Wavetek signal generator has the capability of having its output phase-locked to a desired signal. This signal generator was inserted in series with the fundamental modulating generator of a Boonton 211-A signal generator. The input for the phase lock circuitry was taken directly across the modulation generator. Figure 4-5 is a simplified schematic of the experiment for generating harmonics of 90 Hz. The Wavetek is tuned to the desired harmonic, the generator phase locked to the 90 Hz fundamental frequency and its amplitude adjusted for the desired harmonic content. For harmonics of the 150 Hz signal the Wavetek generator is connected in series with the 150 Hz modulating generator and the process repeated.

The phase of the harmonic selected, for example, the second harmonic of 90 Hz or 180 Hz was varied to yield the maximum change in receiver output. The amount of harmonic content was varied and the output of the receiver recorded.

Frequency (Hz)	Response (μa)
75	10
77	20
78	30
79	50
82	75
83	100
85	120
90	127
95	129
99	120
98	120
101	100
102	75
105	50
107	30
108	20
111	10
117	~0
123	10
126	20
128	30
130	50
134	75
138	100
139	110
146	120
150	125
162	110
164	100
168	75
173	50
177	30
181	20
185	10
216	~0

Table 4-2. Low-Level Bandpass Response 51R-3 (125 μa).

Frequency (Hz)	Response (μa)
74	25
76	50
78	75
79	100
80	125
81	150
82	175
83	200
85	225
95	250
101	225
102	200
103	175
104	150
105	125
106	100
107	75
109	50
112	25
117	~0
121	25
123	50
126	75
129	100
130	125
132	150
134	175
136	200
138	225
150	250
163	225
166	200
168	175
170	150
173	125
175	100
179	75
183	50
189	25
216	~0

Table 4-3. High-Level Bandpass Response 51R-3 (250 μa).

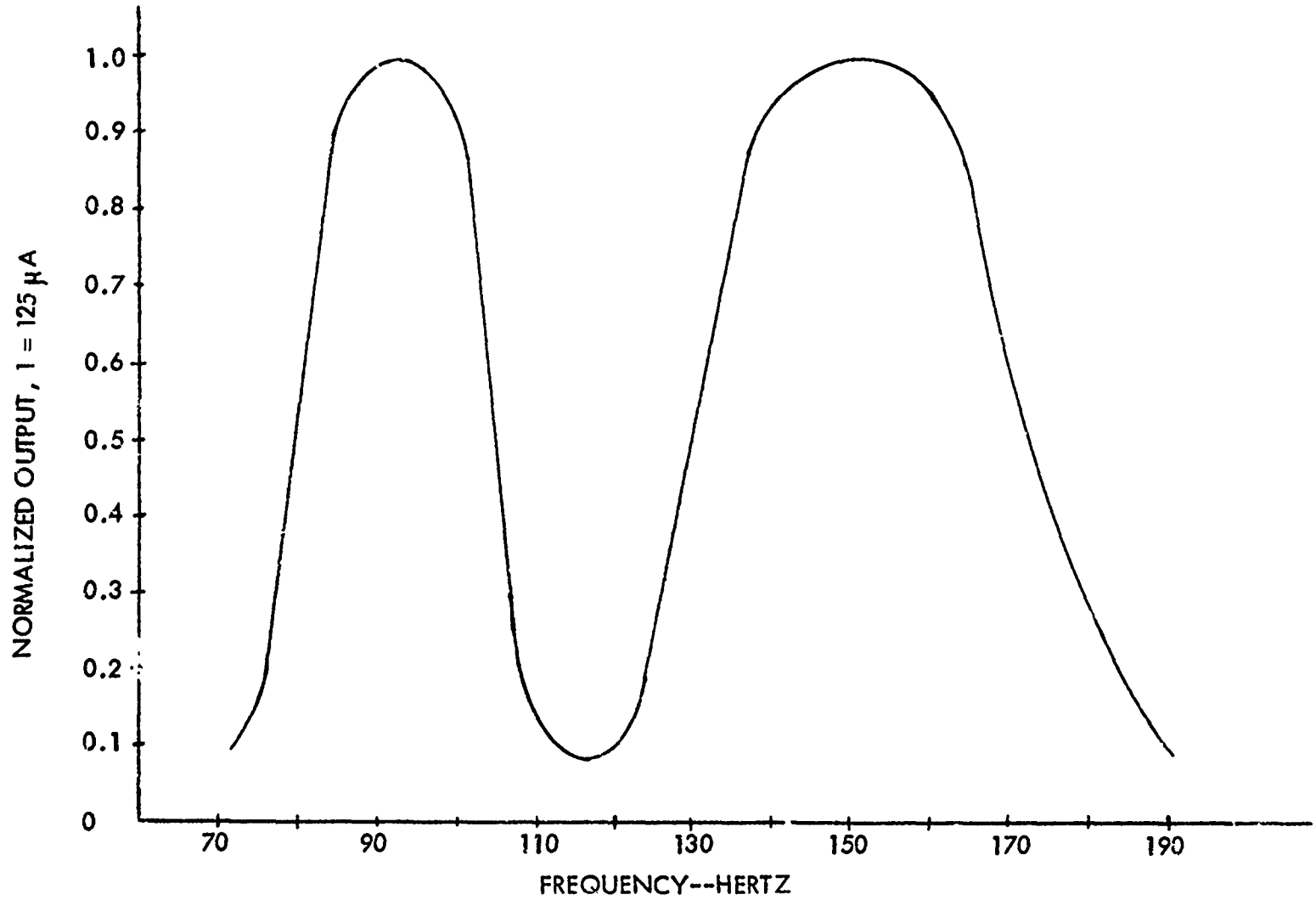

Figure 4-3. Bandpass Response. 51R-3 Receiver -- High Level.

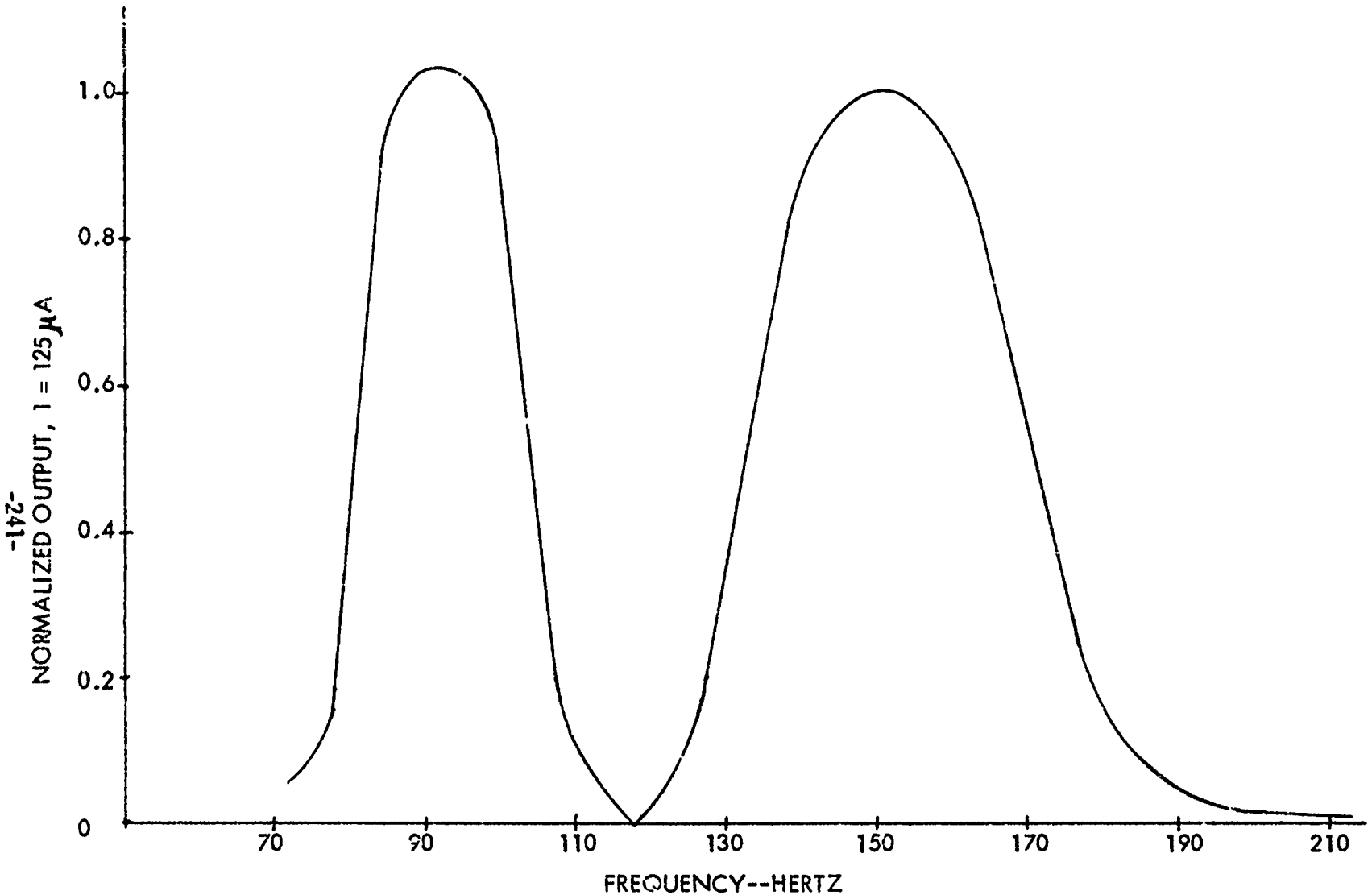

Figure 4-4. Bandpass Response. 51R-3 Receiver -- Low Level.

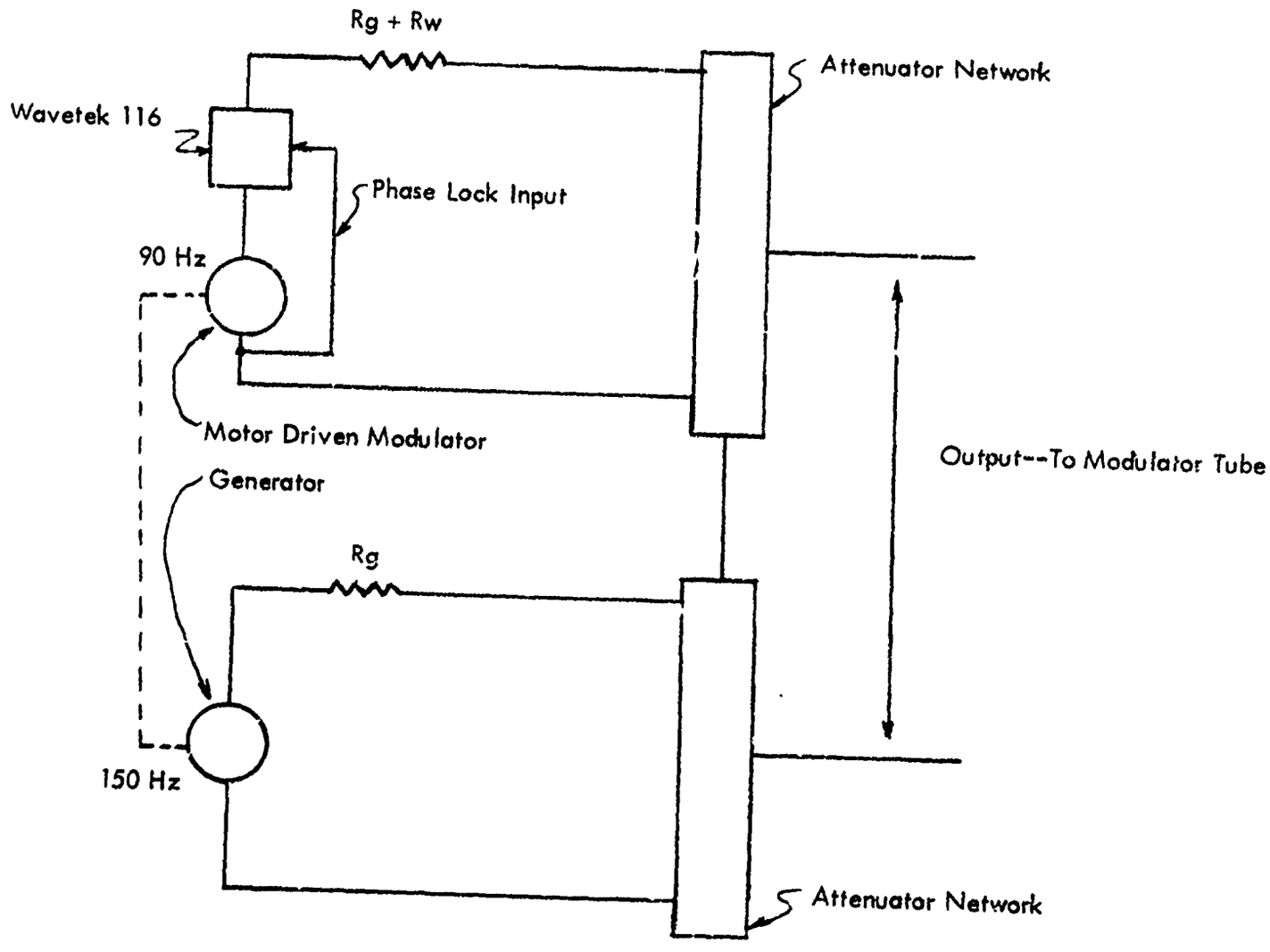

Figure 4-5. 90 Hz Harmonic Generation.

b. Laboratory Test Results. The following data, Tables 4-4 through 4-9, was obtained from the laboratory tests.

Boonton 211-A Attenuator Setting	Output Current μa	
	150 Hz	90 Hz
0DB	-20	-20
0.5	-32	-8
2.0	-70	30
4.	-110	7
7.5	-190	150

Table 4-4. 150 Hz in 90 Hz - 10%.

Boonton 211-A Atrenuator Setting	Output Current μa	
	150 Hz	90 Hz
0DB	-6	-6
0.5	-18	7
2.0	-52	45
4.0	-97	88
7.5	-174	168

Table 4-5. 180 Hz in 90 - 25%.

Boonton 211-A Attenuator Setting	Output Current μa	
	150 Hz	90 Hz
0DB	0	0
0.5	-12	12
2.0	-50	50
4.0	-93	90
7.5	-170	170

Table 4-6. 270 Hz in 90 - 33%.

Boonton 211-A Attenuator Setting	Output Current μa	
	150 Hz	90 Hz
0DB	20	20
0.5	8	32
2.0	-30	70
4.0	-70	110
7.5	-150	190

Table 4-7. 90 Hz in 150 Hz - 10%.

Boonton 211-A Attenuator Setting	Output Current μa	
	150 Hz	90 Hz
0DB	-5	-5
0.5	-17	7
2.0	-55	45
4.0	-97	90
7.5DB	-175	168

Table 4-8. 300 Hz in 150 Hz - 33%.

Boonton 211-A Attenuator Setting	Output Current μa	
	150 Hz	90 Hz
0DB	0	0
0.5	-12	12
2.0	-50	50
4.0	-90	90
7.5	-170	170

Table 4-9. 450 Hz in 150 Hz - 45%.

As an analytical verification of the results, each table was checked as follows:

180 Hz in 90 Hz
25% harmonic distortion at 180 Hz
Fundamental 90 Hz modulation depth 20%
Passband amplitude factor @ 180 Hz 0.16

Total 180 Hz modulation depth (0.20 x 0.25 = .050 = 5%
Total effective signal in receiver 150 Hz passband

$$M_{150+180} = 0.2 + (0.16 \times 0.05) = 0.2080$$

$$M_{150+180} - M_{90} = 0.2080 - 0.2 = 0.008 \sim 7\mu a$$

7 μa deflection toward the 150 Hz side expected
6 μa deflection measured.

In all cases the calculated and measured receiver responses to the harmonic content of the signal generator correlated within the experimental accuracy of the laboratory instrumentation.

c) The Effects of Distortion. The harmonic content of the signal from the modulator bridge has a detrimental effect upon course alignment and clearances. If the course is aligned by unbalancing the 90 and 150 Hz voltages to compensate for the harmonic content the detrimental effects usually are manifested by the presence of asymmetrical clearances with respect to the on-course line. That is, the side-frequency radiation fields to the right of the on-course line will not be the mirror image of those to the left of this position.

By making use of the computer simulation and laboratory tests described before the following results are evident. The 150 and 90 Hz cross-talk components are radiated from the array and processed by the receiver unattenuated. With the assumption that the cross-talk is either in phase or 180° out-of-phase (worst case) then the 3% tolerance indicated in SM P 6750-2 represents a 6 μa unbalance in the course position. With the appropriate adjustment to make the course alignment proper, the resultant asymmetry in the clearance pattern is such that the clearance is reduced 8% for a 3.6° width beam and 40% for 7.2° width beam.

The 7.5% tolerance on the 180 Hz harmonic in the 90 Hz signal results in a 16.5% reduction in the 7.2° width beam.

The 270 Hz, 300 Hz and 450 Hz signals are greatly attenuated by the receiver bandpass filters. However, due to the nonlinearities in the detection process beat frequency between the 90, 150, 270, 300 and 450 Hz signals fall within the passband. The laboratory test shows that this response is enough to account for an additional 20% reduction in the clearance at a path width of 7.2°.

Since it is expected that the occurrence of the relationships between amplitude of the harmonics will be statistically related to the root-sum-square of the contribution of each element to the total results in a total reduction of clearance of

$$\underset{90\text{ Hz}}{(.16} + \underset{140\text{ Hz}}{.16} + \underset{270\text{ Hz}}{02 + .04)^{\frac{1}{2}}} = 0.615 \qquad (4.2)$$

That is, it is expected that 61.5% of the clearance limit that exists for Category II operations with a 7.2° path width can be consumed by the modulator bridge tolerance above.

F. Fourier Analysis of Waveforms

To verify the results of the computer analysis and laboratory tests described above waveforms of the modulator bridge were photographed and subjected to a graphical Fourier analysis.

The harmonic content from the modulator bridge waveforms were then inserted into the computer program, the change in clearance symmetry calculated and compared to an actual orbit obtained in the V-Ring fault analysis program. The waveforms obtained are shown in Figures 4-6 and 4-7. The results of the Fourier analysis are shown in Table 4-10.

Because of the phase relationships of the 150 Hz distortion in the 90 Hz channel and the 90 Hz distortion in the 150 Hz channel the effects nearly cancel. The total result is that a 6 μa unsymmetry should appear in the clearance pattern on the 150 Hz side. Figure 4-8 is an orbit for a 7.2° width localizer course. Superimposed is the calculated orbit with the harmonics obtained from the Fourier analysis. Good agreement is evident.

G. Digital Modeling of Glide Slope Signals in Space.

A computer program was written to compute the field of the signal and any harmonics at a desired point in space relative to the desired glide path angle. Use is made of the radiation patterns of the glide slope array and in the worst case results in the following formula.

$$M_{150} = m \frac{(1 - B) \sin (H/2 \sin X) + D (1 - B) \sin (H \sin X)}{(1 + B) \sin (H/2 \sin X)} \qquad (4.3)$$

$$M_{90} = m \frac{(1 + C) \sin (H/2 \sin X) + D (1 - C) \sin (H \sin X)}{(1 + C) \sin (H/2 \sin X)} \qquad (4.4)$$

where

M_{150}	=	Total Modulation of Carrier at 150 Hz.
M_{90}	=	Total Modulation of Carrier at 90 Hz.
m	=	Modulation Index (%).
B	=	Total Effective Distortion in the 150 Hz Pass Band Receiver (%).
C	=	Total Effective Distortion in the 90 Hz Pass Band Receiver (%).
D	=	Path Width Factor.
H	=	Height of Sideband Antenna.
H/2	=	Height of Carrier Antenna.

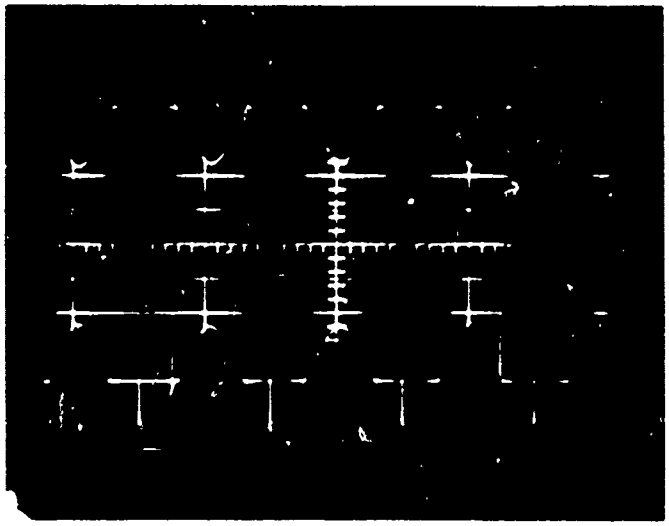

Figure 4-6. 90 Hz Output From Mechanical Modulator.

Reproduced from best available copy.

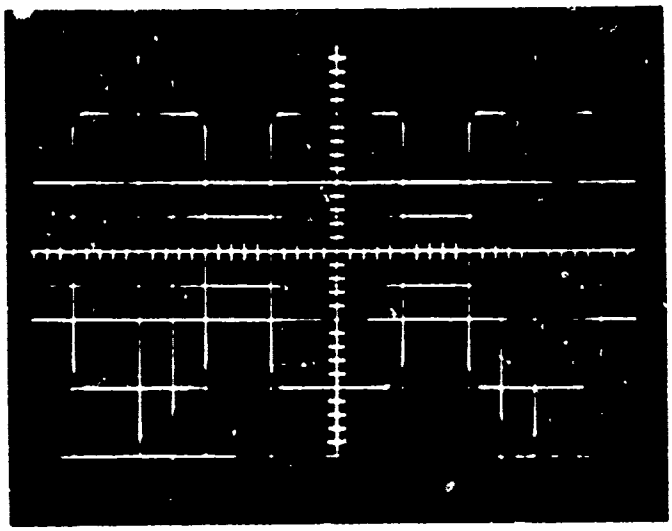

Figure 4-7. 150 Hz Output From Mechanical Modulator.

90 Hz			150 Hz		
Hz	Amount	Angle	Hz	Amount	Angle
30	1.1%	89.55	75	8.34%	176.87
60	2.38%	39.75	90	5.2%	41.82
120	1.55%	-10.[illegible]	225	4.37%	5.15
150	7.09%	59.55	300	6.97%	15.39
180	5.43%	12.12	375	3.02%	16.97
210	1.23%	48.59	450	1.31%	33.2
240	1.98%	52.61	525	3.36%	1.51
270	3.01%	24.77	600	3.44%	178.75
300	1.21%	151.01			
330	0.86%	95.03			
360	1.00%	21.65			
390	0.57%	114.70			
420	0.43%	62.45			
450	1.02%	85.24			

Table 4-10. Harmonic Content of 90 and 150 Hz Outputs of Mechanical Modulator.

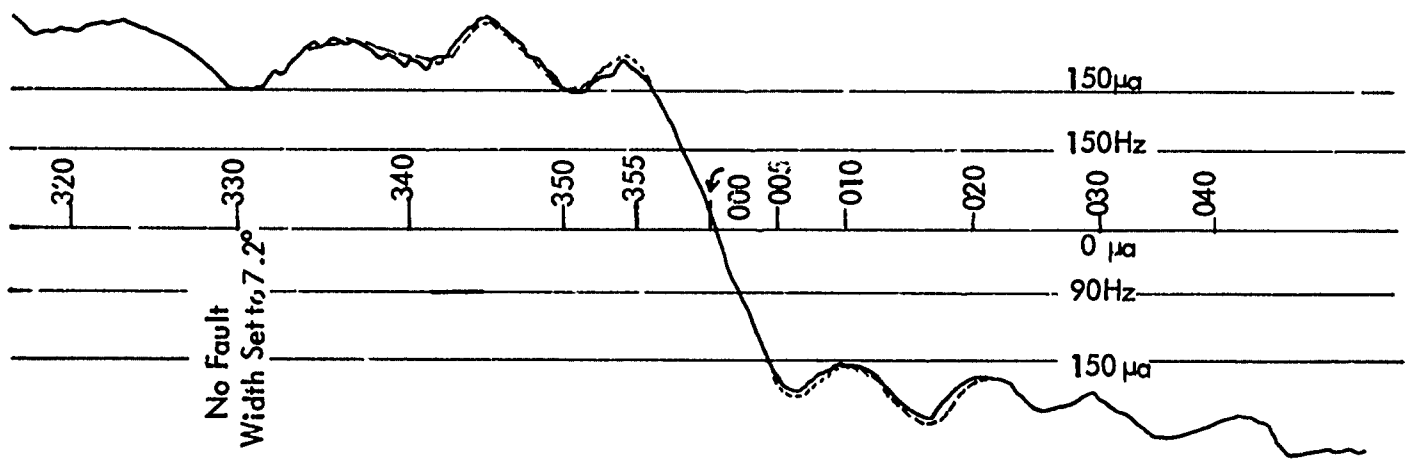

Figure 4-8. Comparison of Actual and Calculated Orbit. Actual——. Calculated ---.

Receiver characteristics used were those of the Collins 51V receiver. These characteristics were abstracted from the FAA Instrument Landing System Glide Slope Manual, No. FV-301. They are reproduced in Figure 4-9 for convenience.

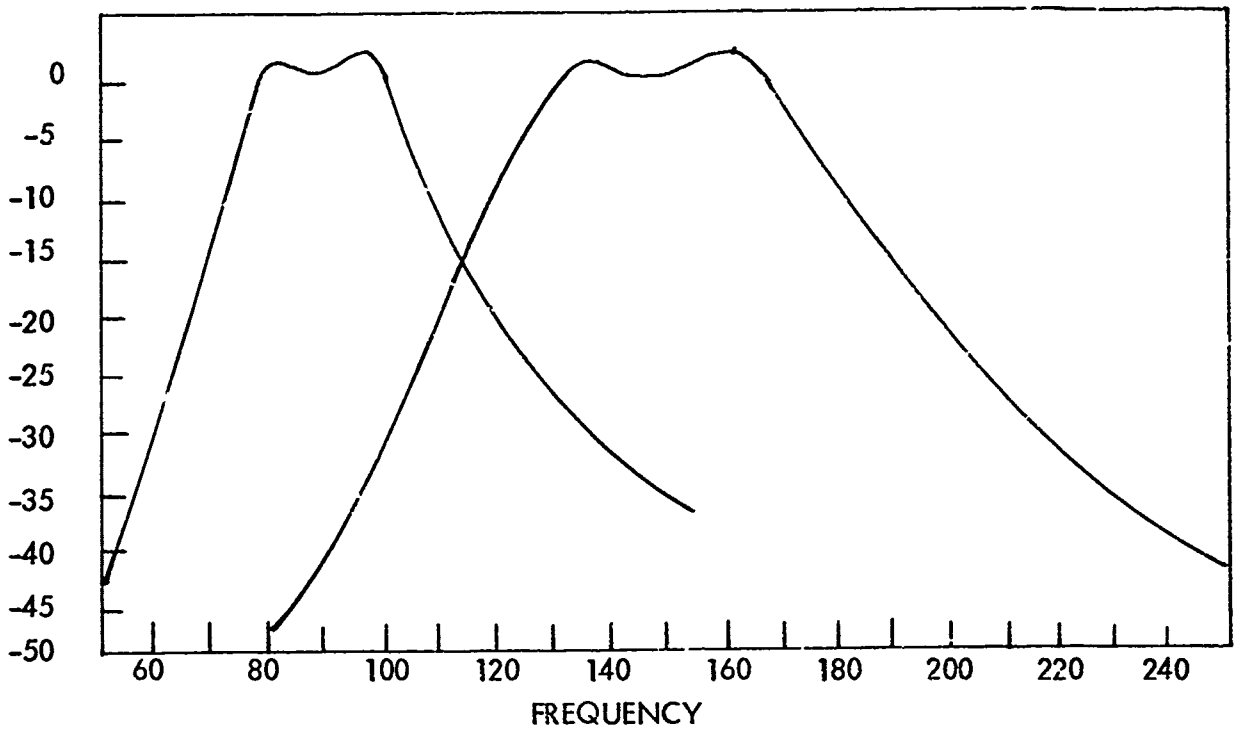

Figure 4-9. Filter Sensitivity, Collins 51V.

1. Effects of Distortion

The harmonic content of the signal from the glide path modulator bridge has a detrimental effect upon path width. By making use of the computer simulation and receiver characteristics described above the following results can be arrived at. The 150 and 90 Hz cross-talk components are radiated from the array and processed by the receiver unattenuated. With the asumption that the cross-talk is either in phase or 180° out-of-phase (worst case) then the 8% tolerance indicated in SM P 6750.2 results in 40% of the width tolerance being consumed. The 7.5% tolerance on the 180 Hz harmonic in the 90 Hz signal results in a 20% of the width tolerance being consumed. The 270 Hz, 300 Hz and 450 Hz signals are attenuated by the receiver bandpass filters. It is expected that the occurrence of the relationships between the amplitude of the harmonics will be statistically related therefore the root-sum-square of the individual contributions will be the expected total contribution.

$$(.2^2 + .2^2 + .2^2)^{\frac{1}{2}} = .347 \qquad (4.7)$$

That is approximately 35% of the available width tolerance will be consumed by the present modulator bridge tolerances.

H. Conclusions and Recommendations

Based on the analysis and laboratory tests described above it is concluded that the mechanical modulator tolerances for both the localizer and glide path should remain substantially as published in SM P 6750.2.

Because of the bandpass characteristics of the localizer and glide path receivers the 270 Hz and 450 Hz tolerances can be relaxed to 10% from the present 5%.

With this new set of modulator tolerances for localizers operating with a 7.2° beam width, 61.5% of the clearance limit will be consumed by modulator bridge harmonics.

Thirty-five percent of the glide path width tolerance can be expected to be consumed by the modulator bridge tolerance.

It is recommended that the mechanical modulator tolerances published in SM P 6750.2 be amended as follows:

Item	Reference Paragraph	Standard	Initial Tolerance	Operating Tolerance
MECHANICAL MODULATOR TOLERANCES	143,109	----	----	----
a. 90 Hz in 150 Hz		0%	2%	3%
b. 300 Hz in 150 Hz		0%	5%	10%
c. 450 Hz in 150 Hz		0%	5%	10%
d. 150 Hz in 90 Hz		0%	2%	3%
e. 180 Hz in 90 Hz		0%	5%	7.5%
f. 270 Hz in 90 Hz		0%	5%	10%

Table 4-11. Recommended Mechanical Modulator Tolerances.

V INVESTIGATORS AND ACKNOWLEDGMENTS

All personnel performing work on this research and development program are members of the faculty and staff of the Department of Electrical Engineering, College of Engineering and Technology, Ohio University, Athens, Ohio. This team has been provided invaluable support and help from many FAA offices throughout headquarters, the several regions and field units. This help is gratefully acknowledged.

Dr. R. W. Redlich, Professor of Electrical Engineering, has been the major contributor in the work reported on Effects of Truncated Grounds on Image Glide Paths, and the design of the ± 35° V-Ring localizer array. He also investigated the Buffalo siting problem.

Professor G. E. Smith performed and reported the work on the worst case of snow effects and contributed the analysis of errors introduced by the reference theodolite displacement from the glide path coordinate center.

Mr. J. J. Battistelli is responsible for the work reported on the modulator tolerance study, the Detroit test site implementation, the experimentation with the integral and near-field, seven-element monitor, and integral glide path monitor, and the data presented on the effects of deep snow on far-field path angle.

Mr. J. T. Gorman developed the physical optics model presented in section II D and performed many of the calculations to predict critical areas for aircraft location.

Mr. Lewis Drake has worked on solving the overflight problem relating to localizer monitoring and the L-Band conversion scheme.

Dr. G. V. S. Raju participated as editor of this report.

Messrs. William Kennedy, Richard Zoulek, David Hildebrand, Daniel Gibbens, John Andress, Edward Anderson, William Geiger, and David Putnam contributed significantly to the collection of data and the calibration and standardization of the receiving and recording equipment.

Dr. Richard H. McFarland served as Project Director and was responsible for the discussions of theodolite references, for the analysis of the Detroit and Travis siting problems, for the collection of airborne data, and for providing special seminars concerning ILS performance for Category II.

Special acknowledgment is given to the WZZM-TV (Grand Rapids, Michigan) staff, headed by Mr. Dale Wolters, for its fine cooperation in helping establish and maintain the snow monitoring site. Also, Mr. Robert Stream, Ravenna,

Michigan, made a major contribution by providing at no cost a site location for the transmitting station which was used in the snow data collection. This is gratefully acknowledged.

VI REFERENCES AND BIBLIOGRAPHY

[1] "Instrument Landing System Improvement Program," Interim Report, SRDS Report No. 70-9, Avionics Research Group, Department of Electrical Engineering, Ohio University, 1971.

[2] McFarland, R. H., "Radio Theodolite Placement Criteria for Glide Path Measurements," SRDS Technical Report RD 69-4, Federal Aviation Administration, January 1969.

[3] "Earth Cover and Contour Effects on Image Glide Paths, Phase III," SRDS Technical Report RD 68-60, 1, (EER 5-7), Avionics Research Group, Department of Electrical Engineering, Ohio University, for Federal Aviation Administration (Systems Research and Development Service), September 1968.

[4] "Instrument Landing System Improvement Program," Interim Report, SRDS Report No. RD 71-30, Avionics Research Group, Ohio University, Athens, Ohio, October 1971.

[5] Ramo, S. and J. R. Whinnery, "Fields and Waves in Modern Radio," John Wiley and Sons, New York, N. Y., 1953, p. 375.

[6] Gilchrist, Thomas A., "Investigation of Changes in the Near and Far-Field Glide-Path Angle Due to Layers of Snow on the Ground Plane," Masters Thesis, Ohio University, Athens, Ohio, June 1970.

[7] Abbas, M. and D. Pidwell, "Effects of a Stratified Snow Covering on the Near and Far-Fields of an Image Glide Path," Unpublished Technical Memorandum, June 1970.

[8] Keesey, Joseph, "Glide Path Summary," EED 1-5, Avionics Research Group, Department of Electrical Engineering, Ohio University, September 1968.

[9] Redlich, R. W., "Instrument Landing Systems for Aircraft Problems of Installation," Proc IREE (Australia), Vo. 29, No. 11, November 1968, pps. 369-377.

[10] Sondretto, P. C., Electronic Aviation Engineering. New York. International Telephone and Telegraph Corp., 1958, pps. 656-672.

[11] Iden, F. W., "Glide Slope Antenna Arrays for Use Under Adverse Siting Conditions," IRE Trans. Aeronautical and Navigational Electronics, Vol. ANE-6, June 1959, pps. 100-111.

[12] Redlich, R. W., "Image Radiation from a Finite Ground Plane in Two Dimensions," IEEE Trans. Antennas and Propagation, May 1968, Vol. AP-16, No. 3. pps. 334-337.

[13] Harrington, R. F., "Time Harmonic Electromagnetic Fields, " McGraw-Hill, 1961, p. 224.

[14] Gradshtyn and Rhyzik, "Tables of Integrals, Series. and Products," Academic Press, 1965, p. 731.

[15] Baghdady, E. J., "Lectures on Communication Theory," McGraw-Hill Book Company, Inc., New York, N. Y., 1961, p. 4[illegible].

BIBLIOGRAPHY

Dettman, John W., "Applied Complex Variables," The Macmillan Company, New York, 1965, p. 364.

Kraus, John D., "Antennas," McGraw-Hill Book Company, New York, N. Y,. 1950.

VII GLOSSARY

DDM	Difference in Depth of Modulation.
SB-CSB	Sideband Power Radiated on the Carrier.
APCU 28	Antenna Phase and Calibration Unit.
TM Wave Expansion	The Expansion of a Transverse Electromagnetic Wave Expression in Series Form.
Asymptote of the Hyperbola	A Line Which Continually Approaches a Hyperbola, and Becomes Tangent to it at an Infinite Distance.
RRT Reference	Radio Referenced Theodolite.
SWR	Standing Wave Ratio.
PFCD	Portable Field and Course Detector.
Matched Load	A Load that Matches the Characteristic Impedance of the Connecting Transmission Line.
CW Sideband	Continuous Wave Sideband.
AGC	Automatic Gain Control.
Truncated Ground Plane	A Reflecting Plane for an Image Glide Slope Which is Flat Only for a Short Distance in Direction of Intended Glide Slope Use, After Which a Sharp Dropoff Occurs.

VIII APPENDICES

APPENDIX A. Equations Used in the Computation of Radiation Patterns

Generally, the method consists of computing a radiation pattern in the presence of a truncated ground plane of length L from the equation

$$P'(\theta) = P_D(\theta) + \frac{1}{\pi} \int_{-1}^{+1} P_I(\cos^{-1}(v)) \frac{\sin(\beta_o L(\cos\theta - v))}{(\cos\theta - v)} dv \qquad (A.1)$$

In Equation (A.1), $P'\theta$ = radiation pattern, with truncated ground plane, at elevation angle θ

$P_D(\theta)$ = direct radiation from array, excluding image

$P_I(\theta)$ = image pattern with infinite ground plane

β_o = 2π/ wavelength

A common origin of coordinates must be used for $P_D(\theta)$ and P_I. If this origin is taken on the base of the antenna mast,

$$P_D(\theta) = -P_I(-\theta)$$

Equation (A.1) was applied to the following three arrays:

a) Null reference array, with sideband antenna at height 10 λ, carrier antenna at height 5λ. The sideband patterns P_D and P_I are

$$\text{sideband} \begin{cases} P_D = e^{+j(20\pi \sin\theta)} & (A.2) \\ P_I(\cos^{-1} v) = -e^{-j(20\pi\sqrt{1-v^2})} & (A.3) \end{cases}$$

Carrier patterns are obtained by replacing 20π by 10π in Equations (A.2), (A.3).

b) Capture effect array, with antennas at 5λ, 10λ, and 15λ. Parterns are

$$\text{sideband}\begin{cases} P_D = (1 - \cos(10\pi \sin\theta))\, e^{j(20\pi \sin\theta)} & \text{(A.4)} \\ P_I(\cos^{-1} v) = -(1 - \cos(10\pi\sqrt{1-v^2}))\, e^{-j(20\pi\sqrt{1-v^2})} & \text{(A.5)} \end{cases}$$

$$\text{carrier}\begin{cases} P_D = e^{j(10\pi \sin\theta)} - \frac{1}{2} e^{j(20\pi \sin\theta)} & \text{(A.6)} \\ P_I(\cos^{-1} v) = -e^{-j(10\pi\sqrt{1-v^2})} + \frac{1}{2} e^{-j(20\pi\sqrt{1-v^2})} & \text{(A.7)} \end{cases}$$

$$\text{clearance}\begin{cases} P_D = \cos(10\pi \sin\theta)\, e^{j(20\pi \sin\theta)} & \text{(A.8)} \\ P_I(v) = -\cos(10\pi\sqrt{1-v^2})\, e^{-j(20\pi\sqrt{1-v^2})} & \text{(A.9)} \end{cases}$$

c) Modified sideband reference glide slope array with antenna heights 7.5 λ and 2.5 λ. (Path angle is 2.86 for this case).

$$\text{Sideband} \begin{cases} P_D = e^{j(15\pi \sin\theta)} - e^{j(5\pi \sin\theta)} \\ P_I(v) = -e^{-j(15\pi\sqrt{1-v^2})} + e^{-j(5\pi\sqrt{1-v^2})} \end{cases} \tag{A.10}$$

$$\text{Carrier} \begin{cases} P_D = e^{j(5\pi \sin\theta)} \\ P_I(v) = -e^{-j(5\pi\sqrt{1-v^2})} \end{cases} \tag{A.11}$$

APPENDIX B. Glide Path Sites Classified as to Likelihood of Presence of Snow on the Ground Planes

GROUP I CONTINUOUS DEEP LAYERS OF SNOW

1. Anchorage, Alaska
2. Annette, Alaska
3. Cold Bay, Alaska
4. Duluth, Minnesota
5. Fairbanks, Alaska
6. Green Bay, Wisconsin
7. Kincheloe, Michigan
8. King Salmon, Alaska
9. Minneapolis-St. Paul, Minnesota

GROUP II INTERMITTENT DEEP LAYERS OF SNOW

1. Allentown, Pennsylvania
2. Battle Creek, Michigan
3. Battle Creek, Michigan
4. Bedford, Massachusetts
5. Binghamton, New York
6. Boston, Massachusetts
7. Buffalo, New York
8. Burlington, Vermont
9. Chicago, Illinois
10. Columbus, Ohio
11. Eau Claire, Michigan
12. Erie, Pennsylvania
13. Fargo, North Dakota
14. Flint, Michigan
15. Fort Wayne, Indiana
16. Grand Rapids, Michigan
17. Klamath Falls, Oregon
18. Lansing, Michigan
19. Madison, Wisconsin
20. Manchester, New Hampshire
21. Milwaukee, Wisconsin
22. Muskegon, Michigan
23. Niagra Falls, New York
24. Portland, Maine
25. Portland, Oregon
26. Rochester, Minnesota
27. Rochester, New York
28. Spokane, Washington
29. South Bend, Indiana
30. Syracuse, New York
31. Worchester, Massachusetts
32. Yakima, Washington

GROUP iii OCCASIONAL SIGNIFICANT LAYERS OF SNOW

1. Akron-Canton, Ohio
2. Andrews AFB, Maryland
3. Albany, New York
4. Albequerque, New Mexico
5. Amarillo, Texas
6. Asheville, North Carolina
7. Atlantic City, New Jersey
8. Baltimore, Maryland
9. Bismarck, North Dakota
10. Calverton, New York
11. Casper, Wyoming
12. Cedar Rapids, Iowa
13. Champaign, Illinois
14. Charleston, West Virginia
15. Chattanooga, Tennessee
16. Cheyenne, Wyoming
17. Chicago (ION), Illinois
18. Chicago, Illinois
19. Cincinnati, Ohio (Luken)
20. Cleveland, Ohio
21. Covington, Kentucky
22. Dayton, Ohio
23. Denver, Colorado
24. Des Moines, Iowa
25. Detroit, Michigan
26. Dulles International
27. Eugene, Oregon
28. Fayetteville, North Carolina
29. Fort Worth, Texas
30. Great Falls, Montana
31. Greensboro, North Carolina
32. Huron, South Dakota
33. Hutchinson, Kansas
34. Indianapolis, Indiana
35. Joplin, Missouri
36. Kansas City, Missouri
37. Knoxville, Tennessee
38. Laguardia, New York
39. [illegible]ington, Kentucky
40. Lincoln, Nebraska

41. Louisville, Kentucky
42. Lubbock, Texas
43. Lynchburg, Virginia
44. Mansfield, Ohio
45. Meachem Field, Oregon
46. Medford, Oregon
47. Memphis, Tennessee
48. Middletown, Pennsylvania
49. Midland, Texas
50. Milwaukee, Wisconsin
51. Nantuckett, Massachusetts
52. New Castle, Delaware
53. New Bedford, Massachusetts
54. New York (JFK), New York
55. Norfolk, Virginia
56. Omaha, Nebraska
57. Oshkosh, Wisconsin
58. Pendleton, Oregon
59. Peoria, Illinois
60. Philadelphia, Pennsylvania
61. Pittsburgh, Pennsylvania
62. Pocatello, Idaho
63. Portland, Oregon
64. Providence, Rhode Island
65. Pueblo, Colorado
66. Quincy, Illinois
67. Reading, Pennsylvania
68. Reno, Nevada
69. Richmond, Indiana
70. Rockford, Illinois
71. Rock Springs, Wyoming
72. St. Joseph, Missouri
73. St. Louis, Missouri
74. Salem, Oregon
75. Salt Lake City, Utah
76. Seattle, Washington
77. Sioux City, Iowa
78. Sioux Falls, South Dakota
79. Springfield, Illinois
80. Springfield, Missouri
81. Teterboro, New Jersey
82. Terra Haute, Indiana
83. Toledo, Ohio
84. Topeka, Kansas
85. Trenton, New Jersey
86. Tri-City, Tennessee

87. Tulsa, Oklahoma

88. Utica, New York

89. Waco, Texas

90. Waterloo, Iowa

91. Washington, D. C.

92. Wheeling, West Virginia

93. White Plains, New York

94. Wichita, Kansas

95. Wilkes-Barre, Pennsylvania

96. Williamsport, Pennsylvania

97. Willow Run, Michigan

98. Wilmington, North Carolina

99. Windsor Locks, Connecticut

GROUP IV NO SIGNIFICANT SNOW EFFECTS

01. Abilene, Texas
02. Andrews (OIL), Maryland
03. Arcata, California
04. Atlanta, Georgia
05. Augusta, Georgia
06. Austin, Texas
07. Bakersfield, California
08. Baton Rouge, Louisiana
09. Beaumont, Texas
10. Billings, Montana
11. Birmingham, Alabama
12. Boise, Idaho
13. Brownsville, Texas
14. Burbank, California
15. Charleston, South Carolina
16. Charlotte, North Carolina
17. Columbia, South Carolina
18. Columbus, Georgia
19. Corpus Christi, Texas
20. Covington, Kentucky
21. Dallas, Texas
22. Daytona Beach, Florida
23. El Paso, Texas
24. Evansville, Inidana
25. Fort Smith, Arkansas
26. Freeland, Missouri
27. Fresno, California
28. Grand Junction, Colorado
29. Grant County, Washington
30. Green, South Carolina
31. Greenville, South Carolina
32. Gregg County, Texas
33. Honolulu, Hawaii
34. Houston, Texas
35. Huntsville, Alabama
36. Jackson, Mississippi
37. Jacksonville, Florida
38. Kahului, Maui, Hawaii
39. Lafayette, Louisiana
40. Lake Charles, Louisiana

41. Little Rock, Arkansas

42. Long Beach, California

43. Los Angeles, California

44. Macon, Georgia

45. Meridian, Mississippi

46. Miami, Florida

[illegible], Alabama

48. Moline, [illegible]nois

49. Monroe, Louisiana

50. Monterey, California

51. Mon[illegible]omery, Alabama

52. Nashville, Tennessee

53. New Orleans, Louisiana

54. Newport News, Virginia

55. Oakland, California

56. Oklahoma City, Oklahoma

57. Ontario, California

58. Orlando, Florida

59. Peterson Field, Colorado

60. Raleigh-Durham, North Carolina

61. Roswell, New Mexico

62. Sacramento, California

63. St. Petersburg, Florida

63. San Angelo, Texas

64. San Antonio, Texas

65 San Diego, California

66. San Francisco, California

67. San Jose, California

68. Santa Barbara, California

69. Savannah, Georgia

70. Shreveport, Louisiana

71. Stockton, California

72. Tallahassee, Florida

73. Tampa, Florida

74. Tyler, Texas

75. Wake Island

76. West Palm Beach, Florida

77. Wichita Falls, Texas

APPENDIX C. Glide Path Data Relating to Speed Measurements Made on Snow Effects in February, 1971.

Grand Rapids, Michigan
Kent County Airport

Glide Slope Frequency 333.2 MHz
Published Glide Slope Angle 2.50°

IFR weather at time of tracking. Visibility approximately 1 mile

3 runs accomplished with aircraft sighted just outside middle marker

Run 1	Run 2	Run 3
2.78	2.50	2.52
2.62	2.49	2.48
2.78	2.49	2.52
	2.49	2.52

Run 1 readings taken with wide angle lens to facilitate optical acquisition-tracking not precise and should be ignored

Average glide slope angle runs 2 and 3 2.51°

Monitor Readings:

Path	Width
90 ~ 102%, 150 ~ 100%	90 ~ 103%, 150 ~ 95%

Monitor Alarm Readings:

Path	Width
90 Hz Dial cw 107% meter	166w 127% meter
95% meter	77% meter
150 Hz Dial 105% meter	127% meter
18 ccw 95% meter	16 ccw 78% meter
-16%	

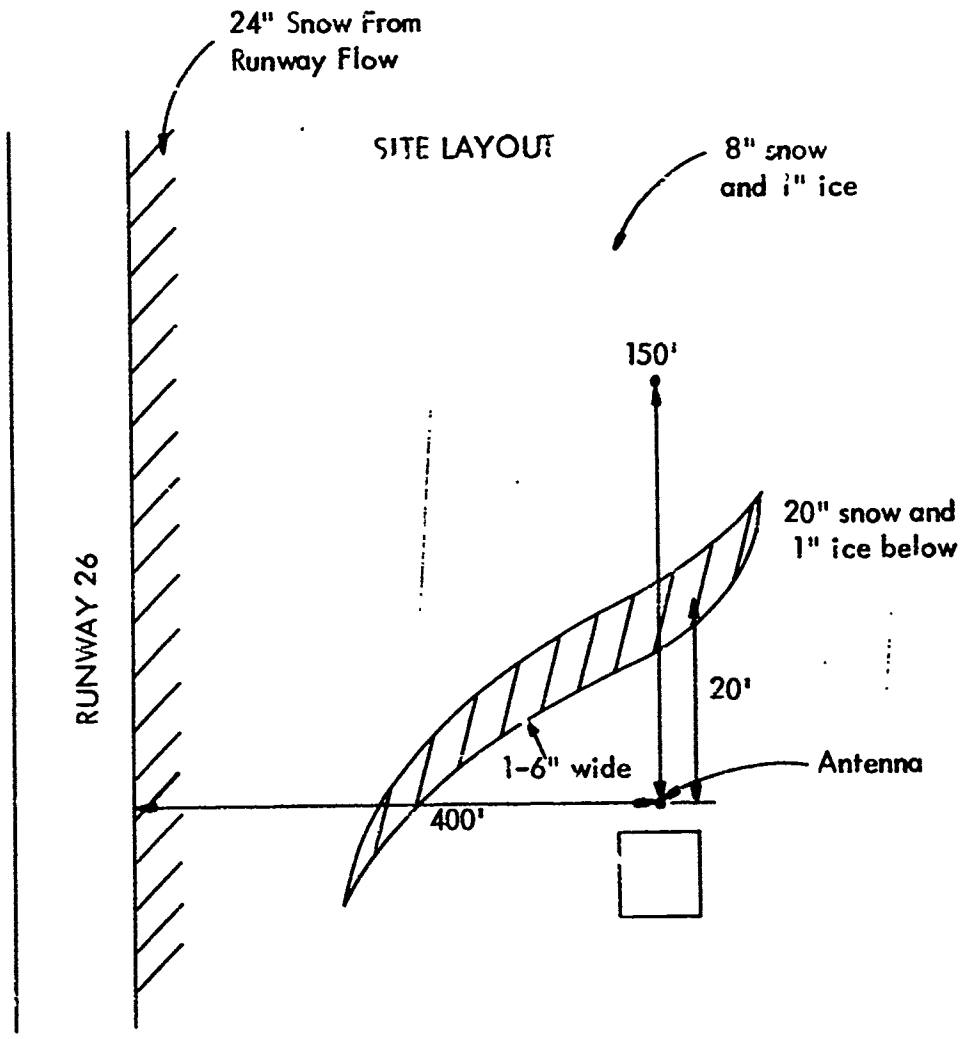
24" Snow From
Runway Flow
SITE LAYOUT
8" snow
and 1" ice
150'
20" snow and
1" ice below
RUNWAY 26
20'
1-6" wide
Antenna
400'

Figure C-1.

Green Bay Wisconsin
Austin-Straubel Airport

Glide Slope Frequency 332.6 MHz
Published Glide Slope Angle 2.65°

Two runs in clear weather, sunset - temp. -20°F

Run 1		Run 2	
2.69	2.69	2.68	2.69
2.69	2.69	2.68	2.69
2.68		2.69	
2.69		2.70	
2.69		2.70	
2.69		2.69	
2.69		2.69	
2.69		2.69	
2.66		2.69	
2.67		2.70	
2.67		2.69	
2.67		2.68	
2.68		2.68	
2.68		2.67	
2.69		2.69	
2.69		2.70	
2.69		2.70	
2.69		2.70	
2.68		2.70	
2.69		2.70	
2.70		2.70	
2.70		2.70	
2.69		2.69	

2.689

Average Glide Slope Angle Runs 1 and 2 2.689

Monitor Readings

Path		Width	
90~ 100%	150~94%	90~ 101%	150~ 100%

Monitor Alarm Reading

Path			Width		
90 Hz Dial	18 cw	110% meter	90 Hz Dial	16 cw	112% Meter
	18 cw	89% meter		20 ccw	91% Meter
	Nominal		150 Hz Dial	18 cw	113% Meter
				18 ccw	92% Meter
150 Hz Dial	15cw	105% meter			
	21ccw	86% meter			

16% to alarm high

10% to alarm narrow

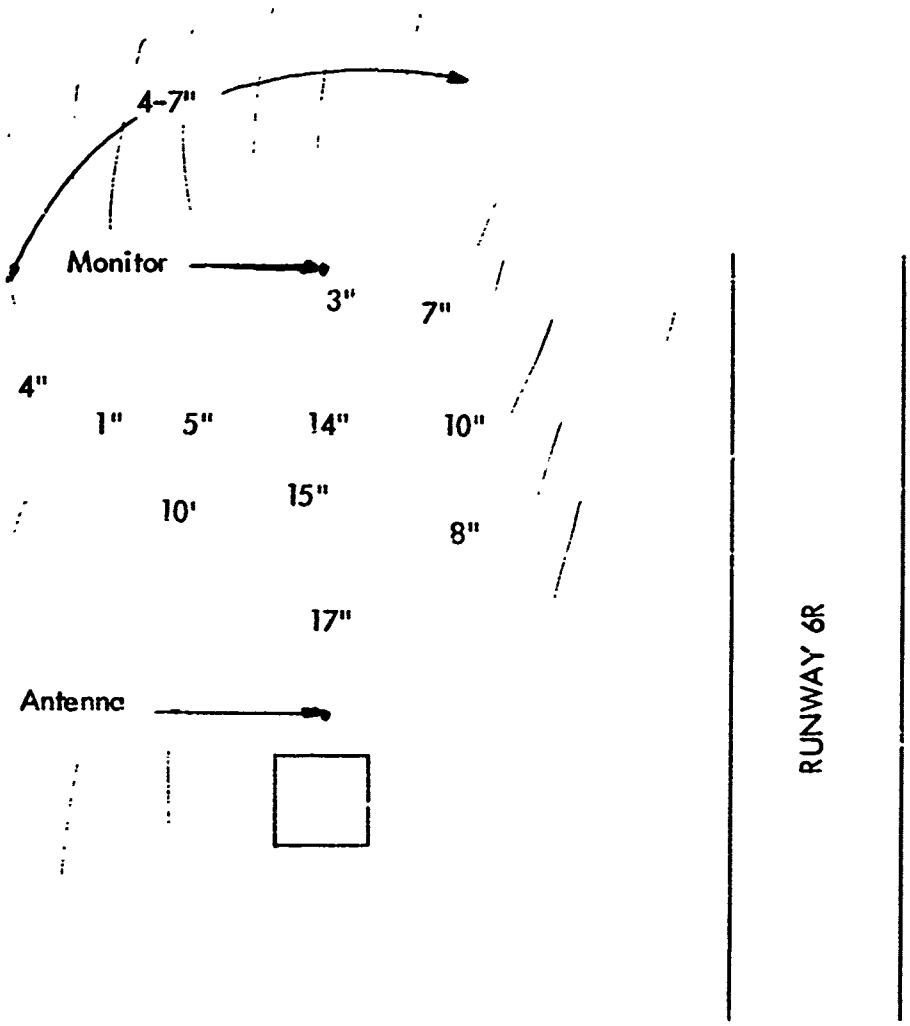

Figure C-2.

Appleton, Wisconsin
Outagamie County

ALL Transistorized Glide Slope Transmitter
Published Glide Slope Angle 2.50°

	Run 1	Run 2	Run 3	
	2.50	2.50	2.52	2.52
	2.50	2.50	1.51	2.52
	2.50	2.50	2.53	2.52
	2.50	2.52	2.53	2.52
	2.51	2.52	2.52	2.52
	2.53	2.51	2.52	2.52
	2.53	2.51	2.52	2.52
	2.50	2.50	2.52	2.52
	2.50	2.52	2.54	2.52
	2.50	2.52	2.53	2.52
	2.50	2.52	2.53	2.52
	2.50	2.52	2.52	2.52
	2.50	2.53	2.52	2.52
	2.50	2.52	2.52	2.52
	2.50	2.52	2.52	
	2.52	2.52	2.52	
	2.51		2.52	
			2.52	
			2.51	
			2.52	
			2.52	
Average Glide Slope		2.516	2.52	
			2.52	
			2.52	
			2.52	

Monitor Readings

Path 26 Width 36

	Monitor Limits		Path
Path	20	80	80% of Alarm Limit
Width	20	88	

Width

47% of Alarm Limit

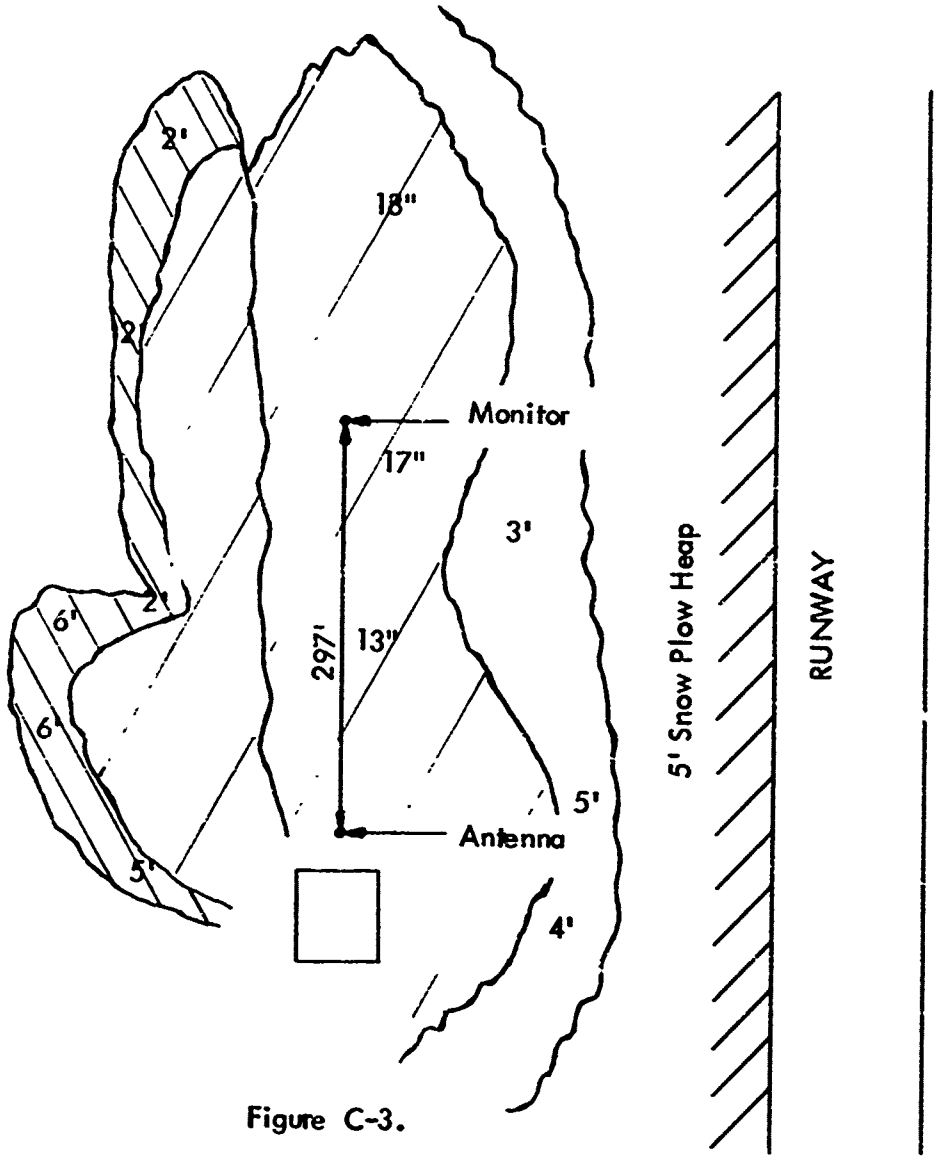

Figure C-3.

Area Between Antenna and Monitor Broken with 3' Furrows Due to Unsuccessful Snow Removal Effort.

Snow Density _____

Duluth, Minnesota
Duluth International Airport

Glide Slope Frequency 33.50 MHz - Capture Effect
Published Glide Slope Angle 2.62°

Run 1	Run 2
2.65	2.64
2.65	2.65
2.64	2.65
2.64	2.66
2.64	2.65
2.67	2.65
2.65	2.65
	2.65
	2.65
	2.65
	2.65
	2.65

Average Angle 2.65°

Monitor Readings

Path		Width	
90 ~ 102%	105 ~ 102%	90 ~ 100%	150 ~ -100%

Monitor Alarm Readings

90 Hz	107% Meter	114%
	96% Meter	92%
150Hz	107% Meter	114%
	98% Meter	92%
0% Toward Alarm		0% Toward Alarm

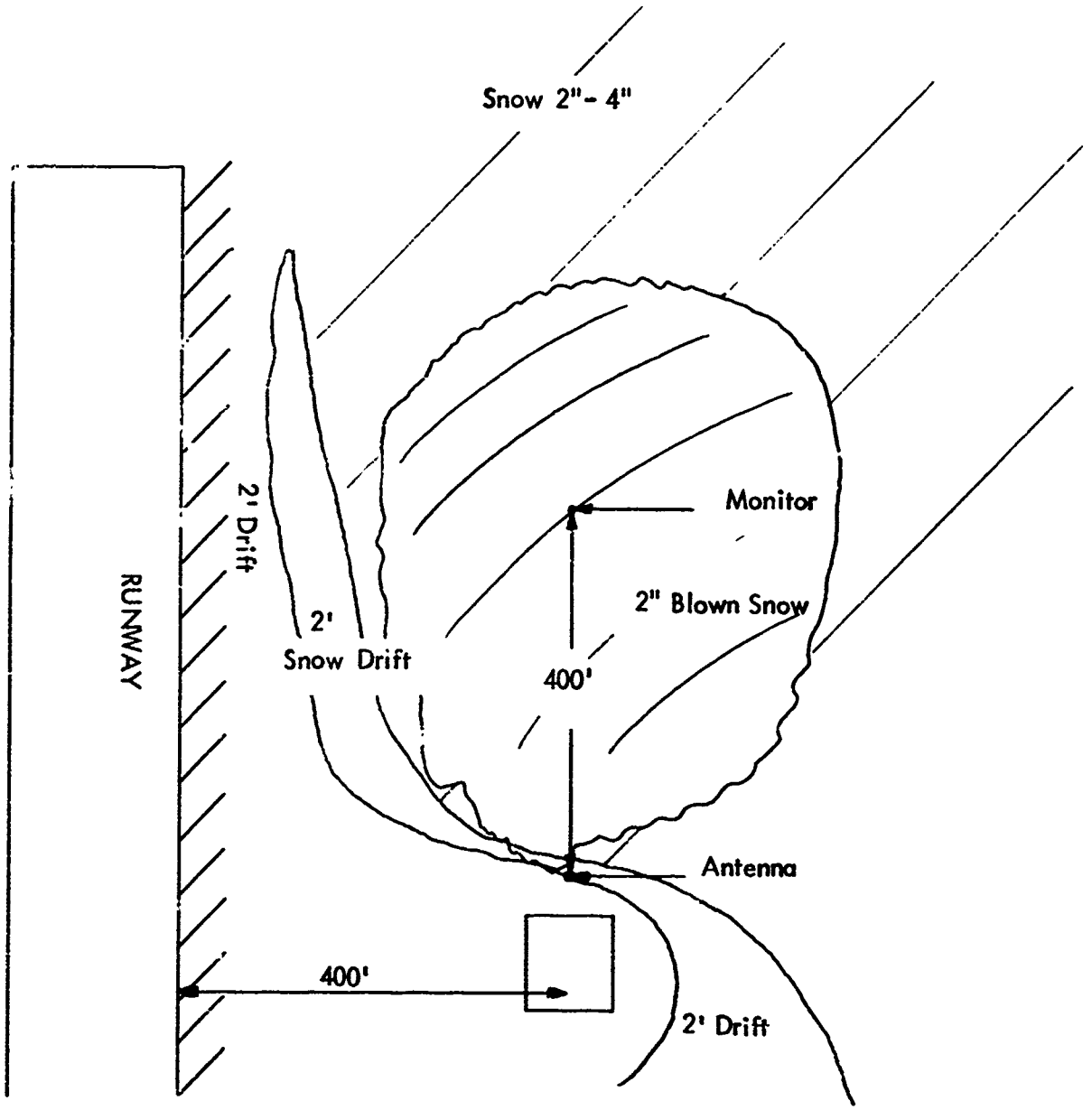
Snow 2"- 4"
RUNWAY
2' Drift
2'
Snow Drift
Monitor
2" Blown Snow
400'
Antenna
400'
2' Drift

Figure C-4.

Minneapolis, Minnesota
World-Chamberlain Field

Runway 29L Cat. II.
Glide Slope Frequency 335.0
Published Glide Slope Angle 2.50°

Run 1	Run 2
2.55°	2.55
2.54	2.55
2.54	2.55
2.55	2.56
2.55	2.56
2.55	2.55
2.56	2.55
2.56	2.56
2.55	2.55
2.55	2.55
2.55	2.55
2.55	2.55
2.55	2.55
2.55	2.56
2.56	2.55

Average Glide Slope Angle 2.55°

Monitor Readings

Path	Width
90 ~ 100% 150 ~ 100%	90 ~ 100% 150 ~ 100%
0% Toward Alarm	0% Toward Alarm

Average Glide Slope Angle - 2.50°

Monitor Reading

Path	Width
90 ~ 100% 150 ~ 100%	90 ~ 107% 150 ~ 107%
0% Toward Alarm	0% Toward Alarm

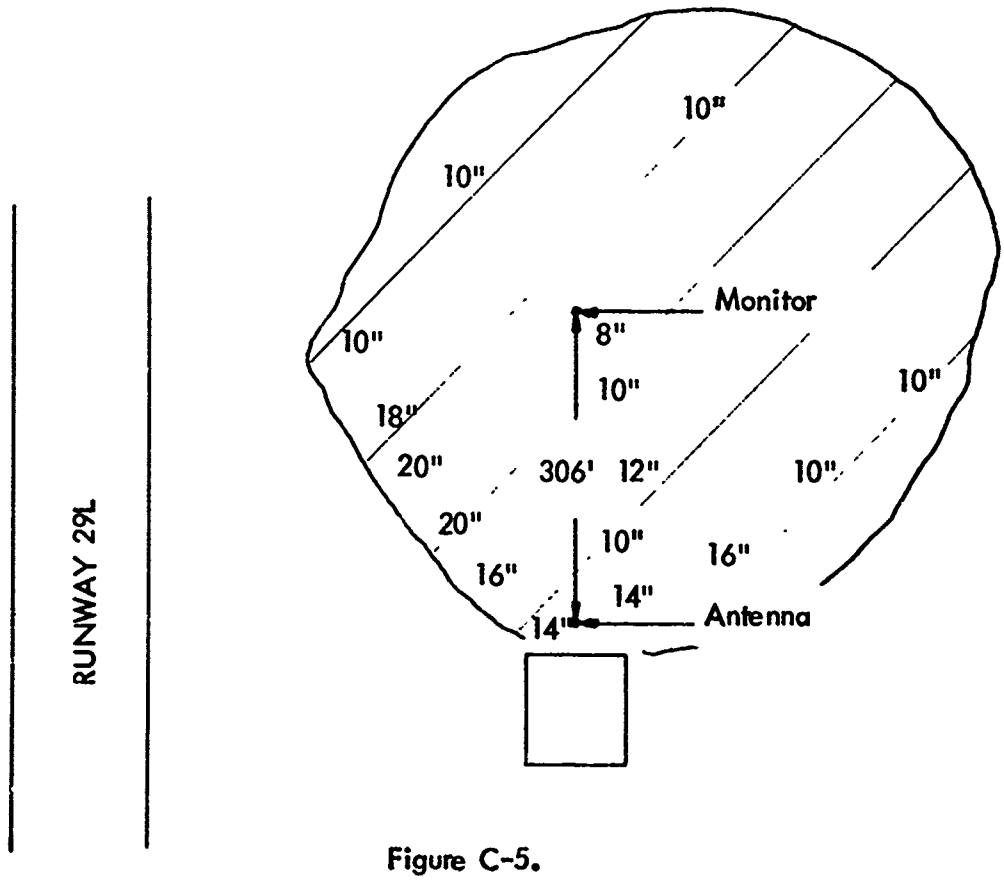

Figure C-5.

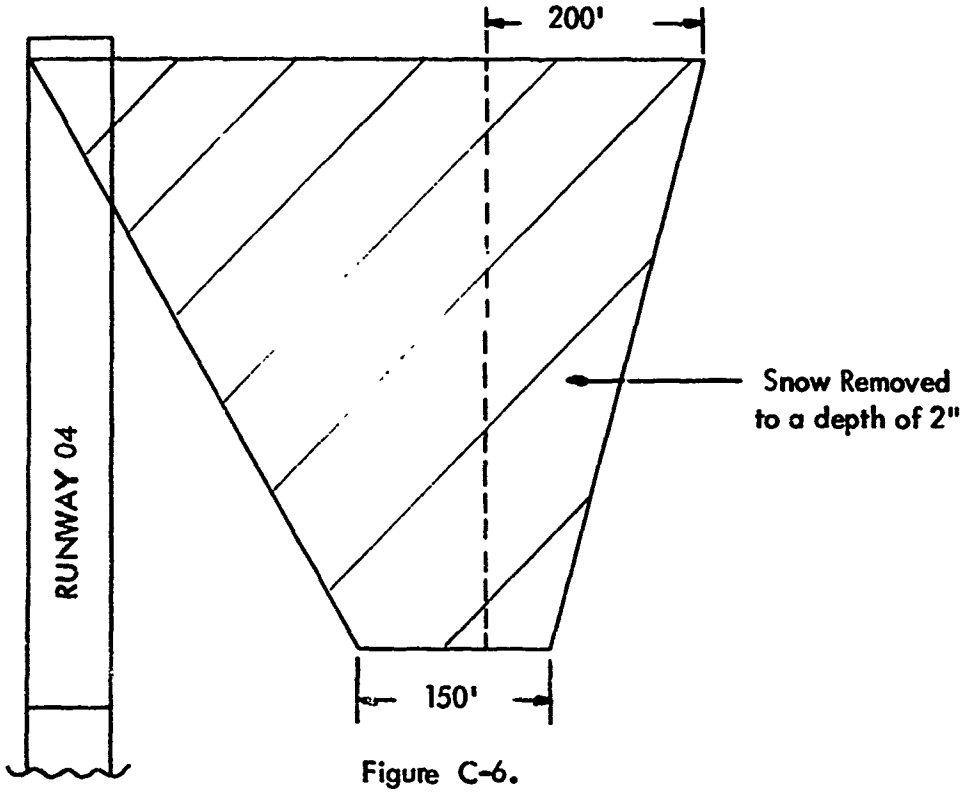

Figure C-6.

Runway 04
Glide Slope Frequency 332.0
Published Glide Slope Angle 2.50°

Run 1	Run 2
2.50	2.50
2.50	2.50
2.50	2.50
2.50	2.50
2.50	2.50
2.50	2.50
2.50	2.50
2.50	2.50
2.51	2.50
2.51	2.50
2.51	2.50
2.51	2.50
2.50	2.50
2.50	2.50
2.50	2.50

Rochester, Minnesota
Rochester Muni

Glide Slope Frequency 329.9
Published Glide Slope Angle 2.75°

Blowing Snow - 30 k Wind Gusts to 45

Run 1	Run 2	Run 3
2.76	2.78	2.78
2.77		
2.77		
2.77		
2.78		
2.78		
2.78		
2.78		
2.78		
		2.78
	2.78	

Average Glide Slope Angle 2.78°

Monitor Alarms

90 ~ 93% 104%
150 ~ 104% 93%

Path 64% Toward Alarm
150 ~ High

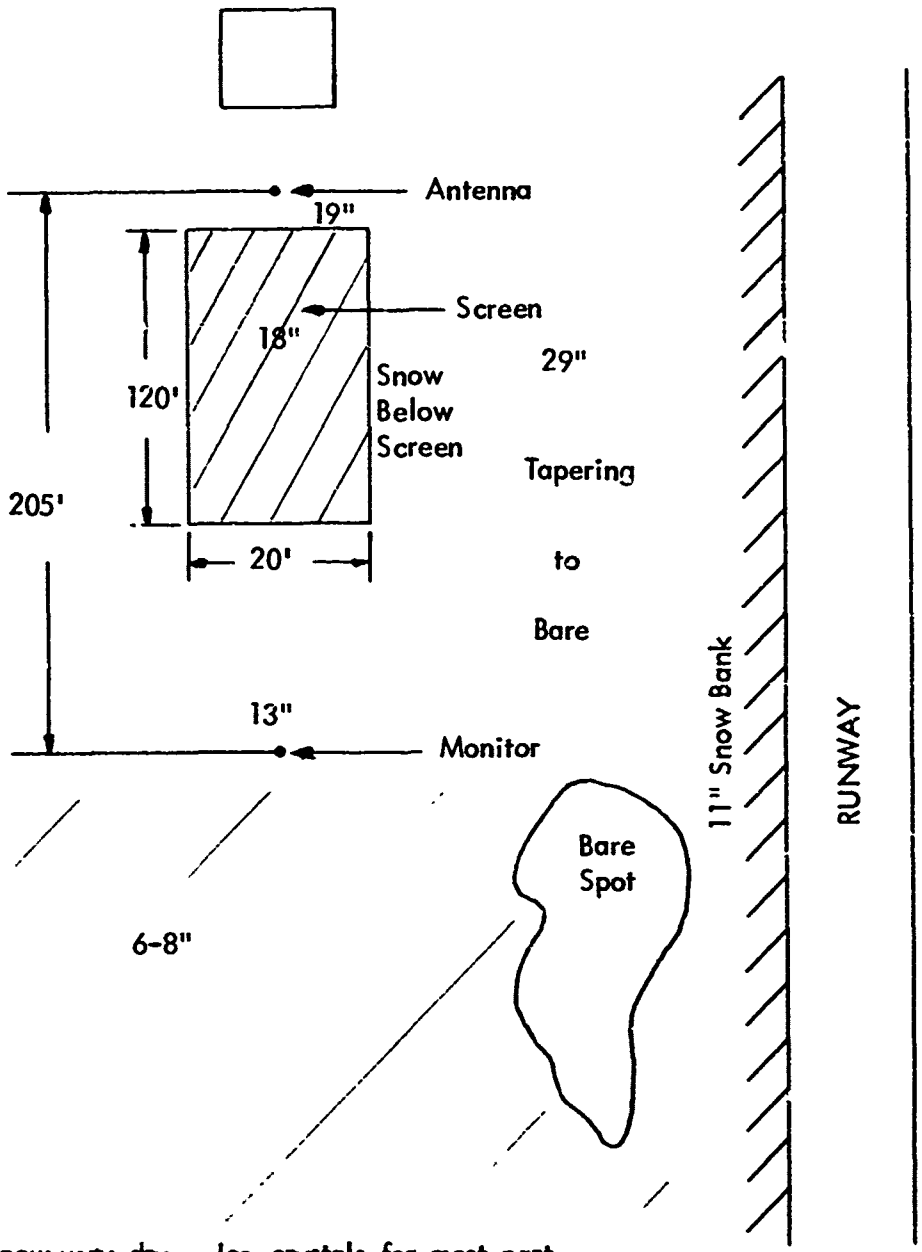

Snow very dry. Ice crystals for most part.

Figure C-7.

Madison, Wisconsin
Truax Field

Glide Slope Frequency 333.8 MHz
Published Glide Slope Angle 2.50°

Equipment No. 2,

Run 1	Run 2	Run 3	Run 4
2.56	2.59	2.59	2.62
2.58	2.58	2.59	2.595
2.58	2.59	2.585	2.59
2.585	2.595	2.59	2.59
2.585	2.595	2.585	2.595
2.585	2.59	2.595	2.58
	2.59	2.59	2.585
	2.59	2.595	2.59
	2.595	2.59	2.59
	2.595		2.59
	2.59		2.59
	2.59		2.59
	2.585		2.595
	2.59		
	2.59		
	2.59		

Average Glide Slope Angle 2.589

Monitor Readings

Path	
90 ~ 100%	150 ~ 100 %

Alarm Limits
90 ~ 95 - 105
150 ~ 105 - 95

Monitor 0% Toward Alarm

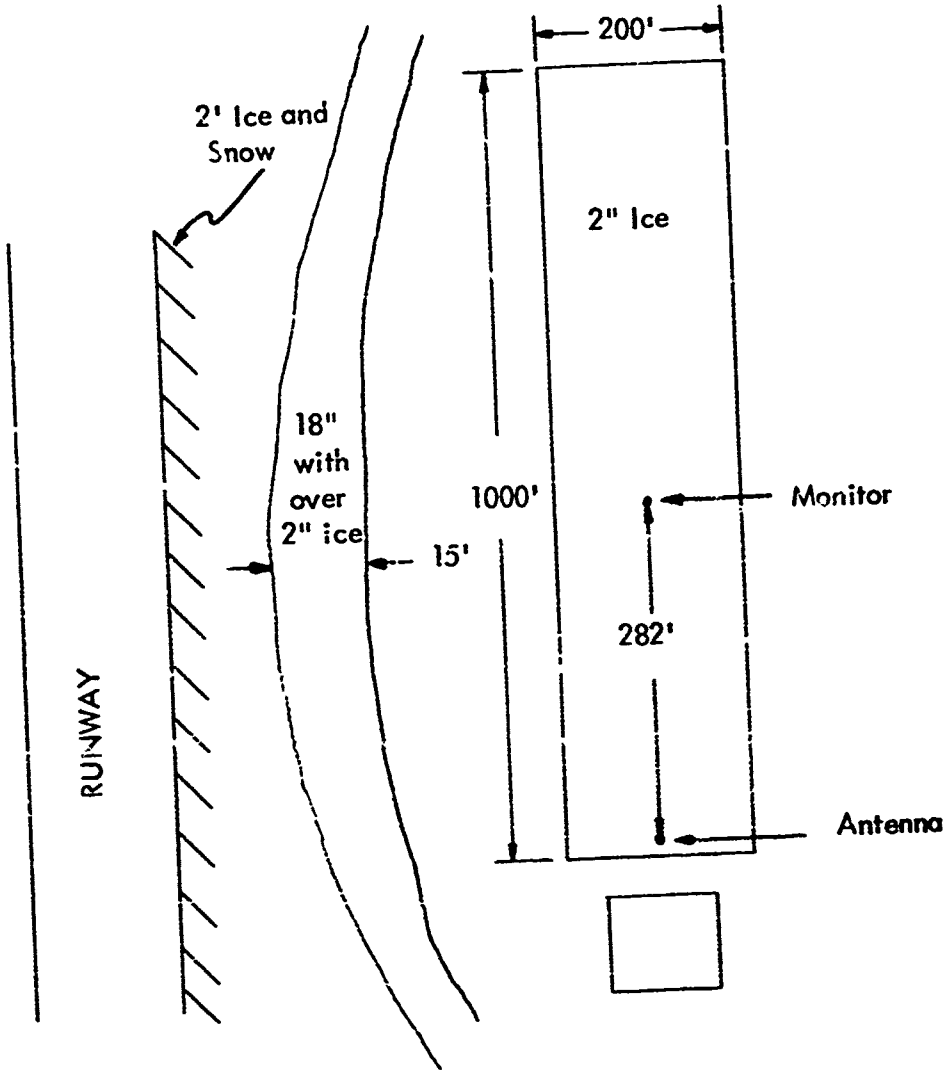
200'
2' Ice and
Snow
2" Ice
18"
with
over
2" ice
1000'
Monitor
15'
282'
RUNWAY
Antenna

Figure C-8.

Milwaukee, Wisconsin
General Mitchell Field. Runway 7R

Glide Slope Frequency 330.2 MHz
Published Glide Slope Angle 2.93°

Run 1	Run 2
2.97	2.99
2.98	3.01
2.98	3.0
2.98	2.99
2.98	2.99
3.0	2.99
3.0	3.0
3.0	3.0
3.0	3.0
3.0	3.0
3.0	3.0
2.98	3.0
2.98	2.99
2.99	2.99
2.99	3.0
3.0	3.0
3.0	2.99
2.99	2.99
2.99	
2.99	
3.0	
3.0	
2.99	
3.0	

Average Glide Slope Angle 2.99

Monitor Readings

Path

90 ~ 92 % 150 ~ 96 %

Alarm Readings

90 ~ 98% 91%
150 ~ 90% 97%

Monitor 66% Toward Alarm

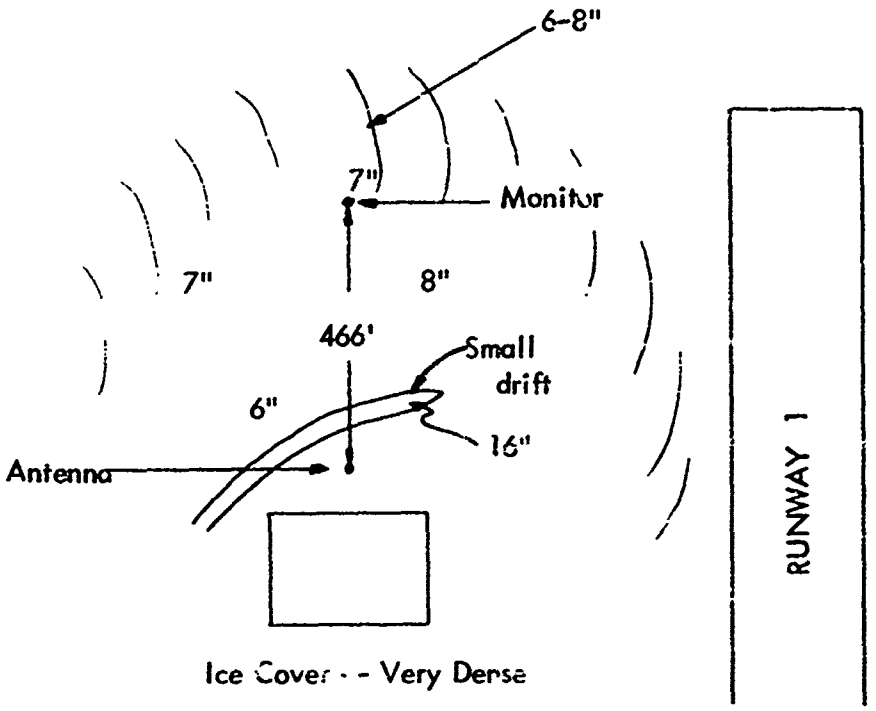

Figure C-9.

MKE Cat. II Runway 1
Published Glide Slope Angle 2.75°

Run 1		
2.75	2.76	2.76
2.76	2.76	2.76
2.76	2.76	2.76
2.77	2.78	2.76
2.77	2.77	2.75
2.77	2.77	
2.76	2.77	
2.76	2.77	

Run 2			
2.77	2.77	2.76	2.77
2.77	2.77	2.76	2.77
2.76	2.77	2.75	2.76
2.76	2.77	2.75	2.76
2.76	2.77	2.76	2.77
2.76	2.76	2.77	2.76
2.78	2.76	2.77	2.77
2.78	2.76	2.77	2.77
2.76	2.76	2.76	2.75
2.75			

Average Glide Slope Angle 2.76°

Monitor Readings

Path
90 ~ 90% 150~ 100%

Monitor Alarm Points
90 ~ 95% 105%
150 ~ 95% 105%

Monitor 40% to Alarm

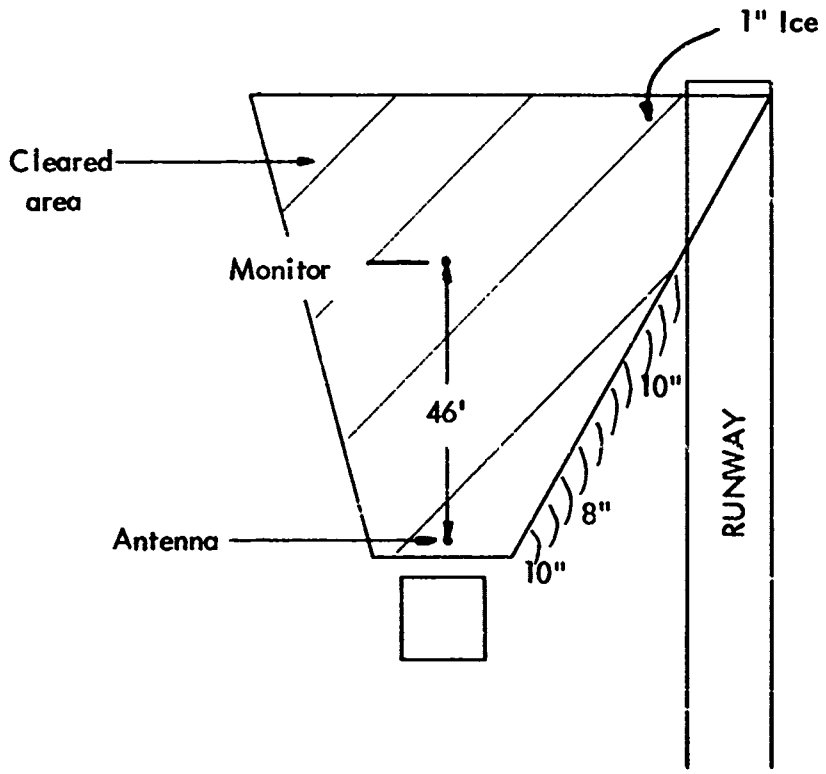

Figure C-10.

Mansfield, Ohio
Published Glide Slope Angle 2.73°

Run 1	Run 2	Width Run 3	Width Run 4
2.75	2.78	2.43	3.11
2.78	2.79	2.41	3.12
2.78	2.78	2.42	3.125
2.78	2.79	2.41	3.125
2.76	2.79	2.41	3.125
2.76	2.79	2.43	3.125
2.77	2.78	2.43	3.13
2.78	2.77	2.44	3.125
2.79	2.79	2.43	3.12
2.78	2.79	2.44	
2.78	2.69	2.43	
2.78	2.79	2.43	
	2.77	2.43	
	2.78	2.44	
	2.78	2.43	
	2.79	2.44	
	2.79	2.45	
	2.79	2.42	
	2.78	2.43	

Width Run 5	Width Run 6	90 μ A Run 7
3.15	3.32	3.30
3.10	3.32	3 20
3.18	3.36	3.29
3.175	3.34	3.27
3.09	3.26	3.28
3.26	3.24	3.39
3.22	3.28	3.37
3.22	3.32	3.37
3.12	3.28	3.37
3.19	3.32	3.35
3.16	3.34	3.33
		3.39
		3.24
		3.34
		3.33
		3.40
		3.38

Average Glide Slope Angle 2.87°

Average Bottom Width 2.43°
Average Top Width 3.15 Runs 4 and 5

Monitor Readings

Path		Clearance	
90 ~ 99%	150 ~ 100%	90 ~ 93%	150 ~ 108%

Alarm Limits

90 ~ 15 Dial 93%	108%	3 Dial 91%	108%
150 ~ 18 Dial 93%	108%	31 Dial 93%	90%

17% Toward Alarm Edge of Too Narrow Alarm

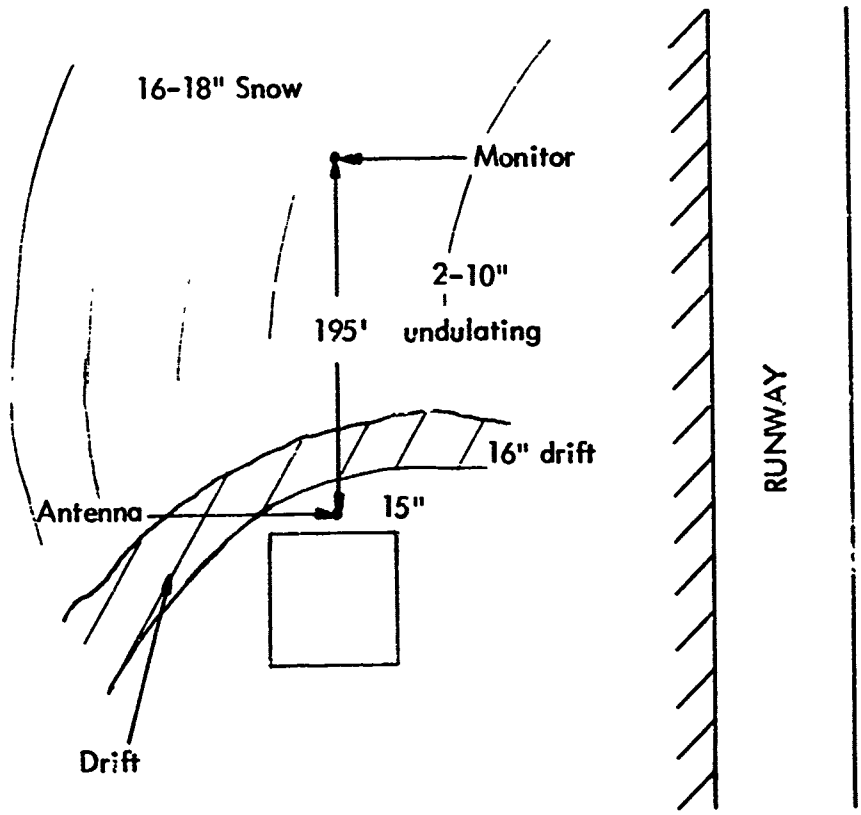

Snow Density--0.20

Figure C-11.

Akron - Canton
Cak.

Published Glide Slope Angle 2.95°

Run 1	Run 2	Width 90 μA Run 3 High
2.96	2.98	3.31
2.97	2.99	3.28
2.98	2.99	3.29
2.98	2.99	3.33
2.98	2.99	3.33
2.98	3.00	3.33
2.99	2.99	3.33
2.99	2.99	3.33
3.0	3.0	3.33
2.99	2.99	3.33
3.0	2.99	3.33
2.99	2.99	3.32
2.99	2.99	3.33
2.97		3.33
		3.32
		3.33
		3.33
		3.33

Average Glide Path Angle 2.99°

Average High 90 μA Run 3.32°

Course	Width
90 ~ 100% 150 ~ 98%	90 ~ 102% 150 ~ 102%

Alarm Limits

10 cw 90 ~ 94% 7 ccw 105 %	105% 150 ~ 93%	8-1/2 90 ~ 96%, 150 ~ 108% 8-1/2 ccw 108% 95%
17% Toward Alarm	0% Toward Alarm	

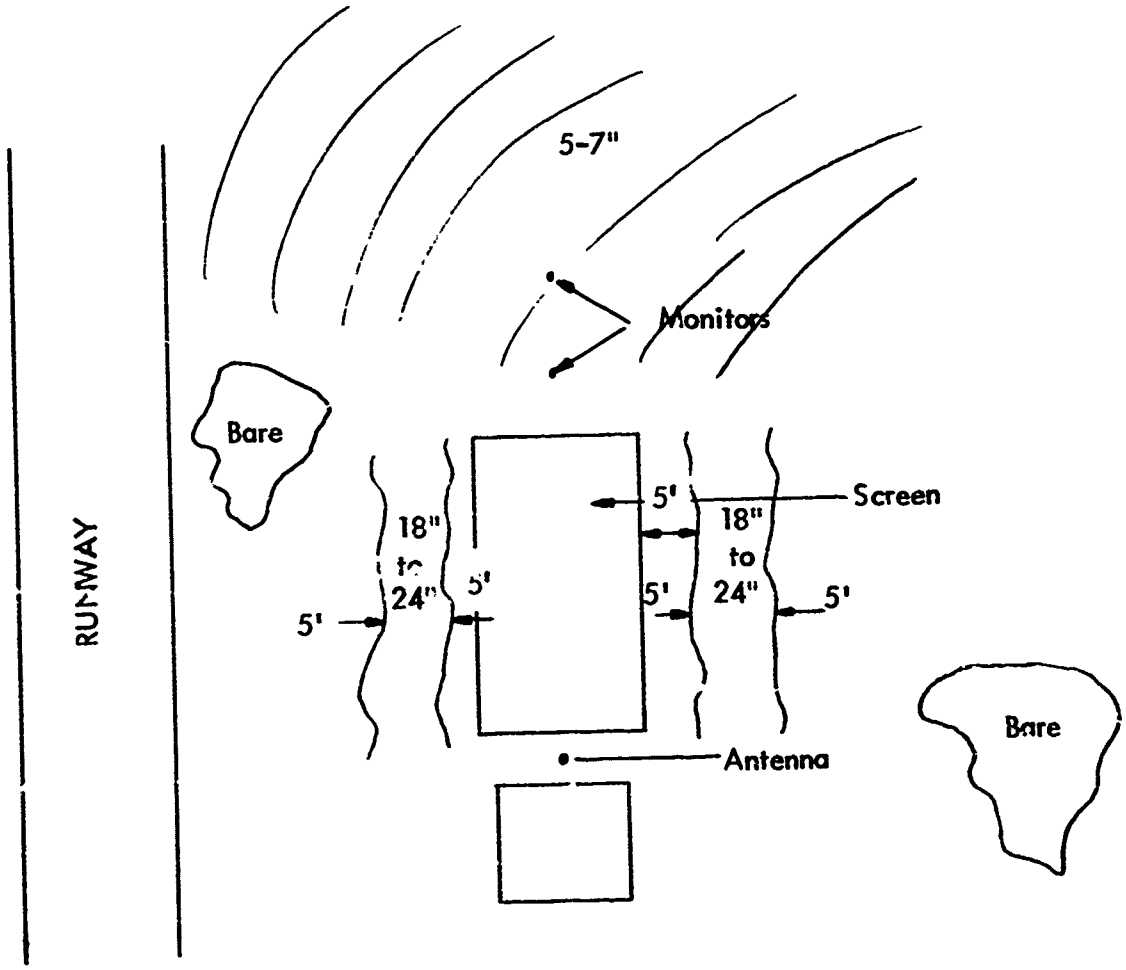

Figure C-12.

Youngstown
YNG.

Published Glide Slope Angle 2.98°

Run 1	Run 2	Run 3
3.05	3.05	3.09
3.07	3.09	3.09
3.07	3.08	3.09
3.06	3.07	3.1
3.06	3.07	3.11
3.06	3.08	3.10
3.04	3.07	3.09
3.04	3.07	3.09
3.06	3.06	3.09
3.08	3.06	3.1
3.06	3.055	3.095
3.04	3.055	3.095
3.04	3.06	3.1
	3.05	3.09
	3.06	3.09
	3.09	3.09
	3.09	3.09
	3.09	3.09
	3.09	3.09
	3.07	3.095
	3.07	3.09
	3.07	3.09

3.08° Average Path Angle

Monitor Readings

Path	Width
90 ~ 82% 150 ~ 87%	90 ~ 105% 150 ~ 105%
Alarm Limits	
8-1/2 ccw 90 ~ 88, 150 ~ 83 4 cw 90 ~ 81 150 ~ 89	6-1/2 ccw 90 ~ 110% 150 ~ 98% 8 cw 90 ~ 101% 150 ~ 108%
35% into Alarm	10% into Alarm

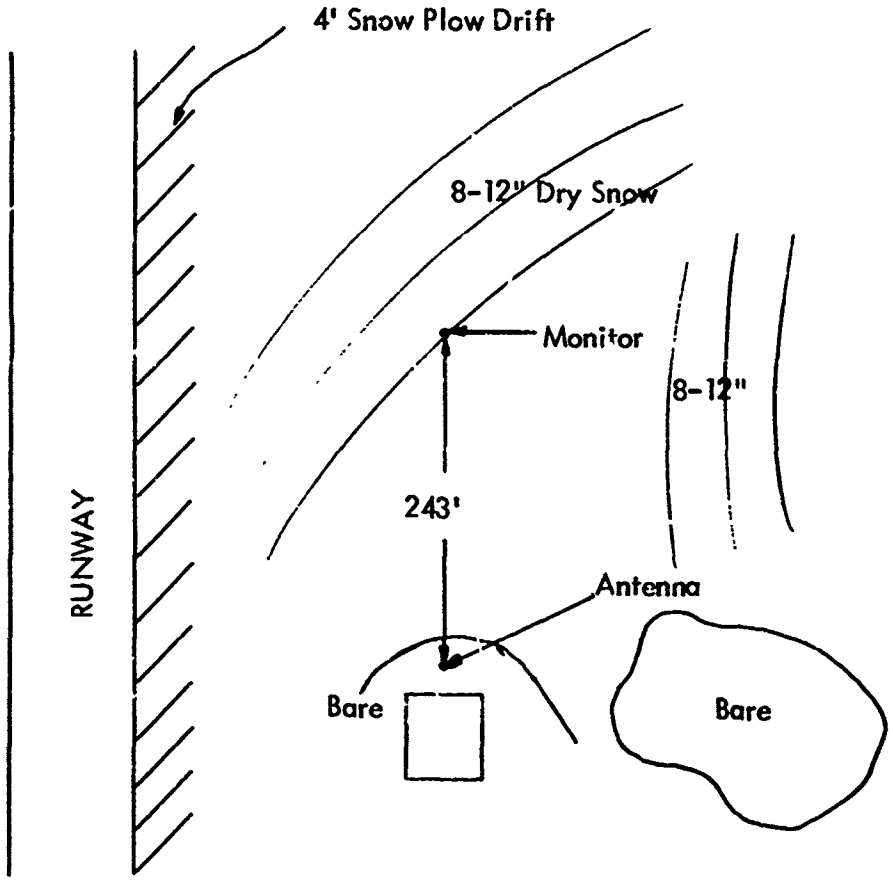

Figure C-13.

Columbus, Ohio
Port Columbus Airport

Published Glide Slope Angle - 3.0°
Average FAA Rtty Angles 3.13° 8200.11A No. 1 Equip.
3.07° 8240.20 No. 1 Equip.

Call received from Columbus that glide slope path was on edge of alarm.

Run 1 and 2 made at 11:00 AM with monitor reading.

Monitor

Width		Course	
150 ~	90 ~	150 ~	90 ~
100	112	105	113

Alarm Test 2.5 DDM into 90

Width		Course	
cw	ccw	cw	ccw
23	6	13	3

62.5% to Alarm

Run 1			Run 2				
3.12	3.11	3.12	3.11	3.12	3.13	3.1	3.11
3.1	3.09	3.12	3.13	3.13	1.31	3.1	
3.1	3.12	3.12	3.13	3.13	3.12	3.1	
3.12	3.11		3.12	3.13	3.12	3.11	
3.11	3.11		3.13	3.12	3.11	3.11	
3.10	3.11		3.13	3.12	3.12	3.105	
3.08	3.12		3.12	3.12	3.12	3.11	
3.10	3.11		3.12	3.13	3.12	3.11	
3.10	3.1		3.12	3.12	3.1	3.11	

Average Measured Glide Slope 3.114° 11:00 AM

12 Noon Monitor Readings

Width		Course	
150 ~	90	150	90
102	112	106	116

Alarm Test 2.75 DDM into 90 ~ Path

Width		Course	
cw	ccw	cw	ccw
22	8	14	2

75% to Alarm

12 Noon Run Run No. 3

3.14	3.13	3.10
3.13	3.13	3.12
3.14	3.13	3.11
3.13	3.12	
3.13	3.13	
3.13	3.12	
3.13	3.12	
3.13	3.13	
3.13	3.11	
3.13	3.12	

Average Glide Slope Angle 3.126°

2:30 PM Monitor Readings

Width		Path	
150 ~	90 ~	150 ~	90~
102	104	106	110

Runs
1. 3.108
2. 3.114
3. 3.126
4. } 3.125
5. }

Alarm Test

Width		Path	
cw	ccw	cw	ccw
17	13	11	5

37.5% to Alarm

Run 4			Run 5			
3.13	3.06	3.12	3.13	3.13	3.14	3.13
3.13	3.10	3.11	3.13	3.13	3.13	3.12
3.13	3.13	3.11	3.13	3.13	3.13	3.12
3.13	3.13	3.11	3.14	3.14	3.13	3.12
3.13	3.13	3.13	3.14	3.13	3.13	3.12
3.13	3.13		3.14	3.13	3.14	3.09
3.13	3.13		3.12	3.14	3.12	3.09
3.13	3.12		3.12	3.13	3.13	3.09
3.13	3.12		3.13	3.13	3.12	3.13
3.11	3.13		3.13	3.13	3.13	3.11
			3.13	3.12	3.14	3.13
			3.11	3.12	3.12	3.13

Average Glide Slope 3.125°

APPENDIX D. Calculation of H-Fields on Fuselage

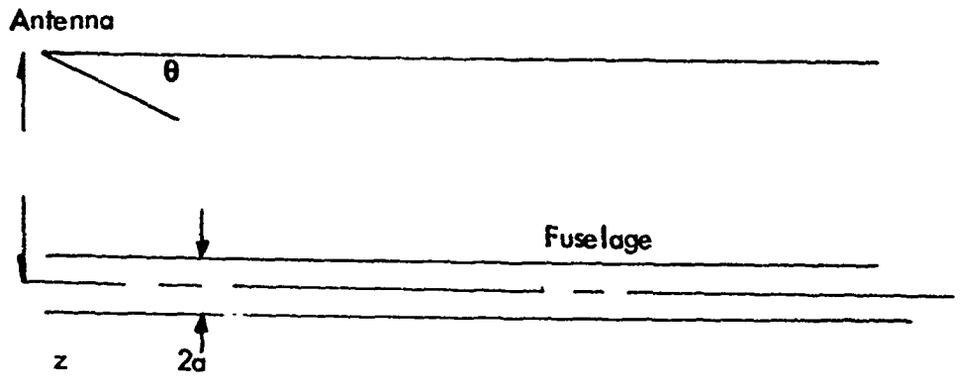

Figure D-1. Assume Antenna and Fuselage in Plane of Paper.

Incident

$$E_z^{\,i} = (z,\Phi) = A\,(z,\Phi)\,e^{i\Phi(z,\Phi)} \qquad \text{(Exact Solution)}$$

where

$E_z^{\,i}\,(z,\Phi)$ is even in Φ

$E_\Phi^{\,i}\,(z,\Phi)$ is negligible

Fourier transform of incident E_z

$$g(\beta_z,\Phi) = \int_{-\infty}^{\infty} A(z',\Phi)\,e^{i\Phi(z',\Phi)}\,e^{i\beta_z z'}\,dz'$$

Scattered

$$E_z^{\,s} = -E_z^{\,i} \text{ at } \rho = a$$

and

$$\beta_y = (\beta^2 - \beta_z^{\,2})^{\frac{1}{2}}$$

$$2\pi \sum_n H_n^{(2)}(\beta_y a)\,A_n(\beta_z)\cos n\Phi = g(\beta_z,\Phi)$$

$$A_n(\beta_z) = \frac{1}{2\pi^2 H_n^{(2)}(\beta_y a)} \int_0^{2\pi} g(\beta_z, \Phi) \cos n\Phi \, d\Phi$$

Exact $H_\Phi(z,\Phi)$ at $\rho = a$

$$H_\Phi(z,\Phi) = \frac{-j\beta}{\eta} \int_{\beta_z} \left(\frac{1}{\beta_y} \sum_n H_n^{(2)'}(\beta_y a) A_n(\beta_z) \cos n\Phi \right) e^{-j\beta_z z} d\beta_z$$

Substituting for $A_n(\beta_z)$ and $g(\beta_z, \Phi)$ and interchanging the integration on β_z and the summation on n

$$H_\Phi(z,\Phi) = \frac{-j\beta}{2\pi^2 \eta} \sum_n \cos n\Phi \int_{\Phi'} \int_{z'} \int_{\beta_z} \frac{H_n^{(2)'}(\beta_y a)}{\beta_y H_n^{(2)}(\beta_y a)}$$

$$A(z', \Phi') e^{j\psi(z', \Phi')} e^{j\beta_z (z'-z)} \cos n\Phi' \, d\Phi' \, dz' \, d\beta_z$$

rearrange to separate the integration on Φ' and the integration on z' and β_z

$$H_\Phi(z,\Phi) = \frac{-j\beta}{2\pi^2 \eta} \sum_n \cos n\Phi \int_{\Phi'} \cos n\Phi' \int_{\beta_z} \int_{z'} \frac{H_n^{(2)'}(\beta_y a)}{\beta_y H_n^{(2)}(\beta_y a)}$$

$$A(z', \Phi') e^{j\psi(z', \Phi')} e^{j\beta(z'-z)} dz' \, d\beta_z \, d\Phi'$$

Note $\int e^{j\beta(z'-z)} d\beta$ cannot be set equal to $\delta(z'-z)$ in the integral on β_z

because of the term $\dfrac{H_n^{(2)'}(\beta_y a)}{\beta_y H_n^{(2)}(\beta_y a)}$

$$\left(\int_{\beta_z} f(\beta_z) e^{j\beta_z (z'-z)} d\beta_z \neq \delta(z'-z) \text{ in general.} \right)$$

Main contribution to double integral on β_z and z' comes from neighborhood of "srationary phase", that is, where

$$\frac{\partial}{\partial z'} \left[\psi(z',\Phi') + \beta_z (z'-z)\right] = 0 \tag{1}$$

$$\frac{\partial}{\partial \beta_z} \left[\psi(z',\Phi') + \beta_z (z'-z)\right] = 0 \tag{2}$$

If z' and β_z are far removed from stationary phase point, then integrand is rapidly oscillatory and adjacent positive and negative half cycles cancel closely. Let $\beta_z^s(z,\Phi')$ value of β_z at stationary phase point and note that (2) is satisfied if $z' = z$. Also, let

$$f(\beta_z, z', \Phi') = \frac{H_n^{(2)'}(\beta_y a)}{\beta_y H_n^{(2)}(\beta_y a)} A(z',\Phi')$$

If $f(\beta_z, z', \Phi')$ is essentially constant in neighborhood of stationary phase point, then the double integral on β_z and z' can be approximated by

$$f(\beta_z^s, z, \Phi') \int_{\beta_z} \int_{z'} e^{j\psi(z',\Phi')} e^{j\beta_z(z-z')} d\beta_z dz'$$

and since

$$\int_{\beta_z} e^{j\beta_z(z-z')} d\beta_z = 2\pi\delta(z-z')$$

a further approximation is

$$2\pi f(\beta_z^s, z, \Phi') e^{j\psi(z,\Phi')}$$

or $$H_\Phi(z,\Phi) = \frac{-i\beta}{\pi\eta} \sum_n \cos n\Phi \int_{\Phi'} \cos n\Phi' \frac{H_n^{(2)'}(\beta_y^s a)}{\beta_y^s H_n^{(2)}(\beta_y^s a)} A(z,\Phi') e^{i\psi(z,\Phi')} d\Phi' \tag{3}$$

where in (3) $A(z,\Phi') e^{i\psi(z,\Phi')} = E_z(\text{inc})$

$$\beta_y^s(z,\Phi') = (\beta^\partial - \beta_z^s(z,\Phi')^2)^{\frac{1}{2}}$$

Determination of $\beta_z^s(z,\Phi)$

From (1) and (2)

$$[\ \beta_z^s(z,\Phi') + (\frac{\partial\psi}{\partial z'})_{z-z'}\ ] = 0$$

where $\psi(z',\Phi') = -\beta[(L + a\cos\Phi)^2 + z'^2 + (a\sin\Phi)^2]^{\frac{1}{2}}$

$$\beta_z^s(z,\Phi') = \frac{\beta z}{D(z,\Phi')}$$

where $D = [(L + a\cos\Phi')^2 + z^2 + (a\sin\Phi')\ ]^{\frac{1}{2}}$

further approximation, take β_y^s for all Φ as value for fuselage center, i.e.

$\beta_y^s = \beta(1 - (\frac{z}{D})^2)^{\frac{1}{2}}$ and $A(z,\Phi')$ as value for fuselage center.

$$H_\Phi(z,\Phi) = -\frac{i\beta}{\pi\eta} \sum_n \cos n\Phi \frac{A(z)\, H_n^{(2)'}(\beta_y^s a)}{\beta_y^s H_n^{(2)}(\beta_y a)} \int_\Phi e^{i\psi(z,\Phi')} \cos n\Phi' d\Phi'$$

APPENDIX E. Radiation Field of an Antenna Placed Over Irregular Terrain

The radiation field at evaluation angle θ, of an antenna at height h placed over irregular terrain can be expressed as

$$F(\theta) = e^{j\beta h \sin\theta} - \int_{\psi=0}^{\pi/2} f(\psi, \theta)\, e^{-j\beta h \sin\psi}\, d\psi \qquad (E.1)$$

where $f(\psi, \theta)$ is the reradiation into elevation θ of a plane wave directed toward depression angle ψ, and $\beta = 2\pi/\lambda$. If the terrain is flat, infinite, and perfectly conducting, $f(\psi, \theta) = \delta(\psi - \theta)$, where the right side is a delta function, and (1) becomes the ordinary expression for radiation from an antenna and its image.

If the antenna is placed over smooth, but not flat terrain, with slope angles not exceeding about 0.5%, then $f(\psi, \theta)$ will consist of a narrow central peak near $\psi = \theta$. Thus, approximately,

$$F(\theta) = e^{j\beta h \sin\theta} - e^{-j\beta h \sin\theta} \int_{0}^{\pi/2} f(\psi, \theta)\, d\psi \qquad (E.2)$$

For flat infinite perfectly conducting terrain the integral on the right side would equal unity. For slightly rolling terrain, it can be written

$$1 + \alpha_R(\theta) + j\,\alpha_I(\theta) \qquad (E.3)$$

where

$$\alpha_R \ll 1$$

$$\alpha_I \ll 1$$

The functions α_R and α_I represent anomalous reflection. They will manifest themselves in a glide path system through the sideband pattern, by generation of a spurious in-phase component of sidebands which will affect the measured DDM. From E.2 and E.3, the spurious in-phase sideband component in the vicinity of the first sideband null is, to the first order, simply

$$\alpha_I(\theta)$$

Spurious sideband signal is then, to the first order, a function of elevation angle which depends only on terrain and not on antenna height. Changes of antenna height will not alter the shape of DDM disturbances or the angle at which they occur.

APPENDIX F. Nature of the Doppler-Shifted Interferences Encountered During Over Flights

Consider the localizer-monitor system shown in Fiugre F-1. Here, the plane is approaching the two arrays (a) and (c) from the far-field. A doppler shifted localizer signal (reflected from the plane) arrives at the monitor antenna (c) in addition to the direct signal. The doppler shift f_d is expressed below as a function of the rates of change of the length L_{ab} and L_{bc} (i.e., v cos c and v cos β).

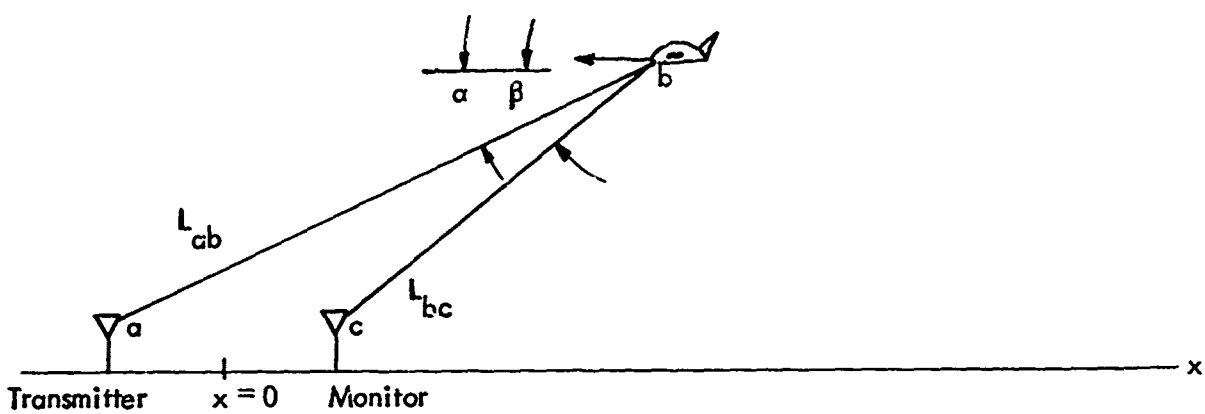

Figure F-1. Overflight Geometry.

v	=	velocity of aircraft = dx/dt
f_o	=	transmitted frequency = 110 MHz
f_r	=	received doppler frequency
f_d	=	doppler shift
c	=	speed of light
f_d	=	$f_o \frac{v}{c}$ (cos + cos)

The doppler shift can be sketched roughly as a function of x as shown in Figure F-2. The absolute doppler shift is asymptotic to $f_d = 2 f_o v/c$ in the far-field. In order for the reflected doppler shifted 90 Hz sideband to interfere with the direct 150 Hz sideband, $f_d = 60$ Hz, hence: $v = c f_d / 2 f_o = 175$ mph. This velocity will then cause perturbations in the monitor system.

sideband, f_d = 60 Hz, hence: $v = c\ f_d / 2 f_o$ = 175 mph. This velocity will then cause perturbations in the monitor system.

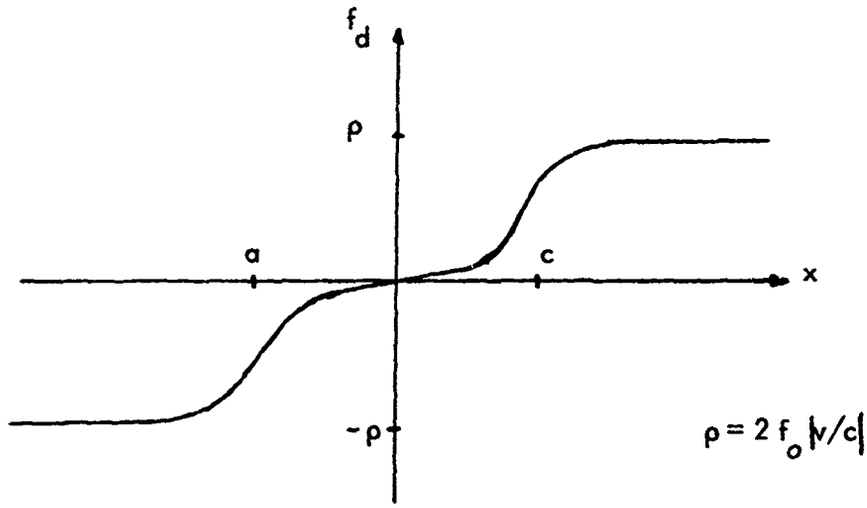

Figure F-2. Doppler Shift.

The doppler shift $f_d(x)$ is plotted in Figure F-2 for a constant velocity aircraft approach at low altitude. The transmitter is located at x = a and the monitor at x = c. Note that the doppler shift is zero as the plane approaches x = 0 (halfway between the two antennas).

APPENDIX G. Mathematical Model of a Monitor Receiver

A mathematical model of a monitor receiver is developed in this section. The basic configuration to be considered is shown in Figure G-1. The voltages at various points are identified in the following text.

The input to the second detector is assumed to be of the form

$$E_1 = E_s \cos \omega_c t + a E_s \cos [\omega_c t + \Phi(t)]$$

where, E_s = $1 + m_1 \cos \omega_1 t + m_2 \cos \omega_2 t$ (normal modulation)

ω_c = localizer carrier translated to the IF frequency

$\Phi(t)$ = doppler shift translated to the IF frequency (less than 10 Hz)

a = reflection loss coefficient ($0 \leq a \leq 1$)

ω_1 = 180π m_1 = 90 Hz modulation index

ω_2 = 300π m_2 = 150 Hz modulation index

An envelope detector as a second detector would produce an output equal to the magnitude (envelope) of $E_1 \cdot E_1$ can be written as [13].

$$E_1 = E_s [\cos \omega_c t + a \cos \Phi(t) \cos \omega_c t - a \sin \Phi(t) \sin \omega_c t]$$

$$E_1 = E_s \sqrt{1 + 2a \cos \Phi(t) + a^2} \cos [\omega_c t + \theta(t)]$$

where, $\theta(t) = -\tan^{-1} \{ a \sin \Phi(t) / [1 + a \cos \Phi(t)] \}$

and for simplicity let $\Phi(t) = \omega_d t$.

Therefore, $E_2 = E_s \sqrt{1 + 2a \cos \omega_d t + a^2}$

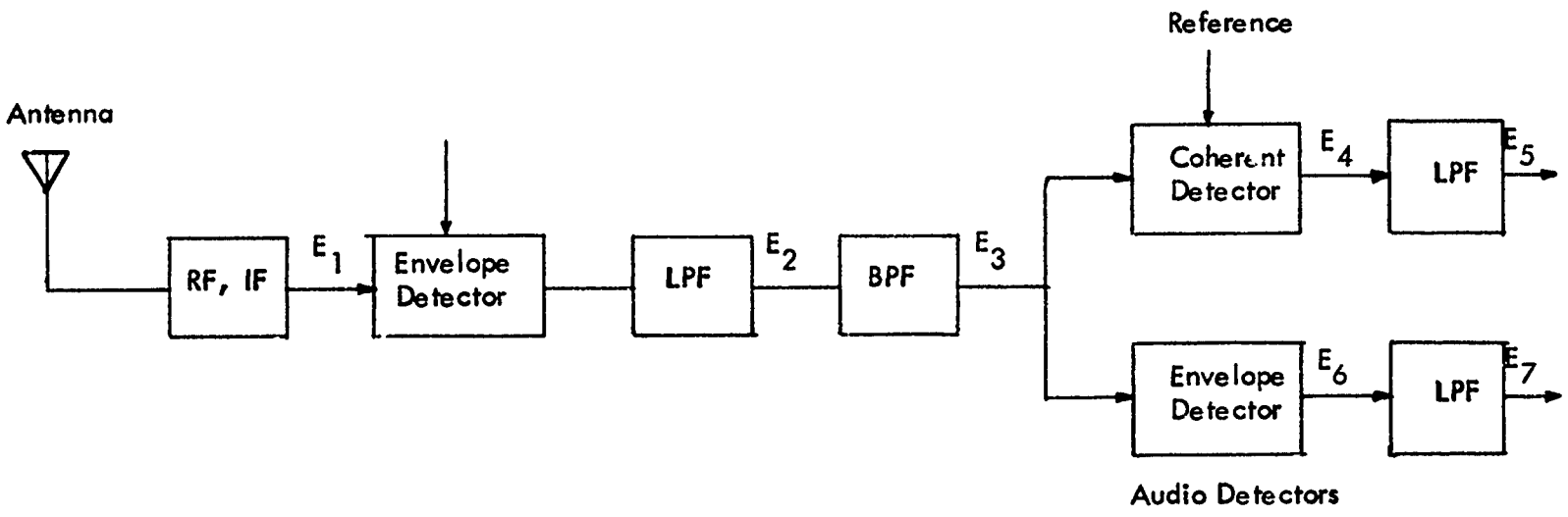

Figure G-1. Monitor Receiver Configuration I.

The Fourier series representing the radical is [13]

$$\sqrt{1+2a\cos\omega_d t+a^2}=\sum_{n=0}^{\infty} A_n(a)\cos n\,\omega_d t$$

with, $A_0(a) = 1+(a/2)^2+\frac{1}{4}(a/2)^4+\ldots$

$$A_1(a) = a\,[\,1-\tfrac{1}{2}(a/2)^2-\tfrac{1}{4}(a/2)^4-\ldots\,]$$

$$A_2(a) = -(a/2)^2\,[\,1-(a/2)^2-\ldots\,]$$

$$\vdots$$

$$A_n(a)\quad (a/2)^n$$

This radical will be approximated by considering only the first three terms in the cosine series neglecting the terms containing a^3 and higher.

$$\sqrt{1+2a\cos\omega_d t+a^2}\simeq[\,1+(a/2)^2\,]+a\cos\omega_d t-(a/2)^2\cos 2\,\omega_s t$$

Using this approximation, the expression for the components of E_2 very near the 90 Hz sideband can be expressed as (E'_2 is the component of E_2 near 90 Hz)

$$E'_2 = m_1\{\,(1+a^2/4)\cos\omega_1 t+(a/2)\,[\,\cos(\omega_1-\omega_d)t+\cos(\omega_1+\omega_d)t\,]$$
$$-(a^2/8)\,[\,\cos(\omega_1-2\omega_d)t+\cos(\omega_1+2\omega_d t\,]\,\}$$

This component will pass through the 90 Hz band pass filter (BPF) with minimal amplitude change. The BPF is assumed to have a linear (with frequency) phase shift over its useable range. Its output will then be, (E'_3 is the component of E. near 90 Hz)

$$E'_3 = m_1\{-(a^2/8)\cos[\,(\omega_1-2\omega_d)t-2\alpha]+(a/2)\cos[\,(\omega_1-\omega_d)\,t-\alpha]$$
$$+(1+a^2/4)\cos\omega_1 t+(a/2)\cos[\,(\omega_1+\omega_d)t+\alpha]-(a^2/8)\cos[\,\omega_1+2\omega_d)t+2\,\alpha]\,\}$$

Here α is the phase shift due to the BPF.

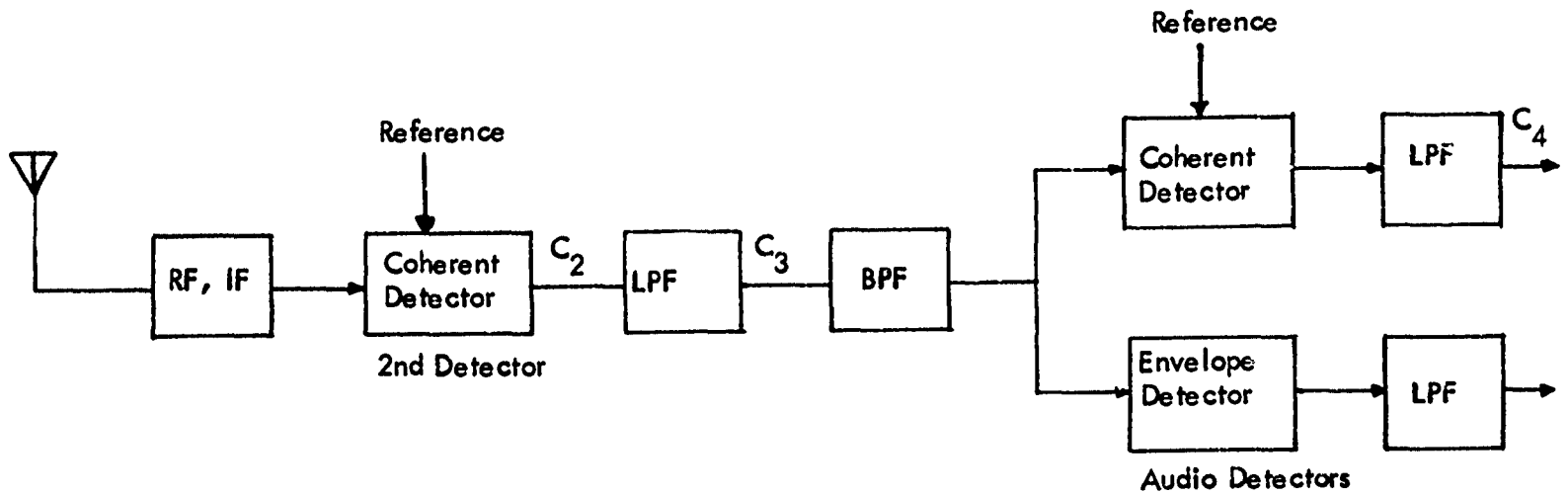

Figure G-2. Monitor Receiver Configuration II.

The following shows that the output E_5 due to the coherent (at 90 Hz) detector is identical to E_7 due to the envelope detector. E'_3 can be written as

$$E'_3 = m_1 \{ (1 + a^2/4) + a \cos(\omega_d t + \alpha) - (a^2/4) \cos^2(\omega_d t + \alpha) \} \cos \omega_1 t .$$

Assuming the low pass filter cuts off at some frequency higher than the second harmonic of the doppler we can write,

$$E_5 = E_7 = m_1 \{ (1 + a^2/4) + a \cos(\omega_d t + \alpha) - (a^2/4) \cos 2(\omega_d t + \alpha) \} .$$

Note that the dc value of E_5 is a function of the reflection coefficient a regardless of the cutoff frequency chosen for the low pass filter. The low pass filter affects only the terms slowly varying at the doppler frequency and its harmonics.

Consider the receiver performance (see Figure G-2) if the second detector is a coherent detector. This can be approximated in practice as a phase lock arrangement with a long time constant. The second detector output in accordance with Figure G-2 is

$$C_2 = E_s \{ \cos \omega_c t + a \cos(\omega_c + \omega_d) t \} \cos \omega_c t$$

Since the low pass filter removes the higher frequency terms

$$C_3 = E_s \{ 1 + a \cos \omega_d t \} .$$

The 90 Hz components of C_3 will now be considered as done previously,

$$C'_3 = m_1 [1 + a \cos \omega_d t] \cos \omega_1 t$$

It can be seen that if C_3' is detected by an envelope detector or a coherent detecior that the results will be

$$C_4 = m_1 [1 + a \cos \omega_d t + a] .$$

The dc component of this term is not corrupted by the interfering signal if $\omega_d \neq 0$. The final low pass filter can be adjusted in this case to remove a large portion of the disturbance caused by the doppler shift.